Liquid-Crystalline Perylene Bisimide and Diketopyrrolopyrrole Assemblies

15 83

Dissertation zur Erlangung des

naturwissenschaftlichen Doktorgrades

der Julius-Maximilians-Universität Würzburg

vorgelegt von

Markus Hecht

aus Marktredwitz

Würzburg 2020

Eingereicht bei der Fakultät für Chemie und Pharmazie

am: 21.09.2020

Gutachter der schriftlichen Arbeit:

1. Gutachter: Prof. Dr. Frank Würthner

2. Gutachter: Jun.-Prof. Dr. Ann-Christin Pöppler

Prüfer des öffentlichen Promotionskolloquiums:

1. Prüfer: Prof. Dr. Frank Würthner

2. Prüfer: Jun.-Prof. Dr. Ann-Christin Pöppler

3. Prüfer: Prof. Dr. Volker Engel

Datum des öffentlich Promotionskolloqiums:

26.11.2020

Doktorurkunde ausgehändigt am:

____

List of Abbreviations

1D	One-dimensional
2D	Two-dimensional
3D	Three-dimensional
A	Acceptor
An	Analyzer
AFM	Atomic force microscopy
aPP	Amorphous polypropylene
BOC	*Tert*-butyloxycarbonyl
CCD	Charge-coupled device
Col$_{\text{h}}$	Columnar hexagonal
Col$_{\text{obl}}$	Columnar oblique
Col$_{\text{r}}$	Columnar rectangular
Col$_{\text{rhomb}}$	Columnar rhombohedral
COMPASS	Condensed-phase Optimized Molecular Potentials for Atomistic Simulation Studies
CT	Charge transfer
CV	Cyclic voltammetry
D	Donor
DBR	Distributed Bragg reflectors
DCC	*N*,*N'*-dicyclohexylcarbodiimide
DFT	Density functional theory
DMF	*N*,*N'*-Dimethylformamide
DMSO	Dimethyl sulfoxide
DPP	Diketopyrrolopyrrole
DPTS	4-(Dimethylamino)pyridinium *p*-toluenesulfonate
DSC	Differential scanning calorimetry
ESI	Electrospray ionization
ET	Energy transfer
FP-TRMC	Flash photolysis time-resolved microwave conductivity
fsTAS	Femtosecond transient absorption spectroscopy
FT-IR	Fourier-transform infrared spectroscopy
FWHM	Full width at half maximum

h	Hour(s)
H-bond	Hydrogen bond
HOMO	Highest occupied molecular orbital
HOPG	Highly oriented pyrolytic graphite
HRMS	High resolution mass spectrometry
ITO	Indium tin oxide
LC	Liquid-crystalline
LUMO	Lowest unoccupied molecular orbital
m.p.	Melting point
MALDI	Matrix-assisted laser desorption ionization
MAXS	Middle angle X-ray scattering
MCH	Methylcyclohexane
min	Minute(s)
m.p.	Melting point
NMR	Nuclear magnetic resonance
OD	Optical density
OTES	Octadecyltriethoxysilane
P	Polarizer
PBI	Perylene bisimide
PES	Potential energy surface
PET	Photoinduced electron transfer
POM	Polarized optical microscopy
rpm	Revolutions per minute
S	Shearing direction
S_0	Singlet ground state
S_1	First singlet excited state
S_2	Second singlet excited state
SAED	Selected area electron diffraction
SAXS	Small angle X-ray scattering
SC	Soft-crystalline
SEM	Scanning electron microscopy
SWV	Square wave voltammetry
TAPOT	Trialkoxyphenylene-oligothiophene

TBAHFP	Tetrabutylammonium hexafluorophosphate
TCSPC	Time-correlated single photon counting
TDM	Transition dipole moment
THF	Tetrahydrofurane
TLC	Thin-layer chromatography
TOF	Time of flight
UV	Ultraviolet
Vis	Visible
WAXS	Wide angle X-ray scattering
XRS	X-ray scattering

Variables and constants

α	Torsion angle
α_{agg}	Degree of aggregation
δ	Chemical shift
$\sum\mu$	Sum of the charge carrier mobility
ε	Extinction coefficient
θ	Bragg angle
λ	Wavelength
$\tilde{\nu}$	Wavenumber
ξ	Correlation length
ρ	Density
σ	Cooperativity parameter
σ_{ϕ}, σ_{θ}	Fiber disorder parameters
τ	Lifetime
Φ_{Fl}	Fluorescence quantum yield
φ	Quantum yield of charge carrier generation
ψ	Light intensity
A	Absorbance, sensitivity factor
a, b, c	Lattice parameters
a.u.	Arbitrary units
c	Concentration
d	Path length, distance between two parallel lattice planes
E	Energy
$E_{½}$	Half-wave potential
F_{light}	Filling factor
h	Height
hkl	Miller indices
$\Delta\mathrm{H}_{\mathrm{elong}}$	Elongation enthalphy
K	Shape factor
K_a	Dimensionless equilibrium constant for the activation step of the supramolecular polymerization
K_2	Dimerization constant
K_{elong}	Elongation constant

K_{nuc}	Nucleation constant
I	Current
L	Layer lines, Length
m	Mass
I_{DS}	Drain current
J_{Coulomb}	Coulomb coupling energy
J_{CT}	Charge transfer coupling energy
J_{total}	Total coupling energy
M	Molar mass
N	Number of correlated molecules
N_{A}	Avogadro constant (6.022×10^{23})
P_{r}	Reflected microwave power
r	Center-to-center distance
T	Temperature
T_{elong}	Elongation temperature
V_{aliph}	Molecular volume of the aliphatic part
V_{ar}	Molecular volume of the aromatic part
V_{CH}	Volume of the CH units
V_{CH2}	Volume of the CH_2 units
V_{CH3}	Volume of the CH_3 units
$V_{col\text{-}strat}$	Volume of the columnar stratum
V_{DS}	Drain-source voltage
V_{mol}	Molecular volume
V_{UC}	Unit cell volume
W	Width
Z	Number of molecules per unite cell
$\varnothing$	Diameter

Table of Contents

Chapter 1

–

Introduction and Aim of the Thesis

In recent years, the interest in π-conjugated materials for organic electronics increased since they provide desirable properties such as mechanical flexibility,[1,2] bio-compatibility[3,4] and can potentially be used in low-cost roll-to-roll processing.[5-7] Hence, significant effort has been devoted to the investigation of both small molecules[8,9] and polymers[10-12] for the application in optoelectronic devices.[13] Within the realm of small molecules, liquid crystals have had great impact on the advancement of technologies based on organic compounds as they provide orientational and dielectric anisotropy.[14-19] Furthermore, their self-healing properties[20,21] and fluidity enable macroscopic alignment by external forces such as mechanical friction,[22] electric fields[23] or light.[24] On the one hand, rod-like nematic liquid crystals majorly changed the way we experience technology nowadays as they paved the way to thin displays with low energy demand.[25] On the other hand, discotic liquid crystals are well known for their ability to form ordered one-dimensional (1D) structures with high charge carrier mobility, enabling the implementation in organic field effect transistors and solar cells.[26-30] The efficiency of the electronic processes in such applications is mainly determined by two factors: The molecular properties and the intermolecular arrangement. While the former is well understood and energy levels of molecules can be easily adjusted by structural modification of the monomers, the precise control of the intermolecular arrangement that is required to form, e.g., percolation pathways for charge transport remains challenging.[31]

Supramolecular chemistry is a versatile approach to organize monomeric building blocks into self-assembled structures utilizing non-covalent interactions like hydrogen bonds (H-bonds), dispersion interactions or metal-ligand interactions.[32-40] Consequently, applying the supramolecular approach to liquid crystals is promising for the realization of functional materials with exciting anisotropic optic and electronic properties.[15,26,41] Particularly intriguing materials can be realized with dyes like perylene bisimides (PBIs)[14,35,42-44] or diketopyrrolopyrroles (DPPs)[45-49] that are already well-established in the field of organic electronics, exhibit outstanding photochemical and thermal stability, are excellent fluorophores, and show a high tinctorial strength.

Such self-assembled structures of dye-based liquid crystals exhibit optical properties that deviate from their monomeric building blocks due to Coulomb, charge-transfer (CT) and vibrational interactions between transition dipole moments (TDMs) of chromophores in close proximity.[50-56] Depending on their relative orientation, either H- or J-aggregates are formed, which show distinct optical properties. While the former exhibit hypsochromically shifted absorptions bands and quenched fluorescence with respect to the monomer, the latter are known to exhibit narrowed, bathochromically shifted absorbtion bands and almost resonant fluorescence with an increased radiative rate.[33,57] Therefore, the preparation of liquid-crystalline (LC) J-aggregates based on chromophores such as PBIs is intruiging for the exploitation as functional materials.

In this regard, the first strongly coupled PBI J-aggregates with high fluorescence quantum yield could be realized in 2007 by Kaiser *et al.*.[58] The design was based on a PBI with free imides and four phenoxy substituents in bay positions that induce a contortion of the PBI π-core.[42] The phenoxy groups are further decorated with trialkoxyphenyl units via an ester functionality to provide sufficient solubility in organic solvents (Figure 1a). The complementary π-π-interactions between the contorted PBI π-core and H-bonding between free imides promotes the formation of 1D supramolecular polymers with slip-stacked chromophores and, hence, J-type excitonic coupling.[58,59] Herbst *et al.* could later demonstrate that the contrast between the rigid π-core and the flexible alkyl chains of the trialkoxyphenyl units causes nanosegregation facilitating the formation of liquid-crystalline (LC) phases.[60,61] This new approach is advantageous compared to the common strategy towards LC PBIs which constitutes the functionalization of the imide position with mesogenic units and yields columnar mesophases with cofacially π-stacked chromophores that exhibit H-type or only weak J-type excitonic coupling.[62-67] In contrast, the new design allows to produce materials that retain strong J-coupling in the LC state.[60,61,68] These phases consist of helical multistranded arrangements of H-bonded PBIs. Importantly, this encodes the orientation of the PBI's S_0-S_1 transition dipole moment (TDM) parallel to the columnar long axis. Thus far, such arrangements were unprecedented as conventional columnar phases of discotics feature the TDM perpendicular to the columnar long axis (Figure 1b).[26] In addition, Herbst *et al.* could demonstrate that the number of strands incorporated in these multistranded PBI J-aggregates can be adjusted from two to four strands by minor modifications of the monomeric building blocks[60,61] and spectroscopic investigations revealed how the particular supramolecular architecture influences the exciton mobility.[69,70]

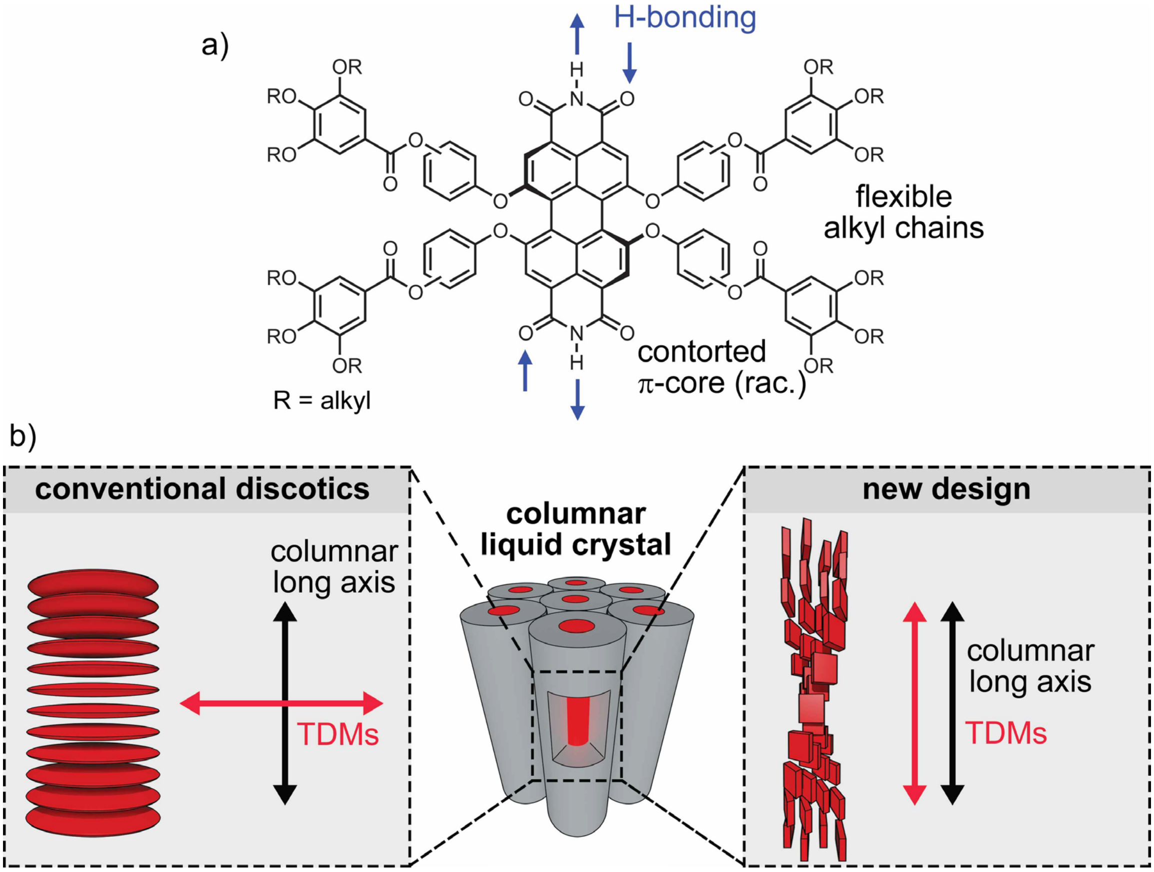

Figure 1. a) General chemical structure of tetraphenoxy substituted PBIs that self-assemble into J-aggregates by H-bonding interactions. b) Schematic illustration of the orientation of molecules within columnar LC phases of conventional discotics (left) and in LC PBI J-aggregates (right).

Based on the exciting results obtained for PBI J-aggregates, one aim of this thesis was to enhance the functionality of these LC materials by introducing electron-rich trialkoxyphenyl-oligothiophene (TAPOT) units comprising one to three thiophene units to generate columnar mesophases with narcissistically arranged donors and acceptors. The optic and electronic properties of the molecules as well as the self-assembly process in solution should be investigated with UV/Vis and fluorescence spectroscopy as well as cyclic voltammetry (CV). Their structure in the respective LC phase should be investigated with a combination of polarized optical spectroscopy and microscopy, differential scanning calorimetry (DSC), wide- and middle-angle X-ray scattering (WAXS and MAXS) experiments as well as modelling approaches. The structure-property relationship arising from the different electronic properties of the monomers and the distinct packing arrangement in the LC state should be investigated with respect to possible applications as functional materials.

Previous studies could demonstrate that LC PBI J-aggregates exhibit outstanding exciton transport properties along the columnar domains, which is of great interest for applications based on supramolecular materials where coherently coupled chromophores or exciton transport to specific locations are desired.[69-74] Accordingly, the preparation of two-dimensional (2D) mesophases in form of lamellar structures could pave the way towards exciton transport in two dimensions. In this regard, another goal was to extend the accessible LC architectures from columnar to lamellar phases by fine-tuning the steric requirements of the appended substituents. Therefore, a general approach to obtain defined multistranded columnar or lamellar arrangements should be developed.

The majority of the research presented in this thesis deals with the precise control of the intermolecular arrangement of LC PBI materials. However, towards the preparation of functional materials it is necessary to be able to translate the control over the intermolecular arrangement on the nanoscale to macroscopic length scales. For this, design principles applied in *Chapters 3* to *5*, namely the use of trialkoxyphenyl minidendrons to facilitate nanosegregation and H-bond directed self-assembly, should be applied to DPP chromophores. The resulting LC materials should then be investigated regarding the propensity for electrospinning into macroscopic fibers with defined intermolecular arrangement.

The first part of ***Chapter 2*** gives an introduction on J-aggregates including some historical background and theoretical considerations necessary to understand their distinct optical properties. Furthermore, the structural considerations that enabled the preparation of PBI J-aggregates are explained. Their self-assembly process in solution and structural modifications to generate homochiral fibers, NIR-absorbing J-aggregates as well as organo- and hydrogels are discussed. The physical properties of PBI J-aggregates as well as the concomitant application in organic electronic and photonic devices are presented. The second part of this chapter elaborates the basic methods required to investigate the LC phases presented in this thesis.

Chapters 3 and ***4*** describe how the introduction of electron-rich TAPOT units into the molecular structure of tetraphenoxy substituted PBIs facilitates the formation of narcissistically arranged acceptor–donor core–shell structures of LC PBI J-aggregates. Moreover, their optic and electronic properties as well as the structure elucidation of the LC phases are discussed. Additionally, the application of the materials as photoconductor in two-contact devices and approaches towards aligned active layers for improved functional properties are presented. Lastly, the intrinsic charge separation and transport properties arising from the particular supramolecular structure, which are not dominated by macroscopic effects, such as film quality, are investigated by femtosecond transient absorption spectroscopy (fsTAS) and flash photolysis time-resolved microwave conductivity (FP-TRMC).

In ***Chapter 5***, the formation of columnar and lamellar phases of a tetra-bay-acyloxy substituted PBI with distinct absorption profiles is discussed. The two LC mesophases can be prepared by fast and slow cooling of a hot monomeric solution in methylcyclohexane (MCH), respectively. The structural properties were investigated by WAXS measurements and exciton-vibrational pattern analysis. Concentration- and time-dependent UV/Vis absorption spectroscopy shine light on the pathway complexity of the supramolecular polymerization.

Chapter 6 deals with the formation of supramolecular polymers and columnar liquid crystals of DPP molecules. Concentration- and temperature-dependent UV/Vis absorption spectroscopy reveals the cooperative self-assembly into nanofibers and the structure in the LC state is elucidated. Furthermore, electrospinning experiments into fibers are discussed focusing on the defined interchromophoric arrangement on macroscopic length scales.

In ***Chapter 7*** and ***8*** the research presented in this thesis is summarized and critically discussed in English and German.

Chart 1. Chemical structures of the molecules investigated in this thesis.

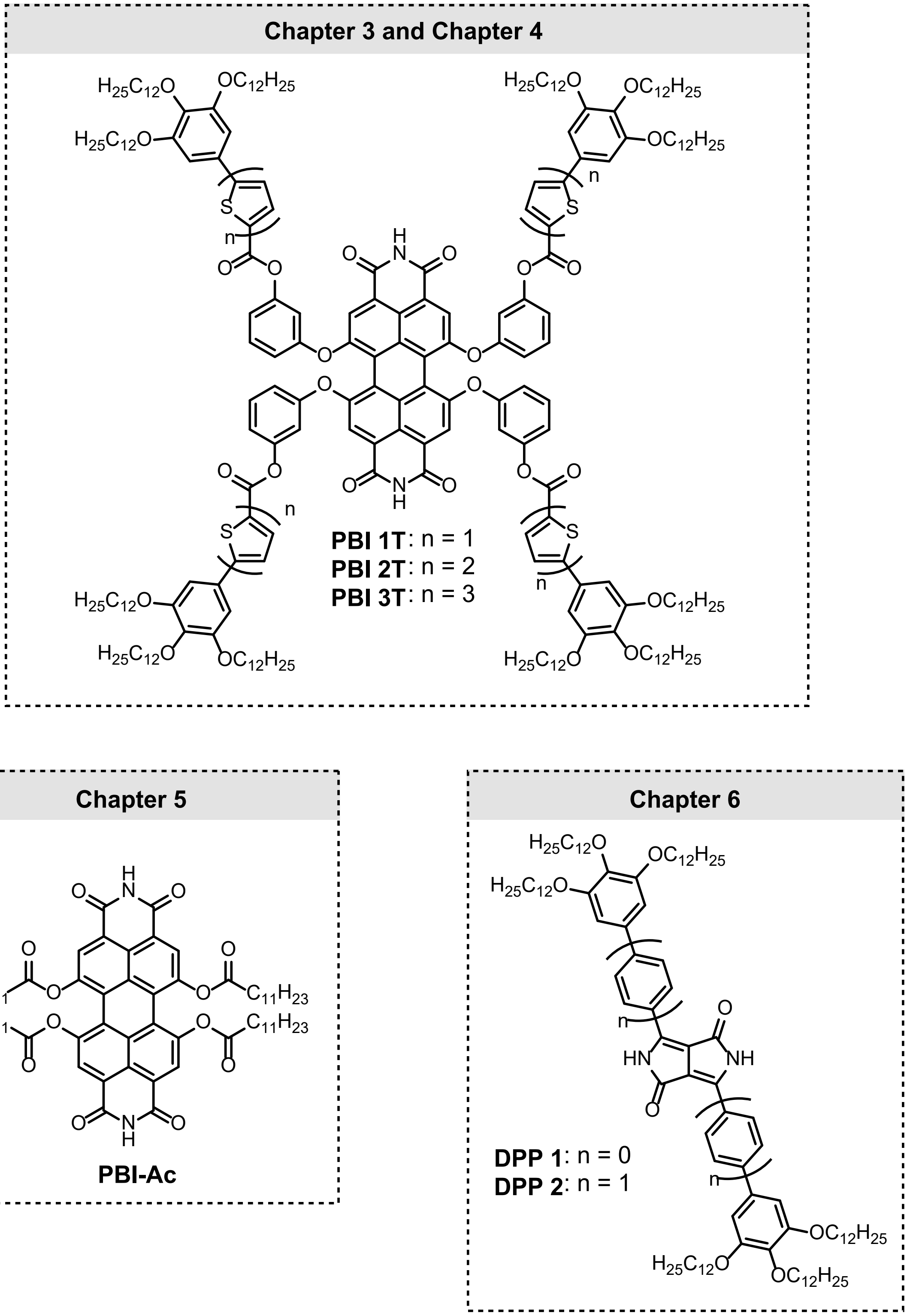

Chapter 2

–

State of Knowledge

2.1. Supramolecularly Engineered J-Aggregates Based on Perylene Bisimide Dyes

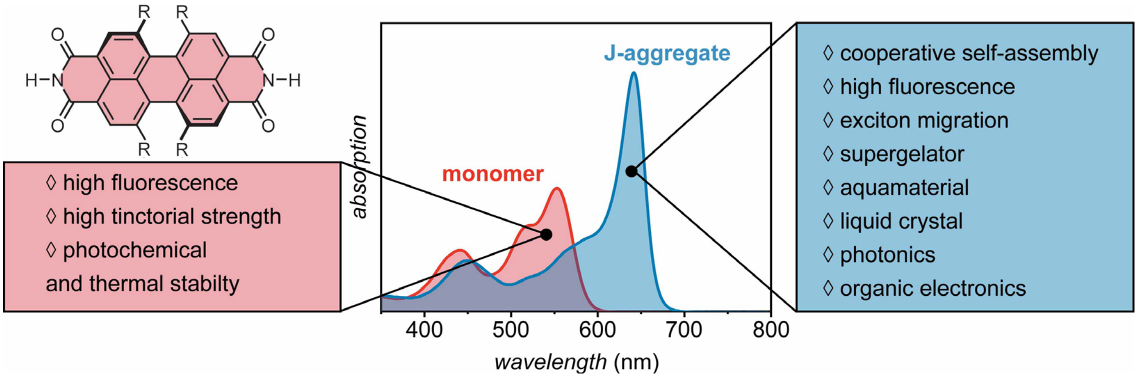

Abstract: The discovery of the self-assembly of cyanine dyes into J-aggregates had a major impact on the development of dye chemistry due to the emergence of new useful properties in the aggregated state. The unique optical features of these J-aggregates are narrowed, bathochromically shifted absorption bands and almost resonant fluorescence with an increased radiative rate that result from the coherently coupled molecular transition dipoles arranged in a slip-stacked fashion. Due to their desirable properties, J-aggregates gained popularity in the field of functional materials and enabled efficient photosensitization of silver halide grains in color photography. However, despite of a good theoretical understanding of structure-property relationships by the molecular exciton model, further examples for J-aggregates remained scarce for a long time as supramolecular designs to guide the formation of dye aggregates into the required slip-stacked arrangement were lacking.

Drawing inspiration from the bacteriochlorophyll *c* self-organization found in the chlorosomal light harvesting antennas of green sulphur bacteria, we envisioned the use of nature's supramolecular blueprint to develop J-aggregates of PBIs. This class of materials is applied for high performance color pigments and as n-type organic semiconductor in transistors and solar cells. Combining outstanding photochemical and thermal stability,

high tinctorial strength and excellent fluorescence, PBIs are therefore an ideal model system for the preparation of J-aggregates with a wide range of potential applications.

In this Chapter, we elucidate how a combination of sterical constraints and hydrogen bonding receptor sites can guide the self-assembly of PBI dyes into slip-stacked packing motifs with J-type exciton coupling. We will discuss the supramolecular polymerization of multiple hydrogen-bonded PBI strands in organic and aqueous media and how minor structural modifications in monomeric PBI molecules can be used to obtain near-infrared absorbing J-aggregates, organogels or thermoresponsive hydrogels. In order to fully explore their potential, we have studied PBI J-aggregates in collaborative work with spectroscopists, physicists and theoreticians. This way, exciton migration over distances of up to 180 nm was shown and insights into the influence of static disorder on the transport of excitation energy in PBI J-aggregates was derived. Further, application of PBI J-aggregates as functional materials was demonstrated in photonic microcavities, thin-film transistors and organic solar cells.

2.1.1 Introduction

Self-assembled chromophores, i.e. dye aggregates, usually exhibit optical properties that differ distinctively from those of the corresponding monomers. A most prominent feature in the UV/Vis absorption spectra of dye aggregates is either a bathochromic or a hypsochromic shift of the absorption maximum caused by the coupling of the dyes' TDMs. Depending on the direction of the spectral shift, these dye aggregates are then called either J-aggregates or H-aggregates, respectively.

About 20 years after the discovery of J-aggregates by Scheibe[75,76] and Jelley[77,78] in the late 1930s, the theory required to explain their optical properties, namely a narrow, bathochromically shifted absorption maximum with respect to the monomer and a nearly resonant fluorescence with an increased radiative rate, was developed by Davydov[50] and Kasha.[51,52] Davydov correctly interpreted the electronic and vibrational spectra of organic crystals as a result of interacting molecules.[50] According to his theory, an excited state is treated as a delocalized Frenkel exciton resulting in changes of the photophysical properties upon aggregation. Kasha advanced this theory further and established structure-property relationships for self-assembled molecular aggregates.[51,52] Using the Born-Oppenheimer and point-dipole approximation, Kasha described the exciton coupling energy by the Coulomb interaction between TDMs of the chromophores as a function of their relative orientation. Figure 2a (top) shows how the Coulomb coupling energy (J_{Coul}) of two PBI molecules with linearly aligned TDMs (green arrows) at a constant π-π-distance of 3.5 Å changes upon longitudinal displacement of the dyes according to Kasha's theory. The strongest coupling is expected for the cofacial stacking (longitudinal shift of 0 Å) in H-aggregates that are non-emissive due to a forbidden lowest energy transition. J_{Coul} undergoes a change of sign at a longitudinal shift of ~6.75 Å, where the hypsochromic shift of an H-aggregate inverts to the bathochromic shift of a J-aggregate. Since the lowest excited state is now allowed, fluorescence is observed. This relatively simple model is often the first choice for chemists to explain the optical features of self-assembled chromophores.

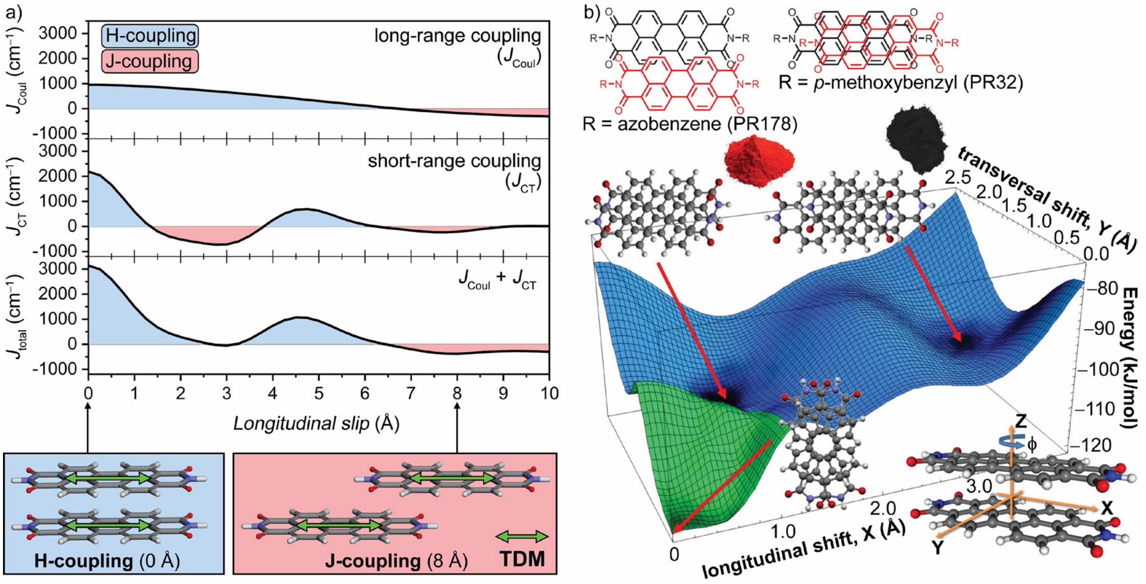

Figure 2. a) Long-range (top) and short-range (middle) exciton coupling for a PBI dimer with a constant distance of 3.5 Å between the π-planes as a function of the longitudinal slip. The long-range coupling was calculated employing the transition charge method[79] (ωB97/def2-SVP) in combination with the Mulliken population analysis. The short-range coupling was determined by $J_{CT} = -2t_e t_h / E_{CT} - E_{S1}$. The electron and hole transfer integrals t_e and t_h were calculated by using the energetic splitting in dimer model[80] (B3LYP/def2-SVP). A large energetic separation of the CT and Frenkel exciton state ($E_{CT} - E_{S1} = 5600$ cm^{-1}), and thus the validity of the perturbation regime, has been assumed. Calculations shown in Figure 2a were carried out by Dr. David Bialas.Sum of long- and short-range coupling as a function of the longitudinal slip (bottom) and illustration of the corresponding intermolecular arrangement for 0 Å and 8 Å longitudinal displacement. b) Two commercial perylene pigments with packing arrangement in the crystal and PES of ground state PBI dimers depending on translational shifts (blue) and rotational shifts (green). Figure 2b was adapted from ref. [62], copyright 2008 American Chemical Society.

However, this simple picture fails at interchromophoric distances smaller than the spatial extent of the TDM. A profound advancement in the understanding of the influence of the interchromophoric arrangement on the optical properties was provided by Spano and co-workers.[53-55] They could show that π-stacked chromophores exhibit significant wave function overlap between neighboring molecular orbitals facilitating short-range charge transfer in addition to the long-range Coulomb interactions considered in Kasha's model. This creates effective short-range exciton coupling, thereby inducing J- or H-aggregate properties, depending on the sign. For PBI chromophores, the sign changes several times upon longitudinal displacement of two side-by-side arranged molecules (Figure 2a, middle). The total exciton coupling (J_{total}, Figure 2a, bottom), neglecting vibrational contribution,[56] is composed of both, long-range Coulomb interactions (Figure 2a, top) and short-range CT interactions (Figure 2a, middle). J_{total} is maximized in the cofacial arrangement of the chromophores (0 Å, H-coupling) and undergoes a change of sign at 2.75 Å, 3.25 Å and 6.5 Å at which $J_{\text{total}} = 0$. The strongest J-coupling is then reached at a longitudinal shift of 8 Å.

Accordingly, chromophores need to stack in a slip-stacked arrangement to exhibit J-type exciton coupling. However, this is commonly not favored for larger π-systems like PBI chromophores which tend to maximize dispersion interactions between π-scaffolds by cofacial stacking. The calculated potential energy surface (PES) for PBI dimers (Figure 2b) reveals two minima if only translational shifts are considered and a third deeper minimum if rotational shifts are included.[62] Interestingly, most of the commercial red and black pigments of PBIs show packing arrangements that are close to either of the two calculated minima of the blue PES, respectively, whilst most of the PBI dye aggregates in solution are packed with rotational displacement as suggested by the green PES.[81,82] The comparison of Figure 2a and b highlights that the slip angle for the black pigments is not sufficiently large to attribute the coloristic properties to a pristine J-aggregate. Instead, the bathochromic shift arises from the short-range CT coupling at the longitudinal shift of about 3 Å and concomitantly none of the black pigments shows fluorescence. There were accordingly no J-aggregates known for this class of dyes prior to our first report[63] and examples of J-aggregates are in general scarce for most of the common dyes and pigments. Exceptions are found for cationic cyanines in water, squaraines and chlorophylls, which exploit either the hydrophobic effect, donor–acceptor interactions or specific embedding in protein matrices to achieve the required slip-stacked interchromophoric arrangement.[33,57,83] Nevertheless, by proper use of steric constraint or self-sorting induced by amphiphilic features, researchers were able to induce J-type coupling also in molecules with extended π-surfaces, e.g. dibenz[*a,j*]anthracene-based macrocycles,[84] hydroazaacene dicarboximides,[85,86] and BF_2-azadipyrromethene.[87]

While these examples mainly rely on the steric effect that leads to the formation of slip-stacked arrangements, the light-harvesting complex in green sulphur bacteria, the chlorosome, illustrates a smarter approach towards J-coupled chromophore aggregates. Here an interplay of metal-ligand coordination, H-bonding and π–π-interactions accomplishes spatial assembly of chlorophyll dyes to attain J-type exciton coupling and efficiently direct excitation energy to the reaction center.[88,89] This synergistic use of multiple intermolecular forces to arrange chromophores inspired us to mimic nature for the creation of functional J-aggregates of PBI dyes. PBIs are used as high performance pigments with outstanding photochemical and thermal stability, high tinctorial strength, excellent fluorescence with quantum yields up to unity and intriguing optoelectronic properties, rendering them highly desirable as building blocks for J-aggregates.[35,81]

In this Account, we summarize our research efforts on the J-aggregate forming PBIs depicted in Chart 2. After a discussion of the design principle and the construction of PBI J-aggregates in solution, we will summarize our collaborative efforts on applications of PBI J-aggregates as functional materials.

Chart 2. Chemical structures of the PBIs discussed in *Chapter 2.1*.

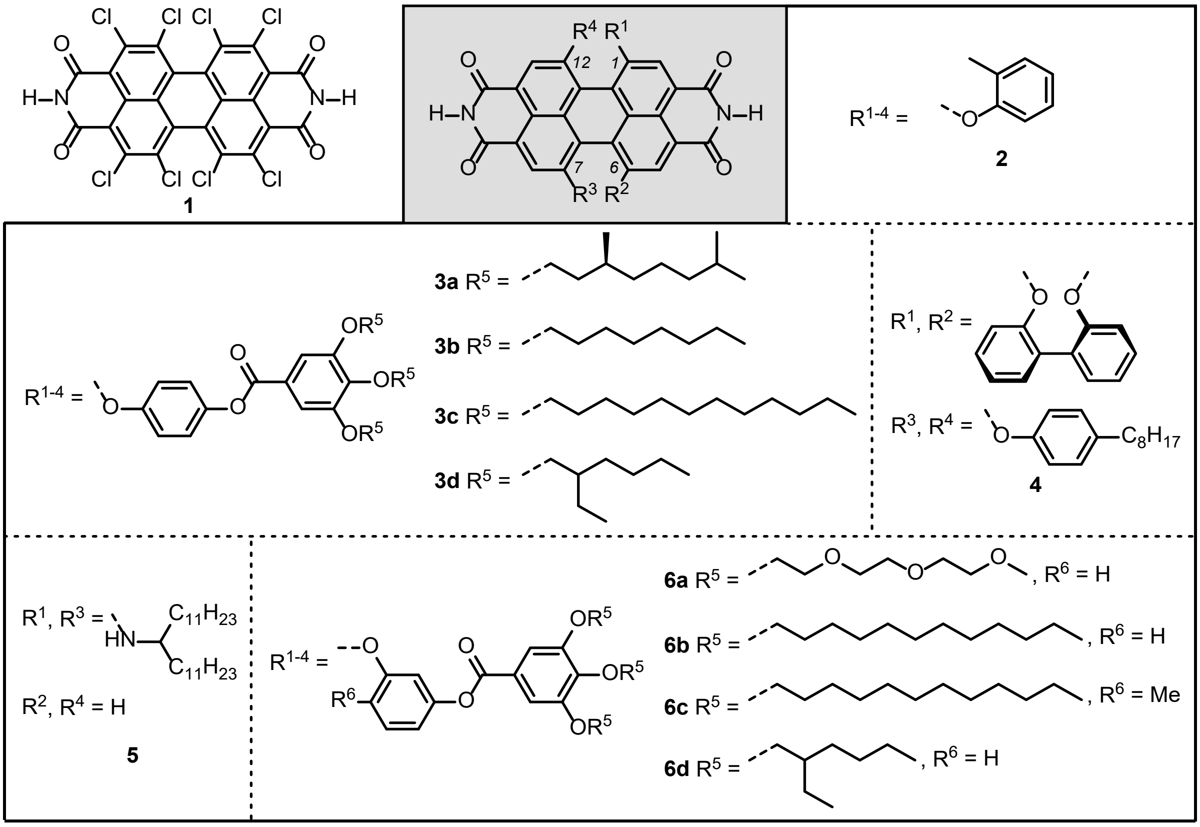

2.1.2. Structural Considerations

Whilst the packing in molecular solids is governed by the optimization of intermolecular interactions in all directions which is mostly achieved by the densest three-dimensional packing arrangement, aggregation in solution can be controlled by suitable substituents in monomeric building blocks towards one- or two-dimensional structures. For the parent PBI dyes with their planar π-scaffold and a large quadrupole moment, rotationally displaced arrangements are energetically preferred and it is accordingly not easy to direct a packing arrangement that is substantially different from the minimum shown in Figure 2b.[62,63] However, with the distortion of the π-scaffold upon functionalization of the bay area with two or more substituents this situation changes and slip-stacked arrangements become more common.[63] Such slip-stacked arrangements have indeed already been observed for a variety of PBIs bearing various substituents at the imide nitrogens.[64-67] The core-twist induced by the steric congestion in the bay area causes the formation of the respective *P*- and *M*-atropoenantiomer (Figure 3a). The conversion barrier between the two conformers depends strongly on the size of the substituent attached to the 1,6,7,12 bay-positions. Here only large substituents such as bromine afford an energy barrier sufficiently high for the separation of atropoenantiomers under ambient conditions (Figure 3b).[42,90] The best way to encode a sufficiently large longitudinal slip with desirable longitudinal displacement of >6.5 Å to afford J-aggregates is, however, provided if the distortion of the PBI π-scaffold by tetra-bay-substitution is combined with H-bonding between imide units. Generally, such H-bond directed self-assembly supports the formation of 1D or 2D structures depending on the arrangement of the respective atropoenantiomers. While homochiral self-assembly appears to prevail especially in solution leading to the formation of helices (Figure 3c),[91] the alternating stacking of *P*- and *M*-strands of H-bonded PBIs can be observed in crystals of octachloro-substituted PBI **1** which forms an extended, brickwork-like arrangement,[92] or tetra(2-methylphenoxy)-substituted PBI **2** which forms a double-stranded arrangement of *P*- and *M*-strands (Figure 3d).[93]

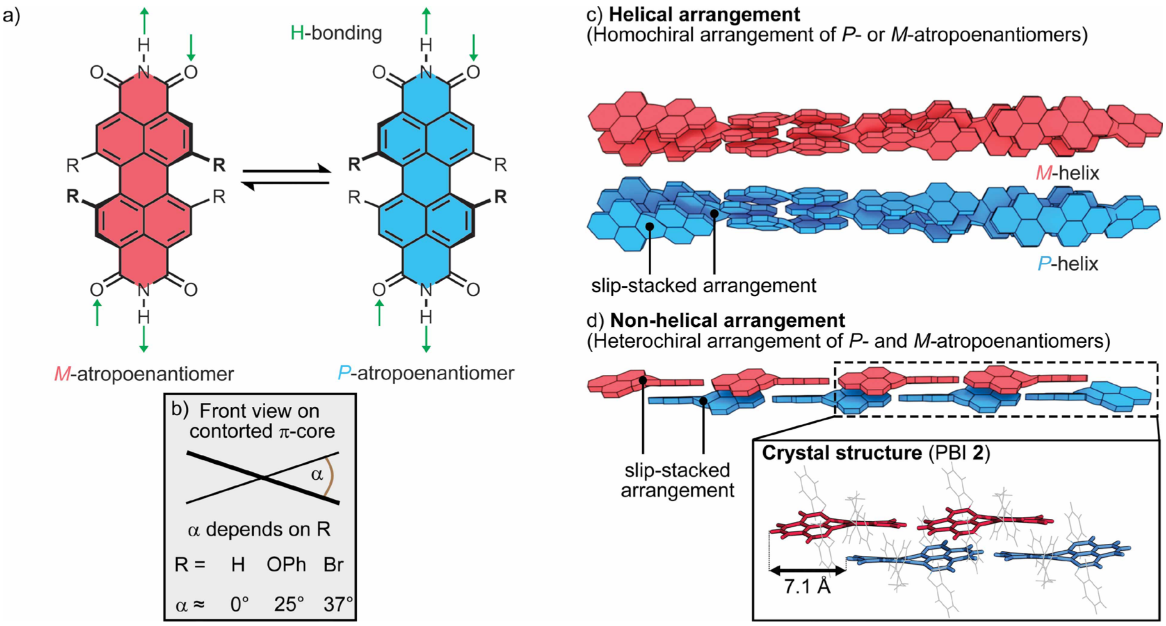

Figure 3. a) Equilibrium between the P- and M-atropoenantiomer of tetra-bay substituted PBIs. b) Influence of the bay-substituent on the torsion angle α between the two naphthalene subunits. c) Homochiral and d) heterochiral slip-stacks of the atropoenantiomers leading to c) helical and d) non-helical structures.

2.1.3. PBI J-Aggregates in Solution

The contorted π-core required for the slip-stacked arrangement can be programmed into the molecular structure by fourfold substitution in bay-position with substituents of sufficient steric demand. Phenoxy groups proved to be an excellent choice as they can easily be further modified, e.g. with trialkoxyphenyl units connected *via* an ester functionality to enhance the solubility of the dyes (Figure 4a). Monomers based on this design exhibit UV/Vis absorption profiles with the S_0-S_1 transition at around 570 nm, and a rather broad full-width-at-half-maximum (FWHM) of around 2500 cm^{-1} (Figure 4b).[42,58,59] These dyes are typically highly emissive with quantum yields close to unity.

In non-polar solvents like MCH, in which H-bonds and π-π-interactions are strong, these PBIs form supramolecular polymers. The absorption maximum of these aggregates is shifted to about 640 nm with a narrowed FWHM of around 1000 cm^{-1} and the extinction coefficient is increased (Figure 4b). Furthermore, these dyes typically retain strong fluorescence in the aggregated state with quantum yields of up to > 90% and with small Stokes shifts.[58,59] Therefore, the resulting structures can be unambiguously classified as J-aggregates.

The self-assembly into supramolecular polymer chains follows a cooperative nucleation-elongation mechanism[94,95] as determined by temperature- and concentration-dependent UV/Vis (exemplarily shown for PBI **3a**, Figure 4b) and fluorescence spectroscopy. The J-aggregates consist of 1D nanofibers (Figure 3c) formed by intertwined strands of H-bonded PBIs that are longitudinally displaced inducing the distinct optical features. The crucial role of H-bonds in the aggregation process and the orientation of the PBIs within the fibers could be confirmed by concentration- and temperature-dependent Fourier-transform infrared spectroscopy (FT-IR) and ^{1}H NMR spectroscopy as well as linear dichroism experiments. Using chiral alkyl chains (PBI **3a**), the equilibrium between the *P*- and *M*-atropoenantiomer (Figure 3a) is swayed and chiral amplification can be observed upon self-assembly of mixtures of dyes bearing non-chiral (PBI **3b**) and homochiral (PBI **3a**) alkyl chains in sergeants-and-soldiers experiments.[58,59]

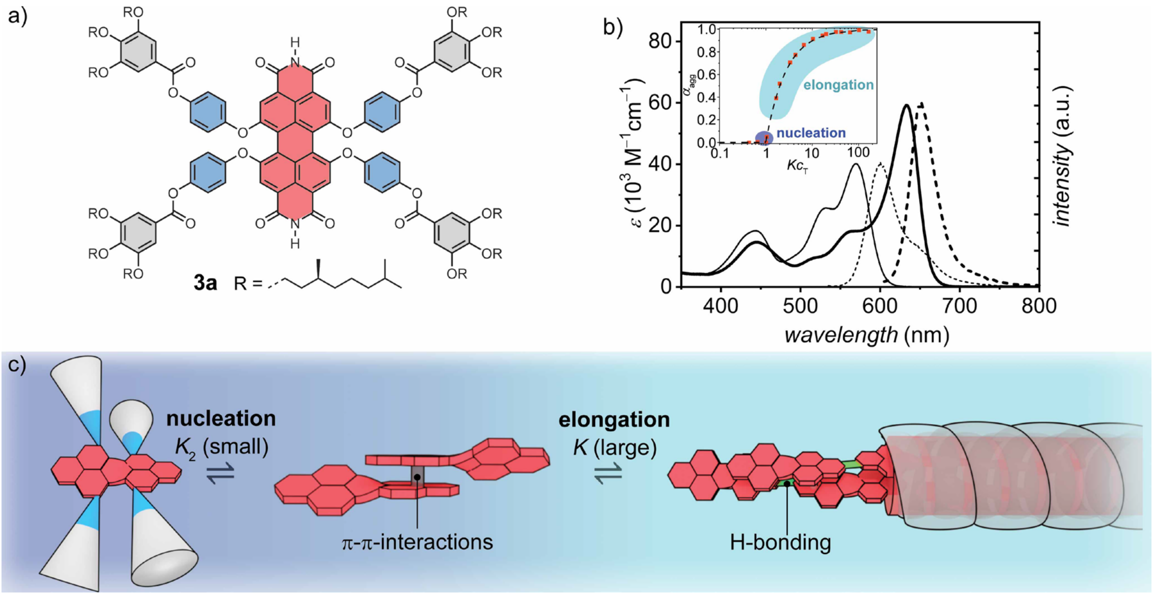

Figure 4. a) Structure of PBI **3a** and color code. b) UV/Vis (solid lines) and fluorescence spectra (dashed lines) of PBI **3a** in CH_2Cl_2 (10^{-5} M, thin line) and MCH (10^{-5} M, bold line). Inset: Degree of aggregation α_{agg} of PBI **3a** in MCH as a function of Kc_T and fit according to the cooperative nucleation-elongation model. Dark and light blue regions highlight the nucleation and elongation regime, respectively. c) Schematic illustration of the self-assembly of tetraphenoxy substituted PBIs into J-aggregates. Figure 4b was adapted with permission from reference [59]. Copyright 2009 American Chemical Society.

Generally, such tetraphenoxy-substituted PBIs are isolated as racemic mixtures of the respective *P*- and *M*-atropoenantiomers that cannot be resolved due to a low barrier of dynamic interconversion.[90] In an attempt to create highly ordered, enantiopure PBI J-aggregates, we introduced a 2,2'-biphenoxy bridge in 1,12-positions that increases the barrier of dynamic interconversion to an extent facilitating the separation of both enantiomers (PBI **4**). While the enantiopure dye self-assembles into well-defined helical double cable structures with characteristic J-type optical features, the racemic mixture forms nanoparticles of irregular size (Figure 5a). Concentration-dependent absorption studies revealed that the enantiopure and racemic mixture exhibit distinctively different equilibrium constants for the nucleation process in the cooperative self-assembly

($K_{2,\text{enantiopure}} = 2.7 \times 10^3$, $K_{2,\text{rac}} = 6.3\times 10^4$). These results indicate that heterodimerization is favored over homodimerization and that the dimeric nuclei of the cooperative self-assembly of tetraphenoxy-substituted PBI J-aggregates are composed of π-stacked rather than H-bonded chromophores.[91]

The applied design principle towards PBI J-aggregates is very versatile and the properties of the monomeric dyes and the self-assembled nanostructures are governed by the choice of bay-substituents. For example, employing the approach of H-bond directed self-assembly en route to mimic natural BChl J-aggregates which show intense NIR absorption bands in the cyclic and tubular arrays of the light harvesting complexes of green and purple bacteria,[88,89,96] we modified the structure of "green" PBIs[97] as synthetic analoga of natural chlorophylls. Thus, incorporation of amino substituents in bay-position (PBI **5**) induces a bathochromic shift of the absorption of the monomer and an even more pronounced shift in the self-assembled J-aggregate to give an absorption maximum at 822 nm (Figure 5b).[98]

The use of alkyl chains in the PBIs so far discussed provides the solubility of the dyes in most common organic solvents including alkanes. However, we could demonstrate that appending of alkyl chains is not a prerequisite for solubilizing the dyes and the consecutive formation of PBI J-aggregates. Introduction of *ortho*-methylphenoxy groups in the bay area (PBI **2**) leads to a more rigid framework that cannot easily crystallize. This structural feature provides appreciably high solubility and kinetic retardation of the nucleation process in most organic solvents, thereby endowing the molecule with extraordinary gelation properties. Importantly, the J-type character is retained in the organogel leading to black gels with fluorescence quantum yields of up to 77% (Figure 5c).[99] Furthermore, the absence of extended alkyl chains enabled the preparation of single crystals by thermal gradient sublimation revealing a heterochiral double-stranded arrangement of H-bonded PBIs in the solid state.[93]

So far, we have demonstrated that H-bonds and π-π-interactions can be rationally applied to direct supramolecular polymerization of PBIs in organic solvents. However, formation of such well-defined functional structures in water poses difficulties as hydrophobic interactions are the prevailing driving force in this solvent. Nevertheless, we were able to produce a water-soluble PBI J-aggregate using triethylene glycol units instead of aliphatic chains (PBI **6a**, Figure 5d).[68] This material forms thermoresponsive hydrogels (5−40 wt%), which at temperatures below 30 °C are non-emissive and retain the absorption profile of monomeric tetraphenoxy-substituted PBIs. Upon increasing the temperature, however, entropic gain by release of water molecules from solvated triethylenyglycol chains to the bulk solvent supports the formation of J-aggregates by the symbiotic interplay of the hydrophobic effect, H-bonds and π-π-interactions. Importantly, a fluorescence turn-on can be observed upon the formation of the J-aggregated state.[68]

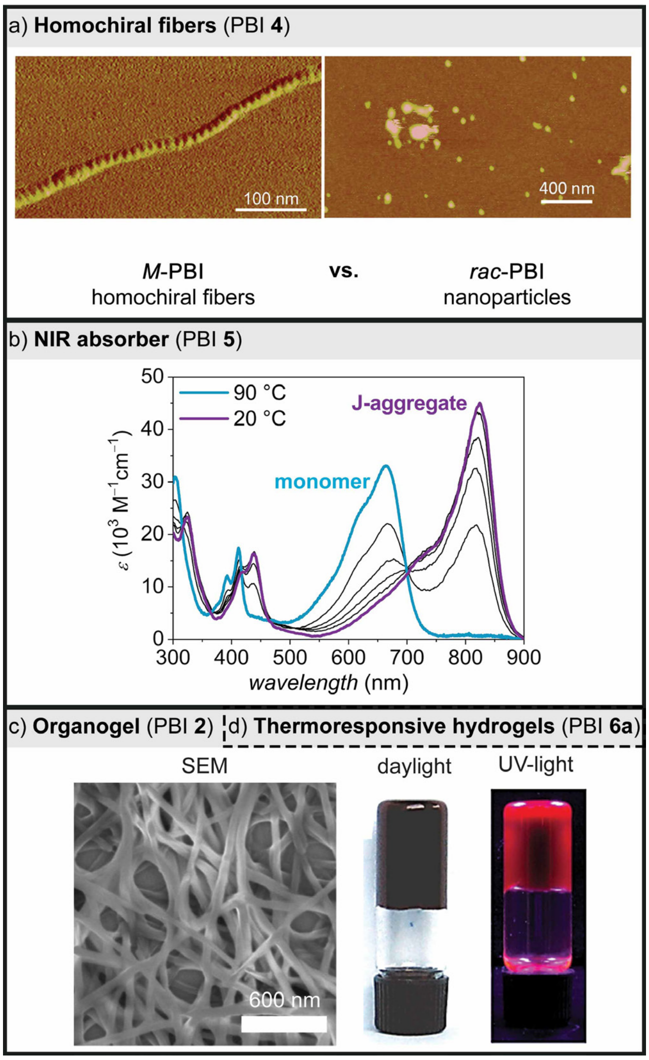

Figure 5. Versatility of the general design for PBI J-aggregates enabling the synthesis of a) homochiral fibers, b) NIR absorbers, c) organogels or d) thermoresponsive hydrogels. Figure 5a was adapted with permission from reference [91]. Copyright 2012 Wiley-VCH Verlag GmbH & Co. KGaA, Weinheim. Figure 5b was adapted with permission from reference [98]. Copyright 2008 The Royal Society of Chemistry. Figure 5c was adapted with permission from reference [99]. Copyright 2014 The Royal Society of Chemistry.

2.1.4 Physical Properties and Application of PBI J-Aggregates

Natural photosynthetic systems employ light harvesting antennas based on chlorophyll dyes that are capable of guiding solar energy to the reaction center. The exciton coupled chromophores in low-dimensional PBI J-aggregates render them as intriguing model systems to study the exciton migration of such supramolecular structures. This is not only of scientific interest but also of relevance for applications of supramolecular materials in organic photonics and photovoltaics where coherently coupled chromophores or exciton transport to a p/n heterojunction are desired.

Thus, in several collaborative research projects we have investigated the exciton diffusion in J-aggregates of PBIs **3c**, **6b**, **6c**, and **6d** by temperature-dependent absorption and fluorescence spectroscopy at 5 to 300 K (PBI **3c**),[71] TAS (PBI **6b-d**)[69,70] and single-molecule fluorescence spectroscopy (PBI **3c**).[72,73] Absorption and fluorescence studies suggested a large level of disorder for these aggregates, however, with unusually low thermal activation energy for exciton migration.[71] Accordingly, whilst only a small number of two to three chromophores are coherently coupled in these aggregates, high exciton mobilities were observed by TAS for PBI J-aggregates that exhibit either two- (PBI **6c**) or four-stranded (PBI **6b**) helices in the self-assembled state.[69] Here the two-stranded system revealed a more than two-fold enhanced diffusion length of 188 nm compared to 77 nm for the four-stranded PBI J-aggregate. These differences were attributed to the more pristine J-coupling between all PBI neighbor molecule and a thermodynamically more stable aggregate in the case of the two-stranded aggregate. Further studies on the exciton-exciton interaction for a three-stranded PBI J-aggregate (PBI **6d**) with a newly developed coherent 2D spectroscopic method confirmed these results with a value of 70 nm for the exciton diffusion length.[70]

Further insights into exciton migration properties and the direct detection of resulting spatial fluorescence quenching was achieved by SMS. In these experiments the phenomenon of fluorescence blinking, i.e. the collective fluorescence quenching of individual PBI **3c** J-aggregates, was exploited to investigate the exciton migration properties. Like for the previously discussed methods, also here migration distances up to 70 nm corresponding to 100 collectively quenched monomers could be observed.[72] Using fluorescence super-resolution microscopy, the simultaneous spectral, spatial localization and blinking behavior of individual PBI **3c** J-aggregates could be investigated (Figure 6). This research revealed some particularly interesting lower energy emissive states that enabled unprecedented insights into the funneling and trapping of excitons at locally disordered structures by means of the light-up of a red-shifted blinking fluorescence band. These emissive states were assigned to Frenkel states with substantially lower energy than the regular exciton states of the PBI J-aggregates whose population could be theoretically described by a Lévy distribution (Figure 6).[73] These experiments provided important insights into the mechanism for the migration and trapping of excitons in molecular aggregates that might also be valid for disordered molecular solid state materials. The results of these studies implicate the possibility of using disorder purposefully to direct excitons through supramolecular polymers acting as nanoantennas to desired locations by manipulating the environment rather than the antenna itself.[71,74]

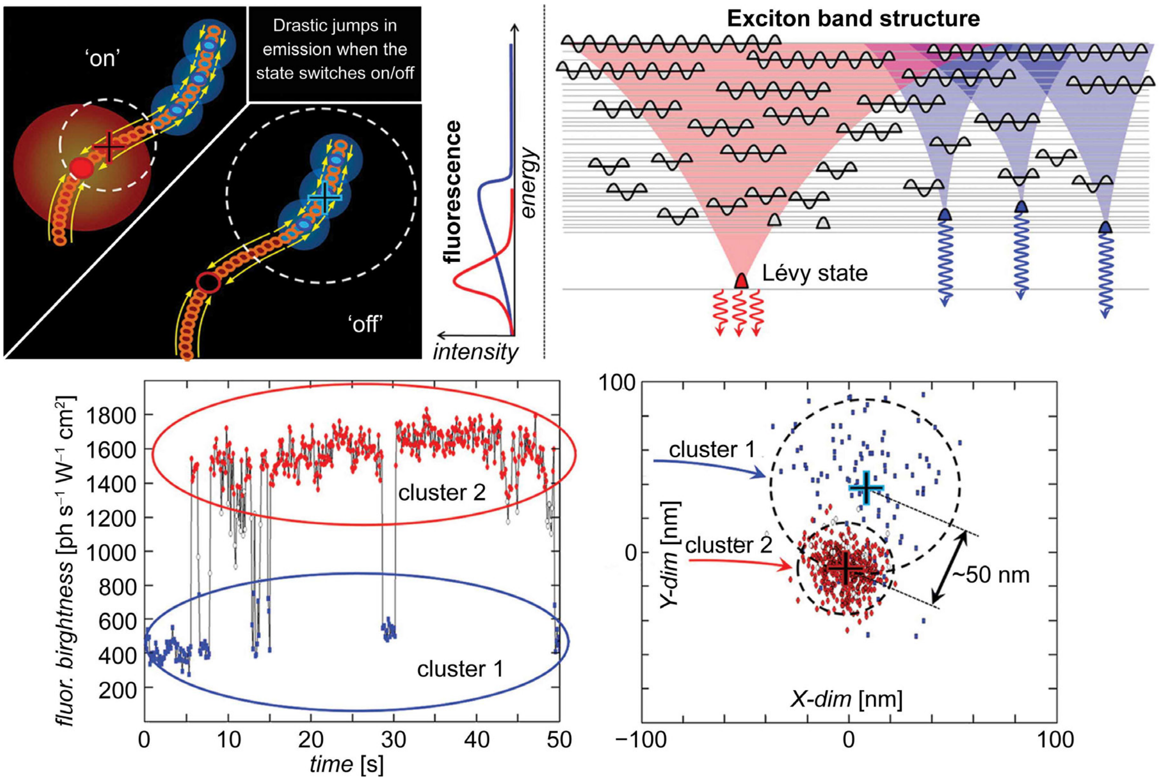

Figure 6. Schematic illustration of exciton migration in PBI J-aggregates with correlation of fluorescence intensity and spatial location of high energy (blue) and low energy (red) emission (top) and implications for exciton migration in molecular materials with exciton trapping on the lower energy Lèvy states. Adapted with permission from reference [73]. Copyright 2014 American Chemical Society.

With their favorable optical and electronic properties, PBIs have already been utilized as functional materials for a broad variety of applications which include beyond the classical field of color pigments the advanced fields of organic electronics,[9,13,100] and here in particular n-channel field-effect transistors,[101,102] and organic solar cells[9,103] as well as photonics.[104] The versatility of PBIs for these applications is attributed to the easy engineering of highest occupied molecular orbital (HOMO) and lowest unoccupied molecular orbital (LUMO) levels and band gap by PBI core substitution with appropriate functional groups[105] that can be readily translated to PBI J-aggregates when bearing the general design principles described in this Account in mind. Thus, we could implement PBI J-aggregates into a selection of devices by tailoring the optic and electronic properties to the requirements of the specific application while retaining the J-type excitonic coupling, and with this, the distinct optical properties and the high exciton mobility.

However, electronically isolating alkyl chains that are usually required to solubilize the otherwise insoluble PBI pigment are particularly disadvantageous once it comes to applications that require two- or three-dimensional percolation pathways for excitons or charge carriers in organic electronics devices. Therefore, we have employed two different approaches to circumvent this obstacle. One successful approach was the introduction of *ortho*-methyl substituted phenoxy groups in bay-position that induced fixation of the twisted PBI π-core and thus conferred high solubility (PBI **2**).[106] Indeed, PBIs designed by this strategy could be used as cathode modifiers in inverted polymer solar cells to lower the work function of the indium tin oxide (ITO) electrode and act as hole blocking layer due to its low lying HOMO level. Accordingly, the device performance of a polymer solar cell (ITO/PBI/PTB7:$PC_{71}BM/MoO_3$/Al) could be improved by 60% compared to a device setup without the PBI cathode modifier to achieve a power conversion efficiency of 9.11% (Figure 7a).[106] Another approach comprises the functionalization of both the bay- and headland-positions of the PBI with chloro substituents (PBI **1**) leading to a thermally stable electron acceptor material that can be sublimed and therefore does not require appended alkyl chains for solubilization (Figure 7b).[92] This material forms a brickwork-like structure of alternating H-bonded strands of *P*- and *M*-atropoenantiomeric PBIs that arrange in a slip-stacked fashion as evidenced by single crystal X-ray analysis.[92,107] This packing motif provides a substantial π-π overlap for 2D charge transport as well as close chlorine-chlorine contacts in the third dimension. Accordingly, top-contact bottom-gate organic thin-film transistors prepared with this material showed remarkable charge carrier mobility of up to $0.91\ \mathrm{cm^2V^{-1}s^{-1}}$ and outstanding air-stability with on-off-ratios of up to 10^8 (Figure 7b).[92] Notably, waveguiding application could be demonstrated as well for rod- and 2D plate-shaped crystals of this compound[107] as well as for a related tetrachloro-PBI material.[108,109]

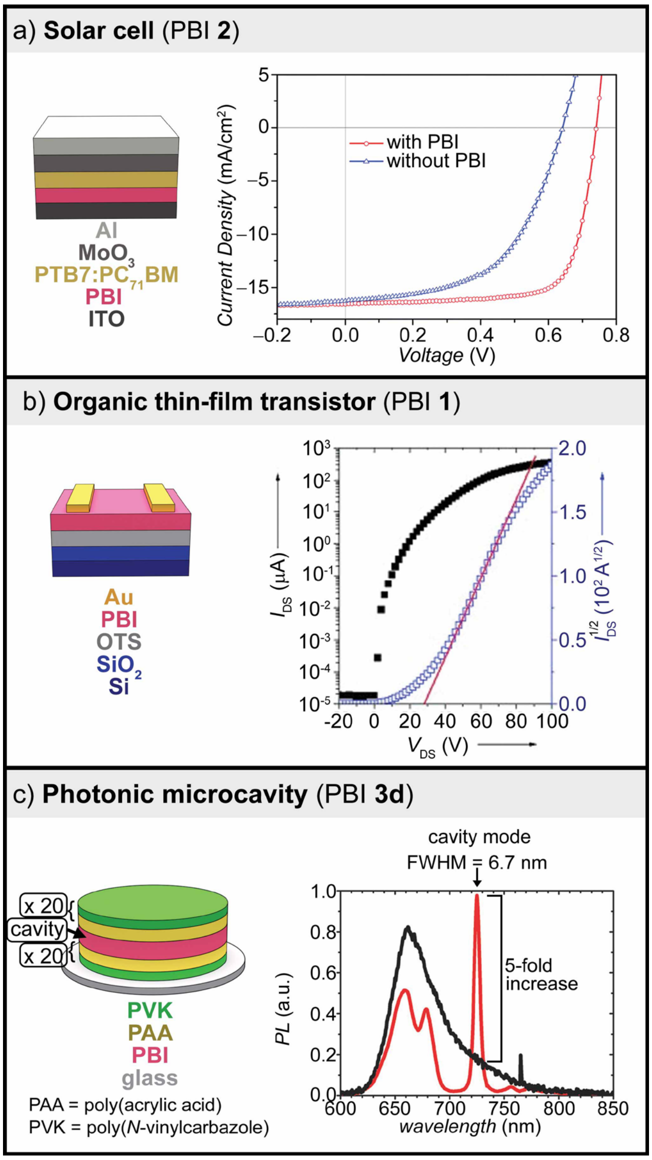

Figure 7. Application of PBI J-aggregates in a) solar cells, b) organic thin-film transistors and c) photonic microcavities (bottom right). Figure 7a was adapted with permission from reference [106]. Copyright 2015 Royal Society of Chemistry. Figure 7b was adapted with permission from reference [92]. Copyright 2010 Wiley-VCH Verlag GmbH & Co. KGaA. Figure 7c was adapted with permission from reference [110]. Copyright 2017 The Authors (published by Wiley-VCH Verlag GmbH & Co. KGaA).

However, alkyl chains do not have to be a disadvantage in the pursuit of functional materials. Using them purposefully, complex architectures can be realized utilizing the nanosegregation of the flexible alkyl chains and the rigid π-core of the PBI to create soft materials (*vide infra*).[60,61,111] Such soft materials with fine-tuned optical properties are for example desirable for purely optical applications like for photonic microcavities. Such microcavities are based on the interaction of photons and excitons in a resonant cavity which leads to the formation of hybrid light-mater quasiparticles called cavity exciton-polartions.[112] This interaction is particularly strong in systems which exhibit small Stokes shifts.[113,114] PBI J-aggregates are ideal candidates as they not only fulfil this essential criterion but additionally show hyperchromicity and fluorescence in the solid state.[93] Accordingly, J-aggregates of PBI **3d** and **6d** could be implemented in all-polymer photonic microcavities,[110] pillar microcavities[115] and open microcavities.[116] For the former, a film of PBI **3d** J-aggregate in amorphous polypropylene (aPP) was prepared between two polymeric distributed Bragg reflectors (DBR) to afford a 5-fold increase of photoluminescence intensity compared to a reference sample and a narrow FWHM of 6.7 nm at the cavity mode wavelength (725 nm) (Figure 7c).[110]

2.1.5 Conclusion and Outlook

In *Chapter 2.1*, we have demonstrated how nature's blueprint for the organization of chromophores into functional supramolecular architectures for efficient light harvesting can be transferred to one of the most relevant classes of dyes, namely PBIs, to precisely position them in slip-stacked packing arrangements with J-type exciton coupling. Once equipped with proper substituents, these dyes self-assemble into J-aggregates in organic or even in aqueous solutions as well as in the crystalline phase. In-depth photophysical studies revealed the high exciton mobility of PBI J-aggregates and how the inherent static disorder within these supramolecular polymers can be exploited to spatially guide excitation energy. While initial endeavors have been made to employ PBI J-aggregates as functional materials in form of photoconductive systems, organic field-effect transistors, solar cells and photonic microcavities, such supramolecular materials have still room to live up to their full potential, e.g. in biological applications as hydrogels with emission in the therapeutically relevant window. We anticipate that this Account would provide guidelines on how to rationally design monomeric structures to engineer J-aggregates as an important class of functional supramolecular elements[117] also from various other functional chromophores by exploiting symbiotic and directional intermolecular interactions. Thus, we hope that the examples and guidelines outlined in this Account will encourage chemists to extend the library of functional J-aggregates and further explore their application potential.

2.2 Methods for the Investigation of Liquid-Crystalline Phases

LC phases are one of the most intriguing states of matter as they feature orientational long-range order while retaining fluidity. In addition to the anisotropic behavior, smectic and columnar phases show positional long-range and are therefore particularly interesting LC phases. This can be used to generate functional materials with e.g. charge transport in one or two dimensions.[22] Such properties, however, strongly depend on the precise intermolecular arrangement of the building blocks and it is of fundamental importance to elucidate the structural features to enhance the understanding of structure-property relationships.[26,118,119] Unlike single-crystals whose structure can be unambiguously identified by single-crystal X-ray diffractometry in well-established routines, liquid crystals require a diverse approach to elucidate the structure of the ordered, yet mobile phases. While X-ray scattering (XRS) experiments of LC phases do give information about the structure, the limited amount of reflections makes validation with further methods essential. Therefore, the following section is focused on methods that were used to shine light on the intermolecular arrangement of the supramolecular structures presented in this thesis.

2.2.1. Polarized Optical Microscopy

Polarized optical microscopy (POM) is a straight-forward approach to investigate the birefringence of potential LC phases. For this, a set of two crossed polarizers is used to study a sample that is typically placed between a glass slide and a cover slip (Figure 8a). In this setup, one polarizer is used to impose linear polarization on the incident light (polarizer) and one is used after the light passes the sample (analyzer). Accordingly, if the sample is isotropic, the orientation of the linearly polarized light is not altered and the light will not pass the analyzer (Figure 8a right). However, if an anisotropic sample such as a columnar or lamellar liquid crystal are used, the orientation of the linearly polarized light is changed and a certain fraction will pass through the analyzer resulting in distinct observable textures (Figure 8a left).[22] Such textures originate in the orientational changes of the director of the liquid crystal caused by defects.[120]

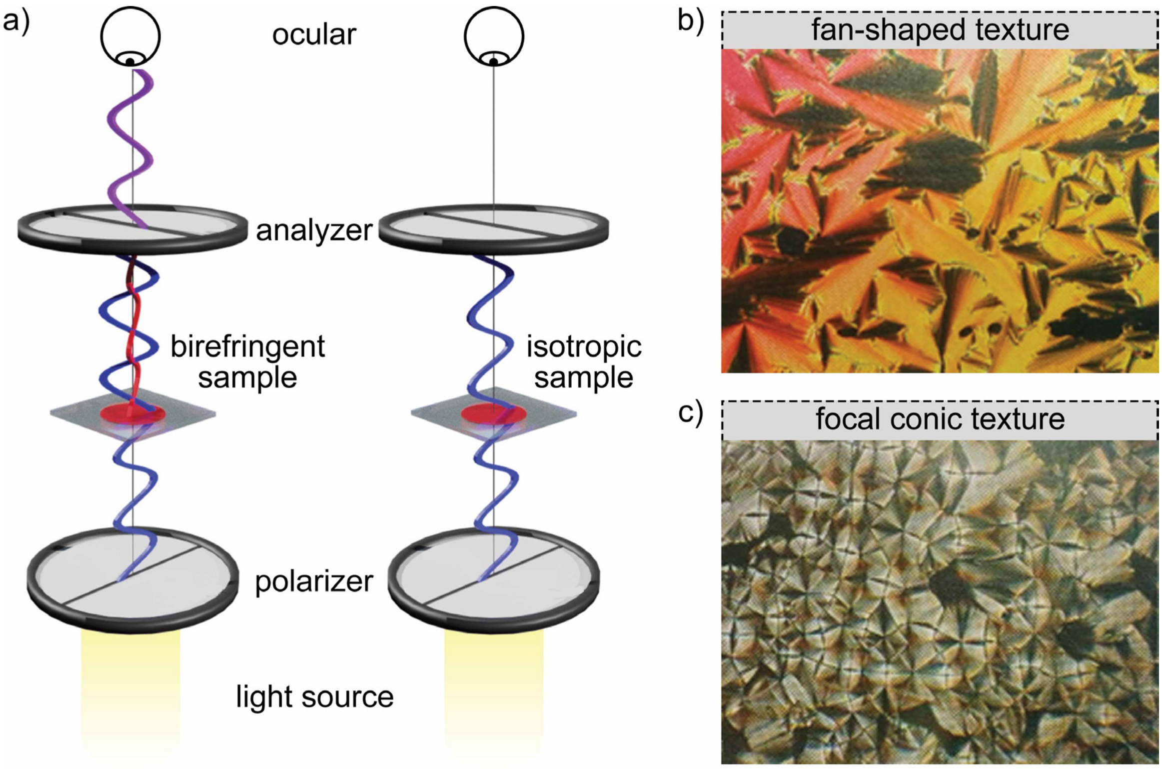

Figure 8. a) Schematic illustration of a POM setup. The birefringent sample (left) changes the polarization of the incidental light beam, while the isotropic sample (right) does not. Textures observed for LC phases: b) fan-shaped and c) focal conic textures. Images in b and c were reprinted with permission from reference [120]. Copyright 2004 Wiley-VCH Verlag GmbH & Co. KGaA.

Depending on the nature of the liquid crystal, typical textures can be observed. Accordingly, smectic phases often appear as fan-shaped (Figure 8b), focal conic (Figure 8c) or polygonal textures, but also four-brush schlieren textures can be observed for certain smectic phases.[120] Columnar mesophases mainly appear as pseudo focal conic or focal conic textures (Figure 8c).[120] However, typical textures can commonly only be observed upon cooling from the isotropic into the LC phase. Therefore, LC materials should exhibit low clearing temperatures to avoid decomposition upon heating the sample. The molecules presented in this thesis show very high clearing temperatures above 230 °C with concomitant decomposition, which prevents in-depth analysis of LC textures with POM. Nevertheless, birefringence and alignability can still be observed using POM proving the LC nature of the material.

2.2.2 Differential Scanning Calorimetry

DSC is a widely used method to investigate phase transitions of materials. It measures the difference in heat flow relative to a reference as a function of the temperature. Accordingly, at phase transitions which either consume (endothermic) or release energy (exothermic), a change in heat flow that is directly correlated to the enthalpy of the phase transition can be observed in the thermogram. Such transitions are called first order transitions. Transitions that do not change the enthalpy but only the heat capacity of the sample like glass transitions, are called second order phase transitions. Accordingly, DSC allows to determine the enthalpy, as well as the onset and peak temperatures of a phase transition. While the peak temperature depends on the heating or cooling rate applied to the sample, the onset temperature is constant. Phase transitions can be either monotropic or enantiotropic if they are irreversible or reversible, respectively, when performing consecutive heating-cooling cycles. For enantiotropic transitions, the DSC measurement gives information about the hysteresis of a particular phase transition between the heating and cooling cycle. Together with the enthalpy, hints whether a sample is crystalline or LC can be readily obtained. Generally, crystalline phases exhibit high enthalpies for the melting transition with large hysteresis upon recrystallization. In contrast, liquid crystals show comparatively low enthalpies with small hysteresis upon reversible clearing.[22]

2.2.3. Polarized Optical Spectroscopy

LC phases can be macroscopically oriented by external forces like electric and magnetic fields, or most commonly with mechanical force.[22] This allows the investigation of aligned samples by means of polarized optical spectroscopy to obtain further information about the structural features of the liquid crystals. If the LC material is based on dyes, as in this thesis, polarized UV/Vis absorption spectroscopy is a straight-forward approach to obtain information about the chromophore orientation. For example, columnar phases can be aligned by friction transfer leading to an alignment of the columnar long axis parallel to the shearing direction. Accordingly, using linearly polarized light yields either strong or weak absorption signals depending on the orientation of the chromophores and their TDM. In the case of PBIs, the main TDM (S_0-S_1) is aligned along the molecule's *N*-*N*' axis. Therefore, if the PBI *N*-*N*' axis is aligned parallel to the columnar long axis a strong signal is expected for a parallel setup of polarizer and shearing direction. In contrast, a weak signal is expected when measuring with the polarizer perpendicular to the shearing direction (Figure 9). Furthermore, other polarized spectroscopic techniques, like FT-IR spectroscopy can be used to obtain information e.g. about the orientation of H-bonds in the aligned thin film (Figure 9).

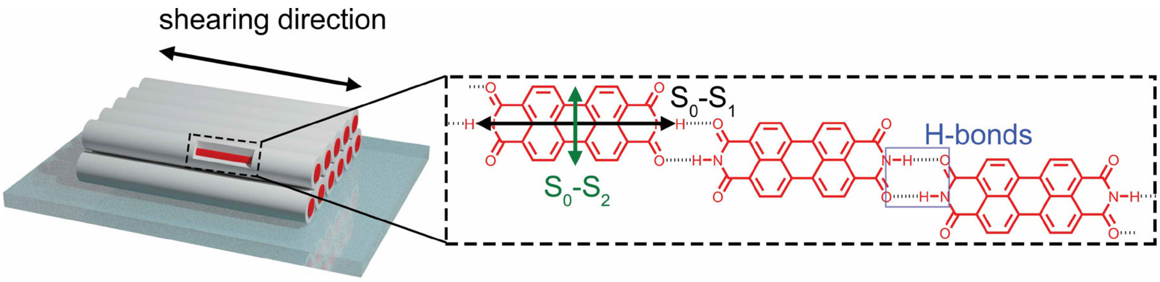

Figure 9. Schematic illustration of an aligned columnar assembly with PBIs oriented parallel to the columnar long axis.

2.2.4 Density Measurements

XRS experiments allow to determine the unit cell parameters of the LC sample (*vide infra*). To further analyze the particular structure, however, it is essential to determine the number of molecules *Z* present in a given volume. This can be calculated using equation (1).

$$Z = \frac{\rho * N_A * V_{UC}}{M} \tag{1}$$

ρ is the density, N_A is the Avogadro's constant, *M* is the molecular mass and V_{UC} is the volume of the unit cell which can be exemplarily calculated by $V_{UC} = a * b * c$ for a rectangular phase or $V_{UC} = a^2 * sin60 * c$ for a hexagonal phase. In case of columnar mesophases it is convenient to calculate the number of molecules for columnar stratum by replacing V_{UC} with $V_{col-strat}$ in equation (1). In this case, the unit cell parameter c can usually be replaced with the height of the columnar stratum, which, in principal, can be chosen arbitrarily. Accordingly, to determine the number of molecules *Z*, it is necessary to determine the density of the LC material. Commonly, pycnometry is used to determine the volumetric mass density. However, this method requires relatively large amounts of material to determine the density accurately.[121] As LC materials are often synthesized on a mg scale due to cumbersome syntheses, the flotation method is a convenient method to experimentally determine the density with less than 10 mg of material.[121] This method is based on the principle that a sample immersed in a liquid is in a state of mechanical equilibrium. Therefore, it neither sinks nor floats when the density of the liquid and the sample are identical. This so called flotation equilibrium can be achieved by either changing the temperature of the liquid or its composition. The latter requires no special equipment and can therefore be readily used if the right solution mixture is chosen. For organic materials with densities between 1.0 g cm^{-3} and 1.2 g cm^{-3}, a mixture of deionized water and aqueous sodium chloride is appropriate.[122] Prior to the measurement, the solvents have to be degassed, e.g. by ultrasonication, to avoid falsification of the measurement. Furthermore, to precisely determine the density, a sample free of air inclusion is required. For LC materials with low clearing temperatures and thermal stability, this can be achieved by heating the material to the isotropic state and keeping it under vacuum for an extended period of time.[123] However, for materials with very high clearing temperatures decomposition is expected and heating the sample into the isotropic state for an extended period of time is not feasible. Nevertheless, such samples can be heated close the clearing temperature under vacuum to realize decreased viscosity which allows air bubbles to escape more easily while preventing decomposition.

For the measurement, a sample of material (0.1 – 0.6 mg) is placed in a sealed vial containing deionized water. The temperature of the liquid needs to be kept constant throughout the measurement. Afterwards, an aqueous sodium chloride solution is added in small portions and the system is allowed to equilibrate after each addition. Once the sample starts floating, the liquid and the sample exhibit identical density.[121] The density of the final liquid at a particular temperature can be calculated according to literature.[122] As a complete exclusion of air bubbles within the sample cannot be guaranteed, the determined value has to be considered as the lower limit.

For practicality reasons, the density measurements are usually performed at temperatures between 20 °C and 25 °C. However, as X-ray measurements are often conducted at elevated temperatures, the experimentally determined material density needs to be extrapolated. The LC compounds discussed in this thesis are composed of an aromatic and an aliphatic part, which exhibit different thermal expansion behavior. Therefore, it is convenient to calculate the molecular volume with equation (2):

$$V_{\mathrm{mol}} = \frac{M}{\rho * N_{\mathrm{A}}} = V_{\mathrm{ar}} + V_{\mathrm{aliph}} \tag{2}$$

V_{ar} and V_{aliph} correspond to the molecular volume of the aromatic and aliphatic part, respectively. V_{aliph} can be calculated according to equations (3), (4), (5) and (6):[124,125]

$$V_{\mathrm{aliph}} = V_{\mathrm{CH}} + V_{\mathrm{CH_2}} + V_{\mathrm{CH_3}} \tag{3}$$

$$V_{\mathrm{CH}} = 1\,\text{Å}^3 \times x * (22.3 + 0.015833 \times (T - 30)) \tag{4}$$

$$V_{\mathrm{CH_2}} = 1\,\text{Å}^3 \times y * (26.5616 + 0.02023 \times T) \tag{5}$$

$$V_{\mathrm{CH_3}} = 1\,\text{Å}^3 \times z * (27.14 + 0.01713 \times T + 0.0004181 \times T^2) \tag{6}$$

x, y and z are the number of CH, CH_2 and CH_3 units per molecule, respectively, and T is the temperature.

For a PBI with branched alkyl substituents in imide position the temperature-dependent change of V_{mol} is reported in literature.[126] Using equations (4), (5) and (6) to determine the change of V_{aliph} and comparing it to the change of V_{mol} it becomes obvious that the change of V_{ar} with temperature is negligible compared to V_{aliph}. Accordingly, for molecules similar to the ones presented in this thesis it is sufficient to consider the thermal expansion of the aliphatic part to extrapolate the experimentally determined density to elevated temperatures.

2.2.5 X-ray Scattering Experiments

Shortly after the discovery of X-rays by Wilhelm C. Röntgen in the late 19th century, methods based on X-ray scattering and diffraction became widely popular to investigate the structure of crystalline and soft matter. X-rays are a type of electromagnetic radiation that is scattered upon interaction with electrons. Consecutively, these scattered waves interact and create interference patterns. This phenomenon is generally termed diffraction. Constructive interference follows Bragg's law:[127]

$$2 * d * sin\theta = k * \lambda \tag{7}$$

d is the distance between parallel lattice planes, θ is the angle between the X-ray beam and the lattice plane, λ is the wavelength of the X-rays (commonly $\lambda = 1.542$ Å for CuK$_{\alpha}$ radiation) and k is a positive integer that describes the order of the diffraction.[127]

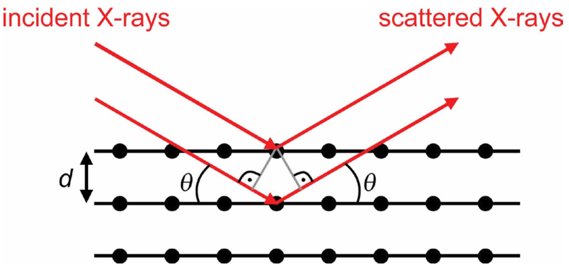

Figure 10. Schematic illustration of Bragg's law

Accordingly, constructive interference is observed if the path difference $2 * d * sin\theta$ between X-rays equals k times the wavelength of the electromagnetic radiation.

The setup used in the present thesis is schematically depicted in Figure 11a. Herein, a linear arrangement of X-ray source, sample and 2D detector is used. The distance between sample and detector determines the coverage of angular range. Therefore, at large sample to detector distances, the small angle regime can be investigated (small angle X-ray scattering, SAXS). Due to the reciprocal relationship of θ and d, this corresponds to large interplanar distances. The opposite is true for small sample to detector distances (wide angle X-ray scattering, WAXS). The accessible angular range can be even further increased upon tilting the detector with respect to the beam direction.

Using isotropic samples, concentric diffraction patterns can be observed when plotting the intensity as false color image in dependence of θ (Figure 11b). This is for example true for silver behenate which can be used as calibration standard as it shows a defined *d*-spacing with $d = 58.380$ Å indicated by the equally distanced signals (Figure 11c).[128]

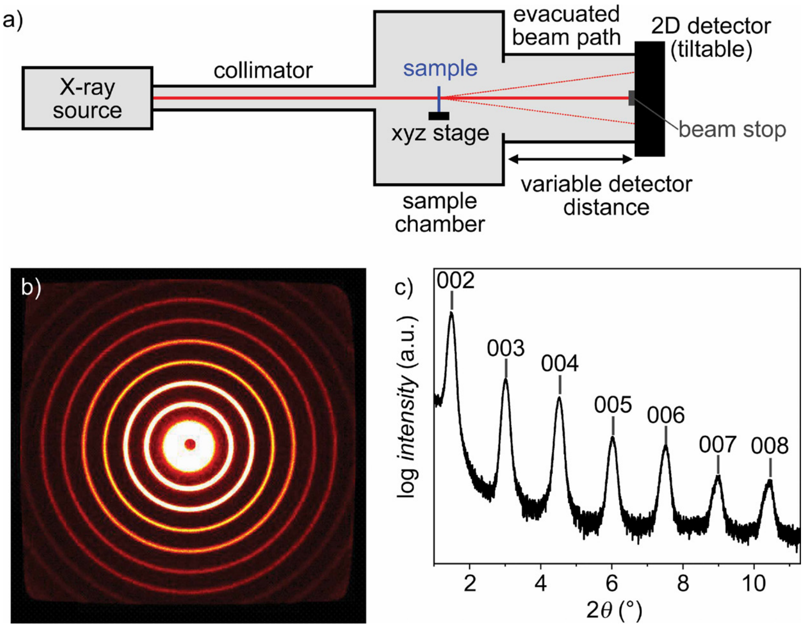

Figure 11. a) Schematic illustration of the experimental XRS setup. b) False color image of the diffraction pattern of a silver behenate calibration sample. c) Integrated intensity of the diffraction pattern of silver behenate and assignment of the signals to Miller indices.

However, 2D detectors are particularly useful for the investigation of anisotropic samples as this allows, exemplarily in the case of columnar phases, to study reflexes that originate in the inter- and intra-columnar arrangement of the molecules separately. This finds application in the method of fiber X-ray diffraction. For this, the LC material is generally heated to temperatures close to the clearing temperature and extruded through a hole (⌀ = 0.7-1.0 mm, Figure 12a). This leads to a macroscopic alignment of the molecules within the fiber.

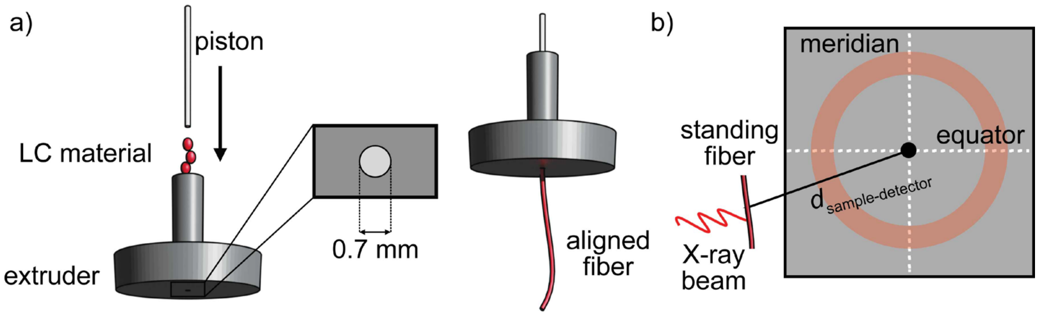

Figure 12. a) Schematic illustration of the extrusion of LC material into aligned fibers. b) Definition of equator and meridian for fiber X-ray diffraction.

In the case of a columnar phase of a conventional discotic molecule, three distinct sets of signals can be observed that can be used to determine its structural features. The diffuse halo in the wide-angle region originates in the liquid-like chain-chain correlation in an average distance of 4.5 Å. The equatorial signals give information about the intercolumnar arrangement. Lastly, meridional and off-meridional signals are a result of the intracolumnar order. Prominently, a signal at wide angles corresponding to $d \approx 3$ -°4 Å corresponds to the π–π-interactions perpendicular to the columnar long axis (Figure 13a).[22,26] In the special case of liquid crystals based on tetra bay substituted PBI J-aggregates with free imides, π–π-contacts are parallel to the columnar long axis. Accordingly, the signal corresponding to the π–π-interactions can be observed on the equator (Figure 13b).[60,61]

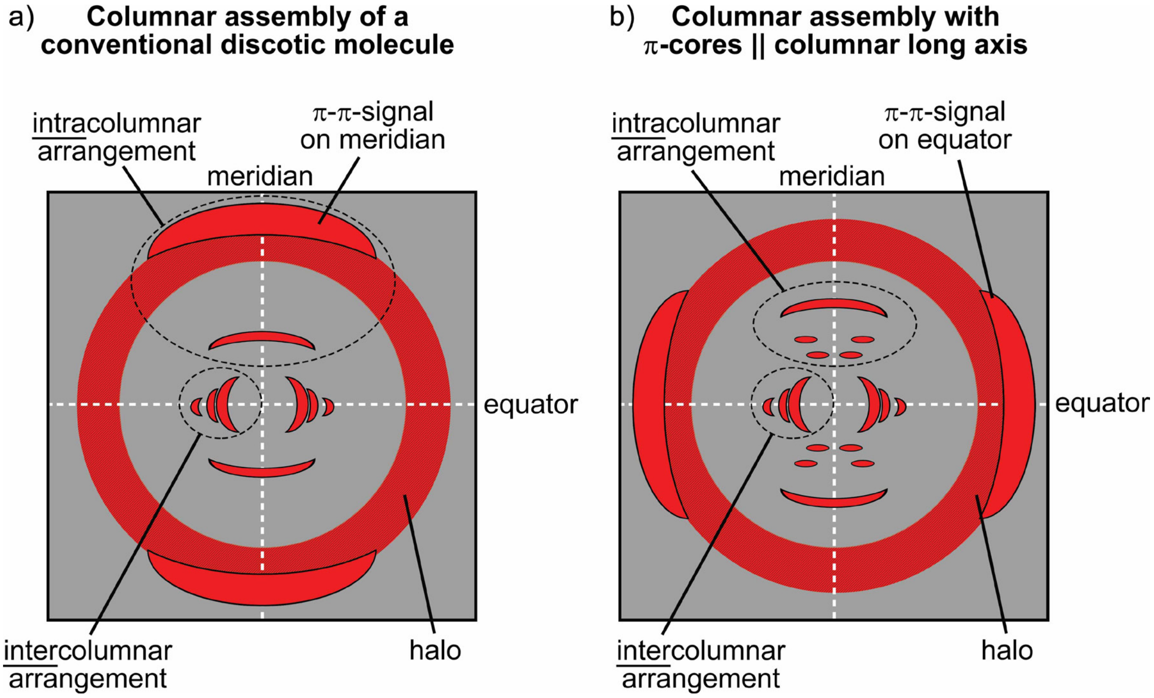

Figure 13. Schematic depiction of WAXS patterns of columnar assemblies a) of conventional discotic molecules and b) with π-cores parallel to the columnar long axis. White dashed lines indicate the equator and meridian. The most prominent signals are labelled.

Raw data can be analyzed with third-party programs. Herein, data was generally processed with the program Datasqueeze (version 3.0.7), which is available for free for academic institutions and was written by Paul Heiney.[129] It provides a graphical user interface with a plethora of functionalities. Most importantly, it allows the analysis of XRS data and referencing it to a calibration standard. The intensity of the scattered signal can be integrated and plotted as a function of 2θ. The reflections can then be adjusted to Miller indices of crystal lattices in two or three dimensions. Autoadjustment of a specific lattice as well as fitting routines help to gain confidence in the proposed assignment of signals.

2.2.6 Modelling

The cumulated data from POM, DSC, density measurements, polarized spectroscopy and XRS experiments aids the elucidation of structural features of the LC material. These insights can then be translated into models of the intermolecular arrangement with programs like BIOVIA Materials Studio.[130] This software package provides a wide range of functions that help to generate and optimize structural models.

Information such as the orientation of TDMs in the respective phase, absorption and fluorescence properties originating in exciton coupling of adjacent chromophores, the direction of H-bonds as determined by FT-IR spectroscopy, and information about symmetry and dimension of the unit cell as well as correlation lengths of specific reflexes gives hints towards the intermolecular arrangement. The monomeric chromophores, often pre-optimized by density functional theory (DFT) calculations, are then arranged in space to accommodate all these features extracted from the various experiments. The assembled structure can be placed in a P1 unit cell which exhibits only symmetry for the translation along the *a*, *b* and *c*-axes. This allows to perform geometry optimization with the *forcite* module in Materials Studio applying the second iteration of the forcefield "Condensed-phase Optimized Molecular Potentials for Atomistic Simulation Studies" (COMPASS II).[131,132] The non-bonding energies can be calculated using the Ewald summation method.[133] Generally speaking, this optimization is performed until the contributions to the non-bonding energy are negative, while retaining feasible molecular and intermolecular structures. Furthermore, Materials Studio's *reflex* module provides a function to simulate powder diffraction data from assembled molecular structures.[130] This enables the user to compare the position and intensity of reflexes assigned to certain crystal planes with experimental data and, therefore, check the structure for feasibility.

Further verification can be obtained by using the modelled structure as input for the program CLEARER, which provides the possibility for retrostructural analysis in form of simulated 2D fiber diffraction patterns.[134] The comparison of experimental and simulated diffraction patterns provides further insight whether the structural model would generate the expected diffraction signals. This is an iterative process as simulations demonstrate how structural models need to be refined to match the experimental results. It is to note that CLEARER is not intended to be used for fluid phases such as liquid crystals. The program simulates the diffraction pattern based on a perfectly ordered domain employing the input unit cell. However, liquid crystals are not built with identical unit cells and peripheral alkyl chains do not possess any periodicity. Accordingly, simulations of the diffraction pattern might deviate from experimental results.

Chapter 3

–

Photoconductive Core–Shell Liquid-Crystal of a Perylene Bisimide J-Aggregate Donor–Acceptor Dyad

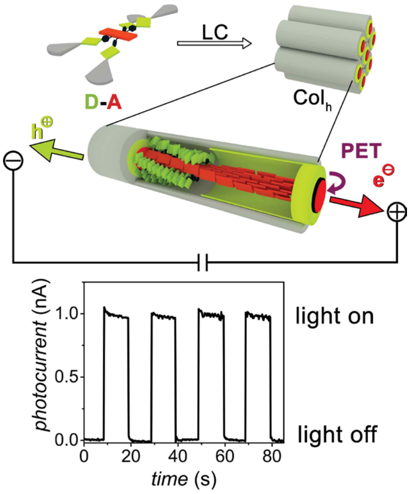

This chapter was published in: M. Hecht, T. Schlossarek, M. Stolte, M. Lehmann, F. Würthner, *Angew. Chem. Int. Ed.* **2019**, *58*, 12979–12983.

Abstract: A novel core–shell structured columnar liquid crystal composed of a donor–acceptor dyad of tetraphenoxy PBI, decorated with four bithiophene units on the periphery, was synthesized. This molecule self-assembles in solution into helical J-aggregates guided by π–π-interactions and H-bonds which organize into a LC Col$_h$ domain in the solid state. Donor and acceptor moieties exhibit contrasting exciton coupling behavior with the PBIs' (J-type) transition dipole moment parallel and the bithiophene side arms' (H-type) perpendicular to the columnar axis. The dyad shows efficient energy and electron transfer in solution as well as in the solid state. The synergy of photoinduced electron transfer (PET) and charge transport along the narcissistically self-assembled core–shell structure enables the implementation of the dye in two-contact photoconductivity devices giving rise to a 20-fold increased photoresponse compared to a reference dye without bithiophene donor moieties.

3.1. Introduction

Self-assembly of low-molecular-weight organic molecules enables the engineering of nanostructured functional materials with potential applications in photonics and optoelectronics.[15,26,32,33,41,135-139] In this regard, PBI dyes gain particular attention because of their outstanding photophysical properties[9,13,140] as well as their tendency to form supramolecular polymers through π–π-interactions in solution and bulk.[35,141] Conventionally, PBIs form 1D arrangements by cofacial π–stacking leading to H-type exciton coupling, which is unfavorable for optoelectronic applications.[142-144] As shown in previous studies it is possible to obtain supramolecular aggregates of bay-substituted PBIs that exhibit J-type coupling by adjusting the delicate interplay of π–π-interactions and H-bonding in solution[58] as well as the LC state.[60,61] In the present study we show that this design principle can be further developed to obtain LC core–shell architectures composed of narcissistically stacked donors and acceptors of a 2,2′-bithiophene-substituted PBI.

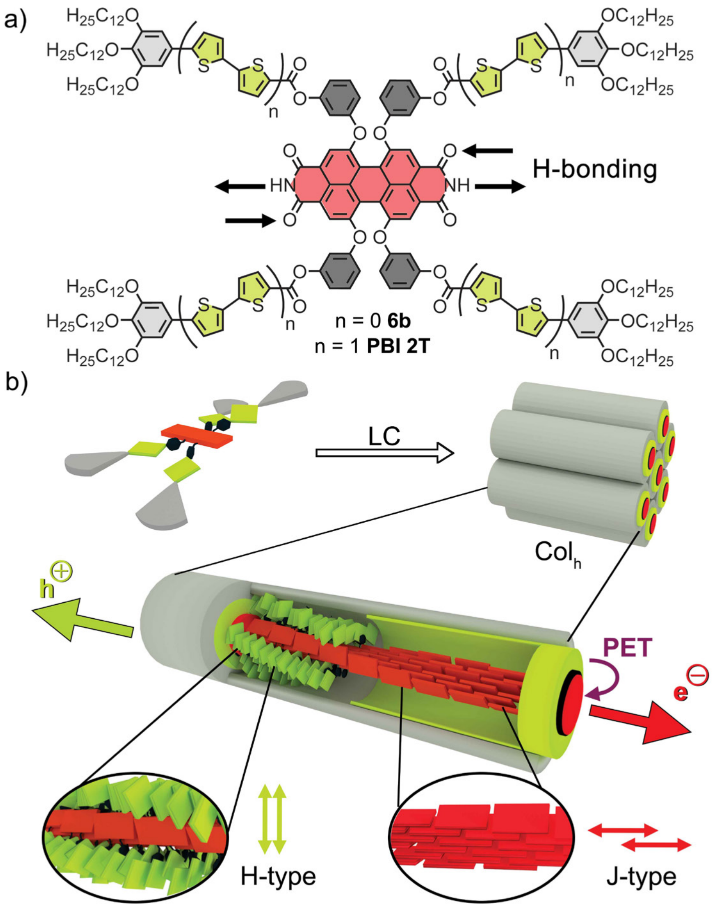

Figure 14. a) Chemical structure of **PBI 2T**. b) Illustration of the molecular arrangement of **PBI 2T** in the Col$_h$ LC phase with J-coupled PBIs (red) and H coupled bithiophene units (green). The purple arrow indicates the PET and the consecutive electron and hole transport along the columnar core–shell structure. The helicity in the shown columnar assembly has been chosen to be (*P*) for graphical representation. Please note that **PBI 2T** is achiral and therefore (*P*) and (*M*) helices may coexist in the LC phase.

This particular arrangement is guided by the molecular design to overcome the formation of alternating donor–acceptor arrangements,[145-147] which typically are formed in such systems because of the electronic complementarity of the two counterparts.[148-151] We report the novel bay-substituted dye **PBI 2T** bearing side arms containing electron-rich bithiophene units connected to a 3,4,5-tris(dodecyloxy)phenyl unit. This dye self-assembles by H-bonding and π–π-interactions into a 1D helical J-aggregate in solution as well as in the LC columnar phase (Figure 14). The PET and energy transfer (ET) properties were studied by UV/Vis absorption and fluorescence spectroscopy. Lastly, we show that the new material **PBI 2T** exhibits photoconductivity in two-contact devices with a 20-fold increased photoresponse compared to the reference dye PBI **6b**, which lacks the 2,2′-bithiophene unit.[60]

3.2. Results and Discussion

The structure of the investigated compound **PBI 2T** consists of a 1,6,7,12-tetraphenoxy PBI which is unsubstituted at the imide-position to enable complementary H-bonding. The phenoxy residues are substituted in the *meta*-position with 3,4,5-tris(dodecyloxy)benzoate dendrons connected by a bithiophene spacer. **PBI 2T** was prepared according to our previously described method (see 3.4. Appendix to *Chapter 3*).[60,61] The UV/Vis absorption spectrum of **PBI 2T** in chloroform shows the optical signature of monomerically dissolved tetraphenoxy-substituted PBIs with the prominent S_0-S_1 transition at 569 nm (Figure 15a). An additional strong absorption band at 385 nm can be observed corresponding to the four electron-rich bithiophene side arms. No significant electronic coupling between the thiophene containing side arms and the PBI core is observed in the UV/Vis absorption spectrum of **PBI 2T** which resembles a superposition of the spectra of its building blocks (Figure A1). The comparison of the UV/Vis absorption spectra of a monomeric solution in chloroform with its thin film reveals the contrasting coupling behavior of the two chromophores within **PBI 2T** (Figure 14b and Figure 15a).

In the thin film, the PBI shows the typical bathochromically shifted absorption profile of a J-aggregate with its intense absorption maximum at 653 nm. The donor side arms exhibit the optical features of H type aggregated thiophenes[152] with their hypsochromically shifted absorption maximum at 378 nm. The self-assembly can be followed in solution by concentration- and temperature-dependent UV/Vis absorption studies revealing a cooperative nucleation-elongation process in nonpolar solvents like toluene and MCH (Figure A2 and Figure A3). The concentration-dependent studies in toluene at 298 K a nucleation constant of $K_{\mathrm{nuc}} = 9\ \mathrm{M}^{-1}$ considering a nucleus size of two molecules, as well as an revealed an elongation constant of $K_{\mathrm{elong}} = 8000\ \mathrm{M}^{-1}$ giving rise to a cooperativity parameter of $\sigma = 1.13 \times 10^{-3}$ and.[94]

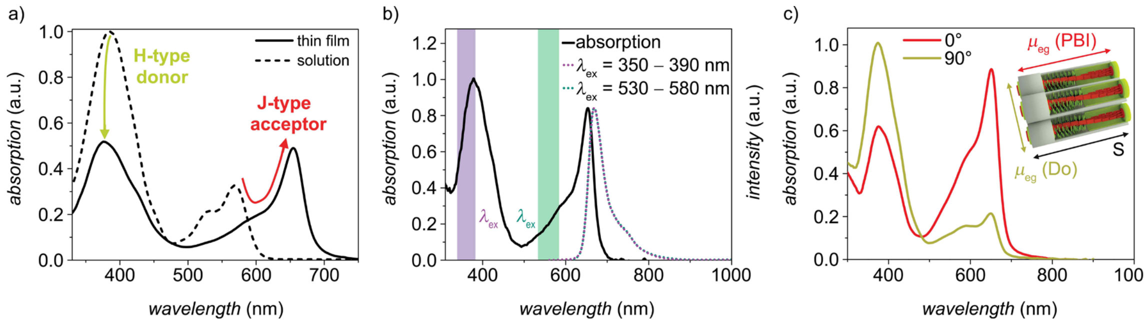

Figure 15. a) UV/Vis absorption spectra of **PBI 2T** in solution (black dotted line, 30 µM, $CHCl_3$) and in the solid state (black solid line, spin-coated from 1 mM solutions in MCH on quartz substrates, annealed for 30 minutes at 180 °C). The arrows indicate the hypso- and bathochromic shift of the bithiophene donor (green) and PBI acceptor (red) upon self-assembly, respectively. b) UV/Vis absorption (black solid line) and emission spectra (dotted lines) of thin films of **PBI 2T** (annealed for 30 minutes at 180 °C) in dependence of the excitation wavelength range (violet: 350-390 nm, green: 530-580 nm). c) UV/Vis absorption spectra of a mechanically aligned thin film of **PBI 2T** on quartz (annealed for 30 minutes at 180 °C) measured with linearly polarized light parallel (red) and perpendicular (green) to the shearing direction. The inset shows a graphical representation of the aligned columnar structure along the shearing direction (S) and the corresponding orientation of the TDMs of donor and acceptor moieties (green and red arrows), respectively.

We studied the influence of the donor units in the side arms on the optical properties of the dyad using fluorescence spectroscopy. Thin-films prepared by spin-coating a 1 mM solution of **PBI 2T** in MCH showed weak emission with the maximum intensity recorded at a wavelength of 669 nm corresponding to a Stokes shift of 370 cm^{-1}. Interestingly, PBI emission can be observed whether the PBI ($\lambda_{\mathrm{ex}} = 530 - 580$ nm) or the bithiophene ($\lambda_{\mathrm{ex}} = 350 - 390$ nm) is excited (Figure 15b and Figure A4), indicating ET from the bithiophene donor to the PBI acceptor. The fluorescence quantum yield of the thin film was determined to be about 2%, independent of the excitation wavelength, implying a highly efficient ET (Figure A5). The fluorescence is strongly quenched in the solid state as well as in solution (Table A2 and Table A3) compared to other bay-substituted tetraphenoxy PBIs indicating an efficient PET between donor and acceptor moieties. This is further supported by time-resolved emission spectroscopy revealing a short fluorescence lifetime for the monomeric **PBI 2T** in chloroform ($\tau = 0.6$ ns, $\lambda_{\mathrm{ex}} = 505$ nm) and self-assembled **PBI 2T** in MCH ($\tau = 0.8$ ns, $\lambda_{\mathrm{ex}} = 635$ nm) which are typically in the range of several nanoseconds for non-donor substituted tetraphenoxy PBIs (Figure A1 and Table A2). To gain further insight into the electronic properties of **PBI 2T**, the material was investigated by CV. The measurements were performed in dichloromethane at room temperature using tetrabutylammonium hexafluorophosphate as electrolyte and the ferrocenium/ferrocene (Fc+/Fc) redox couple as internal standard (Figure A7 and Table A4). **PBI 2T** shows two reversible reduction potentials and one irreversible oxidation process. The driving force for electron transfer from donor to acceptor upon excitation of the acceptor was estimated to be −0.33 eV, explaining the strongly quenched emission of **PBI 2T** by PET.

The thermotropic properties of **PBI 2T** were investigated by POM and differential scanning calorimetry (DSC) and revealed that **PBI 2T** exhibits one LC phase from 20 °C to 281 °C, whereafter the material melts and starts to decompose (Figure A8). The structure of this fluid, anisotropic phase was studied by WAXS and MAXS experiments of aligned fibers prepared by extrusion. The WAXS patterns of standing and lying fibers of **PBI 2T** at 230 °C show a large number of equatorial reflections, which are in perfect agreement with a hexagonal columnar (Col$_h$, *a* = 57.2 Å) lattice (Figure 16a-c).

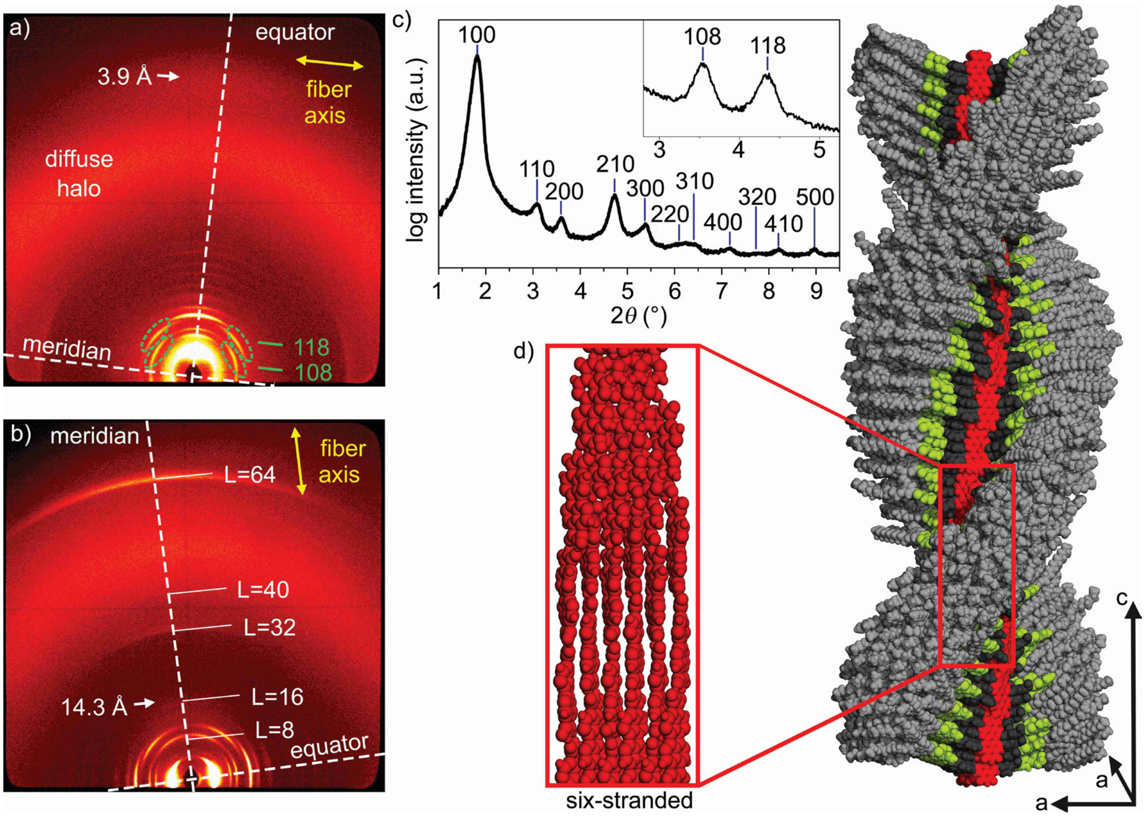

Figure 16. WAXS diffraction pattern of a a) lying and b) standing fiber of **PBI 2T** at 230 °C. The relative orientation of the fibers is indicated by yellow arrows and the meridian and equator are highlighted with white dashed lines. The layer lines are indicated as L = 8, 16, 32 ,40 and 64. Dashed green circles highlight the signals in the small-angle area corresponding to the helical structure. c) Integrated intensities along the equator and assignment of the Miller indices of the Col$_h$ lattice of **PBI 2T**. The inset shows the integration of the off-meridional 108 and 118 signals. d) Self-assembled structure of the sextuple-stranded 16_1 helix of **PBI 2T**. The helicity in the shown columnar assembly has been chosen to be (*P*) for graphical representation. Please note that **PBI 2T** is achiral and therefore (*P*) and (*M*) helices may coexist in the LC phase.

Both patterns reveal various meridional and off-meridional reflections. The most prominent off-meridional signals can be assigned to the 108 and 118 reflections of a 3D correlated hexagonal columnar phase with a periodicity along *c* of 228.8 Å. Such a large parameter for periodically ordered structures along the columns can only be explained by a helical self-assembly, as shown previously.[60,61] The first meridional reflection 0016 corresponds typically to the distance of the axial translational subunit and amounts to 14.3 Å, which is the size of the PBI long axis and indicates that these chromophores are aligned along the columnar axis, where they can form H-bonded strands. Exactly 16 mesogens form the full repeat and the helical pitch of 14.3 Å × 16 = 228.8 Å, implying that the H-bonds and the S_0–S_1 transition of the PBIs are aligned with the columnar axis. This is confirmed by polarized FT-IR- and UV/Vis spectroscopy of shear-aligned thin films (Figure 15c and Figure A9). As expected, the band attributed to the bithiophene absorption reveals the opposite behavior with the highest absorbance perpendicular to the shearing direction, indicating that the donor side arms are oriented perpendicular to the columnar long axis. This periodic helical columnar structure also causes the visible signals on the layer lines L = 32, 40 and 64 (Figure 16b and Figure A12). Further, the lying fiber exhibits a diffuse wide-angle signal corresponding to the typical π–π-distance (3.9 Å) of core-twisted PBIs, with a correlation length of six units, indicating that approximately six strands form the column (see 3.4. Appendix to *Chapter 3*). The latter is confirmed by the extrapolation of the density of 0.948 g cm^{-3} at 230 °C and the subsequent calculation of the number of mesogens in a columnar stratum of a height of 14.3 Å, which amounts also to 5.7 ± 0.3 (see 3.4. Appendix to *Chapter 3*). Therefore, **PBI 2T** forms a sextuple-stranded 16_1 helix with a 22.5° twist per molecule (360°/16) and a slipped stacking of the six H-bonded strands as indicated by the J-coupling of the PBI chromophores (Figure 15c).

To visualize the proposed columnar LC assembly, a model of the helical structure of **PBI 2T** was generated with the program *Accelrys Materials Studio 2017 R2* (Figure 16d and Figure A10). Based on the experimental data, a PBI core twist of 22.5° between the two naphthalene units induced by the four sterically demanding bay substituents and the packing was assumed. The PBIs were then arranged to form a H-bonded sextuple-stranded helix with slip-stacked arranged chromophores, and individual nanosegregated PBIs (acceptors, core), bithiophenes (donors, shell) and peripheral aliphatic chains. The side arms were arranged to maximize space-filling while retaining optimal π–interactions. The helix was geometry optimized with the force field COMPASS II, applying the Ewald summation method in the corresponding hexagonal unit cell until the nonbonding energy was strongly negative. Using the modelled structure, we simulated the fiber diffraction pattern with *CLEARER*[134] providing results which are in rather good agreement with the experimental WAXS and MAXS patterns (Figure A11), thus confirming the modelled acceptor–donor core–shell LC structure.

This sextuple-stranded self-assembly mode should enable highly efficient exciton transport over long distances. Similar PBI J-aggregates with a smaller number of strands exhibit long exciton lifetimes which allow exciton transport over distances of about 70 nm.[73] The increased number of strands in **PBI 2T**'s core–shell structure should improve the capability to circumvent trap-sites within the aggregate which could improve the exciton mobility. Likewise, after PET the well-separated donor and acceptor aggregates are expected to function as either electron- or hole-transport domains, respectively. Therefore, we anticipated **PBI 2T** to be a suitable material for the application as photoconductor. For this purpose, we fabricated devices by spin-casting a solution of **PBI 2T** (1 mg mL^{-1}, $CHCl_3$) onto bottom contact Si/SiO_2 substrates with gridlike gold electrodes (30 nm height, 10 mm channel width and 5 µm channel length, Figure 17a and Figure A16). The 8-10 nm thick films were annealed for 10 mins at 180 °C to improve the intermolecular arrangement of the LC phase (Figure A13). Two-contact measurements (V = +100 V) show a significantly enhanced conductivity upon irradiation with a white-light source at a power density of 38 mW cm^{-2}. While dark currents are in the range of few hundred fA, the photocurrents reach up to 1 nA upon illumination Figure 17b).

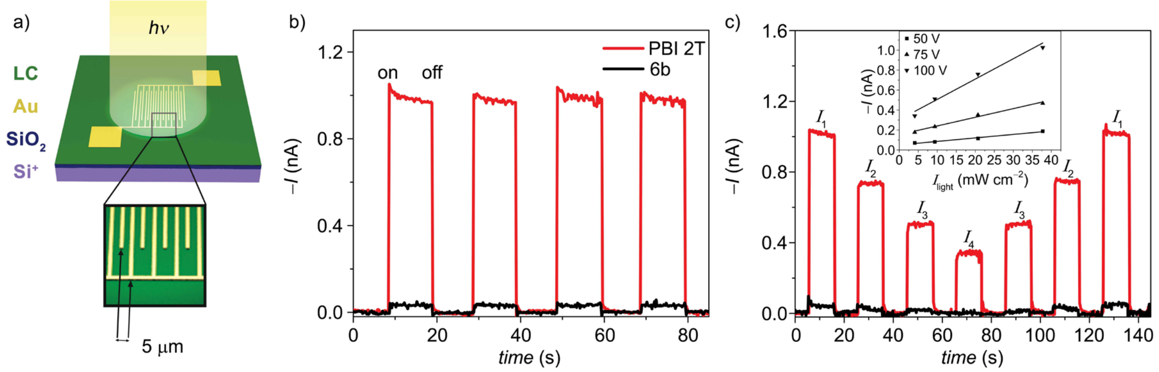

Figure 17. a) Schematic illustration of the two-contact device used to investigate the macroscopic photoconductivity. b) Plot of the photoresponse of **PBI 2T** (red) and the reference dye PBI **6b** (black) at a constant drain-source voltage of +100 V. The samples were illuminated with a white light source with a power density of 38 mW cm^{-2}. c) Plot of the photoresponse of **PBI 2T** (red) and the reference dye PBI **6b** (black) at a constant drain-source voltage of +100 V using white light with varying power densities (I_1 = 38 mW cm^{-2}, I_2 = 21 mW cm^{-2}, I_3 = 9 mW cm^{-2}, I_4 = 4 mW cm^{-2}). The inset shows the plot of the photocurrent depending on the light intensity with constant voltages of 50 V (■), 75 V (▲) and 100 V (▼) with linear regression (solid lines).

The active layer in devices prepared from **PBI 2T** shows a linear response to light intensity (Figure 17c) and switching times are instant within the measuring interval of the experiment (200 ms). The benefits of the acceptor–donor core–shell architecture are particularly clear when comparing these values to devices fabricated from PBI **6b**, the parent compound of **PBI 2T** without any additional absorbing and electron-donating bithiophene units which exhibits a quadruple-stranded 14_1 helix in the LC state.[60] The photoresponse of PBI **6b** upon irradiation is in the range of 50 pA and therefore 20-fold smaller than for the new LC phase of **PBI 2T**. This enhancement is enabled by 1) the donor–acceptor architecture of **PBI 2T** which allows improved charge carrier generation by PET compared to its parent compound, 2) the self-assembly of **PBI 2T** into a six-stranded helix which creates robust percolation pathways for charge carrier transport within two separated nano domains composed of the electron-rich outer shell (hole transport) and the electron-deficient core (electron transport), respectively, and at the same time hinders charge-carrier recombination.

3.3. Conclusion

In conclusion, our observations demonstrate how the jacketing of a hydrogen-bonded PBI J-aggregate core unit by peripheral oligothiophene H-aggregate stacks within a columnar liquid crystal phase affords a customized photoconductive supramolecular material.

3.4. Appendix to *Chapter 3*

Materials and Methods

Materials

Reagents were purchased from commercial suppliers and used as received without further purification. *N*,*N*'-Dicyclohexylcarbodiimide (DCC) was freshly distilled prior to its use. Solvents were distilled and dried by standard procedures. All reactions were carried out under nitrogen atmosphere.

Column Chromatography

Column chromatography was performed with commercial glass columns using silica gel 60M (particle size 0.04-0.063 mm; Macherey-Nagel GmbH & Co. KG, Germany) as stationary phase. Size exclusion chromatography was performed with commercial glass columns using Bio-Beads® S-X3 (Bio-Rad Laboratories Inc., USA) as stationary phase.

NMR Spectroscopy

^{1}H and ^{13}C nuclear magnetic resonance (NMR) spectra were recorded on a Avance-400 spectrometer (Bruker-Daltonics GmbH, Germany) operating at 400 MHz (^{1}H) or 100 MHz (^{13}C), with the residual protic solvent used as the internal standard. The chemical shifts (δ) are reported in parts per million (ppm). Multiplicities for proton signals are abbreviated as s, d and m for singlet, doublet and multiplet, respectively.

High Resolution Mass Spectrometry

High resolution mass spectra (HRMS) were recorded on an ESI micrOTOF focus spectrometer (Bruker Daltonic GmbH, Germany). Elemental analyses were performed on a CHN 932 analyzer (Leco Instruments GmbH, Germany).

UV/Vis Absorption Spectroscopy

UV/Vis absorption spectra in solution were recorded using a V-770 spectrophotometer (JASCO Inc., Japan). The spectra were measured in quartz glass cuvettes using spectroscopic grade solvents. Temperature control was accomplished by a PAC-743R Peltier system (JASCO Inc., Japan). Extinction coefficients were calculated from Lambert-Beer's law. UV/Vis absorption spectra of thin-films were recorded in transmission mode with a Lambda 950 UV/Vis/NIR spectrometer (PerkinElmer Inc., USA) equipped with polarizers and an integration sphere.

Fluorescence Spectroscopy

Fluorescence spectroscopy in solution was carried out with an FLS 980 spectrometer (Edinburgh Instruments Ltd., UK) by optical dilution method ($OD_{\max} < 0.05$). Fluorescence quantum yields were determined as average value of four different excitation wavelengths (525, 530, 535 and 540 nm for monomeric **PBI 2T** in $CHCl_3$ and 585, 590, 595 and 600 nm for aggregated **PBI 2T** in MCH) using *N*,*N'*-bis(2,6-diisopropylphenyl)-1,6,7,12-tetraphenoxy-3,4,9,10-perylenetetracarboxylic diimide[153] (for monomeric **PBI 2T** in $CHCl_3$) and 3,7-bis(diethylamino)phenoxazinum perchlorate[154] (for aggregated **PBI 2T** in MCH) as reference. The signals were corrected for the different refractive indices according to common procedure.[155] Time-resolved measurements were performed with a ps laser diode and a time-correlated single photon counting (TCSPC) detection unit (λ_{ex} = 635 nm, 505 nm). Fluorescence spectroscopy of thin-films was carried out with an Axio Imager 2 (Carl Zeiss AG, Germany) polarizing optical microscope equipped with a Hg arc lamp and a cooled CCD spectrometer MCS-CCD PCI (Carl Zeiss AG, Germany). Fluorescence quantum yields of thin-films were determined with a C9920-02 Absolute PL Quantum Yield Measurement System (Hamamatsu Photonics KK, Japan) using a calibrated integrating sphere system.

Polarized Optical Microscopy

The LC materials were examined under an Axio Imager 2 (Carl Zeiss AG, Germany) polarizing optical microscope equipped with a LTS420+LNP95 heating stage (Linkam Scientific Instruments Ltd., UK).

Differential Scanning Calorimetry

Thermal analyses by differential DSC were performed on a DSC Q1000 with a DSC refrigerated cooling system (TA instrument Inc., USA).

FT-IR Spectroscopy

Temperature-dependent and polarized FT-IR spectra were recorded with an AIM-8800 infrared microscope connected to a IRAffinity FT-IR spectrometer (Shimadzu Corp., Japan). The sample was prepared as a thin-film on a KBr substrate (thickness 2 mm) which was placed on a THMS600 heat stage with a TP94 controller (Linkam Scientific Instruments Ltd., UK). Polarization dependent FT-IR spectra were measured by using a precision automated polarizer (ZnSe) (PIKE Technologies, USA). This includes the PIKE Technologies Motion Control Unit and AutoPro software.

Cyclic Voltammetry

CV was carried out in a three electrode single-compartment cell on a standard electrochemical analyzer (EC epsilon, BAS Instruments, UK). A Pt disc electrode was used as a working electrode, a platinum wire as a counter electrode and an Ag/AgCl reference electrode using ferrocenium/ferrocene (Fc^+/Fc) as an internal standard for the calibration of the potential. The measurements were carried out under an argon atmosphere in dichloromethane and tetrabutylammonium hexafluorophosphate (recrystallized from ethanol/water and dried under vacuum) was added as supporting electrolyte.

Wide- and Middle Angle X-ray Scattering

Temperature-dependent WAXS and MAXS measurements were performed on a Bruker Nanostar (Detector Vantec2000, Microfocus copper anode X-ray tube Incoatec). LC samples were prepared by fiber extrusion using a mini-extruder. The measurements were carried out in Mark capillaries (Hilgenberg) positioned perpendicular to the incident X-ray beam. WAXS experiments were performed at a sample-detector distance of 21 cm, with the detector tilted by 14° upwards in order to study the angular range of $2\theta = 0.8° - 28°$. This allowed only the investigation of a section of the XRS pattern, therefore samples with lying and standing extruded fibers have been prepared to study the equatorial and the meridional signals in detail. Additional MAXS studies have been carried out at a distance of 28 cm with a linearly assembled detector covering an angular range of $2\theta = 0.7° - 12°$. Silver behenate was used as calibration standard for WAXS and MAXS. All X-ray data were processed and evaluated with the program datasqueeze.

Preparation of Two-Contact Devices

Two contact devices were prepared by spin casting the active layer on commercially available bottom gate, bottom contact architectures (n-doped Si, 100 nm SiO_2, 30 nm Au, Fraunhofer IPMS, Germany) with a grid-like structure forming a channel width (*W*) of 5 µm and a length (*L*) of 10 mm. Prior to spin-coating, the substrates were cleaned with acetone and isopropanol (both semiconductor grade VLSI PURANAL^{TM}, Aldrich Chemistry). The samples were prepared by spin-coating a solution in chloroform (1 mg/mL) onto the substrates (5000 rpm, 60 s). The samples were annealed by heating to 180 °C for 10 min.

Electrical Characterization

The electrical characterization of the two-contact devices was carried out by measuring the current with a Micromanipulator 4060 and 4155C semiconductor parametric analyzer (Agilent Technologies, USA) under ambient conditions at room temperature. Photocurrents were determined while illuminating the sample with a Hg arc lamp (120 W) focused onto the device by an optical microscope. The transistor characteristics were determined by measuring the current voltage characteristics with the same setup.

Atomic Force Microscopy (AFM)

AFM measurements were performed under ambient conditions using a Bruker Multimode 8 SPM system operating in tapping mode. Silica cantilevers (OMCL-AC200TS, Olympus) with a resonance frequency of ~150 kHz and a spring constant of ~10 Nm^{-1} were used.

Synthesis and characterization

PBI 2T was prepared according to Scheme A1. Methyl 5'-bromo-[2,2'-bithiophene]-5-carboxylate (**7**)[156] and 4,4,5,5-tetramethyl-2-(3,4,5-tris(dodecyloxy)phenyl)-1,3,2-dioxaborolane (**8**)[157] were synthesized according to literature procedure.

PBI **6b** was prepared according to literature procedure.[60]

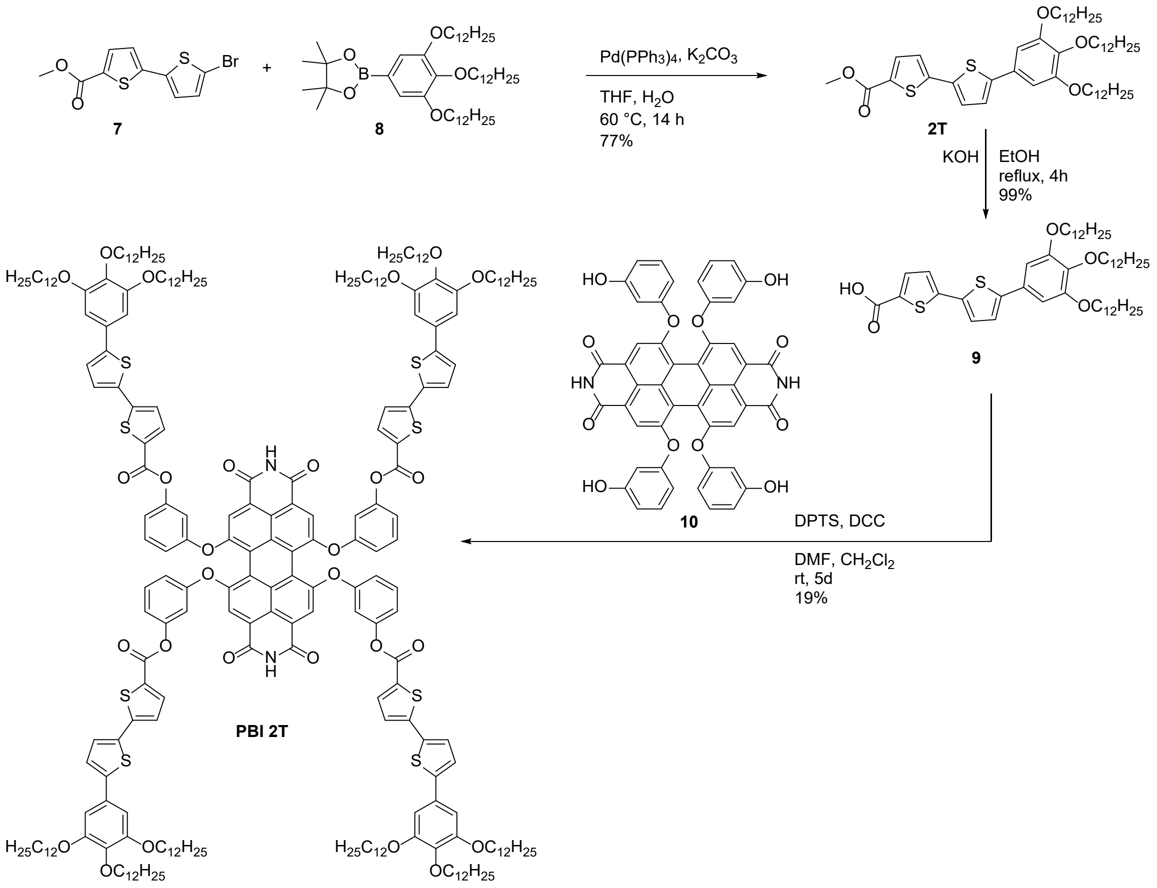

Scheme A1. Synthetic route to **PBI 2T.**

Methyl 5'-(3,4,5-tris(dodecyloxy)phenyl)-[2,2'-bithiophene]-5-carboxylate (2T)

Methyl 5'-bromo-[2,2'-bithiophene]-5-carboxylate **7** (0.60 g, 1.98 mmol, 1 eq.), 4,4,5,5-tetramethyl-2-(3,4,5-tris(dodecyloxy)phenyl)-1,3,2-dioxaborolane **8** (1.50 g, 1.98 mmol, 1 eq.) and 2M K_2CO_3 (aq., 25 mL) were added to tetrahydrofurane (THF, 200 mL) and the mixture was degassed. $Pd(PPh_3)_4$ (220 mg, 0.198 mmol, 0.1 eq) was added and the mixture was stirred at 60 °C for 14 h. TLC (silica, *n*-pentane:ethyl acetate, 98:2) indicated a complete conversion. After cooling to room temperature, the mixture was diluted with dichloromethane (50 mL), washed with brine (3 × 100 mL) and filtered. Flash chromatography (silica, *n*-pentane:ethyl acetate, 100:0 to 98:2) yielded 1.30 g (1.52 mmol, 77%) of a bright yellow solid.

^{1}H NMR (400 MHz, $CDCl_3$): δ = 7.70 (d, ^3J = 3.9 Hz, 1H, Ar*H*), 7.23 (d, ^3J = 3.9 Hz, 1H, Ar*H*), 7.14 (m, 2H, Ar*H*), 6.77 (s, 2H, Ar*H*), 4.00 (m, 6H, OCH_2), 3.90 (s, 3H, OCH_3), 1.80 (m, 6H, OCH_2CH_2), 1.49 (m, 6H, $O(CH_2)_2CH_2$), 1.40-1.24 (m, 48H, alkyl), 0.88 (m, 9H, CH_3). **^{13}C NMR** (100 MHz, $CDCl_3$): δ = 162.7, 153.6, 145.6, 144.4, 138.7, 135.1, 134.5, 131.1, 129.0, 126.2, 123.7, 123.7, 104.9, 73.7, 69.4, 52.4, 32.1, 32.1, 30.5, 29.9-29.8, 29.6-29.5, 26.3, 26.2, 22.8, 14.3. **HRMS** (ESI-TOF, positive mode, MeCN/$CHCl_3$ 1:1): *m/z* calculated for $C_{52}H_{84}O_5S_2$ $[M+Na]^+$: 875.5658; found, 875.5643. **Elemental analysis** calculated (%) for $C_{52}H_{84}O_5S_2$ [M = 853.36 g/mol]: C 73.19 H 9.92 S 7.51; found, C 73.20 H 10.09 S 7.46. **UV/Vis** ($CHCl_3$), λ_{max} (ε_{max}): 379 nm (27300 M^{-1} cm^{-1}). **m.p.** 63 °C.

5'-(3,4,5-tris(dodecyloxy)phenyl)-[2,2'-bithiophene]-5-carboxylic acid (9)

Methyl 5'-(3,4,5-tris(dodecyloxy)phenyl)-[2,2'-bithio-phene]-5-carboxylate **2T** (1.27 g, 1.49 mmol) and KOH (1.66 g, 29.6 mmol, 20 eq) were suspended in ethanol (35 mL). The mixture was refluxed for 4 h. The suspension was then diluted with dichloromethane (70 mL) and washed with 1N HCl (aq.) and sat. $NaHCO_3$ (aq.). The mixture was dried over Na_2SO_4. Removing the solvent under reduced pressure yielded 1.23 g (1.47 mmol, 99%) of a yellow solid.

^{1}H NMR (400 MHz, $CDCl_3$): δ = 7.80 (d, ^3J = 3.9 Hz, 1H, Ar*H*), 7.27 (d, ^3J = 3.9 Hz, 1H, Ar*H*), 7.17 (m, 2H, Ar*H*), 6.78 (s, 2H, Ar*H*), 4.01 (m, 6H, OCH_2), 1.79 (m, 6H, OCH_2CH_2), 1.48 (m, 6H, $O(CH_2)_2CH_2$), 1.40-1.23 (m, 48H, alkyl), 0.88 (m, 9H, CH_3). **^{13}C NMR** (100 MHz, $CDCl_3$): δ = 167.0, 153.6, 146.1, 146.1, 138.8, 136.1, 134.8, 130.1, 128.9, 126.6, 123.9, 123.8, 104.9, 73.8, 69.4, 32.1, 32.1, 30.5, 29.9-29.8, 29.6-29.5, 26.3, 26.3, 22.9, 14.3. **HRMS** (ESI-TOF, positive mode, MeCN/$CHCl_3$ 1:1): *m/z* calculated for $C_{51}H_{82}O_5S_2$ $[M+Na]^+$: 861.5502; found, 861.5470. **Elemental analysis** calculated (%) for $C_{51}H_{82}O_5S_2$ [M = 838.56 g/mol]: C 72.98 H 9.85 S 7.64; found, C 73.03 H 10.01 S 7.50. **m.p.** 80 °C.

PBI 2T

A solution of DCC (174 mg, 843 µmol, 5.2 eq) in CH_2Cl_2 (3 mL) was added to a solution of **9** (600 mg, 715 µmol, 4.4 eq), 4-(dimethyl-amino)pyridinium 4-toluene-sulfonate (DPTS) (95.4 mg, 324 µmol, 2 eq.) and **10** (134 mg, 163 µmol, 1 eq.) in a mixture of DMF (6 mL) and CH_2Cl_2 (12 mL). The mixture was stirred at room temperature for 5 days. The solvent was removed under reduced pressure and the crude product was purified by consecutive column chromatography (silica, $CHCl_3$), size exclusion chromatography and precipitation from $CHCl_3$ by the addition of MeOH yielding 127 mg (30.9 µmol, 19%) of a dark green, wax-like solid.

^{1}H NMR (400 MHz, $CDCl_3$): δ = 8.43 (s, 2H, N*H*), 8.31 (s, 4H, Ar*H*), 7.77 (d, ^3J = 4.0 Hz, 4H, Ar*H*), 7.32 (m, 4H, Ar*H*), 7.17 (d, ^3J = 3.8 Hz, 4H, Ar*H*), 7.11 (d, ^3J = 4.0 Hz, 4H, Ar*H*), 7.08 (d, ^3J = 3.8 Hz, 4H, Ar*H*), 7.05 (m, 4H, Ar*H*), 6.90 (m, 8H, Ar*H*), 6.72 (s, 8H, Ar*H*), 3.98 (m, 24H, OCH_2), 1.78 (m, 24H, OCH_2CH_2), 1.48 (m, 24H, $O(CH_2)_2CH_2$), 1.39-1.20 (m, 192H, alkyl), 0.88 (m, 36H, CH_3). **^{13}C NMR** (100 MHz, $CDCl_3$): δ = 162.7, 159.8, 156.0, 155.2, 153.6, 151.9, 146.0, 145.8, 138.8, 135.8, 134.7, 133.3, 130.7, 129.9, 128.8, 126.5, 123.7, 123.1, 121.4, 121.2, 120.6, 118.1, 116.9, 113.7, 104.7, 73.7, 69.4, 32.1, 32.1, 30.5, 29.9-29.8, 29.6-29.5, 26.3, 22.8, 14.3. **HRMS** (ESI-TOF, positive mode, MeCN/$CHCl_3$ 1:1): *m/z* calculated for $C_{252}H_{346}N_2O_{28}S_8$ $[M+2Na]^{2+}$: 2076.6669, found: 2076.6591. **Elemental analysis** calculated (%) for $C_{252}H_{346}N_2O_{28}S_8$ [M = 4108.01 g/mol]: C 73.68 H 8.49 S 6.24; found, C 73.65 H 8.52 S 6.00. **m.p.** >281 °C (decomposition). **UV/Vis** ($CHCl_3$): λ_{max} (ε_{max}) = 569 nm (41400 M^{-1} cm^{-1}).

Optical spectroscopy

UV/Vis Spectra of PBI 2T and the Corresponding Building Blocks

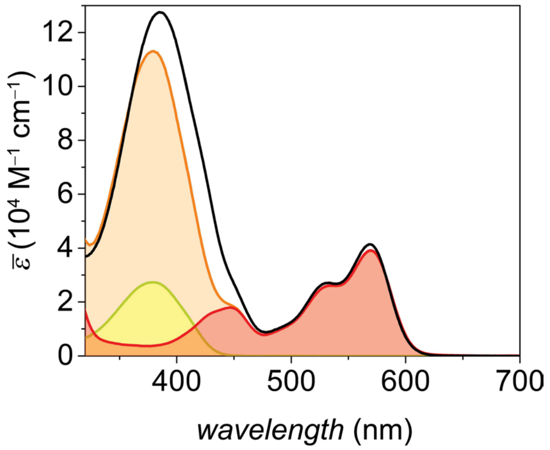

Figure A1. UV/Vis absorption spectra of **PBI 2T** (black), PBI **6b** (red), **2T** (yellow) and the equimolar superposition of PBI **6b** and **2T** (orange) recorded for 30 µM solutions in $CHCl_3$**.**

Concentration-Dependent UV/Vis Spectroscopy

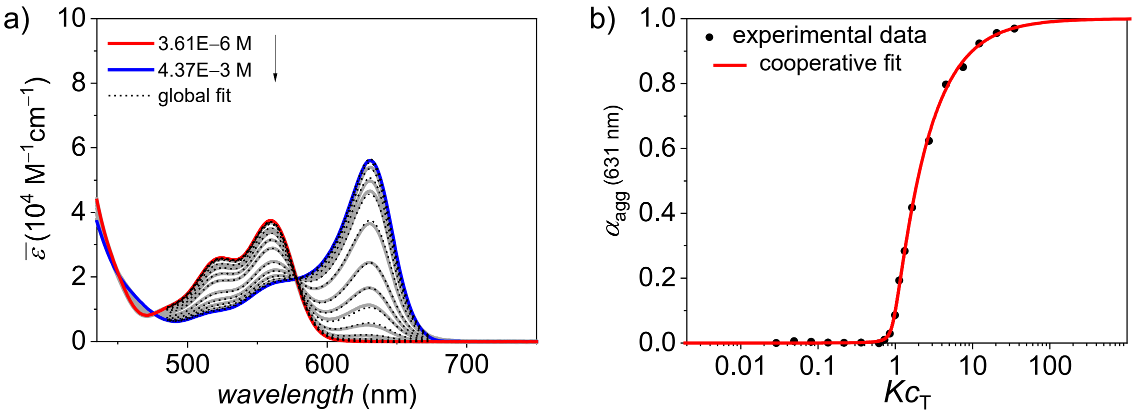

Figure A2. a) Concentration-dependent UV/Vis absorption spectra ($3.61 \times 10^{-6} - 4.37 \times 10^{-3}$ M, colored and grey lines) of **PBI 2T** in toluene at 295 K and reconstructed spectra from the cooperative nucleation-elongation fit (black dotted lines). The absorption spectra at wavelength below 440 nm are not shown due to the high absorptivity of the bithiophene units relative to the PBI leading to artefacts in concentration-dependent measurements for higher concentrations.[94] b) Plot of the experimental degree of aggregation α_{agg} over Kc_T (black dots) for **PBI 2T** at 631 nm and the corresponding fit according to the cooperative nucleation-elongation model (red).[94]

In concentration-dependent UV/Vis absorption studies of **PBI 2T** in toluene at 298 K a transition from monomers to J-aggregates with bathochromically shifted absorption bands could be observed. At low concentration PBI monomers with absorption maxima at 560 nm and 524 nm are present which self-assemble upon increasing concentration into J-aggregates with the main absorption band at 631 nm (Figure A2a). The occurrence of isosbestic points at 578 nm and 476 nm indicates the transition between two distinct species. The calculated degree of aggregation (α_{agg}) could be well described with the cooperative nucleation-elongation model.[94] From the global fit, an elongation constant of $K_{\mathrm{elong}} = 8000\ \mathrm{M}^{-1}$ and a cooperativity constant of $\sigma = 1.13 \times 10^{-3}$ was obtained considering a nucleus size of 2 molecules. The nucleation constant could therefore be calculated as $K_{\mathrm{nuc}} = 9\ \mathrm{M}^{-1}$.

Temperature-Dependent UV/Vis Spectroscopy

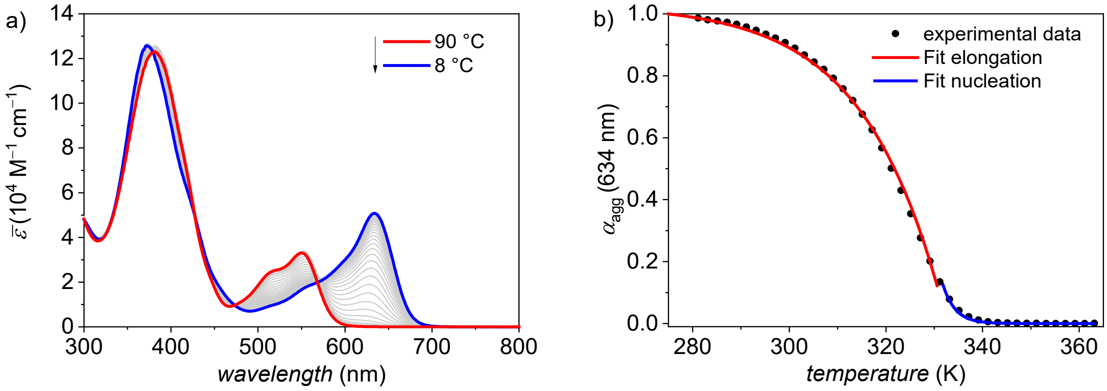

Figure A3. a) Temperature-dependent UV/Vis absorption spectra (90-8 °C; colored and grey lines) of **PBI 2T** in MCH / toluene (v/v, 1/1) at $c = 2.09 \times 10^{-4}$ M. (b) Plot of the degree of aggregation α_{agg} at 634 nm over the temperature and the corresponding fit according to the cooperative nucleation-elongation model (red: elongation; blue: nucleation).[95,158]

In temperature-dependent UV/Vis absorption studies of **PBI 2T** in MCH / toluene (v/v, 1/1, $c_0 = 2.09 \times 10^{-4}$ M), a transition from monomerically dissolved PBI at high temperatures with absorption bands at 552 nm, 516 nm and 381 nm to self-assembled **PBI 2T** at low temperatures with the main transitions at 634 nm and 372 nm could be observed (Figure A3a). The occurrence of isosbestic points at 474 nm and 569 nm indicates the transition between two distinct species. The calculated degree of aggregation could be well described with the cooperative nucleation-elongation model (Figure A3b).[95,158] From this fit, an elongation temperature of $T_{\mathrm{elong}} = 333$ K, an elongation enthalpy of $\Delta H_{\mathrm{elong}} = -56$ kJ/mol and a K_{a} value of 7.4×10^{-4} could be obtained.

Fluorescence spectroscopy

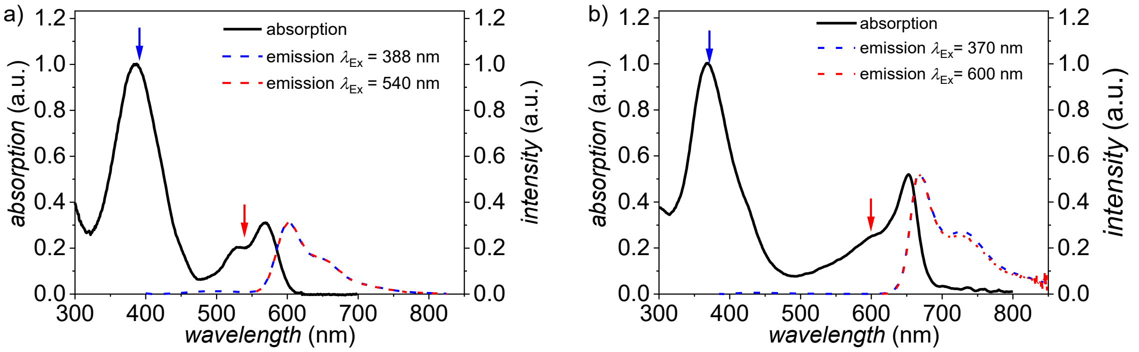

Figure A4. Normalized absorption (black) and emission (red and blue) spectra of a) monomeric **PBI 2T** ($c = 3.5 \times 10^{-7}$ M, $CHCl_3$, 295 K) and b) self-assembled **PBI 2T** ($c = 1.2 \times 10^{-7}$ M, MCH, 295 K). The blue and red arrows indicate the selective excitation wavelengths corresponding to the donor (blue) and acceptor (red) moieties.

The fluorescence quantum yields were determined as 2.9±0.2% for monomeric **PBI 2T** ($CHCl_3$) and 0.8±0.1 % for aggregated **PBI 2T** (MCH).

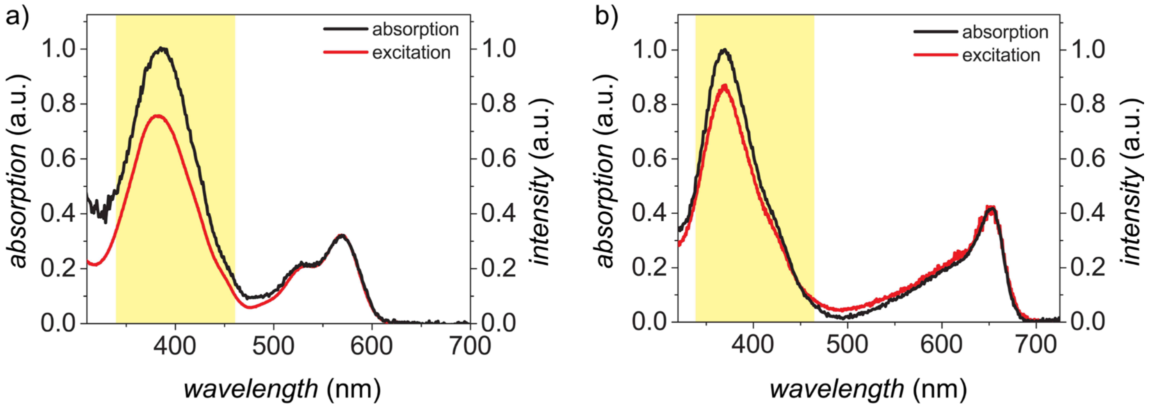

Figure A5. Normalized absorption (black) and excitation (red) spectra of a) monomeric **PBI 2T** (3.5×10^{-7} M, $CHCl_3$, $\lambda_{em} = 640$ nm, 295 K) and b) self-assembled **PBI 2T** (1.2×10^{-7} M, MCH, $\lambda_{em} = 750$ nm, 295 K). The areas highlighted in yellow indicate the range of integration.

By comparing the integrated area in absorption and excitation spectra in the region of the donor absorption (highlighted in yellow) the resonance ET efficiency was estimated to be appromately 74 % for monomeric **PBI 2T** in chloroform and 87 % for aggregated **PBI 2T** in MCH. The results from optical spectroscopy studies of **PBI 2T** in solution are summarized in Table A1 and Table A2.

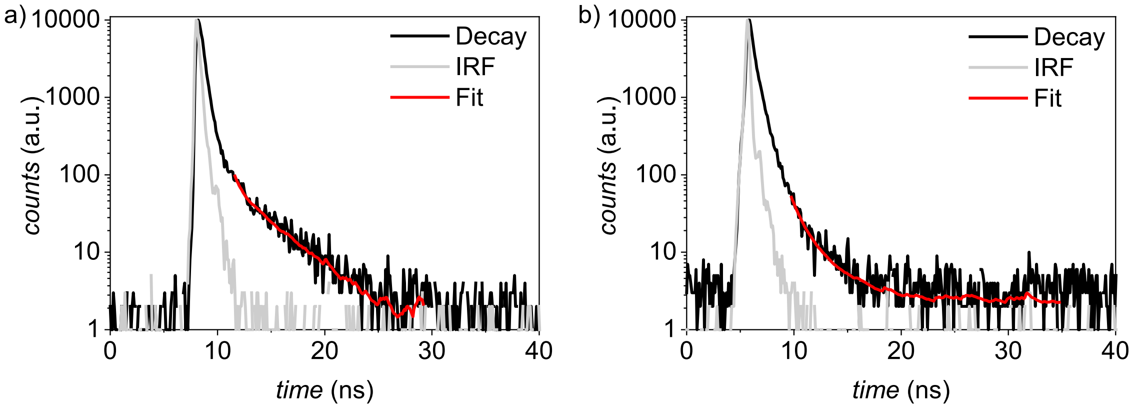

Figure A6. Lifetime measurement (black) of a) monomeric **PBI 2T** ($c = 3.5 \times 10^{-7}$ M, $CHCl_3$, 295 K, $\lambda_{ex} = 505$ nm, $\lambda_{em} = 605$ nm) and b) self-assembled **PBI 2T** ($c = 1.2 \times 10^{-7}$ M, MCH, 295 K, $\lambda_{ex} = 635$ nm, $\lambda_{em} = 660$ nm). The instrument response function (IRF) is shown in grey, the bi-exponential fits in red.

The results obtained from TCSPC experiments are summarized in Table A2.

Summary of the Optical Properties of PBI 2T

Table A1. Optical properties (absorption) of **PBI 2T** in solution.

Monomer (CHCl$_3$)[a]			**Aggregate (MCH)**[b]		
$\lambda_{\text{max, bithiophene}}$ (nm) [ε (M^{-1}cm^{-1})]	$\lambda_{\text{max, PBI}}$ (nm) [ε (M^{-1}cm^{-1})]	FWHM$_{\text{PBI}}$[c] (cm^{-1})	$\lambda_{\text{max, bithiophene}}$ (nm) [ε (M^{-1}cm^{-1})]	$\lambda_{\text{max, PBI}}$ (nm) [ε (M^{-1}cm^{-1})]	FWHM$_{\text{PBI}}$[c] (cm^{-1})
385 [127300]	569 [41400]	960	369 [117200]	654 [63900]	643

[a] CHCl$_3$ ($c = 3.11 \times 10^{-5}$ M) at 22 °C;

[b] MCH ($c = 3.04 \times 10^{-5}$ M) at 22 °C;

[c] FWHM was derived as twice the distance between the absorption maximum to the closest edge (here the red edge) at half maximum of the unsymmetrically shaped absorption bands to prevent falsification by the vibronic progression.

Table A2. Optical properties (emission) of **PBI 2T** in solution.

Monomer (CHCl$_3$)[a]					**Aggregate (MCH)**[b]				
λ_{max} (nm)	$\Delta\tilde{\nu}_{\text{stokes}}$ (cm^{-1})	Φ_{Fl}[c] (%)	τ_{Fl}[d] (ns) [%]	ET eff. (%)	λ_{max} (nm)	$\Delta\tilde{\nu}_{\text{stokes}}$ (cm^{-1})	Φ_{Fl}[e] (%)	τ_{Fl}[f] (ns) [%]	ET eff. (%)
601	−940	2.9±0.2	0.56 [95], 3.58 [5]	74	667	−300	0.8±0.1	0.81 [95], 2.74 [5]	87

[a] CHCl$_3$ ($c = 3.5 \times 10^{-7}$ M) at 22 °C;

[b] MCH ($c = 1.2 \times 10^{-7}$ M) at 22 °C;

[c] Relative to *N*,*N*'-bis(2,6-diisopropylphenyl)-1,6,7,12-tetraphenoxy-3,4,9,10-perylenetetracarboxylic diimide[153];

[d] $\lambda_{\text{ex}} = 505$ nm, $\lambda_{\text{em}} = 605$ nm;

[e] Relative to 3,7-bis(diethylamino)phenoxazinum perchlorate[154];

[f] $\lambda_{\text{ex}} = 635$ nm, $\lambda_{\text{em}} = 660$ nm.

Table A3. Optical properties of thin films of **PBI 2T**.

Absorption			**Emission**		
$\lambda_{\text{max, bithiophene}}$ (nm)	$\lambda_{\text{max, PBI}}$ (nm)	FWHM$_{\text{PBI}}$[b] (cm^{-1})	λ_{max} (nm)	$\Delta\tilde{\nu}_{\text{stokes}}$ (cm^{-1})	Φ_{Fl}[c] (%)
378	653	730	669	−370	2

[a] Spin-coated from 1 mM solutions in MCH on quartz substrates and annealed for 30 minutes at 180 °C;

[b] FWHM was derived as twice the distance between the absorption maximum to the closest edge (here the red edge) at half maximum of the unsymmetrically shaped absorption bands to prevent falsification by the vibronic progression;

[c] Determined as absolute quantum yield with an integration sphere (see Materials and Methods section).

Cyclic Voltammetry

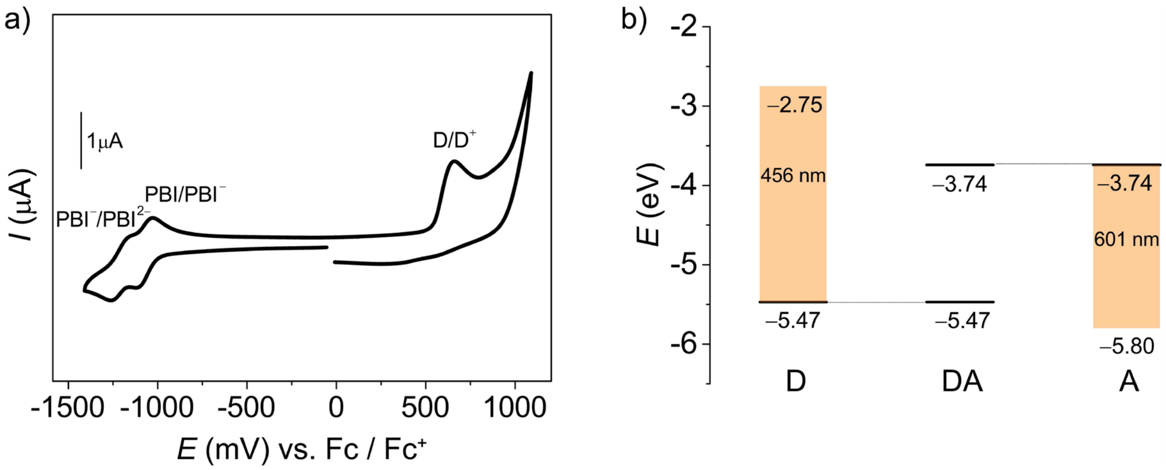

Figure A7. a) CV trace of **PBI 2T**. The reduction and oxidation processes are labelled with PBI and D (D = Donor = electron rich side arm), respectively. The measurement was performed in dichloromethane ($c \approx 2 \times 10^{-4}$ M) at room temperature with tetrabutylammonium hexafluorophosphate (0.1 M) as electrolyte (scan rate: 100 mV s^{-1}). b) Energy level diagram of **PBI 2T**. Orange bars indicate the optical bandgaps corresponding to the PBI (A = Acceptor) and electron rich side arm (D = Donor).

Using the redox potentials obtained from the CV measurements and optical bandgaps obtained from UV/Vis absorption studies, the HOMO and LUMO energy levels were estimated according to common procedure using the experimentally determined redox potentials and the energy level of Fc$^+$/Fc with respect to the vacuum level (−4.8 eV, $E_{\mathrm{LUMO}} = -[E\,(\mathrm{M/M^-}) + 4.8\ \mathrm{eV}]$ and $E_{\mathrm{HOMO}} = -[E\,(\mathrm{M/M^+}) + 4.8\ \mathrm{eV}]$). These results are summarized in Table A4.

Table A4. Summary of the redox properties of **PBI 2T** as determined by CV in dichloromethane ($c \approx 2 \times 10^{-4}$ M) at room temperature with tetrabutylammonium hexafluorophosphate (0.1 M) as electrolyte (scan rate: 100 mV s^{-1}).

E^{ox1} (V)	$E_{1/2}^{\mathrm{red1}}$ (V)	$E_{1/2}^{\mathrm{red2}}$ (V)	E_{HOMO} (eV)	E_{LUMO} (eV)
0.67[a]	−1.06	−1.19	−5.47	−3.74

[a] Oxidation is irreversible, therefore peak potential is given.

Polarized Optical Microscopy and Differential Scanning Calorimetry

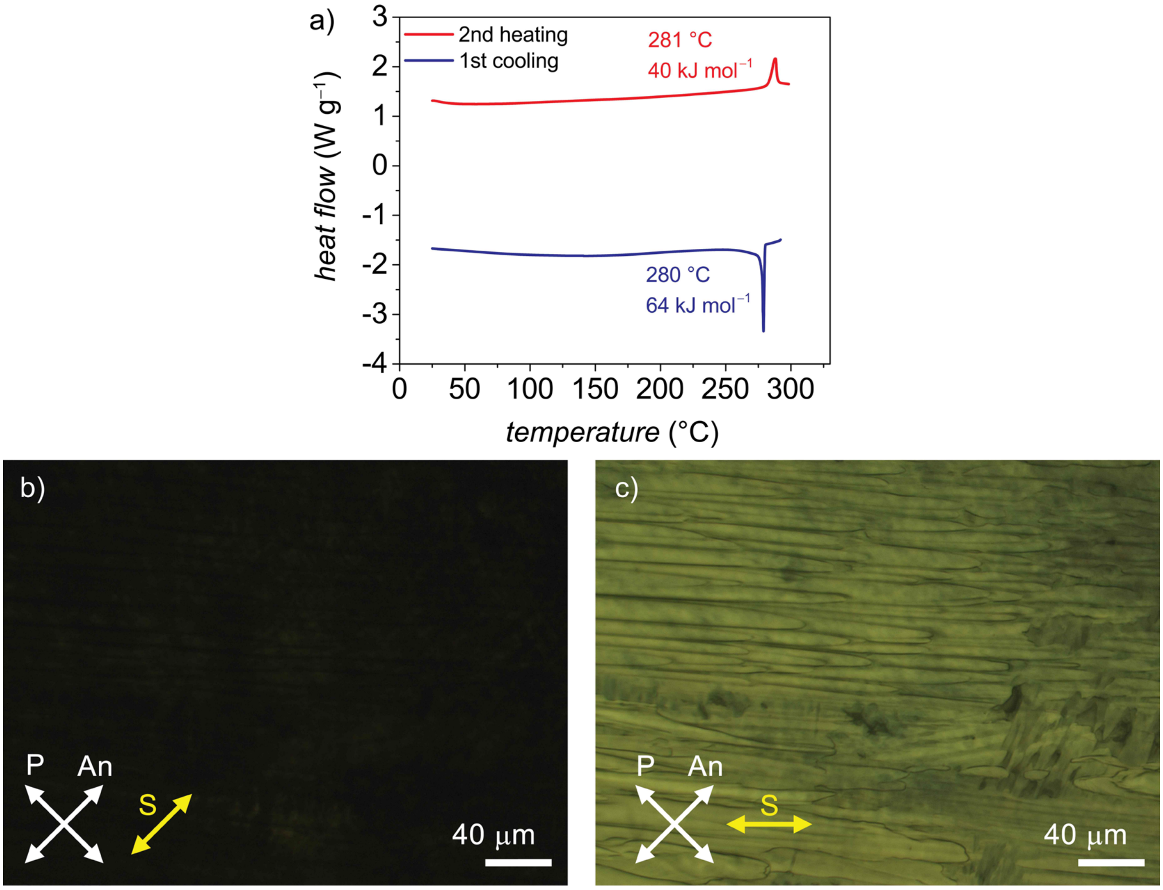

Figure A8. a) DSC traces of **PBI 2T** in the first cooling (blue) and second heating (red) process. The heating and cooling rates were 10 °C/min. POM images of a mechanically aligned sample of **PBI 2T** on quartz substrates at 200 °C with crossed polarizer (P) and analyzer (An) with the shearing direction (S) b) parallel and c) in a 45° rotational displacement with respect to the analyzer.

Polarized FT-IR Spectroscopy

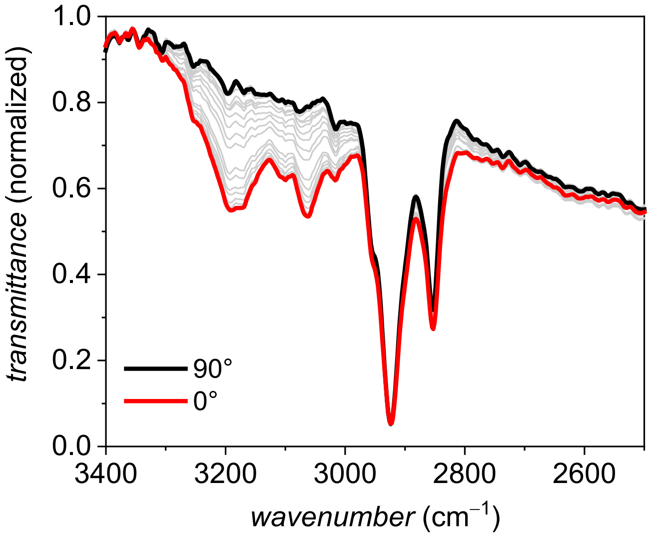

Figure A9. Polarized FT-IR spectra with different polarization angles of an aligned sample of **PBI 2T** at 180 °C. The sample was sheared using an extruded fiber for friction transfer on a KBr substrate. The black and red line show the spectra for the polarizer orientated perpendicular and parallel to the shearing direction, respectively.

The sample for the FT-IR experiments was prepared by friction transfer of an extruded fiber of **PBI 2T** on a KBr substrate. The polarized FT-IR measurements show that the NH stretching vibration at 3190 cm^{-1} corresponding to the hydrogen-bonded imide units is maximal when measuring along the shearing direction (red) while it practically disappears when measuring perpendicular to the shearing direction (black). This indicates that the PBIs are oriented with their long axis along the shearing direction and therefore along the columnar long axis.

Density Measurements and Calculation of the Number of Molecules

Density measurements were carried out by the buoyancy method at 23 °C in mixtures of deionized water and aqueous sodium chloride solution (20 wt%). Sodium chloride (*pro analysi*) was dried under reduced pressure (1×10^{-3} mbar). The solvents were degassed by ultra-sonication prior to the measurement. **PBI 2T** was heated to 240 °C under reduced pressure and extruded in vacuum in order to minimize the inclusion of air bubbles within the sample. The fiber was cut into several pieces of varying size (0.1-0.6 mg). The samples were put in a sealed vial containing deionized water at 23 °C and aqueous sodium chloride (20 wt%) solution was added in small portions and the mixture was allowed to equilibrate between additions until the sample started floating in the center of the vial. The necessary weight percentage of sodium chloride was determined and the density was calculated according to literature.[122] The density of **PBI 2T** at 23 °C was determined to be $\rho = 1.076 \pm 0.002$ g cm^{-3}. Please note that for materials with much lower clearing temperatures and high thermal stability in the isotropic liquid, the samples can be prepared by melting them under reduced pressure to eliminate the inclusion of air bubbles.[123] However, as **PBI 2T** starts decomposing at very high temperatures, the probability of air inclusion can only be limited but not eliminated. Therefore, this density value displays a lower limit.

The molecular volume V_{mol} can be calculated using equation (2). The temperature dependence of the molecular volume of a PBI with aliphatic substituents in imide position is reported in literature.[126] Calculating the temperature-dependent change in molecular volume of the aliphatic chains it becomes obvious that the change in molecular volume of the aromatic part is rather small.[60,124,125] Thus for the estimation of V_{mol} at higher temperatures the aromatic volume can be kept constant.

Calculating the change in molecular volume according to the equations reported in literature, one obtains values that are summarized in Table A5.

Table A5. Summary of the values corresponding to the temperature-dependent density calculation for **PBI 2T**.

T (°C)	V_{ar} (Å^3)	V_{aliph} (Å^3)	V_{mol} (Å^3)	ρ (g cm^{-3})
23	2440.51	3900.61	6341.14	1.076
230	2440.51[a]	4769.07	7209.58	0.948

[a] Assuming a negligible gradient for the expansion of V_{ar} as described above.

The number of molecules Z per columnar stratum was calculated using equation (1).[159]

The volume of the columnar stratum $V_{\mathrm{col-strat}}$ can be calculated according to equation (8) for a $\mathrm{Col_h}$ unit cell:

$$V_{\mathrm{col-strat}} = a^2 * sin60° * h \tag{8}$$

Thereby, a is the unit cell parameter for the hexagonal phase and h is the height of the columnar stratum, which can be in principle chosen arbitrarily. Since the axial translational subunit is a PBI with the length of 14.3 Å, this has been naturally chosen as stratum height. Using these X-ray parameters and the density extrapolated to 230 °C, the number of molecules per columnar stratum was calculated to be 5.7±0.3 molecules (assuming an error of 0.5 Å for the determination of the cell parameters). Considering that the experimentally determined density is a lower limit it is reasonable to assume six molecules per columnar stratum leading to the formation of a sextuple-stranded helix.

Molecular Modelling and X-Ray Scattering

The model of self-assembled **PBI 2T** is based on π-stacked hexamers. These hexameric units were built by cofacial stacking of the molecules in a π–π distance of 3.9 Å with a longitudinal and rotational displacement of 7.15 Å and 11.5 °, respectively (Figure A10a and b). 16 hexamers were then arranged along the long axis of the PBIs in a distance of 14.3 Å to form one helical column (six-stranded 16_1 helix) consisting of 96 molecules (Figure A10c). This assembly was placed in a hexagonal unit cell ($a = 57.2$ Å) and geometry optimized using the forcefield COMPASS II applying the Ewald summation method until the non-bonding energy was strongly negative.

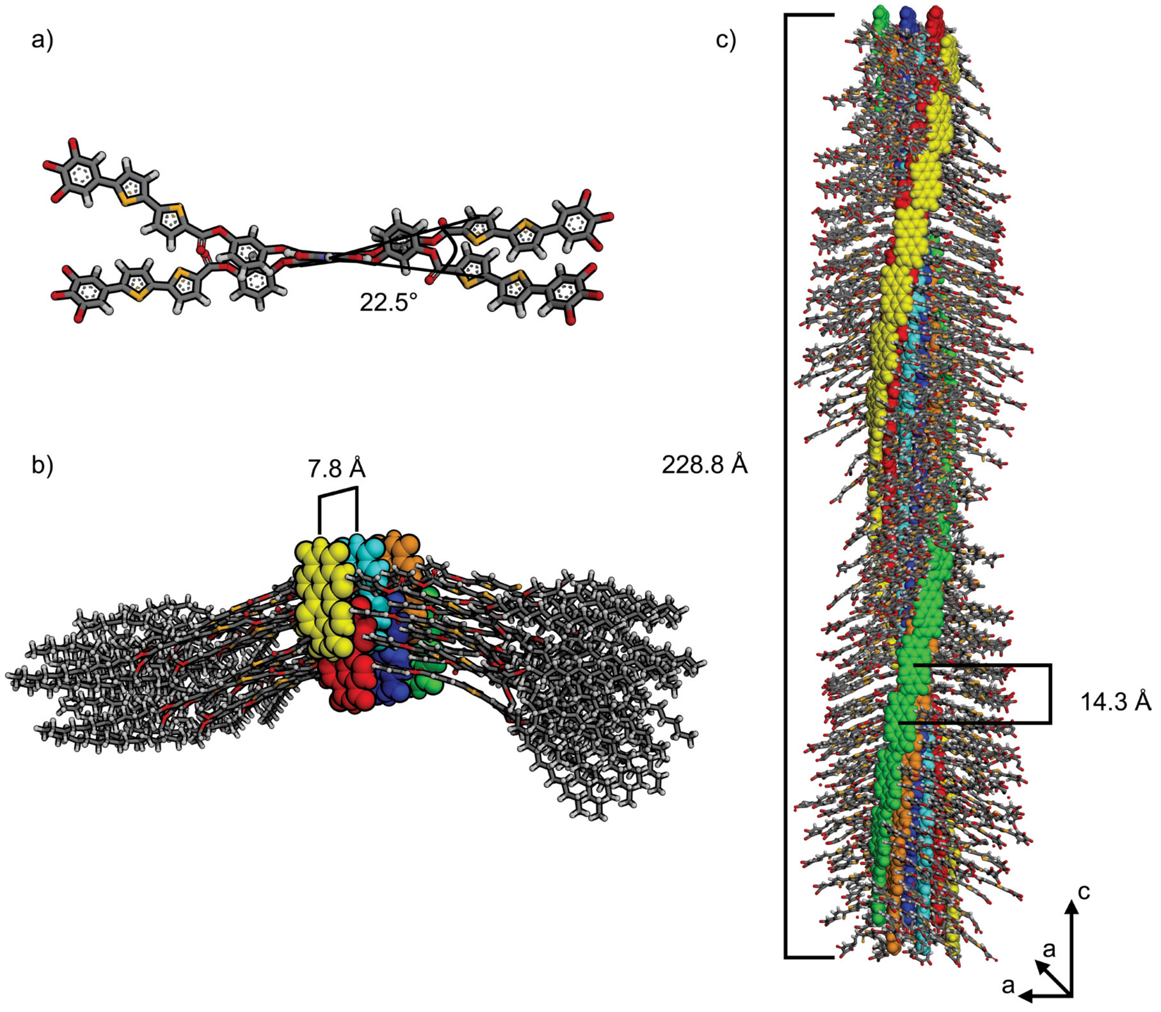

Figure A10. a) Single molecule of **PBI 2T** in top view. Dodecyl chains were omitted for clarity. b) Hexameric unit in side view. The PBI cores were individually colored for clarity. c) Side view of the assembled helix. The strands were individually colored to visualize the helical arrangement. The helicity in the shown columnar assembly has been chosen to be (*P*) for graphical representation. Please note that **PBI 2T** is racemic and therefore (*P*) and (*M*) helices may coexist in the LC phase.

The fiber diffraction pattern was simulated with the program *CLEARER*[134] using the modelled and geometry optimized structure obtained in Materials Studio.[130] The structure was exported as pdb-file and imported into the fiber diffraction simulation module of *CLEARER*. The fiber axis was set to (0,0,1) with a crystallite size of $a = 100$ nm, $b = 100$ nm and $c = 120$ nm. The fiber disorder paramters σ_ϕ and σ_θ were set to infinity and 0.5, respectively. The crystallite size and contrast were adjusted to best fit the experimental pattern. It has to be considered that *CLEARER* simulates the diffraction pattern based on a perfectly ordered domain. However, a real liquid crystal is not built with identical unit cells. Therefore, the intensity of the simulated signals can vary from the experimentally observed. Nevertheless, it is to note that the position and relative intensity of the signals are in rather good agreement with those observed experimentally.

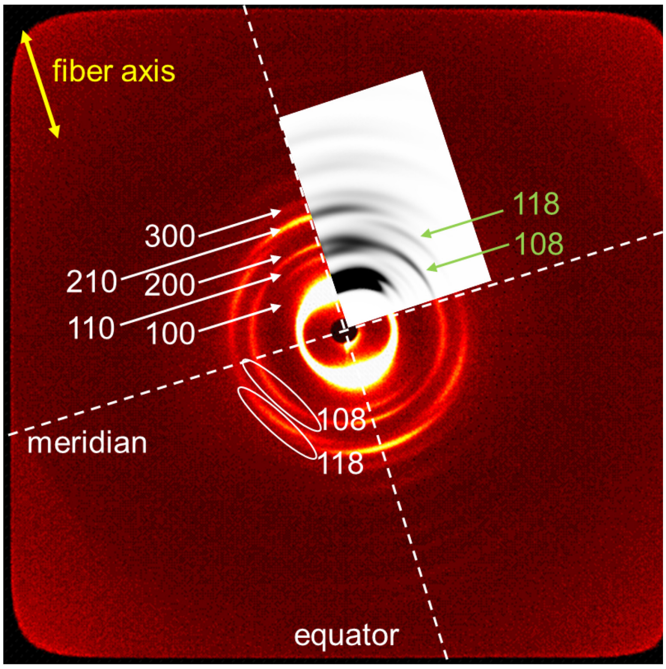

Figure A11. Superposition of the MAXS pattern of **PBI 2T** at 230 °C and the simulated diffraction pattern calculated using *CLEARER* and the geometry optimized model generated with Materials Studio. The yellow arrow indicates the orientation of the fiber. The white arrows and circles indicate the assignment of the signals according to the Col$_h$ phase.

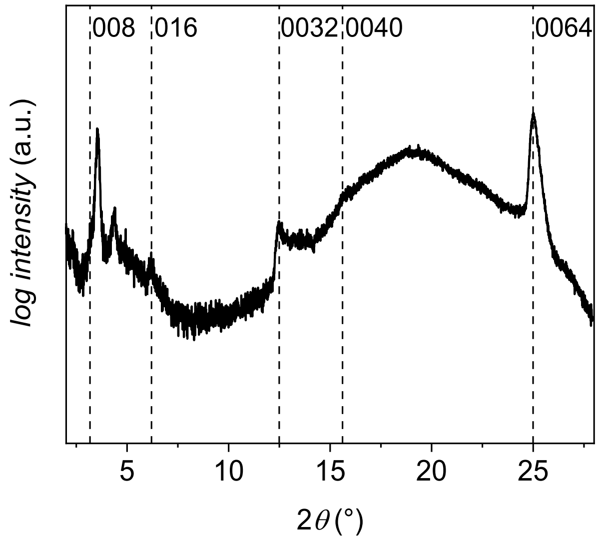

Figure A12. Integrated intensity along the meridian of the WAXS pattern of **PBI 2T** at 230 °C. Dashed lines indicate the position of the meridonal signals on the layerlines.

The correlation length ξ in the LC state can be calculated according to the Scherrer equation[160]:

$$\xi = \frac{K * \lambda}{\Delta(2\theta) * \cos(\theta)} \tag{9}$$

where K is the dimensionless shape factor with a typical value of 0.9, λ the X-ray wavelength, $\Delta(2\theta)$ the full width at FWHM in radians and θ the Bragg angle in degrees.

By this method we calculated the correlation length for the π-stacked PBIs perpendicular to the columnar direction. $\Delta(2\theta)$ and θ were determined by fitting the signal on the equator belonging to the π–π stacking distance. The number of correlated molecules *N* was then calculated by dividing the correlation length by the π-distance.

By this method, a correlation length of 22.24 Å was determined. This correlates to 22.24 Å/3.9 Å = 5.7 molecules and is in perfect agreement with the determined number of molecules per columnar stratum by the estimated density as described above.

UV/Vis Spectroscopy of Thin Films

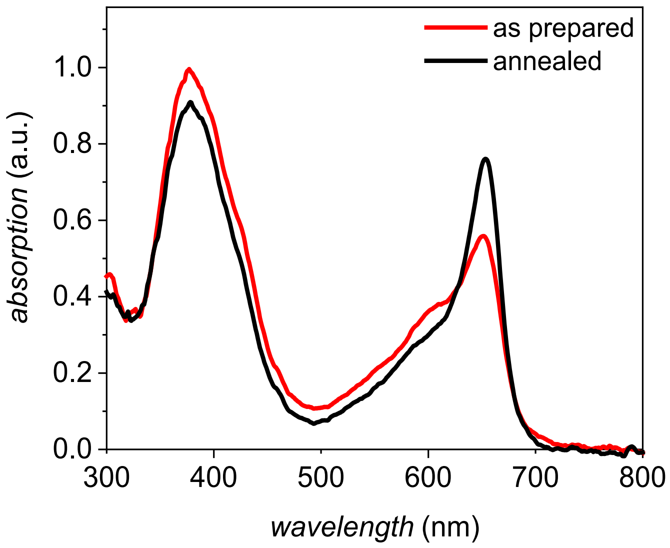

Figure A13. UV/Vis absorption spectra of thin films prepared by spin-coating a 1 mM solution of **PBI 2T** in MCH onto quartz substrates at 5000 rpm for 1 minute. The red and black line show the absorption spectra of the as-prepared sample and after annealing the sample at 180 °C for 30 minutes, respectively.

Optoelectronic Investigations

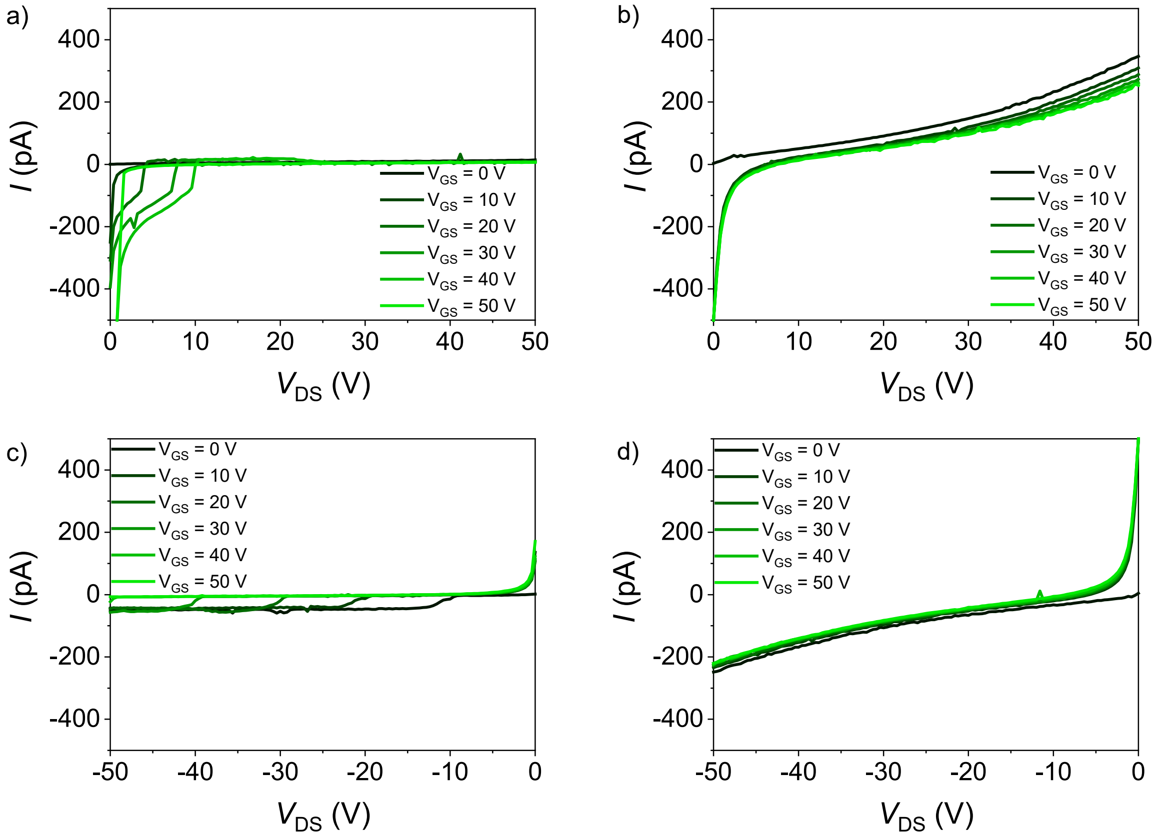

Figure A14. Output characteristics for n-channel (a, b) and p-channel (c, d) operation of spin-cast and thermally annealed thin-films of **PBI 2T** in the dark (a, c) as well as under illumination (b, d) with a white light source (38 mW cm^{-2}).

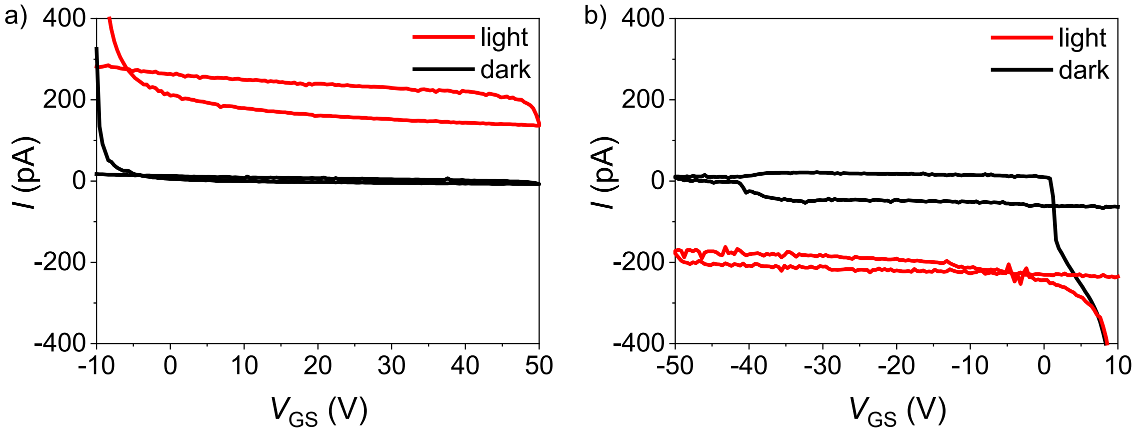

Figure A15. Transfer characteristics under a) n-channel and b) p-channel operation of spin-cast and thermally annealed thin-films of **PBI 2T** in the dark (black) and under illumination with a white light source (red, 38 mW cm^{-2}).

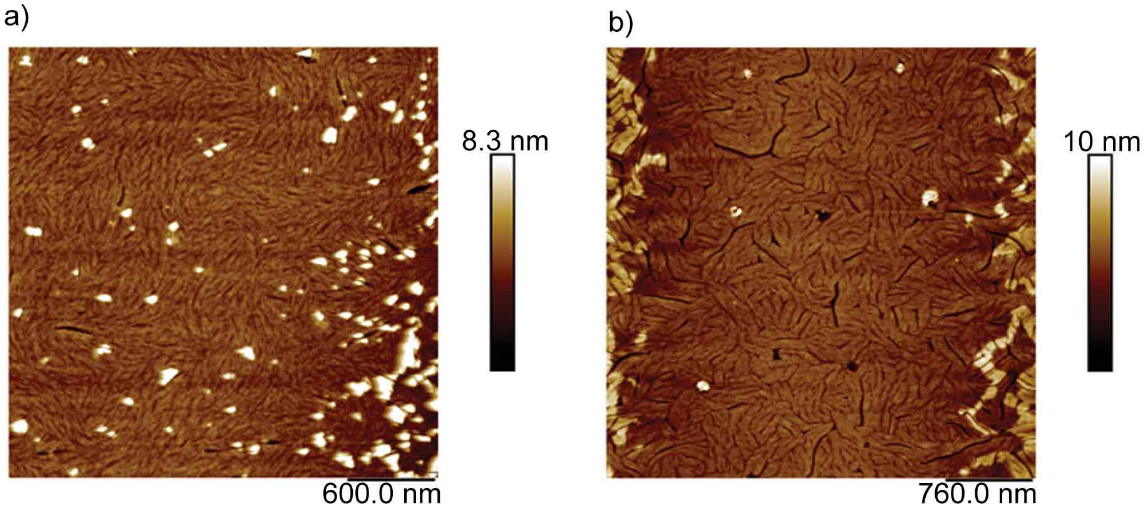

Figure A16. AFM height images of two-contact devices of a) **PBI 2T** and b) PBI **6b**.

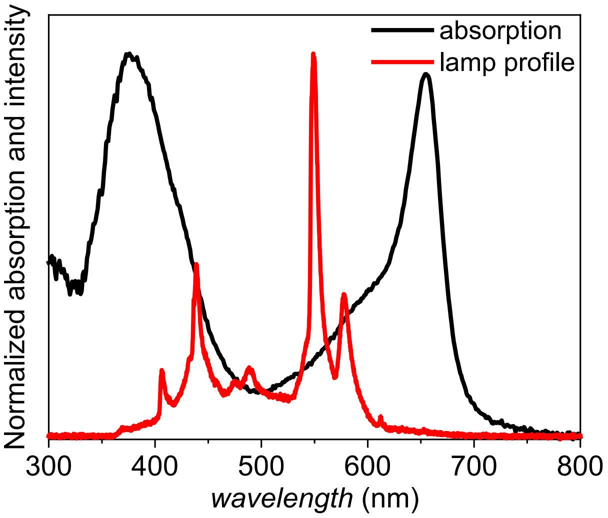

Figure A17. Superposition of the normalized absorption profile of spin-cast thin-films of **PBI 2T** and the emission profile of the Hg arc lamp used in the photoconductivity experiments.

NMR and MS spectra

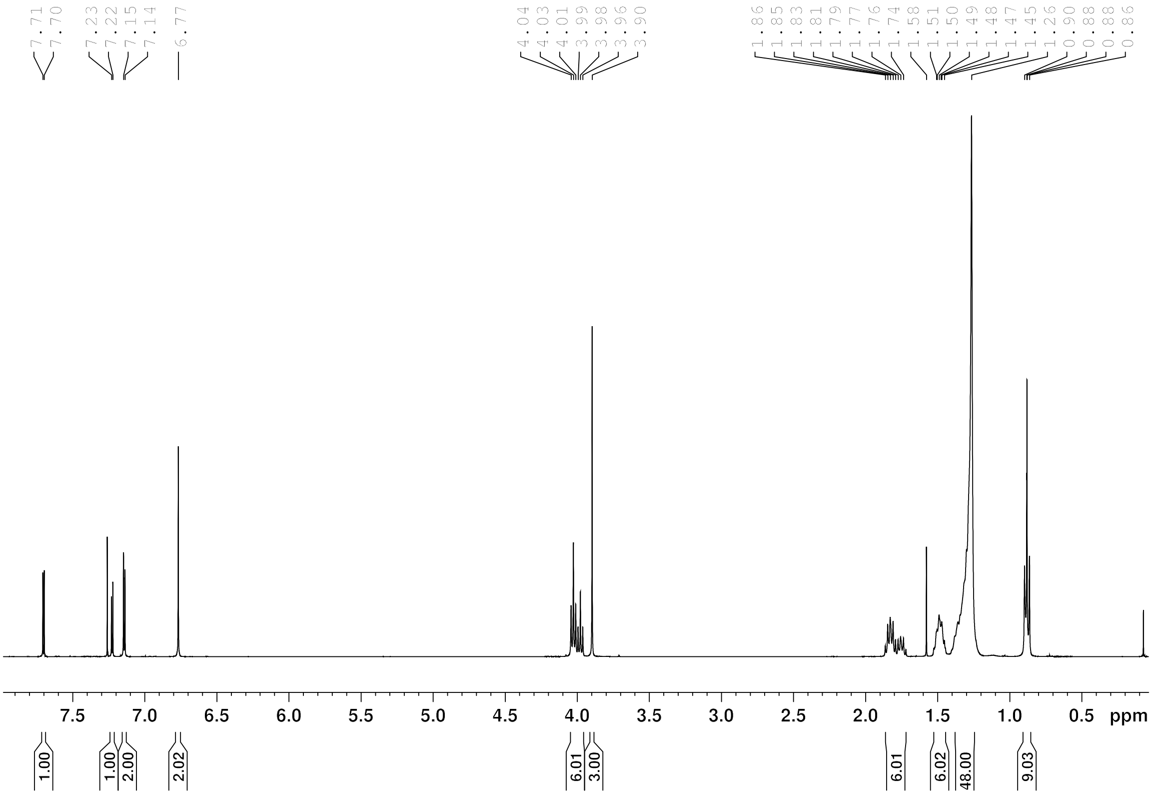

Figure A18. ^{1}H NMR (CDCl$_3$, 400 MHz, 295 K) of compound **2T**.

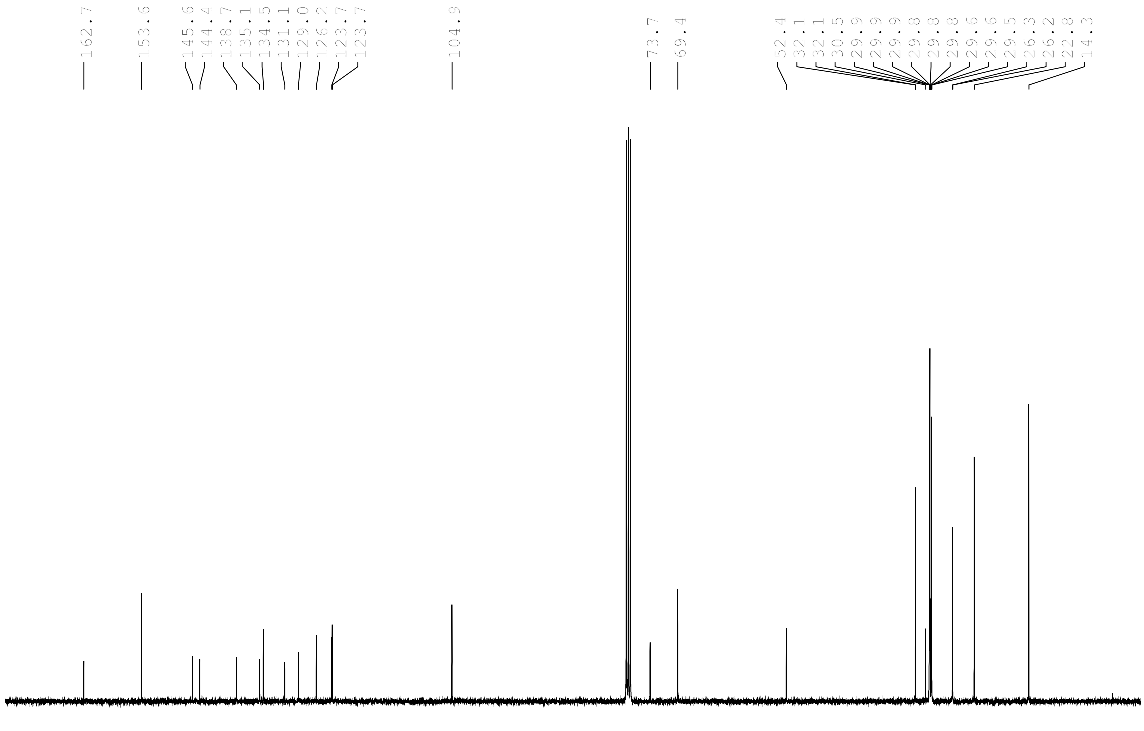

Figure A19. ^{13}C NMR (CDCl$_3$, 100 MHz, 295 K) of compound **2T**.

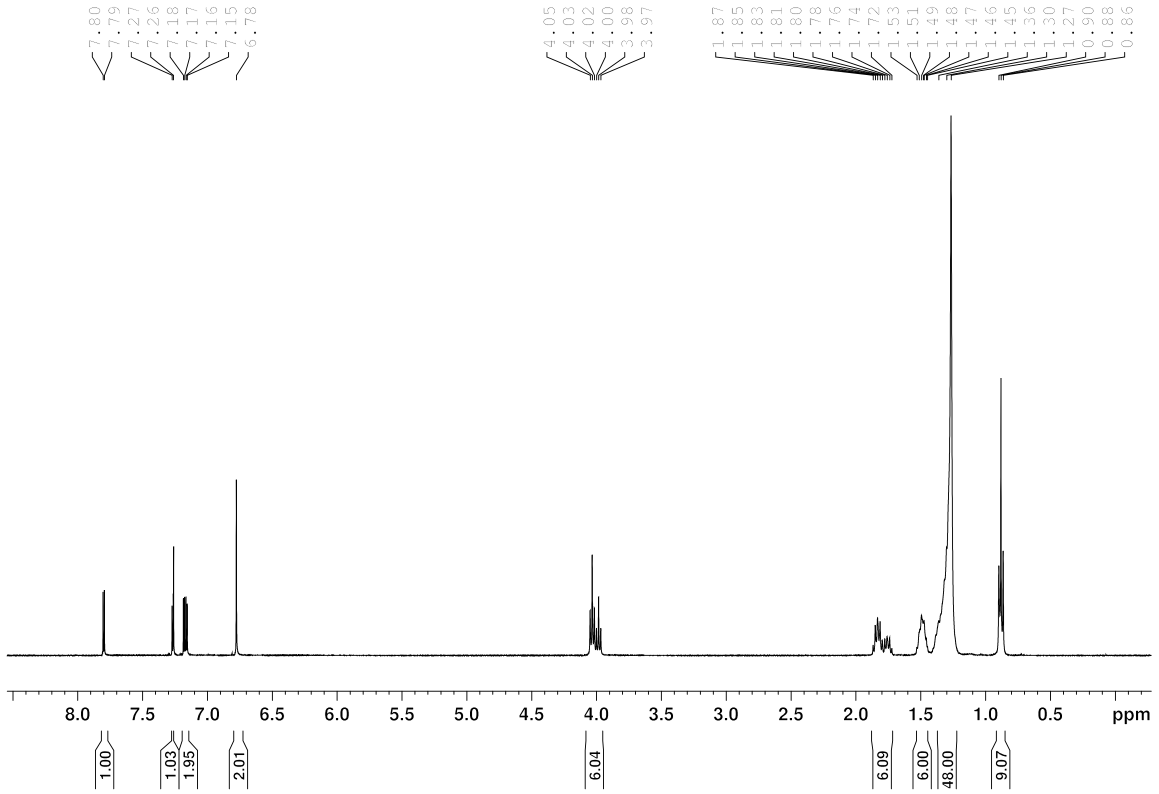

Figure A20. ^{1}H NMR (CDCl$_3$, 400 MHz, 295 K) of compound **9**.

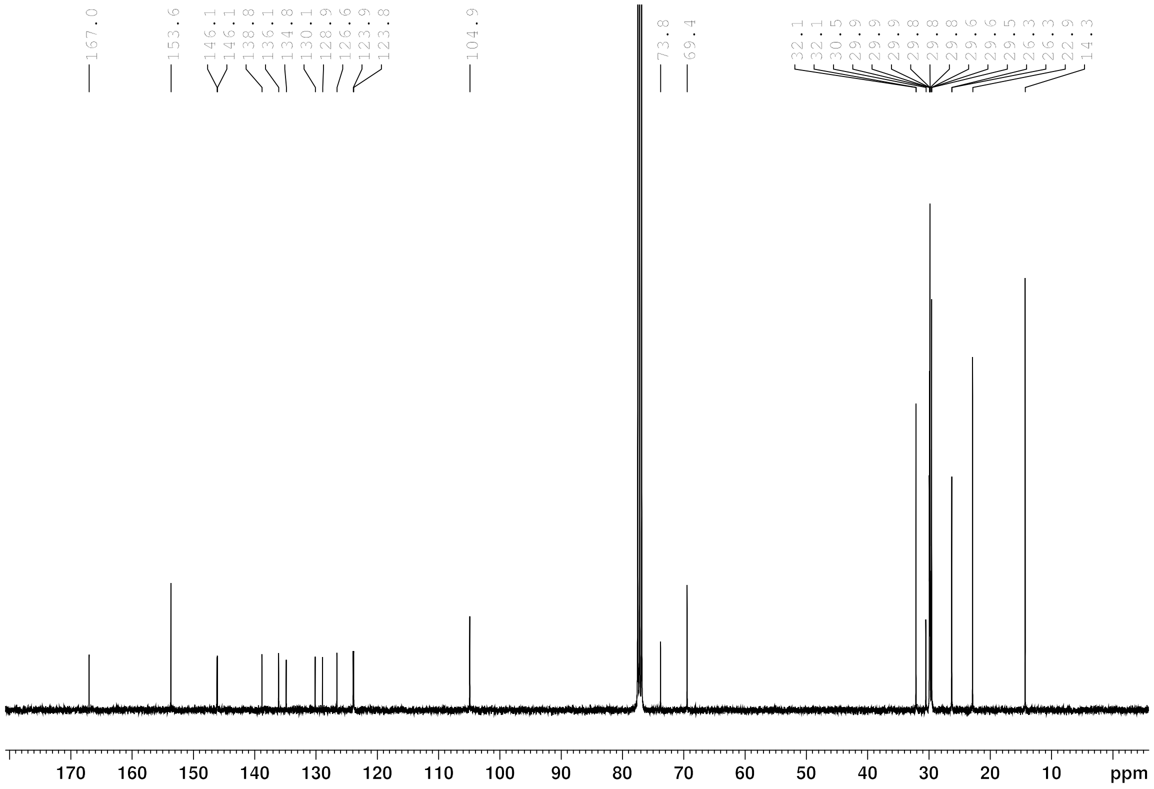

Figure A21. ^{13}C NMR (CDCl$_3$, 100 MHz, 295 K) of compound **9**.

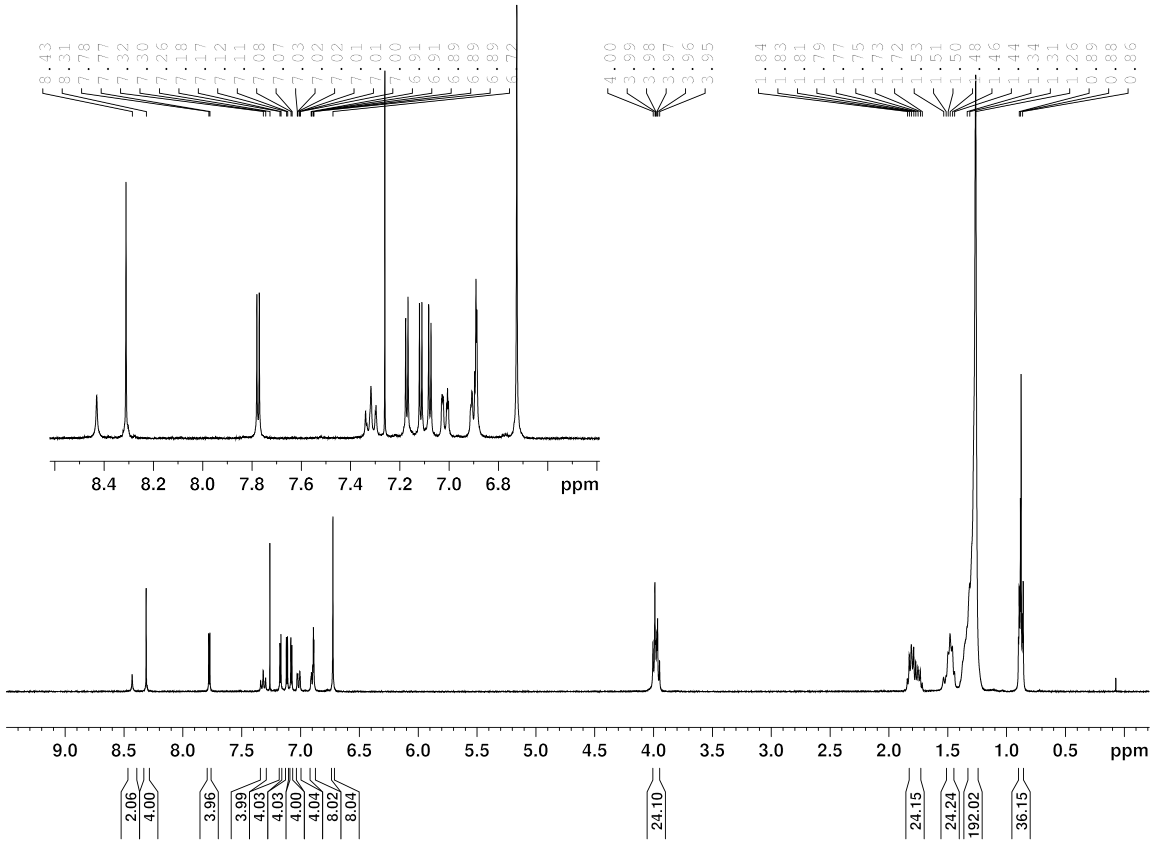

Figure A22. ^{1}H NMR (CDCl$_3$, 400 MHz, 295 K) of **PBI 2T**.

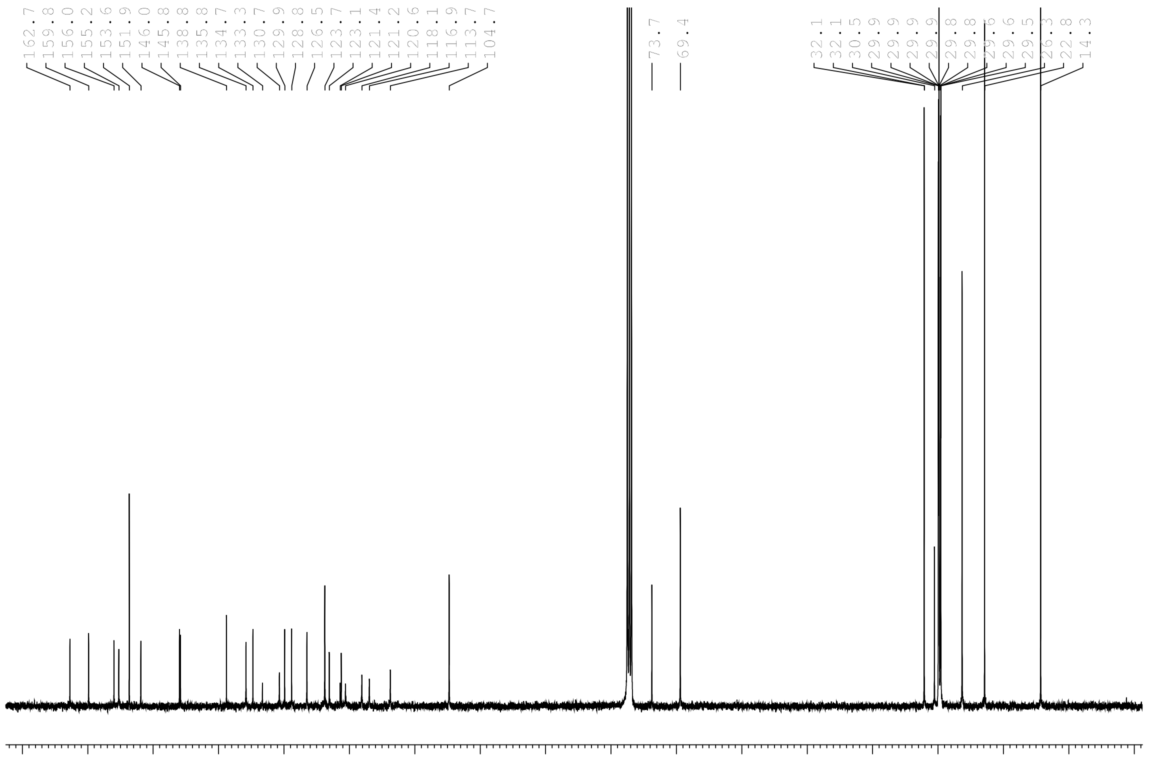

Figure A23. ^{13}C NMR (CDCl$_3$, 100 MHz, 295 K) of **PBI 2T**.

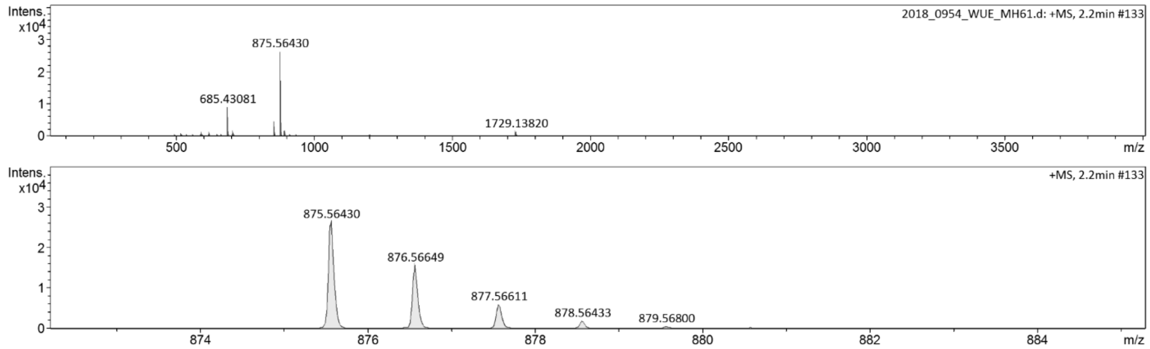

Meas. m/z	#	Ion Formula	m/z	err [ppm]	mSigma	# mSigma	Score	rdb	e^- Conf	N-Rule
875.56430	1	C52H84NaO5S2	875.56524	1.07	22.8	1	100.00	10.5	even	ok

Figure A24. HRMS (ESI, pos. mode, $CH_3CN/CHCl_3$) of compound **2T**.

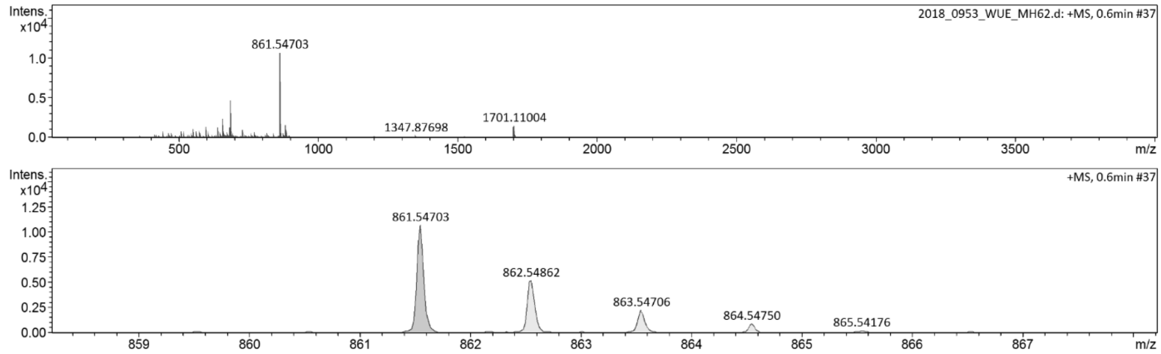

Meas. m/z	#	Ion Formula	m/z	err [ppm]	mSigma	# mSigma	Score	rdb	e^- Conf	N-Rule
861.54703	1	C51H82NaO5S2	861.54959	2.97	48.8	1	100.00	10.5	even	ok

Figure A25. HRMS (ESI, pos. mode, $CH_3CN/CHCl_3$) of compound **9**.

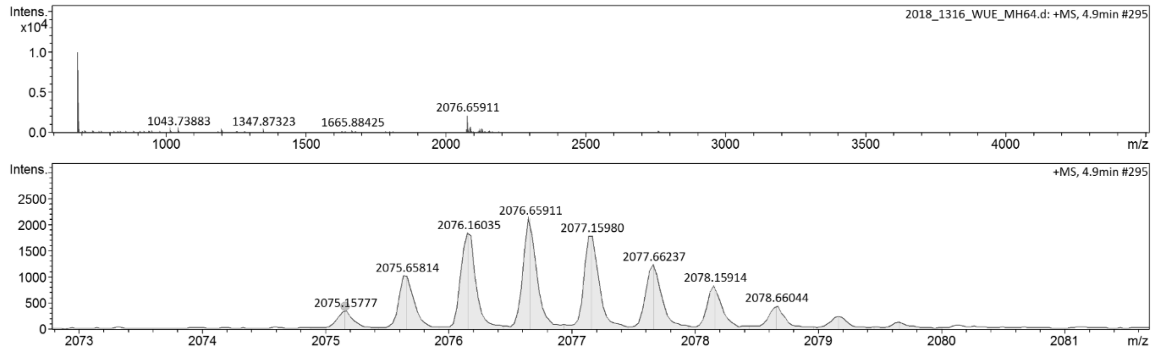

Meas. m/z	#	Ion Formula	m/z	err [ppm]	mSigma	# mSigma	Score	rdb	e^- Conf	N-Rule
2075.15777	1	C252H346N2Na2O28S8	2075.16311	2.57	43.0	1	100.00	80.0	even	ok

Figure A26. HRMS (ESI, pos. mode, $CH_3CN/CHCl_3$) of **PBI 2T**.

Chapter 4

–

Nanoscale Columnar Bundles Based on Multistranded Core–Shell Liquid Crystals of Perylene Bisimide J-Aggregate Donor–Acceptor Dyads for Photoconductivity Devices with Enhanced Performance Through Macroscopic Alignment

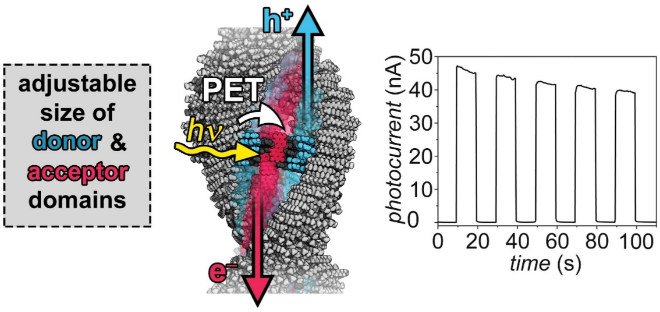

This chapter was published in: M. Hecht, T. Schlossarek,† S. Ghosh, Y. Tsutsui, A. Schmiedel, M. Holzapfel, M. Stolte, C. Lambert, S. Seki, M. Lehmann, F. Würthner, *ACS Appl. Nano Mater.* **2020**, DOI: 10.1021/acsanm.1020c02189.

Abstract

Donor-acceptor dyads consisting of PBI and trialkoxyphenyl-oligothiophene (TAPOT) units are reported that self-assemble into helical four-, six- and seven-stranded hydrogen-bonded supramolecular polymers in solution and the columnar LC state. It is shown that the number of closely stacked and J-coupled PBI strands can be controlled by the incremental extension of the TAPOT wedge units in bay position and the thereby tailored steric demand. Narcissistic self-sorting of TAPOT donor and PBI acceptor subunits facilitates the formation of core–shell structures creating individual percolation pathways for 1D transport of photogenerated charge-carriers. Macroscopic alignment of the nanoscale columnar structures by solution-shearing enables anisotropic photoconductivity. Thus, selective orientation of the 1D charge transporting domains parallel and perpendicular to the electrodes gives rise to an up to 90-fold increased photoresponse depending on the alignment quality. The intrinsic charge-separation and transport properties were investigated by fsTAS and FP-TRMC. These studies reveal a rising

---

† Part of this chapter has been described in: T. Schlossarek, Master Thesis, Universität Würzburg, 2019.

propensity for charge-separation and transport upon increasing conjugation length of the TAPOT donor and thereby increasing size of the individual percolation pathways. Contrasting observations for intrinsic and macroscopic photoconductivity demonstrate the importance of processability on device performance.

4.1 Introduction

Spatial organization of molecules and the resulting morphology on a macroscopic level are key aspects in the development of functional materials.[162-166] This is particularly important in donor–acceptor systems commonly applied in organic photovoltaics, where segregated domains of the donor and acceptor counterparts are quintessential to generate percolation pathways for charge-carriers.[29,119,167] Thus, whilst columnar π-stacks of e.g. hexabenzocoronenes[168] or PBIs[169] demonstrated their suitability for 1D hole or electron transport, respectively, the design of supramolecular architectures that support both processes within one material is by far more challenging because the migration of holes and electrons in their respective domain competes with charge carrier recombination. In the past, such systems were prepared by either mixing electron donors with acceptors in two-component systems[146,170-174] or by covalently linking them.[150,151,173,175-178] Toward this goal, HOMO and LUMO levels are tailored to be beneficial for charge separation. From this work, the relationship between the electronic properties of the molecular system and the propensity for charge carrier generation is well understood and a driving force of ~0.3 eV is considered appropriate. However, the predictable intermolecular arrangement and morphology in the bulk needed to create percolation pathways for their transport remains challenging. Simple co-assembly of donor and acceptor molecules was shown to be less promising because donor–acceptor systems exhibit a tendency to form alternating packing arrangements, leading to fast charge recombination and thereby hampering efficient charge transport over long distances (Figure 18b).[150,167] In contrast, the self-assembly of donor and acceptor molecules by means of specific non-covalent interactions such as H-bonds[171,172] enabled the formation of highly defined structures that avoid such alternating arrangements of donors and acceptors.[32,33,41,135-137,179] Accordingly, a variety of supramolecular designs have been applied to form 1D self-assembled columnar structures[150,176] with separated stacks of donor and acceptor molecules or coaxial nanotubes[145,179,180] (Figure 18c and d) that exhibit separated pathways for hole and electron transport, respectively. Combining the orientational order encoded by the supramolecular approach with the positional long-range order and propensity for macroscopic alignment of liquid crystals, materials with exciting functional properties could be realized.[15,26]

Despite of successful proof-of-principle studies for such systems, the limited size of the molecular components makes such materials prone to charge carrier recombination. Thus, whilst successful bulk heterojunction solar cell materials exhibit domains of about 10 nm size, typical donor–acceptor dyad systems illustrated in Figure 18a-d have domain sizes of only about 1 nm, i.e. the size of the utilized donor and acceptor molecules. This leads inevitably to a very critical interplay of the respective processes upon illumination, i.e. desired charge carrier separation, desired hole and electron transport and undesired charge carrier recombination. In a recent communication we introduced a new possibility for the self-assembly of core–shell columnar liquid crystals of PBI acceptors jacketed with electron-rich trialkoxyphenyl-bithiophene donors.[111] In contrast to common discotic columnar liquid crystals (Figure 18a), under the influence of H-bonding between the imide units an orthogonal alignment of PBIs is achieved (Figure 18e). Accordingly, PBIs are oriented with their long axis directed along the columnar axis in a slip-stacked packing motif, inducing the properties of J-aggregates that are known to exhibit high exciton mobility.[181]

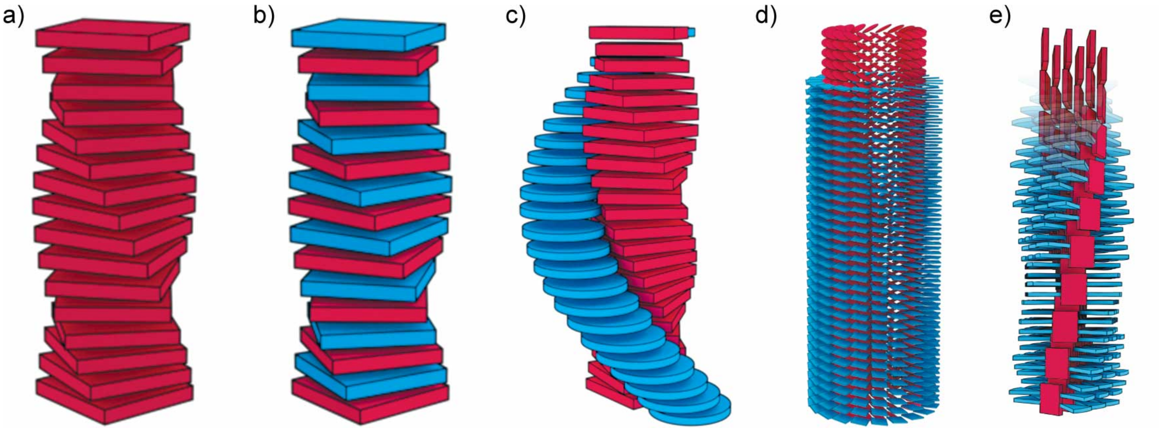

Figure 18. Schematic arrangements of a) cofacially stacked acceptor molecules (red), b) alternating cofacial stacks of acceptor and donor (blue) molecules as well as coaxially separated donors and acceptors in c) cofacially stacked structures, d) nanotubular structures and e) multistranded helical columnar structures.

In the present study, we accordingly explore a new way to control the dimension of the individual percolation pathways in the nanoscale core–shell structure by modifying the length of the TAPOT wedge units (Figure 19). Specifically and different from previous approaches, our design not only provides separated charge transport channels for electrons and holes but the possibility for the adjustment of the number of strands in the core of the coaxial cable (Figure 19b). As we will show, the increase in the number of thiophene units from one to three alters the steric demand of the monomer facilitating the formation of quadruple-, sextuple- and septuple stranded helices in the columnar LC phase while simultaneously increasing the electron-donating character of the jacketing TAPOT units. We demonstrate how the meniscus guided method of solution shearing[182-185] can be used to produce two-contact devices with aligned supramolecular structures for enhanced photoconductivity that outperform devices with an isotropic active layer. Detailed investigations of the relation between the supramolecular structure and the functional properties by fsTAS and FP-TRMC measurements reveal improved charge separation and transport properties for the derivative with the most complex seven-stranded architecture. Contrasting observations between the photoconductivity on the macroscopic and supramolecular level demonstrate the relevance of the processability for functional organic materials.

4.2 Results

4.2.1 Molecular Design and Synthesis

The structure of the investigated compounds **PBI 1T**, **PBI 2T**[111] and **PBI 3T** consists of a 1,6,7,12-tetraphenoxy-substituted PBI core which possesses free imides (Figure 19a). The phenoxy spacers are substituted in *meta*-position with mono- (**PBI 1T**), bi- (**PBI 2T**) and terthiophene-appended (**PBI 3T**) 3,4,5-tris(dodecyloxy)phenyl minidendron via an ester functionality. The carboxylic acids of the TAPOT side-arms were prepared from 5-bromothiophene-2-carboxylic acid methyl ester, 2,2′-bithiophene-5-boronic acid and 4,4,5,5-tetramethyl-2-(3,4,5-tris(dodecyloxy)phenyl)-1,3,2-dioxaborolane via a series of Suzuki-Miyaura cross couplings and bromination reactions in good yields. The carboxylic acids were appended to 1,6,7,12-tetra(3-hydroxyphenoxy)perylene-3,4:9,10-bis(dicarboximide) under peptide coupling conditions to yield **PBI 1T**, **PBI 2T** and **PBI 3T** (see 4.3. Appendix to *Chapter 4* for details).[59-61,111]

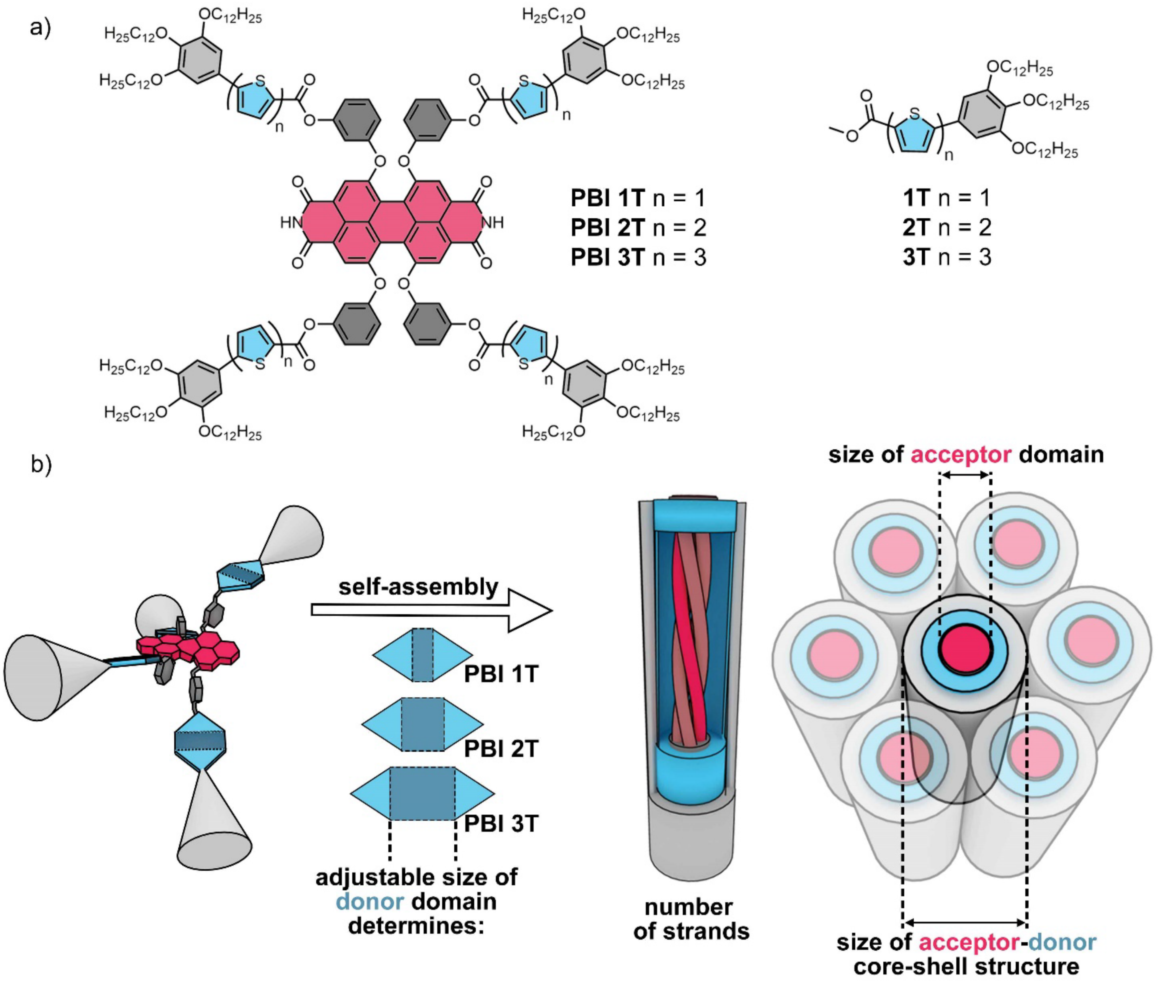

Figure 19. a) Chemical structure of **PBI 1T**, **PBI 2T**, **PBI 3T**, **1T**, **2T** and **3T**. b) Concept for the self-assembly of PBIs into donor–acceptor core–shell columnar structures with control of the domain size of the central core.

4.2.2 Optical and Redox Properties of Monomers in Solution

The UV/Vis absorption spectra resemble superpositions of the individual building blocks indicating that no electronic coupling between the electron rich TAPOT donors and the PBI acceptor is present in the ground state as additional signals corresponding to, e.g., charge-transfer interactions are not observable (see Figure A27). The UV/Vis absorption spectra of the three dyes in chloroform show the optical signature of monomerically dissolved tetraphenoxy-substituted PBIs with the S_0-S_1 transition at 569 nm (41500 M^{-1} cm^{-1}) and a FWHM of 960 cm^{-1}. The spectra show each an additional prominent signal corresponding to the TAPOT units which undergoes a red-shift and significant increase in intensity upon increasing conjugation length from 340 nm (98000 M^{-1} cm^{-1}, **PBI 1T**) to 385 nm (128000 M^{-1} cm^{-1}, **PBI 2T**) and 420 nm (170000 M^{-1} cm^{-1}, **PBI 3T**) (Figure 20a and Table 1). The strong conjugation between the trialkoxyphenyl group and the oligothiophene unit becomes evident if we compare these absorption bands with those of

2,5-position linked oligothiophenes, i.e. bithiophene (303 nm, 12400 M^{-1} cm^{-1}), terthiophene (354 nm, 22100 M^{-1} cm^{-1}), quarterthiophene (392 nm, 31600 M^{-1} cm^{-1}) and quinquethiophene (417 nm, 42700 M^{-1} cm^{-1}).[186] Accordingly, the major absorption band at higher energy attributable to the oligoarylene unit of **PBI 1T**, **PBI 2T** and **PBI 3T** corresponds to those of ter-, quarter- and quinquethiophenes, respectively, due to similar electron donor character of a bithiophene and a trialkoxyphenyl unit.

Table 1. Summary of the optical properties of monomers of **PBI 1T**, **PBI 2T** and **PBI 3T** in $CHCl_3$.

	Absorption[a]			**Emission**[b]			
	$\lambda_{max,\ TAPOT}$ (nm) [ε ($M^{-1}cm^{-1}$)]	$\lambda_{max,\ PBI}$ (nm) [ε ($M^{-1}cm^{-1}$)]	$FWHM_{PBI}$[c] (cm^{-1})	λ_{max} (nm)	$\Delta\tilde{\nu}_{stokes}$ (cm^{-1})	Φ_{Fl}[d] (%)	τ_{Fl}[e] [Rel.] (ns [%])
PBI 1T	340 [98000]	569 [41400]	960	603	−990	35.0±0.4	2.63 [85], 4.56 [15]
PBI 2T[111]	385 [128000]	569 [41400]	960	601	−940	2.9±0.2	0.56 [95], 3.58 [5]
PBI 3T	420 [170000]	569 [41600]	960	599	−880	<1.0	<0.2 [79], 3.70 [21]

[a] $CHCl_3$ (c = 30 μM) at 22 °C;
[b] $CHCl_3$ ($c \approx$ 100 nM) at 22 °C
[c] FWHM was derived as twice the distance between the absorption maximum to the red edge at half maximum of the unsymmetrically shaped absorption bands to prevent falsification by the vibronic progression;
[d] Relative to *N*,*N*'-bis(2,6-diisopropylphenyl)-1,6,7,12-tetraphenoxy-3,4:9,10-perylenetetracarboxylic acid bisimide[187];
[e] λ_{ex} = 505 nm, λ_{em} = 605 nm. Biexponential fit was performed with free parameters for the short and long component of the fluorescence lifetime; lifetimes shorter than 200 ps cannot be resolved due to the pulse frequency and the instrumental limitation. Therefore <0.2 ns is given as an upper limit.

All monomeric compounds exhibit fluorescence with small Stokes shifts in the range of 1000 cm^{-1} in chloroform (Figure 20a and Table 1). Fluorescence of the PBI can be observed whether the PBI or the TAPOT units are excited indicating ET of the electron-rich TAPOT to the PBI (see Figure A28). Using excitation spectroscopy, the efficiency of the ET is estimated to 82% (**PBI 1T**), 74% (**PBI 2T**) and 69% (**PBI 3T**) (see Figure A29). The fluorescence of the monomeric dyes in chloroform is strongly quenched compared to common tetraphenoxy-PBIs without appended donors which exhibit quantum yields close to unity.[42,59] Accordingly, the fluorescence quantum yield drops with increasing number of thiophenes in the TAPOT units from 35.0±0.4% (**PBI 1T**) to 2.9±0.2% (**PBI 2T**) and <1.0% (**PBI 3T**) (Figure 20b). This trend hints towards an increased rate of PET from the donor to the acceptor with increasing conjugation length of the electron-rich unit. Time-resolved fluorescence spectroscopy revealed biexponential decays with a dominant short- and a minor long-lived component. The short-lived components were determined as 2.63 ns

(**PBI 1T**), 0.56 ns (**PBI 2T**)[111] and <0.20 ns (**PBI 3T**). These lifetimes are short compared to a reference tetraphenoxy-substituted PBI acceptor **17** (Scheme A3) which shows a fluorescence lifetime of 5.79 ns which is typical for tetraphenoxy-substituted PBIs (see Figure A30 and Table A7).[59,188] This pronounced reduction of the fluorescence lifetime underlines the gain in PET efficiency upon increasing conjugation length of the TAPOT unit.

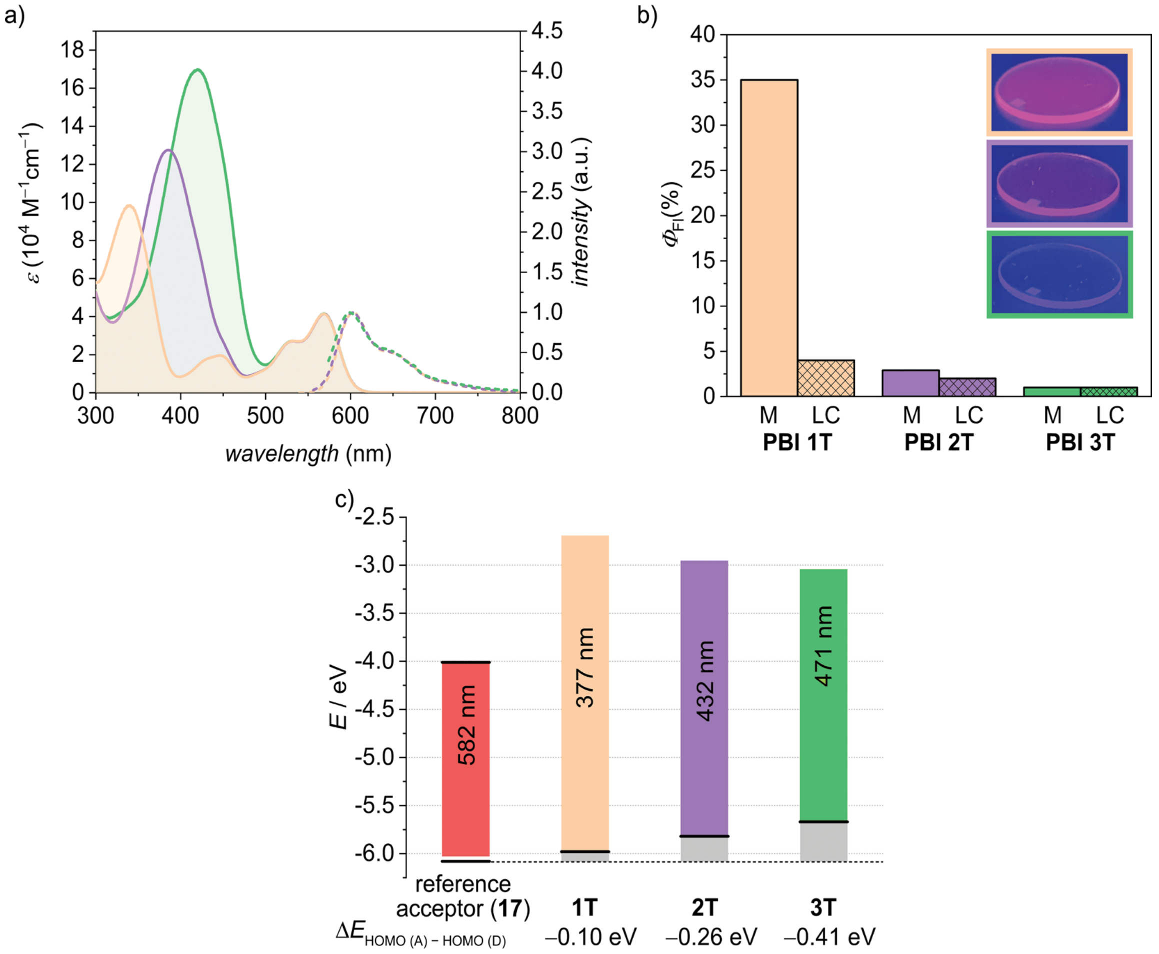

Figure 20. a) UV/Vis absorption spectra (solid lines) of **PBI 1T** (orange), **PBI 2T** (purple) and **PBI 3T** (green) in $CHCl_3$ with $c_0 = 30$ µM and the respective fluorescence spectra ($c_0 \approx 1$ µM, dashed lines, $\lambda_{ex} = 530$ nm − 560 nm). b) Fluorescence quantum yields of **PBI 1T** (orange), **PBI 2T** (purple) and **PBI 3T** (green) in the monomeric state in $CHCl_3$ (M, relative to *N*,*N*'-bis(2,6-diisopropylphenyl)-1,6,7,12-tetraphenoxy-3,4:9,10-perylenetetracarboxylic acid bisimide[187]) and in thin films (LC, $\lambda_{ex} = 550$ nm − 620 nm, absolute quantum yield) prepared by spin-coating solutions in MCH with $c_0 = 1$ mM on quartz substrates and subsequent annealing at 180°C for 30 mins. The inset shows the respective thin-film samples under UV-light (365 nm). c) Energy level diagram of reference acceptor **17**[189], **1T**, **2T** and **3T** with corresponding optical bandgaps (colored bars). Grey bars show $\Delta E_{HOMO(A)\text{-}HOMO(D)}$ for **1T**, **2T** and **3T** with respect to reference acceptor **17**.

CV and SWV of the individual methyl esters of the electron rich TAPOT side-arms (**1T**, **2T** and **3T**) was conducted in dichloromethane at room temperature using tetrabutylammonium hexafluorophosphate as electrolyte and the ferrocenium/ferrocene (Fc^+/Fc) redox couple as internal standard (see Figure A31). The measurements show one reversible and one irreversible oxidation for **1T**, two irreversible oxidations for **2T** and four irreversible oxidations for **3T**. The potential of the first oxidation (D/D$^+$) decreases with increasing length of the conjugated system leading to an increase of the HOMO level of the electron donating groups from −5.98 eV (**1T**) to −5.82 eV (**2T**) and −5.70 eV (**3T**) (Figure 20c and Table 2). Therefore, the driving force $\Delta E_{\mathrm{HOMO(A)\text{-}HOMO(D)}}$ for PET upon excitation of the PBI acceptor can be estimated to −0.10 eV (**1T**), −0.26 eV (**2T**) and −0.44 eV (**3T**) relative to a reference tetraphenoxy-substituted PBI in the given solvent dichloromethane (**17**; see Scheme A3, Table 1).[189] This is in accordance with the increasing fluorescence quenching of **PBI 1T**, **PBI 2T** and **PBI 3T** by PET upon increasing side-arm length (Figure 20b).

Table 2. Summary of the redox properties of **1T**, **2T**, **3T** and **17**[189]as determined by CV and SWV in dichloromethane (c = 200 µM) at room temperature with tetrabutylammonium hexafluorophosphae (0.1 M) as electrolyte (scan rate: 100 mV s^{-1}) against the ferrocenium/ferrocene (Fc$^+$/Fc) redox couple.

	$E_{1/2}^{\mathrm{ox1}}$ (V)	$E_{1/2}^{\mathrm{ox2}}$ (V)	$E_{1/2}^{\mathrm{ox3}}$ (V)	$E_{1/2}^{\mathrm{ox4}}$ (V)	$E_{1/2}^{\mathrm{red1}}$ (V)	$E_{1/2}^{\mathrm{red2}}$ (V)	E_{HOMO}[c] (eV)	E_{LUMO}[c] (eV)	$\Delta E_{\mathrm{HOMO(A)\text{-}HOMO(D)}}$ (eV)
1T	0.83	1.27[a]	–	–	–	–	−5.98	−2.69[b]	−0.10
2T	0.67[a]	0.91[a]	–	–	–	–	−5.82	−2.95[b]	−0.26
3T	0.55[a]	0.78[a]	1.16[a]	1.34[a]	–	–	−5.70	−3.07[b]	−0.44
17[189]	0.93	1.25	–	–	−1.14	−1.35	−6.08	−4.01	–

[a] Oxidation is irreversible, therefore the peak potential obtained from square wave voltammetry is given;

[b] Calculated using the optical bandgap of 30 µM solutions in $CHCl_3$;

[c] Calculated according to $E_{\mathrm{HOMO}} = -[eE\ (\mathrm{M/M^+}) + 5.15\ \mathrm{eV}]$ and $E_{\mathrm{LUMO}} = -[eE\ (\mathrm{M/M^-}) + 5.15\ \mathrm{eV}]$.[190]

4.2.3 Optical Properties of the Self-Assembled J-Aggregates

Similar as for previously investigated related tetraphenoxy PBIs without appended TAPOT electron donating side arms, a stepwise formation of supramolecular polymers from the respective monomers can be followed in solution using a non-polar solvent like toluene in which H-bonding and π–π interactions are both strong. This process can be investigated with concentration-dependent studies, which show monomers at low concentration and aggregates at high concentration. The appearance of isosbestic points indicates the presence of two distinct species for **PBI 1T** (Figure 21a), **PBI 2T**[111] as well as for **PBI 3T** (Figure A32). The highly concentrated solutions in toluene show ~ 80 nm bathochromically shifted absorption of the S_0-S_1 transition of the PBI subunit for all dyes with narrowed FWHM indicative of PBI J-aggregates (see Table A6). The degree of aggregation in dependence of the concentration at 298 K in toluene can be fitted to the cooperative nucleation-elongation model.[34,94] This cooperativity is reasonable as two major intermolecular forces contribute to the self-assembly process (Figure 21; see Figure A32). These studies revealed a nucleation constant of $K_{\mathrm{nuc}} = 8\ \mathrm{M}^{-1}$ and an elongation constant of $K_{\mathrm{elong}} = 2500\ \mathrm{M}^{-1}$ as well as a cooperativity parameter of $\sigma = 3 \times 10^{-3}$ for **PBI 1T** considering a nucleus size of two molecules. Under the same conditions, **PBI 2T** shows a stronger aggregation tendency with $K_{\mathrm{nuc}} = 9\ \mathrm{M}^{-1}$, $K_{\mathrm{elong}} = 8000\ \mathrm{M}^{-1}$ and $\sigma = 1 \times 10^{-3}$.[111] This trend continues upon increasing the number of thiophene units in the side-arm. Thus, **PBI 3T** self-assembles in toluene at 298 K too strongly to realize a monomeric state even at the most diluted conditions of $c_0 = 3\ \mu\mathrm{M}$. The estimated parameters are $K_{\mathrm{elong}} = 7.0 \times 10^5\ \mathrm{M}^{-1}$, $K_{\mathrm{nuc}} = 700\ \mathrm{M}^{-1}$ and $\sigma = 1 \times 10^{-3}$ (see Table A9). Accordingly, we can conclude from these studies that the peripheral TAPOT units support the formation of PBI-J-aggregates via additional π–π-stacking interactions between the side arms. This view is further supported by the fact that the absorption bands of the TAPOT subunits are shifted hypsochromically, attributable to cofacial stacking with H-type exciton coupling,[152] whilst the PBI bands are shifted bathochromically, attributable to slip-stacked arrangements of the PBIs with J-type exciton coupling.[33]

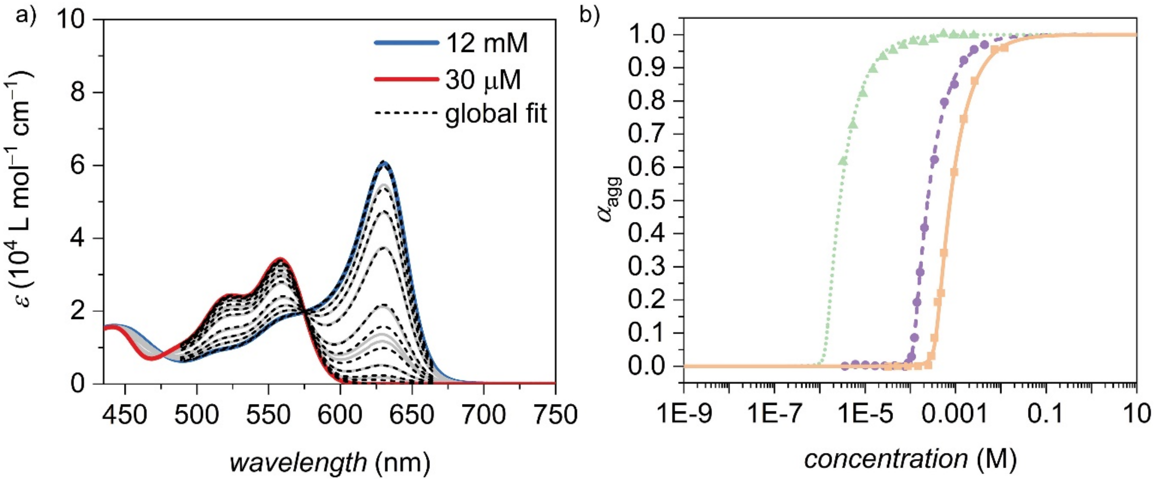

Figure 21. a) Concentration-dependent UV/Vis absorption spectra ($c_0 = 30\ \mu\mathrm{M} - 12\ \mathrm{mM}$, colored and grey solid lines) of **PBI 1T** in toluene at 298 K and reconstructed spectra from the global cooperative nucleation-elongation fit (black dashed lines). The absorption spectra at wavelength below 440 nm are not shown due to the high absorptivity of the TAPOT units relative to the PBI leading to artefacts in concentration-dependent measurements. b) Plot of the degree of aggregation α_{agg} over the concentration of **PBI 1T** (orange squares), **PBI 2T** (purple dots) and **PBI 3T** (green triangles) and the corresponding fits (**PBI 1T**: solid orange line, **PBI 2T**: dashed purple line, **PBI 3T**: dotted green line) according to the cooperative nucleation-elongation model (solid lines).

Thin films prepared by spin-coating solutions of **PBI 1T**, **PBI 2T** and **PBI 3T** on quartz substrates confirm this opposing exciton coupling behavior of the PBIs and the TAPOT units in the self-assembled structures (Figure 22a and c). Thus, all PBIs exhibit the optical features typical for PBI J-aggregates with red-shifted absorption maxima at 660 nm (**PBI 1T**), 653 nm (**PBI 2T**) and 654 nm (**PBI 3T**) and a narrowed FWHM of the S_0-S_1

transition of 760 cm^{-1}. In contrast, the TAPOT units show blue-shifted absorption maxima at 336 nm (**PBI 1T**), 378 nm (**PBI 2T**) and 402 nm (**PBI 3T**) accompanied by a decreased absorptivity indicative of H-type coupling (see Table A8). The thin films show weak fluorescence from originating the PBI J-aggregate with small Stokes shifts in the range of 300–400 cm^{-1} (Figure 22a and c). The quantum yields are quenched compared to the monomer in chloroform with 4% for **PBI 1T**, 2% for **PBI 2T** and <1% for **PBI 3T** (Figure 20b).

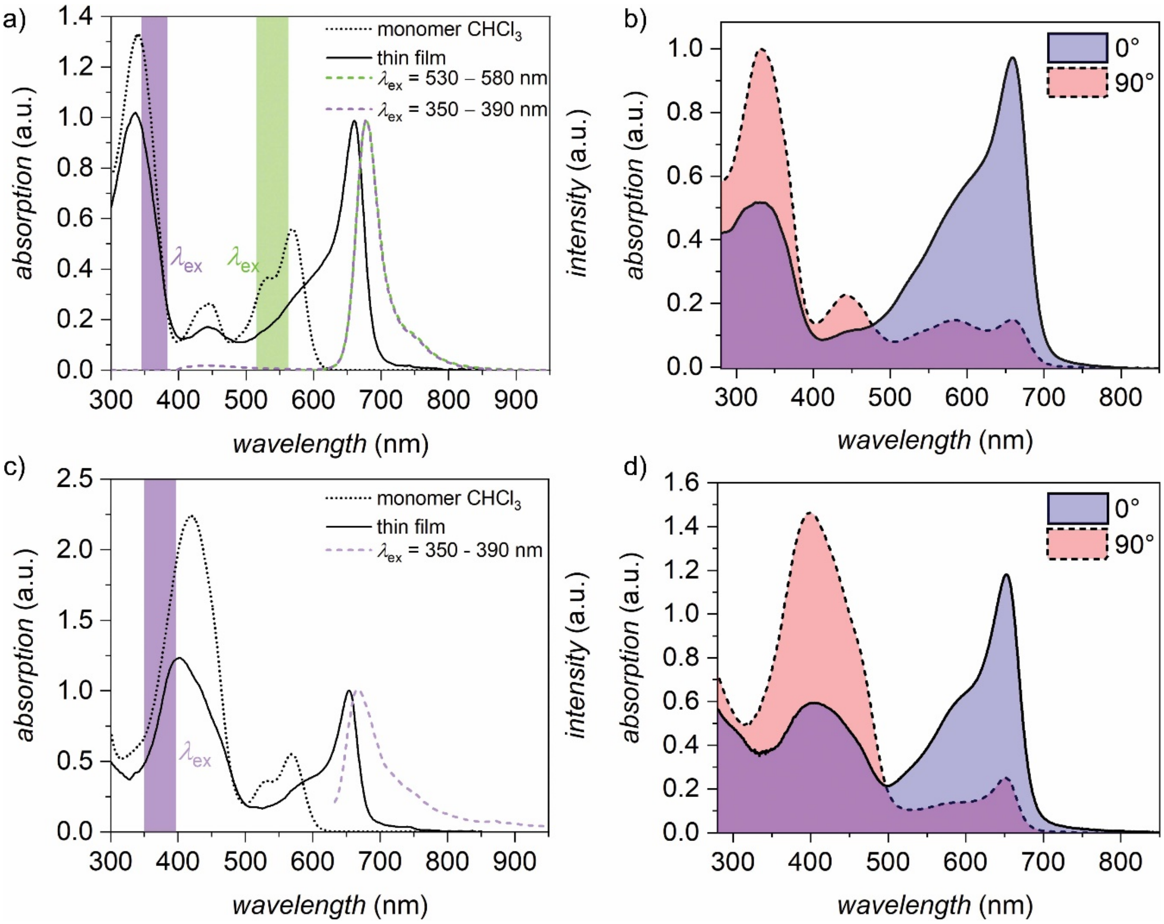

Figure 22. UV/Vis absorption spectra of monomeric a) **PBI 1T** and c) **PBI 3T** in CHCl$_3$ (black dotted line, c_0 = 30 μM) and in the solid state (black solid line, spin-coated from 1mM solutions in MCH, annealed for 30 mins at 180 °C). Colored dashed lines show the emission spectra in dependence of the wavelength range (violet: 350 − 390 nm, green: 530 − 580 nm). UV/Vis absorption spectra of mechanically aligned thin films of b) **PBI 1T** and d) **PBI 3T** on quartz substrates (annealed for 30 mins at 180 °C) measured with linearly polarized light parallel (black solid lines, blue) and perpendicular (black dashed lines, red) to the shearing direction.

4.2.4. Structure Elucidation in the LC State

The LC properties of **PBI 2T** that consist of sextuple-stranded 16_1 helices have been reported previously.[111] Therefore, the following discussion is focused in the thorough analysis of the LC phases of **PBI 1T** and **PBI 3T**. The thermotropic properties of the materials were investigated by POM and DSC. **PBI 1T** and **PBI 3T** exhibit a single LC phase from 20 to 264 °C and 20 to 317 °C, respectively, at which temperatures melting is accompanied by decomposition (see Figure A33).

The structure of the LC phases was characterized by WAXS and MAXS measurements of aligned fibers prepared by extrusion. The WAXS patterns of lying and standing fibers of **PBI 1T** show a large number of reflections corresponding to an oblique columnar lattice (Col_{ob}, $a = 75.6$ Å, $b = 51.8$ Å, $\gamma = 86.4°$) (Figure 23a–c). Diffuse off-meridonal signals at small angles indicate the formation of helical structures with periodicity along the *c*-axis (Figure 23a).[59-61,111] The first meridional signal appears at 14.3 Å and was assigned the Miller indices 0014 (Figure 23b). This signal typically corresponds to the axial translational subunit. The distance is in accordance with the size of the PBI long axis indicating that the columnar structure is formed by H-bonded chromophores which are aligned in the direction of the columnar axis. This could be confirmed by polarized FT-IR (see Figure A34a) and UV/Vis spectroscopy (Figure 22b) of shear-aligned thin films. Polarized FT-IR studies showed that the N-H stretching signal corresponding to H-bonded PBIs is most intense along the shearing direction (see Figure A34a). Further, polarized UV/Vis studies showed that the S_0-S_1 transition of the PBI is most intense along the shearing direction whereas the absorption band corresponding to the TAPOT units is strongest perpendicular to the shearing direction indicating an orthogonal arrangement of donors and acceptors within the columnar structures (Figure 22b).

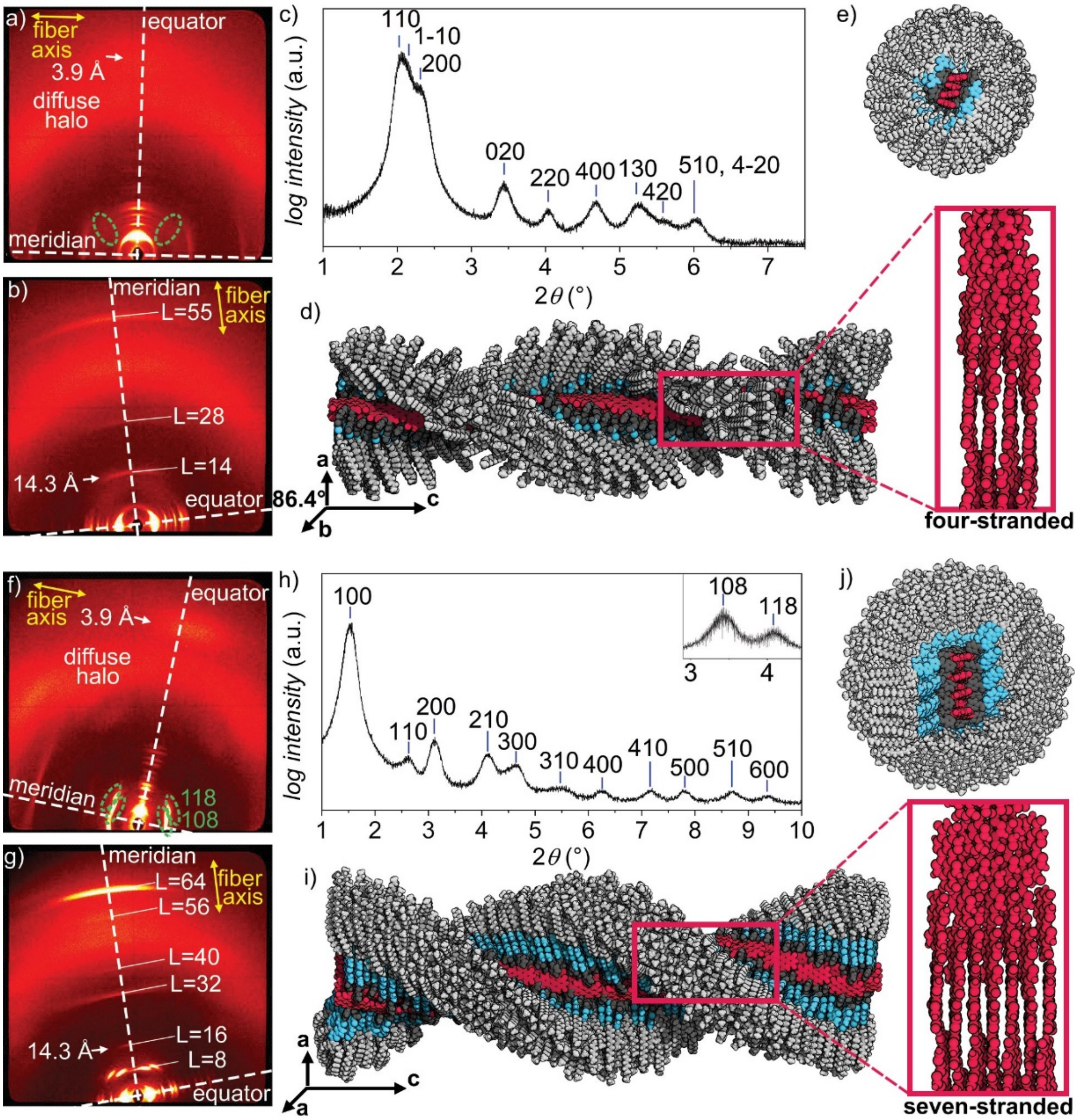

Figure 23. WAXS diffraction patterns of lying fibers of a) **PBI 1T** (230 °C) and f) **PBI 3T** (150 °C) as well as of standing fibers of b) **PBI 1T** (230 °C) and g) **PBI 3T** (150 °C). Yellow arrows indicate the relative orientation of the fibers and the meridian and equator are highlighted with white dashed lines. Dashed green circles highlight the off-meridional signals at small angles corresponding to the helical structures. The layerlines in b) and g) are labelled with L. Integrated intensities along the equator of c) **PBI 1T** and h) **PBI 3T** and assignment of the Miller indices according to the c) Col_{ob} and h) Col_{h} lattice. The inset in h) shows the integration of the off-meridional 108 and 118 signals of **PBI 3T**. Self-assembled structures of the d,e) quadruple-stranded 14_1 helix of **PBI 1T** and i,j) septuple-stranded 16_1 helix of **PBI 3T**. The helicity in the shown columnar assembly has been chosen to be (*P*) for graphical representation. Please note that **PBI 1T** and **PBI 2T** are achiral and therefore (*P*) and (*M*) helices coexist in the LC phase.

According to above described X-ray data, 14 H-bonded **PBI 1T** molecules form the repeat of the helix with a pitch of 14 ×14.3 Å = 200.2 Å which corresponds to a rotational displacement of each molecule of about 25.7°. The periodic helical arrangement of the molecules within the columns further causes the appearance of the L = 28 and L = 55 reflections (Figure 23b; see Figure A35a). WAXS patterns of the lying fiber show a diffuse wide-angle signal on the equator corresponding to the π–π distance of the core-twisted PBIs perpendicular to the column (3.9 Å). According to the Scherrer equation, this signal corresponds to a correlation length of four molecules indicating the formation of a four-stranded helix of H-bonded PBIs (see 4.3. Appendix to *Chapter 4*).[160] This is in agreement with the calculated number of mesogens in a columnar stratum of 14.3 Å using the experimentally determined density of the material extrapolated to 230 °C of 0.91 g cm^{-1} which amounts to 8.1 ± 0.5 molecules per unit cell (see 4.3. Appendix to *Chapter 4*). As each oblique unit cell hosts two columnar assemblies, the number of strands in each column can be calculated as 4.1 ± 0.3. Thus, **PBI 1T** forms a quadruple-stranded 14_1 helix with a rotational displacement of 360°/14 = 25.7° per molecule.

The XRS data of **PBI 3T** was interpreted accordingly. A large number of signals on the equator indicate the formation of a hexagonal columnar lattice (Col_h, $a = 64.4$ Å) (Figure 23f–h). Two intense off-meridional signals at small angles could be assigned to the 108 and 118 reflections of a 3D correlated hexagonal columnar phase with a periodicity along c of 228.8 Å (Figure 23f). This is confirmed by the meridional signal 0016 at 14.3 Å corresponding to the length of the PBI long axis displaying the axial translational subunit and further diffuse signals at layer lines L = 32, 40, 56 and 64 (Figure 23g; see Figure A35b). Such periodicity can be explained by the formation of helical structures as discussed previously.[60,61,111] Polarized FT-IR (see Figure A34b) and UV/Vis spectroscopy (Figure 22d) of shear-aligned thin films show the orientation of the chromophores along the columnar axis similar to **PBI 1T**. A diffuse wide-angle signal on the equator at 3.9 Å is attributed to the π–π-stacking distance of the individual PBI molecules. The correlation length was calculated as seven molecules indicating the formation of a septuple-stranded helix of H-bonded PBIs. This is confirmed by the calculated number of mesogens which amounts to 7.0 ± 0.4 using the experimentally determined density of **PBI 3T** extrapolated to 150 °C of 1.00 g cm^{-3} (see 4.3. Appendix to *Chapter 4*). Therefore, **PBI 3T** forms a septuple-stranded 16_1 helix with a 22.5° twist per molecule.

Accordingly, this series of three J-aggregate forming PBI dyes illustrates how the specific supramolecular architecture can be fine-tuned by engineering the steric requirements of the dendron wedge unit of the monomeric building block.[41] Previously, we could demonstrate that the number of strands in such PBI J-aggregates with simple phenoxy substituents at the four bay positions can be tailored by *ortho*-, *meta*- and *para*-substitution to realize assemblies consisting of one up to four strands.[60] Now we were able to enlarge the accessible range of multistranded PBI J-aggregates up to a seven-stranded helix by lateral extension of the respective bay-substituents. This, so far, appears to be the highest number of strands that can be incorporated into the columnar structure of helical PBI J-aggregates, before the formation of lamellar phases is favored.[191]

Models of the helical structures of **PBI 1T** (Figure 23d and e; see Figure A36) and **PBI 3T** (Figure 23i and j; see Figure A37) were generated with the program *Accelrys Materials Studio 2017 R2*.[130] The molecules were arranged to form a quadruple- (**PBI 1T**) and septuple-stranded (**PBI 3T**) helix composed of H-bonded strands. These individual strands were arranged in a slip-stacked fashion to account for the optical features of the J-aggregates in the LC state. The modelled structures are characterized by the nanosegregation of the PBI acceptor in the core (red) jacketed by the cofacially π-stacked electron-rich (oligo)thiophene shell (blue) and the trialkoxyphenyl units (light grey) (Figure 23e and j). The side-arms in each model were arranged in order to optimize space-filling while retaining good π–π-interactions of the H-type coupled TAPOTs. The helical structures were optimized with the COMPASS II force field applying the Ewald summation method in the corresponding unit cell until the non-bonding energy was strongly negative. We simulated the fiber diffraction pattern using the program CLEARER applying the modelled structure.[134] The resulting signals are in good agreement with the experimentally determined WAXS and MAXS patterns confirming the proposed core–shell structure of the donor–acceptor LCs (see Figure A38).

4.2.5. Photoconductivity and Charge Transport Properties

The particular nanostructure of separated donor and acceptor domains provides percolation pathways for electron and hole transport, respectively. Along this line, we could previously demonstrate that **PBI 2T** functions as photoconductor in two-contact devices reaching photocurrents of 1 nA at a constant drain-source voltage of +100 V using a white light source ($\psi = 38$ mW cm^{-2}).[111] These devices were prepared by spin-coating solutions of **PBI 2T** (1 mg mL^{-1}, $CHCl_3$) onto bottom contact Si/SiO_2 substrates with gridlike electrodes (30 nm height, 10 mm channel width and 5 µm channel length) leading to an isotropic arrangement of the supramolecular structures. As the LC columnar structures provide only 1D charge transport along the columnar long axis, we expected to greatly enhance the observed photocurrent upon alignment of the nanostructures between the electrodes. To achieve macroscopic alignment on the respective bottom-contact substrates, we employed the method of solution shearing, which is widely used in the field of solution-processed organic electronics.[182-185] Accordingly, the substrates were coated by solution shearing from solutions of PBI-TAPOT dyes in *o*-dichlorobenzene ($10\ \mathrm{mg\ mL^{-1}}$) to produce two-contact devices (Figure 24a; for experimental details see 4.3. Appendix to *Chapter 4*). The quality of the films was investigated with polarizing fluorescence microscopy (λ_{ex} = 530-580 nm) revealing a homogeneous alignment of the columnar long axis along the shearing direction (Figure 24b; see Figure A39). Accordingly, depending on the orientation of the substrate, the columnar structures were aligned either perpendicular (90°, Figure 24b left) or parallel (0°, Figure 24b right) to the electrodes, which leads to a favorable or disfavorable orientation of the charge-transport channel, respectively. Two-contact measurements (V_{DS}= +50 V) of samples with an ideal alignment for charge transport between the electrodes show enhanced conductivity upon illumination with a white light source ($\psi = 20\ \mathrm{mW\ cm^{-2}}$) reaching maximum currents of 20 nA (**PBI 1T**), 45 nA (**PBI 2T**) and 14 nA (**PBI 3T**) (Figure 24c). In the case of **PBI 2T** this displays an at least 45-fold increased photoconductivity compared to our previously reported results that can be reached upon selective orientation of the supramolecular structures. Importantly, devices with alignment of the supramolecular structures parallel to the electrodes show significantly lower photocurrents in the range of 3 nA (**PBI 1T**), 0.5 nA (**PBI 2T**) and 2 nA (**PBI 3T**). Thus, $I_{90^\circ} / I_{0^\circ}$ ratios of ca. 7 (**PBI 1T**), 90 (**PBI 2T**) and 7 (**PBI 3T**) can be realized. This is in agreement with the quality of the solution-sheared active layers as observed with polarized fluorescence microscopy as the most homogeneous films could be obtained for **PBI 2T** (Figure 24b, see Figure A39). This approach towards macroscopically aligned supramolecular LC photoconductors demonstrates how the particular orientation of the charge-transport pathways influences the functionality. These investigations, however, also reveal that the performance of the particular device strongly depends on the processability of the material and that the rational design of the molecular and supramolecular structure cannot readily be translated to macroscopic properties indicated by the lack of a trend of photoconductivity upon increasing conjugation length of the TAPOT unit that was expected to improve the performance (better electron donor unit and larger PBI domain size).

To get insight into the intrinsic charge-separation and charge-transport properties of the respective materials that arise from the supramolecular architecture we performed fsTAS and FP-TRMC measurements.

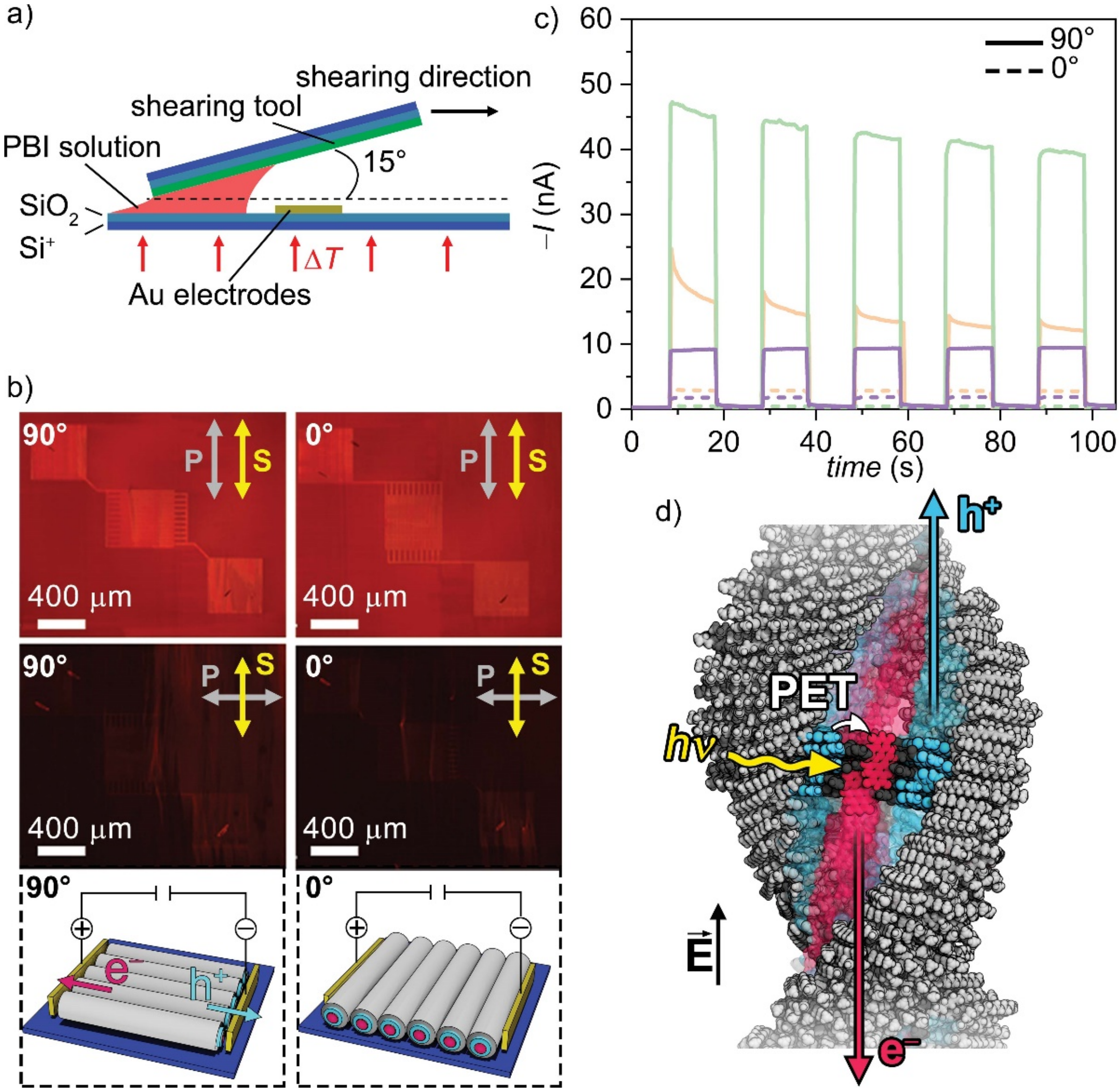

Figure 24. a) Schematic depiction of the solution shearing method. b) Polarizing fluorescence microscopy images of solution-sheared samples of **PBI 2T** on bottom-contact substrates (λ_{ex} = 530 – 580 nm). Orientation of the polarization (P) of the excitation light and the shearing direction (S) indicated in grey and yellow arrows, respectively. The orientation of the electrodes is either perpendicular (left) or parallel (right) to the shearing direction and therefore the columnar axis. The bottom part shows a schematic illustration of the alignment of the columnar structures with respect to the electrodes c) Plot of the photoresponse of two-contact devices with solution-sheared active layer of **PBI 1T** (orange), **PBI 2T** (green) and **PBI 3T** (purple) with the columnar long axis perpendicular (solid lines) and parallel (dashed lines) to the electrodes at a constant drain-source voltage of +50 V. The samples were illuminated with a white light source with a power density of 20 mW cm^{-2}. d) Segment of the self-assembled seven-stranded 16_1 helix of **PBI 3T** and illustration of the charge separation and transport processes upon illumination with a white-light source.

TRMC is a reliable electrodeless method, devoid from the need of alignment and the effect of contact resistance and grain boundaries that allows to precisely monitor the photoinduced charge separation and the local motions of the transiently generated free charge carriers by dielectric loss spectroscopy.[192] It measures photoconductivity in terms of $\varphi\Sigma\mu$,where φ and $\Sigma\mu$ are charge carrier generation yield and total charge carrier mobility, respectively. All the films were photoexcited with 355 nm laser pulses, i.e. primarily into the TAPOT band. Transient photoconductivity curves can be observed reaching maximum values $\varphi\Sigma\mu$ of 1.4×10^{-5} cm^2 V^{-1} s^{-1} for **PBI 1T** and **PBI 2T** and 3.4×10^{-5} cm^2 V^{-1} s^{-1} for **PBI 3T** (Figure 25a). A 2.4-fold increased photoconductivity for **PBI 3T** compared to the other derivatives is in line with our expectations, i.e. that the properties are improved for the derivative with the best electron donor component (terthiophene) and the largest p- and n-transporting domains.

For fsTAS, thin films of the LC material were prepared by spin-coating 5 mM solutions in MCH onto quartz substrates and subsequently annealing them at 180 °C for 30 min. All films were excited at 15400 cm^{-1} (650 nm) into the PBI J-aggregate band (see Figure A41, Figure A42 and Figure A43). A global analysis of the stray-light corrected transient map with exponential functions following a sequential model yields evolution associated difference spectra (EADS) with four components for **PBI 1T** and **PBI 2T**, and five components for **PBI 3T** (Figure 25b). All components show a dominant negative feature in the spectral region of the ground state PBI J-band absorption due to the ground state bleaching. The first component (black spectra in Figure 25b) of the EADS of all three samples additionally reveals excited state absorption from the one to the two-exciton state (16000 cm^{-1}, 625 nm).[64,193] Furthermore, excited state absorption can be observed at lower energies (8000-13000 cm^{-1}, 770-1250 nm) in all components of **PBI 1T** (Figure 25b, top), and in the first and second component (red and blue) of the EADS in **PBI 2T** (Figure 25b, middle) and **PBI 3T** (Figure 25b, bottom). This excited state decays with a lifetime of 20 ps (**PBI 2T**) and 1.6 ps (**PBI 3T**) to form the corresponding radical anion PBI$^{-\bullet}$ which is well characterized by its double maximum spectral signature at 10000 cm^{-1} (1000 nm) and 12000 cm^{-1} (830 nm).[194] The complementary radical cation D$^{+\bullet}$ of the bound electron-hole pair could not be observed in either of the three samples. The PBI$^{-\bullet}$ radical anion in **PBI 2T** decays monoexponentially with a lifetime of 161 ps, while the decay for **PBI 3T** is triexponential with two short components of 9.3 ps and 89 ps as well as a long-lived component of 768 ps. In thin films of **PBI 1T** no formation of PBI$^{-\bullet}$ species could be observed, presumably caused by the weaker electron donating character of the monothiophene-appended trialkoxyphenyl substituents. Accordingly, charge-separation is not only faster in thin films of **PBI 3T** (τ_{CS} = 1.6 ps) than for **PBI 2T** (τ_{CS} = 20 ps), but the charge-separated state of **PBI 3T** also exhibits a 4.8-fold increased lifetime (τ_{CR} = 768 ps) compared to **PBI 2T** (τ_{CR} = 161 ps). It is reasonable to relate this feature to the differences in the supramolecular structure. Thus, the larger domain size of septuple PBI strands in **PBI 3T** is beneficial for creating longer-lived charge-separated species compared to the sextuple strand in **PBI 2T**.

Despite **PBI 3T** outperforming **PBI 1T** and **PBI 2T** both in longevity and mobility of photogenerated charge-carriers as determined with fsTAS and FP-TRMC, it fails to match **PBI 2T**'s macroscopic photoconductivity in two-contact devices. This investigation clearly demonstrates, that whilst the rational design of the electronic properties and supramolecular LC structures can be used to fine-tune intrinsic functionality of the nanomaterials, macroscopic device performance strongly relies on the processability of the material and the concomitant quality of the active layer.

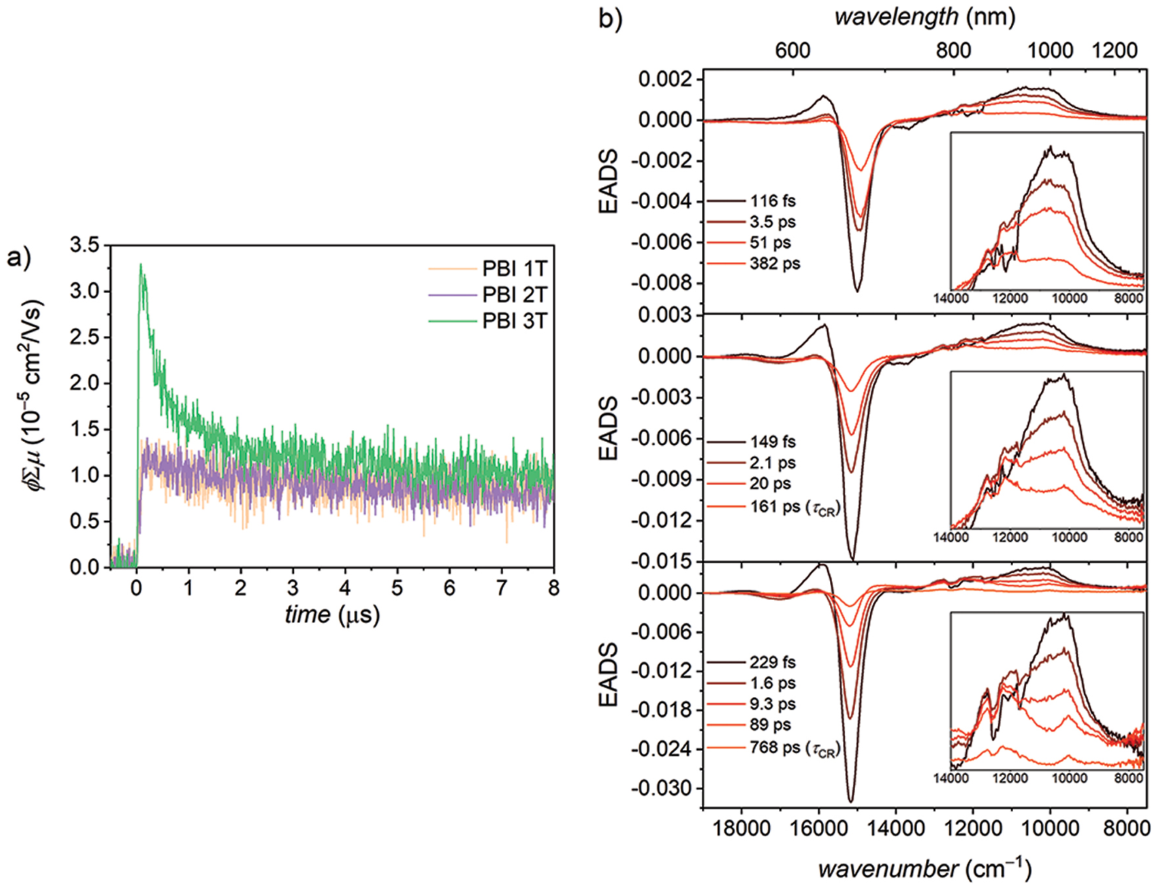

Figure 25. a) Kinetic trances of FP-TRMC observed in LC thin film samples of **PBI 1T** (orange), **PBI 2T** (purple) and **PBI 3T** (green). The wavelength and photon density of excitation laser pulses was 355 nm and 1.8×10^{15} cm^{-1}, respectively. b) Evolution associated difference spectra of the transient absorption measurements (λ_{ex} = 650 nm; $\tilde{\nu}$ = 15400 cm^{-1}) of LC thin films of **PBI 1T** (top), **PBI 2T** (middle) and **PBI 3T** (bottom) with associated time constants τ. The insets show a magnified profile of the EADS.

4.2. Conclusion

In this work, we presented three PBI donor–acceptor dyads and the in-depth investigation of their structural and functional properties. We demonstrated that these materials self-assemble into J-aggregates by the symbiotic interplay of hydrogen-bonding and π-π-interactions of the contorted PBI π-core. X-ray experiments and POM of the LC materials revealed unique packing features, i.e. the formation of four-, six-, and seven-stranded helices in the respective columnar phases for **PBI 1T**, **PBI 2T** and **PBI 3T**, respectively. The particular arrangement is dictated by the steric requirements of the monomeric building block encoded by the lateral extension of the TAPOT units. Two-contact photoconductivity devices prepared by solution shearing show enhanced photocurrents upon alignment of the charge transporting domains perpendicular to the electrodes, thereby demonstrating the high anisotropy of charge carrier flow along the columnar axis. fsTAS and FP-TRMC revealed the highest propensity for charge separation and transport on the nanoscale for the derivative with the largest oligothiopene-substituted derivative that bears the best electron-donating unit and the largest PBI domain size (seven-stranded helix). At the device level, however, this material is outperformed by shorter **PBI 2T** derivative due to better processability into properly aligned columnar structures.

4.3. Appendix to *Chapter 4*

Materials and Methods

Materials

Reagents were purchased from commercial suppliers and used as received without further purification. DCC was freshly distilled prior to its use. Solvents were distilled and dried by standard procedures. All reactions were carried out under nitrogen atmosphere. Column chromatography was performed with commercial glass columns using silica gel 60M (particle size 0.04-0.063 mm; Macherey-Nagel GmbH & Co. KG, Germany) as stationary phase.

NMR Spectroscopy

^{1}H and ^{13}C nuclear magnetic resonance (NMR**)** spectra were recorded on an Avance-400 spectrometer (Bruker-Daltonics GmbH, Germany) operating at 400 MHz (^{1}H) or 100 MHz (^{13}C), with the residual protic solvent used as the internal standard. The chemical shifts (δ) are reported in parts per million (ppm). Multiplicities for proton signals are abbreviated as s, d and m for singlet, doublet and multiplet, respectively.

Mass Spectrometry

High resolution mass spectra (HRMS) were recorded on an ESI micrOTOF focus spectrometer (Bruker Daltonic GmbH, Germany). Elemental analyses were performed on a CHN 932 analyzer (Leco Instruments GmbH, Germany). HRMS MALDI mass spectra were recorded on an autoflex II LRF from *Bruker Daltonics GmbH* using *trans*-2-[3-(*tert*-butylphenyl)-2-methyl-2-propenylidene]malononitrile (DCTB) as a matrix.

UV/Vis Spectroscopy

UV/Vis absorption spectra in solution were recorded using a V-770 spectrophotometer (JASCO Inc., Japan). The spectra were measured in quartz glass cuvettes using spectroscopic grade solvents. Temperature control was accomplished by a PAC-743R Peltier system (JASCO Inc., Japan). Extinction coefficients were calculated according to the Beer-Lambert law. UV-Vis absorption spectra of thin films were recorded in transmission mode with a Lambda 950 UV-Vis/NIR spectrometer (PerkinElmer Inc., USA) equipped with polarizer and an integration sphere.

Fluorescence Spectroscopy

Fluorescence spectroscopy in solution was carried out with an FLS 980 spectrometer

(Edinburgh Instruments Ltd., UK) by optical dilution method ($OD_{\max} < 0.05$). Fluorescence quantum yields were determined as average value of four different excitation wavelengths using *N*,*N*'-bis(2,6-diisopropylphenyl)-1,6,7,12-tetraphenoxy-3,4:9,10-perylenetetracarboxylic acid bisimide[187] as a fluorescence standard. The signals were corrected for the different refractive indices according to common procedure.[155] Time-resolved measurements were performed with a ps laser diode and a TCSPC detection unit (λ_{ex} = 635 nm, 505 nm). Fluorescence spectroscopy of thin films was carried out with an Axio Imager 2 (Carl Zeiss AG, Germany) polarizing optical microscope equipped with a Hg arc lamp and a cooled CCD spectrometer MCS-CCD PCI (Carl Zeiss AG, Germany). Fluorescence quantum yields of thin films were determined with a C9920-02 Absolute PL Quantum Yield Measurement System (Hamamatsu Photonics KK, Japan) using a calibrated integrating sphere system.

Polarized Optical Microscopy

The LC materials were examined under an Axio Imager 2 (Carl Zeiss AG, Germany) polarizing optical microscope equipped with a LTS420+LNP95 heating stage (Linkam Scientific Instruments Ltd., UK).

Differential Scanning Calorimetry

Thermal analyses by DSC were performed on a DSC 8000 from *Perkin Elmer* equipped with an Intracooler 2 refrigerated cooling system from *Perkin Elmer*.

FT-IR Spectroscopy

Polarized FT-IR spectra were recorded with an AIM-8800 infrared microscope connected to an IRAffinity FT-IR spectrometer (Shimadzu Corp., Japan). The sample was prepared as a thin film on a KBr substrate (thickness 2 mm) which was placed on a THMS600 heat stage with a TP94 controller (Linkam Scientific Instruments Ltd., UK). Polarization dependent FT-IR spectra were measured by using a precision automated polarizer (ZnSe) (PIKE Technologies, USA). This includes the PIKE Technologies Motion Control Unit and AutoPro software.

Cyclic and Square Wave Voltammetry

CV and SWV was carried out in a three electrode single-compartment cell on a standard electrochemical analyzer (EC epsilon, BAS Instruments, UK). A Pt disc electrode was used as a working electrode, a platinum wire as a counter electrode and an Ag/AgCl reference electrode using ferrocenium/ferrocene (Fc^+/Fc) as an internal standard for the calibration of the potential. The measurements were carried out under an argon atmosphere in dichloromethane and tetrabutylammonium hexafluorophosphate (recrystallized from ethanol/water and dried under vacuum) was added as supporting electrolyte.

Wide- and Middle-Angle X-Ray Scattering

Temperature-dependent WAXS and MAXS measurements were performed on a Bruker Nanostar (Detector Vantec2000, Microfocus copper anode X-ray tube Incoatec). LC samples were prepared by fiber extrusion using a mini-extruder. The measurements were carried out in Mark capillaries (Hilgenberg) positioned perpendicular to the incident X-ray beam. WAXS experiments were performed at a sample-detector distance of 21 cm, with the detector tilted by 14° upwards in order to study the angular range of $2\theta = 0.8° - 28°$. This allowed only the investigation of a section of the XRS pattern, therefore samples with lying and standing extruded fibers have been prepared to study the equatorial and the meridional signals in detail. Additional MAXS studies have been carried out at a distance of 28 cm with a linearly assembled detector covering an angular range of $2\theta = 0.7° - 12°$. Silver behenate was used as calibration standard for WAXS and MAXS.

Femtosecond Transient Absorption Spectroscopy

The femtosecond laser transient absorption spectrometer was driven by a chirped pulse amplified laser system “Solstice” from Newport-Spectra-Physics. The fundamental wavelength was 800 nm with a pulse length of 100 fs and a repitition rate of 1 kHz. The pump pulses were produced by a travelling wave optical parametric amplifier (TOPAS-C from Light Conversion, Spectra-Physics), with a pulse length shorter than 150 fs. The transient absorption spectrometer “Helios” from Ultrafast Systems was capable to probe the samples in the vis region (400 nm – 850 nm) and in the NIR region (790 – 1600 nm). For creating the white light continuum a small part of the 800 nm beam was guided to a moving, 3 mm thick CaF_2 crystal in the case of visible probing and it was guided to a non-moving, 15 mm thick sapphire crystal in the case of NIR probing. For a more detailed description of the measurement system, see Ref. 62 The transient maps for vis and NIR regions were corrected for stray light and chirp and were combined by the software Surface Xplorer Pro 2.2.3.116 (Ultrafast Systems, LLC). This map was deconvoluted globally between 400 nm and 1400 nm with the software GloTarAn[195,196] using a sequential model with a number of exponential functions to obtain evolution associated difference spectra (EADS). All samples were measured on a 1.25 mm thick fused silica glass substrate. The thin films of the LC material were prepared by spin-coating (1000 rpm, 1000 rpm/s, 60 s)

5 mM solutions in methylcylohexane and subsequently annealing them at 180 °C for 30 mins. The goal was to obtain an OD_{max} of around 0.3 with a clear surface to avoid scattered light, and the samples had between 0.2 and 0.5. The pump energy was varied for different samples between 10 and 50 nJ to obtain best results in respect to the amount of scattered light and highest achievable amplitude of the spectra.

Flash Photolysis Time-Resolved Microwave Conductivity

Transient photoconductivity of all the self-assembled LC samples were evaluated using FP-TRMC technique at room temperature under N_2 atmosphere. Charge carriers were photochemically generated by using a third harmonic generation from a Spectra-Physics INDI-HG Nd:YAG laser with a pulse duration of 5-8 ns operated at 10 Hz. Photon density of a 355 nm pulse was 1.8×10^{15} photons cm^{-2} for FP-TRMC. All the films were prepared by drop casting over quartz slides from their corresponding solutions (solvent: MCH, concentration: 6 mg/ml) at room temperature under ambient condition. For FP-TRMC measurements, microwave frequency and power were set at ~9.1 GHz and 3 mW, respectively so that the electric field of the microwave was sufficiently small and do not disturb the motion of charge carriers. Photoconductivity transients, demodulated through a GaAs crystal-diode with Schottky-barriers (rise time < 1 ns), were monitored by a Tektronix model TDS3032B digital oscilloscope. Time constant (τ) of the present TRMC system was then determined by the Q-value of microwave cavity (Q = 2000), leading to $\tau = Q/2f \sim 100$ ns, where the films over quartzs were loaded at the point of the electric field maximum. Observed conductivities were normalized, given by a photocarrier generation yield (φ) multiplied by sum of the charge-carrier mobilities ($\Sigma\mu$), according to the equation, $\varphi\Sigma\mu = (1/eAI_0F_{\text{light}})(\Delta P_r/P_r)$, where, e, A, I_0, F_{light}, P_r, and ΔP_r are unit charge of a single electron, sensitivity factor (S cm^{-1}), incident photon density of the excitation laser (photon cm^{-2}), correction (or filling) factor (cm^{-1}), and reflected microwave power and its change, respectively.

Solution Shearing

The active layer of the two-contact photoconductivity devices was prepared by solution shearing on commercially available bottom gate, bottom contact architectures (n-doped Si, 100 nm SiO_2, 30 nm Au, Fraunhofer IPMS, Germany) with a grid-like structure forming a channel width of 5 μm and a length of 10 mm. The substrates were cleaned with acetone, chloroform, toluene and isopropanol (acetone and isopropanol were of semiconductor grade VLSI PURANAL$^{\text{TM}}$, Aldrich Chemistry). A octadecyltriethoxysilane (OTES) modified Si/SiO$_2$ substrate was used as shearing tool and was approached to the surface at an angle of 15°. The substrate was heated to 150 °C by a precision heating stage (model PZ 82-2, Harry Gestigkeit GmbH) prior to shearing and the gap between the the bottom-contact substrate and the shearing tool was filled with 50 µL of PBI solution (10 mg mL^{-1} in *o*-dichlorobenzene). The shearing tool was then moved over the substrate with a shearing velocity of 0.017 mm s^{-1}.

Electrical Characterization

The electrical characterization of the two-contact devices was carried out by measuring the current with a Micromanipulator 4060 and 4155C semiconductor parametric analyser (Agilent Technologies, USA) under ambient conditions at room temperature. Photocurrents were determined while illuminating the sample with a Hg arc lamp (120 W) focused onto the device by an Axio Imager 2 optical microscope (Carl Zeiss AG, Germany).

Synthesis and Characterization

PBI 1T and **PBI 3T** were prepared according to Scheme A2. [2,2'-Bithiophen]-5-ylboronic acid (**11**),[197] 4,4,5,5-tetramethyl-2-(3,4,5-tris(dodecyloxy)phenyl)-1,3,2-dioxaborolane (**8**),[198] 1,6,7,12-tetrakis(3-hydroxyphenoxy)perylene-3,4:9,10-bis(dicarboximide) (**10**),[61] **2T**[111] and **PBI 2T**[111] were synthesized according to literature procedures.

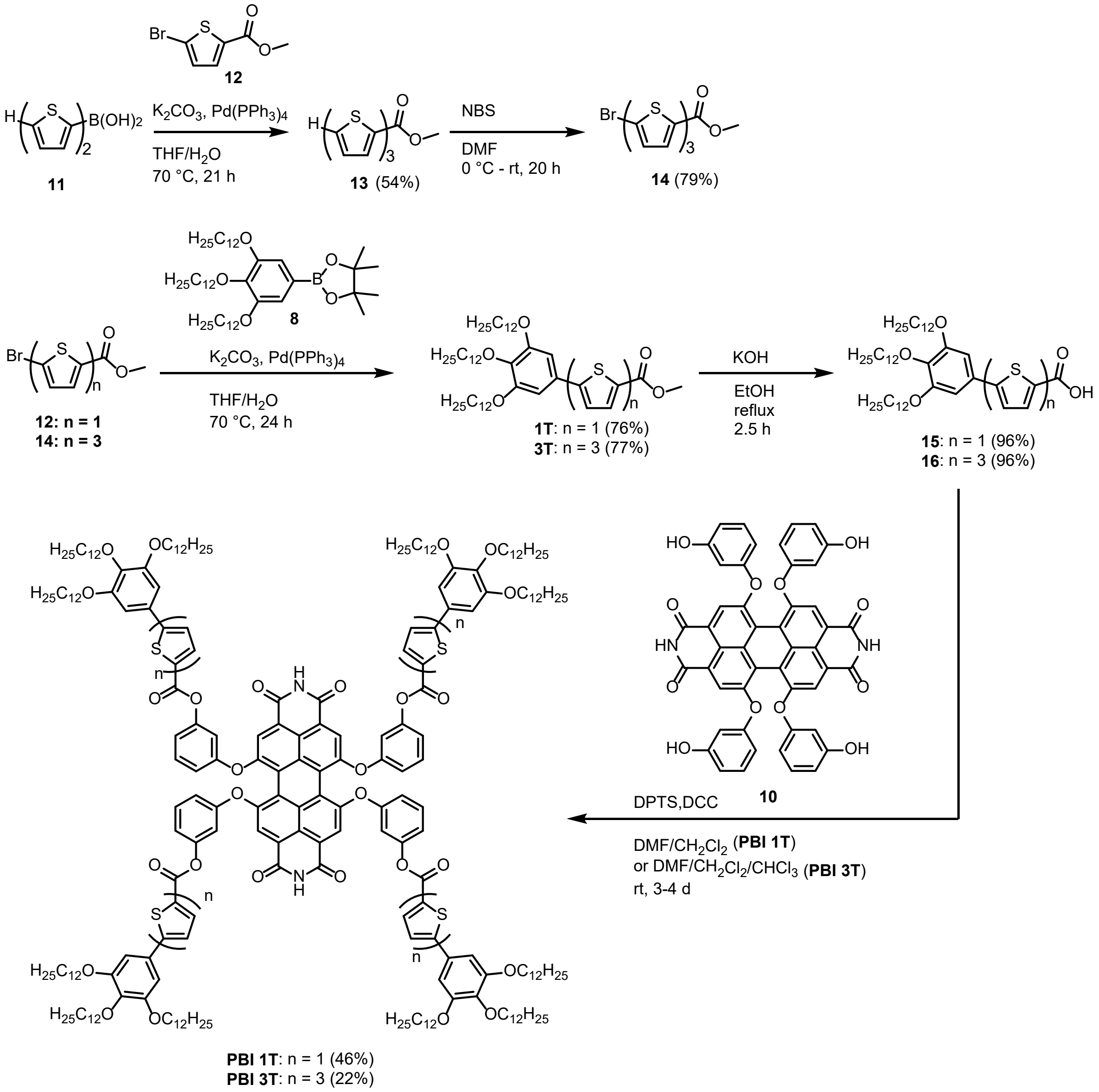

Scheme A2. Synthetic route to **PBI 1T** and **PBI 3T**.

Methyl [2,2':5',2''-terthiophene]-5-carboxylate (13)

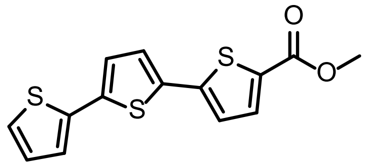

Methyl 5-bromothiophene-2-carboxylate (**12**) (1.68 g, 7.62 mmol, 1.0 eq), [2,2'-bithiophen]-5-ylboronic acid (**11**) (1.60 g, 7.62 mmol, 1.0 eq) and K_2CO_3 (3.16 g, 22.9 mmol, 3.0 eq) were dissolved in water (25 mL) and THF (200 mL) and the resulting solution was degassed. $Pd(PPh_3)_4$ was added and the solution was heated at 70°C for 21 h. After cooling to room temperature, water (50 mL) was added and the solution was extracted with diethyl ether (3 × 75 mL). The combined organic layers were washed with water (2 × 100 mL) and brine (100 mL), dried over Na_2SO_4 and the solvent was removed under reduced pressure. Column chromatography (silica, cyclohexane:ethyl acetate, 95:5) and consecutive recrystallization from acetonitrile gave 1.25 g (4.08 mmol, 54%) of a shiny green solid.

^{1}H NMR (400 MHz, CD_2Cl_2): $\delta = 7.68$ (d, $^3J = 4.0$ Hz, 1H, Ar*H*), 7.29 (dd, $^3J = 5.1$ Hz, $^4J = 1.2$ Hz, 1H, Ar*H*), 7.23 (dd, $^3J = 3.6$ Hz, $^4J = 1.2$ Hz, 1H, Ar*H*), 7.22 (d, $^3J = 3.8$ Hz, 1H, Ar*H*), 7.16 (d, $^3J = 4.0$ Hz, 1H, Ar*H*), 7.13 (d, $^3J = 3.8$ Hz, 1H, Ar*H*), 7.05 (dd, $^3J = 5.1$ Hz, $^3J = 3.6$ Hz, 1H, Ar*H*), 3.87 (s, 3H, C*H*$_3$) ppm. **^{13}C NMR** (100 MHz, CD_2Cl_2): $\delta = 162.6$, 144.0, 138.4, 136.9, 135.2, 134.5, 131.8, 128.4, 126.4, 125.6, 124.9, 124.7, 124.2, 52.5 ppm. **HRMS** (ESI-TOF, positive mode, MeCN/$CHCl_3$ 1:1): *m/z* calculated for $C_{14}H_{10}NaO_2S_3$ $[M+Na]^+ = 328.9740$, found 328.9729. **Elemental analysis** calculated (%) for $C_{14}H_{10}O_2S_3$ [M = 306.41 g/mol]: C 54.88 H 3.29 S 31.39; found, C 54.82 H 3.57 S 31.09. **m.p.** 166–169 °C.

Methyl 5''-bromo-[2,2':5',2''-terthiophene]-5-carboxylate (14)

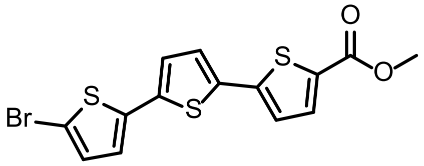

Methyl [2,2':5',2''-terthiophene]-5-carboxylate (**13**) (1.00 g, 3.26 mmol, 1.0 eq) was dissolved in dry dimethylformamide (DMF, 200 mL) and the solution was cooled to 0 °C. *N*-bromosuccinimide (0.64 g, 3.59 mmol, 1.1 eq) was added and the resulting mixture was stirred for 30 min before allowing it to warm to room temperature. The solution was stirred at room temperature for 20 h. Afterwards, water (150 mL) was added. The mixture was extracted with dichloromethane (3 × 100 mL). The combined organic layers were washed with water (100 mL) and brine (100 mL) and dried over Na_2SO_4. Removing the solvent under reduced pressure yielded 992 mg (2.57 mmol, 79%) of a shiny green solid.

^{1}H NMR (400 MHz, CD_2Cl_2): δ = 7.68 (d, ^{3}J = 3.9 Hz, 1H, Ar*H*), 7.21 (d, ^{3}J = 3.8 Hz, 1H, Ar*H*), 7.17 (d, ^{3}J = 3.9 Hz, 1H, Ar*H*), 7.08 (d, ^{3}J = 3.8 Hz, 1H, Ar*H*), 7.02 (d, ^{3}J = 3.9 Hz, 1H, Ar*H*), 6.98 (d, ^{3}J = 3.9 Hz, 1H, Ar*H*), 3.87 (s, 3H, C*H*$_3$) ppm. **^{13}C NMR** (100 MHz, CD_2Cl_2): δ = 162.6, 143.7, 138.5, 137.2, 135.7, 134.5, 132.1, 131.4, 126.4, 125.2, 124.8, 124.5, 112.0, 52.5 ppm. **HRMS** (ESI-TOF, positive mode, MeCN/$CHCl_3$ 1:1): *m/z* calculated for $C_{14}H_9BrO_2S_3$ [M$^+$]: 383.8948; found 383.8937. **Elemental analysis** calculated (%) for $C_{14}H_9BrO_2S_3$ [M = 385.31 g/mol]: C 43.64 H 2.35 S 24.96; found, C 43.78 H 2.62 S 24.97. **m.p.** 172–173 °C.

Methyl 5-(3,4,5-tris(dodecyloxy)phenyl)thiophene-2-carboxylate (1T)

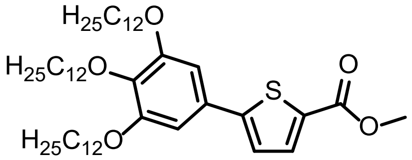

K_2CO_3 (1.50 g, 10.9 mmol, 8.0 eq), methyl 5-bromothiophene-2-carboxylate (**12**) (300 mg, 1.36 mmol, 1.0 eq) and 3,3,4,4-tetramethyl-1-(3,4,5-tris(dodecyloxy)phenyl)-1,3,2,5-bromadioxolane (**8**) (1.03 g, 1.36 mmol, 1.0 eq) were dissolved in a mixture of degassed THF (100 mL) and water (15 mL) under a nitrogen atmosphere. $Pd(PPh_3)_4$ (157 mg, 136 µmol, 0.1 eq) was added and the mixture was heated at 60 °C for 24 h. After the addition of water (70 mL), the mixture was extracted with dichloromethane (3 × 75 mL). The combined organic layers were washed with brine (100 mL), dried over Na_2SO_4 and the solvent was removed under reduced pressure. Column chromatography (silica, cyclohexane : ethyl acetate, 50:1 to 96:4) and consecutive recrystallization from ethanol yielded 796 mg (1.03 mmol, 76%) of a colorless solid.

^{1}H NMR (400 MHz, $CDCl_3$): 7.73 (d, ^{3}J = 3.9 Hz, 1H, Ar*H*), 7.19 (d, ^{3}J = 3.9 Hz, 1H, Ar*H*), 6.80 (s, 2H, Ar*H*), 4.00 (m, 6H, OC*H*$_2$), 3.90 (s, 3H, OC*H*$_3$), 1.76 (m, 6H, OCH_2C*H*$_2$), 1.48 (m, 6H, OCH_2CH_2C*H*$_2$), 1.39–1.23 (m, 48H, C*H*$_2$), 0.88 (m, 9H, C*H*$_3$) ppm. **^{13}C NMR** (100 MHz, $CDCl_3$): δ = 162.9, 153.7, 151.9, 139.3, 134.5, 131.5, 128.7, 123.4, 105.2, 73.7, 69.4, 52.3, 32.1, 30.5, 29.9, 29.8, 29.6, 29.5, 26.3, 26.2, 22.8, 14.3 ppm. **HRMS** (ESI-TOF, positive mode, MeCN/$CHCl_3$ 1:1): *m/z* calculated for $C_{48}H_{82}O_5S$ [M]$^+$: 770.5883; found 770.5887. **Elemental analysis** calculated (%) for $C_{48}H_{82}O_5S$ [M = 771.24 g/mol]: C 74.75 H 10.72 S 4.16; found, C 74.70 H 10.68 S 3.91. **m.p.** 46–47 °C. **SWV** (CH_2Cl_2, 0.1 M TBAHFP, vs. Fc$^+$/Fc): E_{ox1} = 0.83 V, E_{ox2} = 1.27 V. **UV/Vis** ($CHCl_3$): $\lambda_{\max}$ ($\varepsilon_{\max}$) = 333 nm (20000 M^{-1} cm^{-1}).

Methyl 5''-(3,4,5-tris(dodecyloxy)phenyl)-[2,2':5',2''-terthiophene]-5-carboxylate (3T)

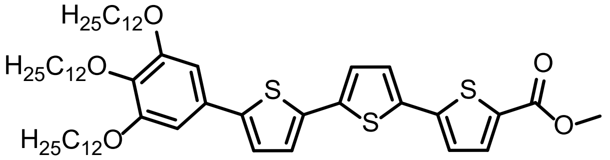

K_2CO_3 (1.21 g, 8.72 mmol, 8.0 eq), methyl 5''-bromo-[2,2':5',2''-terthiophene]-5-carboxylate (**14**) (420 mg, 1.09 mmol, 1.0 eq) and 3,3,4,4-tetramethyl-1-(3,4,5-tris(dodecyloxy)phenyl)-1,3,2,5-bromadioxolane (**8**) (825 mg, 1.09 mmol, 1.0 eq) were dissolved in a mixture of degassed THF (100 mL) and water (15 mL) under a nitrogen atmosphere. $Pd(PPh_3)_4$ (126 mg, 109 µmol, 0.1 eq) was added and the mixture was heated at 60°C for 24 h. After the addition of water (70 mL), the mixture was extracted with dichloromethane (3 × 75 mL). The combined organic layers were washed with brine (100 mL), dried over Na_2SO_4 and the solvent was removed under reduced pressure. Column chromatography (silica, cyclohexane : ethyl acetate, 96:4) and consecutive recrystallization from ethanol yielded 786 mg (840 µmol, 77%) of a yellow solid.

^{1}H NMR (400 MHz, $CDCl_3$): 7.70 (d, $^3J = 3.9$ Hz, 1H, Ar*H*), 7.20 (d, $^3J = 3.9$ Hz, 1H, Ar*H*), 7.13 (m, 4H, Ar*H*), 6.77 (s, 2H, Ar*H*), 4.03 (m, 4H, OCH_2), 3.98 (m, 2H, OCH_2), 3.90 (s, 3H, OCH_3), 1.79 (m, 6H, OCH_2CH_2), 1.49(m, 6H, $OCH_2CH_2CH_2$), 1.41–1.24 (m, 48H, CH_2), 0.88 (m, 9H, CH_3) ppm. **^{13}C NMR** (100 MHz, $CDCl_3$): $\delta = 162.6$, 153.6, 144.5, 144.0, 138.6, 138.3, 135.4, 134.8, 134.5, 131.3, 129.2, 126.1, 125.1, 124.3, 123.9, 123.6, 104.8, 73.7, 69.4, 52.4, 32.1, 30.5, 29.9, 29.8, 29.6, 29.5, 26.3, 22.8, 14.3 ppm. **HRMS** (ESI-TOF, positive mode, MeCN/$CHCl_3$ 1:1): *m/z* calculated for $C_{56}H_{86}NaO_5S_3$ $[M+Na]^+$: 957.5535; found 957.5488. **Elemental analysis** calculated (%) for $C_{56}H_{86}O_5S_3$ [M = 935.48 g/mol]: C 71.90 H 9.27 S 10.28; found, C 71.78 H 9.21 S 10.04. **m.p.** 85–86 °C. **SWV** (CH_2Cl_2, 0.1 M TBAHFP, vs. Fc^+/Fc): $E_{ox1} = 0.55$ V, $E_{ox2} = 0.78$ V, $E_{ox3} = 1.16$ V, $E_{ox4} = 1.34$ V. **UV/Vis** ($CHCl_3$): λ_{max} (ε_{max}) = 410 nm (39000 M^{-1} cm^{-1}).

5-(3,4,5-Tris(dodecyloxy)phenyl)thiophene-2-carboxylic acid (15)

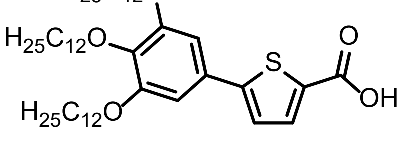

Methyl 5-(3,4,5-tris(dodecyloxy)phenyl)thiophene-2-carboxylate (**1T**) (600 mg, 778 µmol, 1.0 eq) and KOH (2.18 g, 38.9 mmol, 50 eq) were suspended in ethanol (60 mL) and heated to reflux over a period of 2.5 h. After cooling to room temperature, the solution was acidified by the addition of 1M HCl (aq.). The solution was extracted with chloroform (3 × 60 mL). The combined organic layers were washed with water (80 mL) and brine (80 mL) and dried over Na_2SO_4. Removing the solvent under reduced pressure yielded 576 mg (749 µmol, 96%) of a colorless solid.

^{1}**H NMR** (400 MHz, $CDCl_3$): 7.83 (d, ^3J = 4.0 Hz, 1H, Ar*H*), 7.23 (d, ^3J = 4.0 Hz, 1H, Ar*H*), 6.82 (s, 2H, Ar*H*), 4.01 (m, 6H, OCH_2), 1.79 (m, 6H, OCH_2CH_2), 1.49 (m, 6H, $OCH_2CH_2CH_2$), 1.38–1.24 (m, 48H, CH_2), 0.88 (m, 9H, CH_3) ppm. ^{13}**C NMR** (100 MHz, $CDCl_3$): δ = 166.7, 153.7, 153.6, 139.5, 136.0, 130.5, 128.5, 123.7, 105.3, 73.8, 69.4, 32.1, 30.5, 29.9, 29.8, 29.6, 29.5, 26.3, 26.2, 22.9, 14.3 ppm. **HRMS** (ESI-TOF, positive mode, MeCN/$CHCl_3$ 1:1): *m/z* calculated for $C_{47}H_{80}NaO_5S$ $[M+Na]^+$: 779.5624; found 779.5602. **Elemental analysis** calculated (%) for $C_{47}H_{80}O_5S$ [M = 757.21 g/mol]: C 74.55 H 10.65 S 4.23; found, C 74.77 H 10.58 S 3.99. **m.p.** 85–87 °C.

5''-(3,4,5-Tris(dodecyloxy)phenyl)-[2,2':5',2''-terthiophene]-5-carboxylate (16)

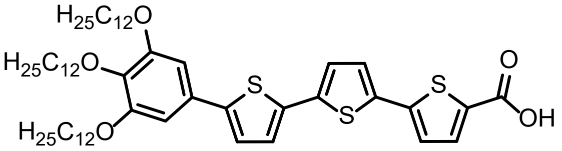

Methyl 5''-(3,4,5-tris(dodecyloxy)phenyl)-[2,2':5',2''-terthiophene]-5-carboxylate (**3T**) (600 mg, 641 µmol, 1.0 eq) and KOH (1.80 g, 32.1 mmol, 50 eq) were suspended in ethanol (200 mL) and heated to reflux over a period of 2.5 h. After cooling to room temperature, the dispersion was acidified by the addition of 1M HCl (aq.). The resulting mixture was extracted with $CHCl_3$ (3 × 200 mL). The combined organic layers were washed with water (3 × 100 mL) and brine (100 mL) and dried over Na_2SO_4. Removing the solvent under reduced pressure yielded 565 mg (613 µmol, 96%) of a yellow solid.

^{1}**H NMR** (400 MHz, $CDCl_3$): 7.79 (d, ^3J = 3.9 Hz, 1H, Ar*H*), 7.24 (d, ^3J = 3.9 Hz, 1H, Ar*H*), 7.15 (m, 4H, Ar*H*), 6.77 (s, 2H, Ar*H*), 4.03 (m, 4H, OCH_2), 3.98 (m, 2H, OCH_2), 1.79 (m, 6H, OCH_2CH_2), 1.50 (m, 6H, $OCH_2CH_2CH_2$), 1.40–1.24 (m, 48H, CH_2), 0.88 (m, 9H, CH_3) ppm. ^{13}**C NMR** (100 MHz, $CDCl_3$): δ = 166.4, 153.6, 145.6, 144.6, 138.7, 138.6, 136.0, 135.4, 134.6, 130.3, 129.1, 126.5, 125.2, 124.4, 124.1, 123.7, 104.8, 73.8, 69.4, 32.1, 30.5, 29.9, 29.8, 29.6, 29.5, 26.3, 22.9, 14.3 ppm. **HRMS** (ESI-TOF, positive mode, MeCN/$CHCl_3$ 1:1): *m/z* calculated for $C_{55}H_{84}NaO_5S_3$ $[M+Na]^+$: 943.5379; found 943.5351. **Elemental analysis** calculated (%) for $C_{55}H_{84}O_5S_3$ [M = 921.45 g/mol]: C 71.69 H 9.19 S 10.44; found, C 71.49 H 9.01 S 10.51. **m.p.** 143–146 °C.

PBI 1T

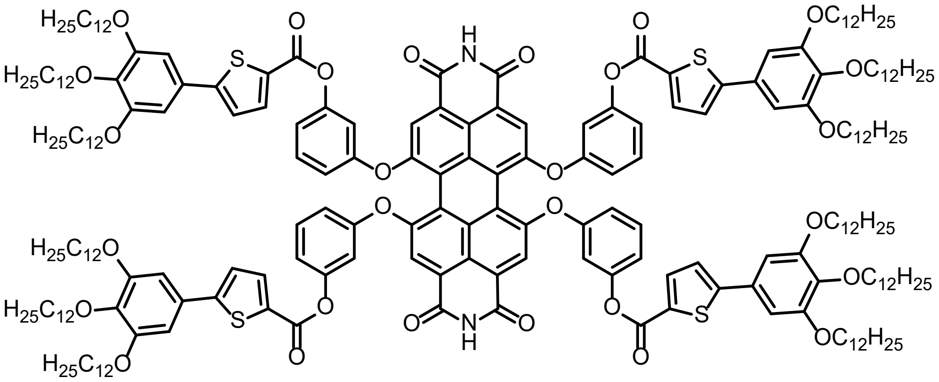

N,N′-dimethylaminopyridinium *para*-toluenesulfonate (DPTS) (70.7 mg, 240 µmol, 2.0 eq), 5-(3,4,5-tris(dodecyloxy)phenyl)thiophene-2-carboxylate (**15**) (400 mg, 528 µmol, 4.4 eq) and 1,6,7,12-tetrakis(4-hydroxyphenoxy)perylene-3,4:9,10-tetracarboxylic acid bisimide (**10**) (98.8 mg, 120 µmol, 1.0 eq) were dissolved in a mixture of dry dichloromethane (10 mL) and dry DMF (3 mL) under nitrogen atmopshere. A solution of DCC (124 mg, 600 µmol, 5.0 eq) in dry dichloromethane (5 mL) was added dropwise at room temperature. The solution was stirred for 3 d. Afterwards, chloroform (70 mL) was added and the resulting solution was washed with water (3 × 50 mL) and brine (50 mL) and the solvent was removed under reduced pressure. Column chromatography (silica, dichloromethane) yielded 210 mg (55.6 µmol, 46%) of a blue solid.

^{1}H NMR (400 MHz, $CDCl_3$): 8.43 (s, 2H, N*H*), 8.30 (s, 4H, Ar*H*), 7.80 (d, ^3J = 4.0 Hz, 4H, Ar*H*), 7.32 (m, 4H, Ar*H*), 7.17 (d, ^3J = 4.0 Hz, 4H, Ar*H*), 7.02 (m, 4H, Ar*H*), 6.89 (m, 8H, Ar*H*), 6.77 (s, 8H, Ar*H*), 3.98 (m, 24H, OCH_2), 1.78 (m, 24H, OCH_2CH_2), 1.47 (m, 24H, $OCH_2CH_2CH_2$), 1.38–1.22 (m, 192H, CH_2), 0.87 (m, 36H, CH_3) ppm. **^{13}C NMR** (100 MHz, $CDCl_3$): δ = 162.7, 160.1, 156.0, 155.3, 153.7, 153.3, 151.9, 139.4, 135.8, 133.3, 130.7, 130.3, 128.4, 123.5, 123.1, 121.4, 121.2, 120.6, 118.1, 117.0, 113.8, 105.1, 73.7, 69.4, 32.1, 30.5, 29.9, 29.8, 29.6, 29.5, 26.3, 22.8, 14.3 ppm. **HRMS** (ESI-TOF, positive mode, MeCN/$CHCl_3$ 1:1): *m/z* calculated for $C_{236}H_{338}Na_2N_2O_{28}S_4$ $[M+2Na]^{2+}$: 1912.1910; found 1912.1810. **Elemental analysis** calculated (%) for $C_{236}H_{338}N_2O_{28}S_4$ [M = 3779.53 g/mol]: C 75.00 H 9.01 N 0.74 S 3.39; found, C 74.92 H 8.99 N 0.69 S 3.26. **m.p.** 264 °C. **UV/Vis** ($CHCl_3$): $\lambda_{max,PBI}$ ($\varepsilon_{max,PBI}$) = 569 nm (41400 M^{-1} cm^{-1}). **Fluorescence** ($CHCl_3$): λ_{max} (λ_{ex}) = 603 nm (531 nm), Φ_{Fl} = 0.35.

PBI 3T

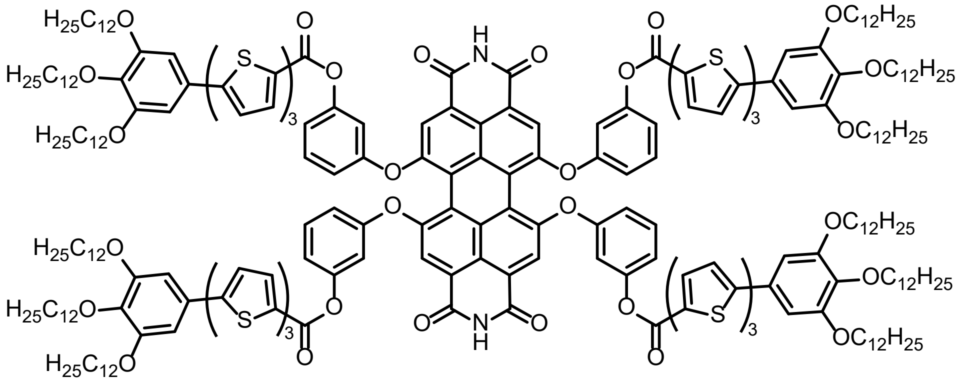

DPTS (58.1 mg, 197 µmol, 2.0 eq), 5''-(3,4,5-tris(dodecyloxy)phenyl)-[2,2':5',2''-terthiophene]-5-carboxylate (**16**) (400 mg, 434 µmol, 4.4 eq) and 1,6,7,12-tetrakis(4-hydroxyphenoxy)perylene-3,4:9,10-tetracarboxylic acid bisimide (**10**) (81.2 mg, 98.6 µmol, 1.0 eq) were suspended in a mixture of dry dichloromethane (60 mL) and dry DMF (9 mL). A solution of DCC (102 mg, 493 µmol, 5.0 eq) in dry dichloromethane (5 mL) was added dropwise at room temperature. The dispersion was stirred at room temperature for 3 d. Afterwards, $CHCl_3$ (50 mL) was added and the resulting solution was stirred for 24 h. After dilution with $CHCl_3$ (100 mL), the solution was washed with water (3 × 50 mL) and brine (50 mL) and the solvent was removed under reduced pressure. Column chromatography (silica, chloroform : methanol, 1:0 to 100:0.5) and consecutive preparative thin layer chromatography (chloroform : methanol, 100:1) yielded 98.0 mg (25.9 µmol, 22%) of a green solid.

^{1}H NMR (400 MHz, $CDCl_3$): 8.44 (s, 2H, N*H*), 8.31 (s, 4H, Ar*H*), 7.76 (m, 4H, Ar*H*), 7.31 (m, 4H, Ar*H*), 7.13 m, 4H, Ar*H*), 7.07 (m, 4H, Ar*H*), 7.03 (m, 16H, Ar*H*), 6.90 (m, 8H, Ar*H*), 6.72 (s, 8H, Ar*H*), 3.98 (m, 24H, OCH_2), 1.78 (m, 24H, OCH_2CH_2), 1.48 (m, 24H, $OCH_2CH_2CH_2$), 1.39–1.22 (m, 192H, CH_2), 0.88 (m, 36H, CH_3) ppm. **^{13}C NMR** (100 MHz, $CDCl_3$): δ = 162.7, 159.8, 155.9, 155.2, 153.6, 151.9, 145.4, 144.5, 138.7, 138.5, 135.7, 135.3, 134.5, 133.3, 130.7, 130.1, 129.1, 126.4, 125.2, 124.2, 123.8, 123.6, 123.0, 121.4, 121.2, 120.5, 118.1, 116.8, 113.8, 104.6, 73.7, 69.4, 32.1, 30.5, 29.9, 29.8, 29.6, 29.5, 26.3, 22.9, 14.3 ppm. **HRMS** (MALDI-TOF, positive mode, DCTB, $CHCl_3$): *m/z* calculated for $C_{268}H_{355}N_2O_{28}S_{12}$ $[M+H]^+$: 4435.3132, found 4435.3349. **Elemental analysis** calculated (%) for $C_{268}H_{354}N_2O_{28}S_{12}$ [M = 4436.49 g/mol]: C 72.56 H 8.04 N 0.63 S 8.67; found, C 72.42 H 7.93 N 0.87 S 8.52. **m.p.** 317°C (decomposition). **UV/Vis** ($CHCl_3$): $\lambda_{max,PBI}$ ($\varepsilon_{max,PBI}$) = 569 nm (41600 M^{-1} cm^{-1}). **Fluorescence** ($CHCl_3$): λ_{max} (λ_{ex}) = 600 nm (560 nm), $\Phi_{Fl} < 0.01$.

Optical Spectroscopy

In the following, results from optical spectroscopy of **PBI 1T** and **PBI 3T** are shown. The corresponding experiments of **PBI 2T** were reported previously.[111]

UV/Vis Spectra of PBI 1T, PBI 3T and the Corresponding Building Blocks

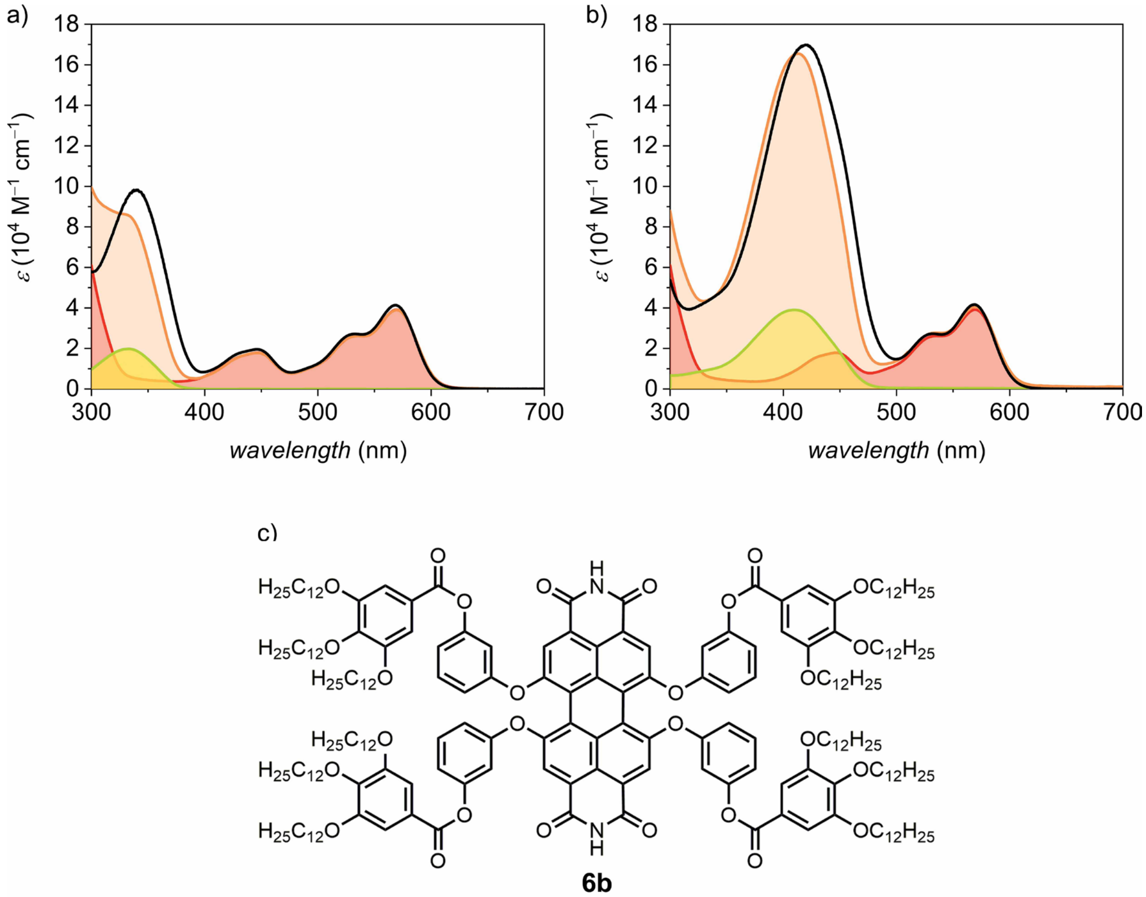

6b

Figure A27. a) UV/Vis absorption spectra of a) **PBI 1T** (black), PBI **6b** (red), **1T** (yellow) and the calculated equimolar superposition of PBI **6b** and **1T** (orange) and b) **PBI 3T** (black), PBI **6b** (red), **3T** (yellow) and the calculated equimolar superposition of PBI **6b** and **3T** (orange) recorded for 30 µM solutions in $CHCl_3$. c) Chemical structure of PBI **6b**.

Fluorescence Spectroscopy

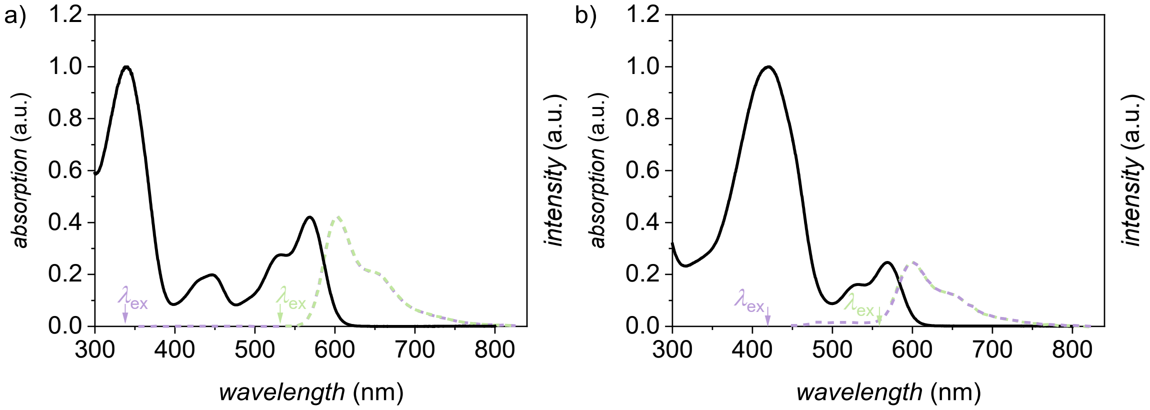

Figure A28. UV/Vis absorption (black solid line, c = 30 μM) and fluorescence spectra (colored dashed lines, c ≈ 100 nM) of a) **PBI 1T** ($\lambda_{\text{ex,purple}}$ = 340 nm, $\lambda_{\text{ex,green}}$ = 531 nm) and b) **PBI 3T** ($\lambda_{\text{ex,purple}}$ = 420 nm, $\lambda_{\text{ex,green}}$ = 560 nm) in $CHCl_3$ at 22 °C.

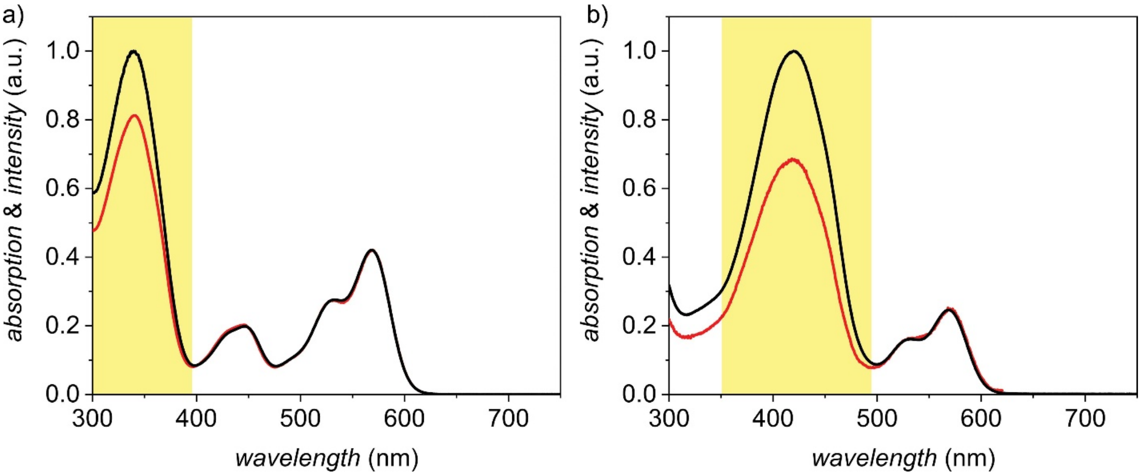

Figure A29. Normalized absorption (black) and excitation (red; λ_{em} = 650 nm) spectra of a) **PBI 1T** and b) **PBI 3T** with c ≈ 100 nM in $CHCl_3$ at 295 K. The areas highlighted in yellow indicate the range of integration.

Fluorescence of the PBI can be observed whether the PBI chromophores (λ_{ex} = 540 nm) or the thiophene-containing donor units (λ_{ex} = 365 − 420 nm) are excited indicating ET of the electron-rich donor to the PBI (see Figure A28). By comparing the integrated area in absorption and excitation spectra in the region of the donor absorption (highlighted in yellow), the resonance ET efficiency was estimated to be approximately 82% for monomeric **PBI 1T** and 69% for monomeric **PBI 3T** in chloroform. The ET efficiency of monomeric **PBI 2T** in chloroform was previously reported to 74%.[111]

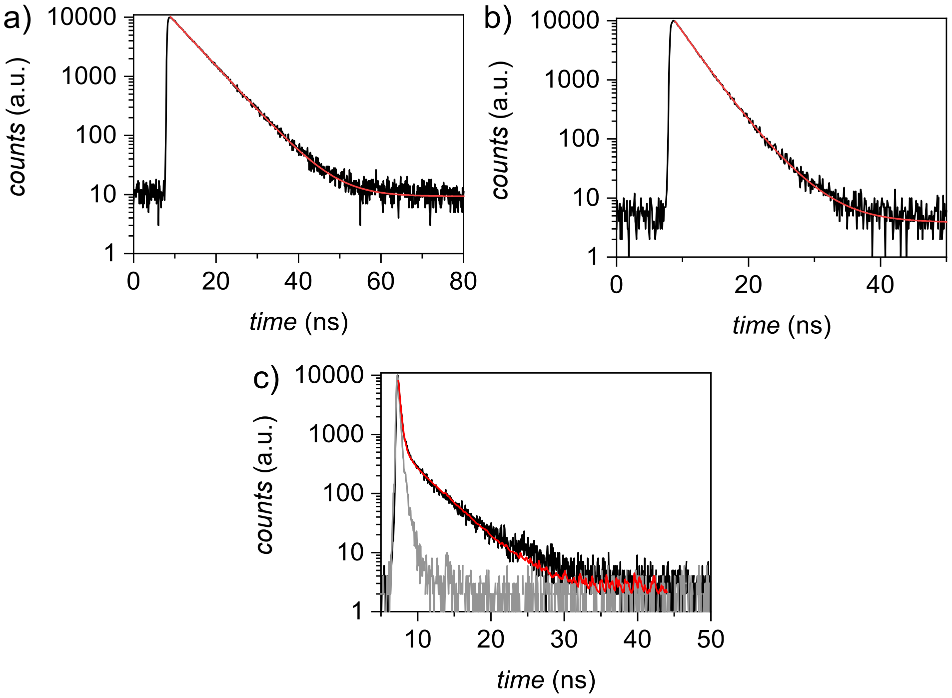

Figure A30. Lifetime measurement (λ_{ex} = 505 nm, λ_{em} = 605 nm) (black) of a) reference acceptor **17** b) **PBI 1T** and c) **PBI 3T** with $c \approx$ 100 nM in $CHCl_3$ at 295 K. The instrument response function is shown in grey, the a) mono- and b,c) bi-exponential fits with free τ_1 and τ_2 parameters in red.

The fluorescence lifetime measurements of **PBI 1T** (Figure A30b) and **PBI 3T** (Figure A30c) show biexponential decay curves with a dominant short- and a minor long-lived component. These decays can be either fitted with free parameters for τ_1 and τ_2 or with τ_2 fixed to 5.79 ns, which corresponds to the unquenched fluorescence lifetime of reference acceptor **17** (Scheme A3). The results of these fits are shown in Table A7 and reveal that the resulting short component varies only negligibly with the two methods.

Summary of the Optical Properties of PBI 1T, PBI 2T and PBI 3T

Table A6. Optical properties (absorption) of self-assembled **PBI 1T**, **PBI 2T** and **PBI 3T** in toluene[a].

	$\lambda_{\text{max, bithiophene}}$ (nm) [ε (M^{-1}cm^{-1})]	$\lambda_{\text{max, PBI}}$ (nm) [ε (M^{-1}cm^{-1})]	FWHM$_{\text{PBI}}$^{b} (cm^{-1})
PBI 1T	332 [94800]	630 [61000]	880
PBI 2T[111]	369 [121300]	631 [55900]]	880
PBI 3T	395 [140700]	656 [58000]	660

[a] (c = 12 mM (**PBI 1T**), c = 2.1 mM (**PBI 2T**), c = 70 μM (**PBI 3T**)) at 295 K;

[b] FWHM was derived as twice the distance between the absorption maximum to the closest edge (here the red edge) at half maximum of the unsymmetrically shaped absorption bands to prevent falsification by the vibronic progression.

Table A7. Comparison of the fits of the fluorescence decay curves of **17**, **PBI 1T** and **PBI 3T** in CHCl$_3$.

	τ_{Fl}^{a} [Rel.] (ns [%])	$\chi^{2,a}$	$\tau\tau_{\text{Fl}}$^{c} [Rel.] (ns [%])	$\chi^{2,c}$
17	5.79 [100]^{b}	1.107	–	–
PBI 1T	2.63 [85] 4.56 [15]	1.175	2.73 [93] 5.79 [7]	1.222
PBI 3T	0.17 [79] 3.70 [21]	1.594	0.22 [91] 5.79 [9]	7.700

[a] λ_{ex} = 505 nm, λ_{em} = 605 nm. Biexponential fit was performed with free parameters for the short and long component of the fluorescence lifetime;

[b] λ_{ex} = 505 nm, λ_{em} = 605 nm. Monoexponential decay fit;

[c] λ_{ex} = 505 nm, λ_{em} = 605 nm. Biexponential fit was performed with the long lifetime fixed as 5.79 ns, which displays the unquenched lifetime of the reference **17**.

Table A8. Optical properties of thin films[a] of **PBI 1T**, **PBI 2T** and **PBI 3T** on quartz substrates.

	Absorption			**Emission**		
	$\lambda_{\text{max, bithiophene}}$ (nm)	$\lambda_{\text{max, PBI}}$ (nm)	FWHM$_{\text{PBI}}$^{b} (cm^{-1})	λ_{max} (nm)	$\Delta\tilde{\nu}_{\text{stokes}}$ (cm^{-1})	Φ_{Fl}^{c} (%)
PBI 1T	336	660	760	678	–400	4
PBI 2T[111]	378	653	760	669	−370	2
PBI 3T	402	654	760	667	–300	<1

[a] Spin-coated from 1 mM solutions in MCH on quartz substrates and annealed for 30 mins at 180 °C;

[b] FWHM was derived as twice the distance between the absorption maximum to the closest edge (here the red edge) at half maximum of the unsymmetrically shaped absorption bands to prevent falsification by the vibronic progression;

[c] absolute quantum yield were measured with an integration sphere.

Cyclic Voltammetry

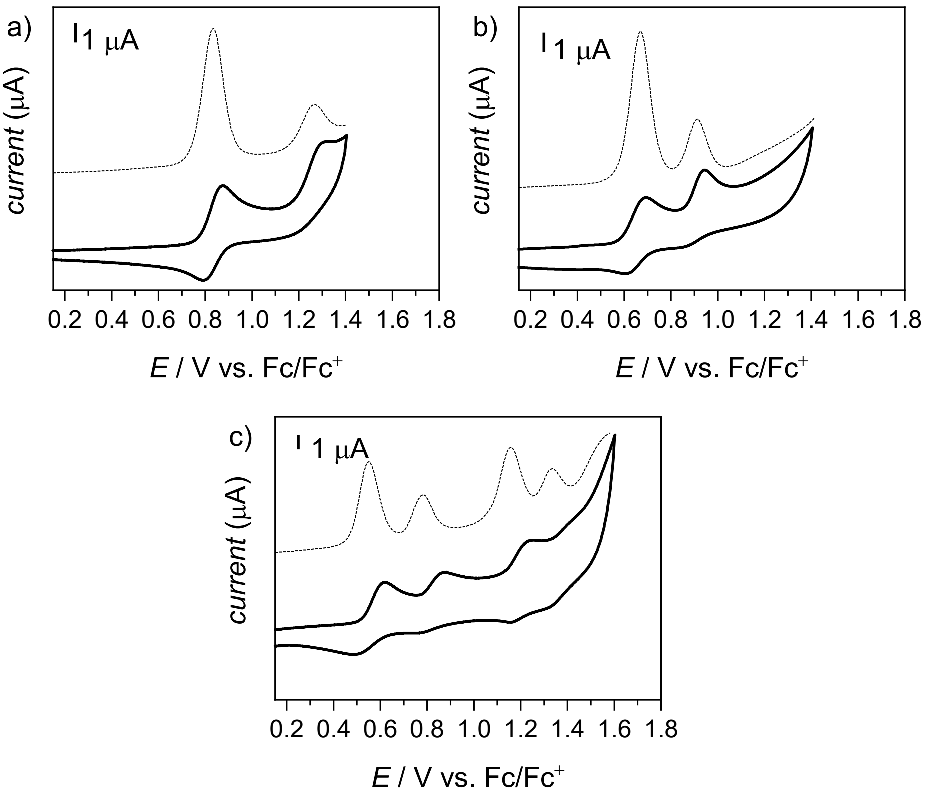

Figure A31. CV (solid lines) and SWV (dashed lines) traces of a) **1T**, b) **2T** and c) **3T**. The measurements were performed in dichloromethane ($c \approx 200$ μM) at room temperature with tetrabutylammonium hexafluorophosphate (0.1 M) as electrolyte (scan rate: 100 mV s^{-1}).

Using the oxidation potentials obtained from the CV and SWV measurements as well as optical bandgaps obtained from UV/Vis absorption studies, the HOMO and LUMO energy levels were estimated according to common procedure using the experimentally determined redox potentials and the energy level of Fc^+/Fc with respect to the vacuum level ($E_{\mathrm{LUMO}} = -\,[\mathrm{e}E\,(\mathrm{M/M^-}) + 5.15\ \mathrm{eV}]$ and $E_{\mathrm{HOMO}} = -\,[\mathrm{e}E\,(\mathrm{M/M^+}) + 5.15\ \mathrm{eV}]$).[190] These results are summarized in Table 2 and compared to a reference acceptor **17** (Scheme A3).[189]

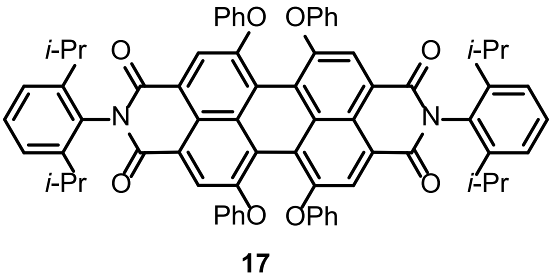

17

Scheme A3. Chemical structure of **17**.

Concentration-Dependent Self-Assembly of PBI 3T

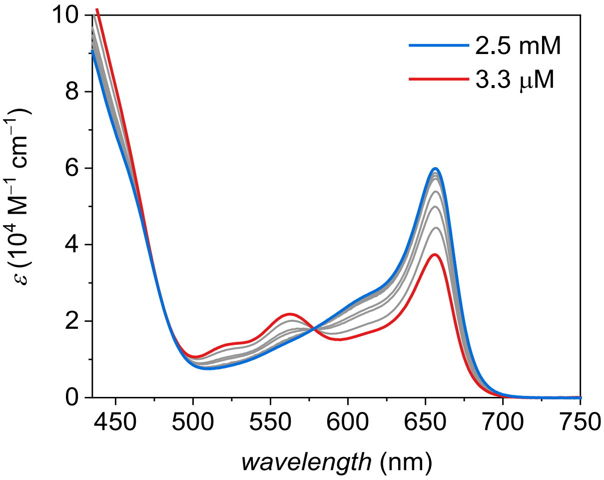

Figure A32. Concentration-dependent UV/Vis absorption spectra (3.3 µM – 2.5 mM, colored and grey lines) of **PBI 3T** in toluene at 298 K. The absorption spectra at wavelength below 440 nm are not shown due to the high absorptivity of the terthiophene units relative to the PBI leading to artefacts in concentration-dependent measurements for higher concentrations.

Table A9. Parameters of the cooperative nucleation-elongation self-assembly process.[94]

	K_{elong} (M^{-1})	K_{nuc} (M^{-1})	σ
PBI 1T	2.5×10^{3}	8	3.0×10^{-3}
PBI 2T[111]	8.0×10^{3}	9	1.1×10^{-3}
PBI 3T	7.0×10^{5}	700	1.0×10^{-3}

Polarized Optical Microscopy and Differential Scanning Calorimetry

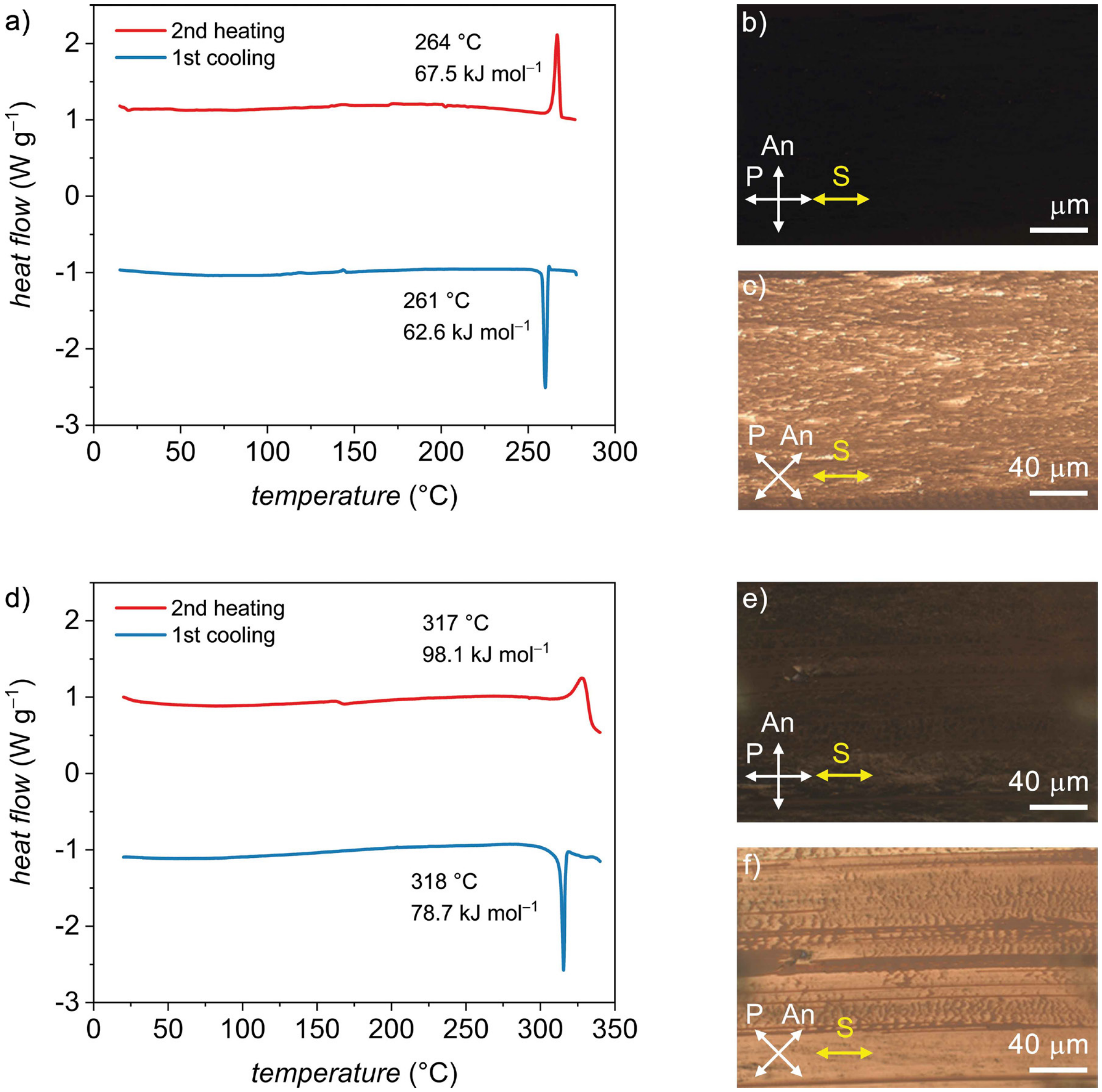

Figure A33. DSC traces of a) **PBI 1T** and d) **PBI 3T** in the first cooling (blue) and second heating (red) process. The heating and cooling rates were 10 °C min^{-1}. POM images of a mechanically aligned sample of b,c) **PBI 1T** and e,f) **PBI 3T** on quartz substrates with crossed polarizer (P) and analyzer (An) with the shearing direction (S) b,e) parallel and c,f) in a 45° rotational displacement with respect to the analyzer.

The thermotropic properties of **PBI 2T** were reported previously.[111]

Polarized FT-IR Spectroscopy

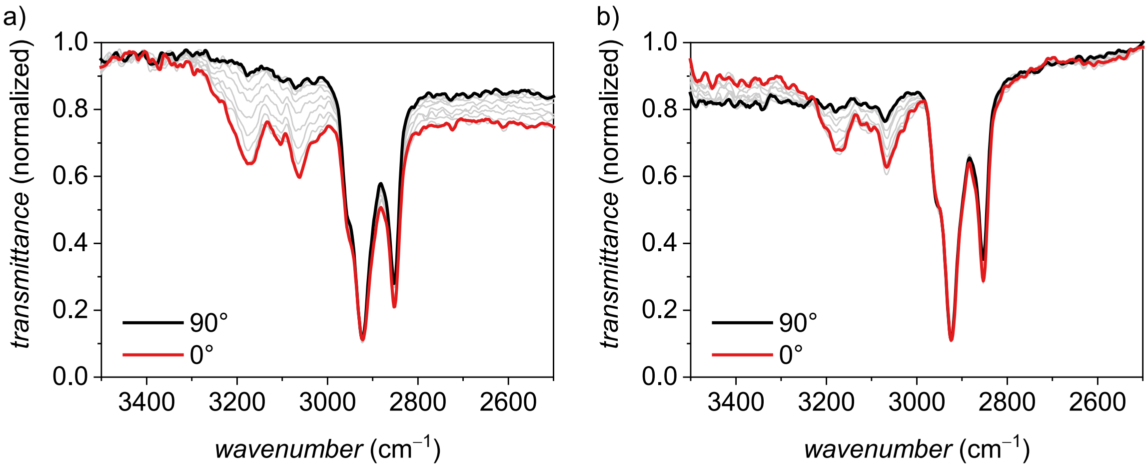

Figure A34. Polarized FT-IR spectra with different polarization angles of an aligned sample of a) **PBI 1T** and b) **PBI 3T**. The sample was sheared using an extruded fiber for friction transfer on a KBr substrate. The black and red line show the spectra for the polarizer orientated perpendicular and parallel to the shearing direction, respectively.

FT-IR experiments were performed with samples prepared by friction transfer of extruded fibers on KBr substrates. The polarized measurements reveal that the NH stretching vibration at around 3190 cm^{-1} corresponding to the hydrogen-bonded imide units reaches a maximum when measuring parallel to the shearing direction (red) and a minimum when measuring perpendicular to the shearing direction (black). This indicates that the PBIs are oriented with their long axis along the shearing direction and therefore along the columnar long axes.

Polarized FT-IR measurements of **PBI 2T** were reported previously.[111]

Density Measurements and Calculation of the Number of Molecules

Density measurements were carried out by the buoyancy method at 23 °C in mixtures of deionized water and aqueous sodium chloride solution (20 wt%). Sodium chloride (*pro analysi*) was dried under reduced pressure (1×10^{-3} mbar). The solvents were degassed by ultra-sonication prior to the measurement. The samples were prepared by heating the material to 240 °C under reduced pressure and extrusion in order to minimize the inclusion of air bubbles. The fibers were cut into several pieces of varying size (0.1–0.6 mg). The samples were put in a sealed vial containing deionized water at 23 °C and aqueous sodium chloride (20 wt%) solution was added in small portions and the mixture was allowed to equilibrate between additions until the sample started floating in the center of the vial. The necessary weight percentage of sodium chloride was determined and the density was calculated according to literature.[122] The density of **PBI 1T** at 23 °C was determined to be $\rho = 1.034 \pm 0.006$ g cm^{-3}. For **PBI 3T** at 23 °C, a density of $\rho = 1.072 \pm 0.005$ g cm^{-3} was determined. Please note that for materials with much lower clearing temperatures and high thermal stability in the isotropic liquid, the samples can be prepared by melting them under reduced pressure to eliminate the inclusion of air bubbles.[123] However, as **PBI 1T** and **PBI 3T** start to decompose at very high temperatures, the probability of air inclusion can only be limited but not eliminated. Therefore, this density value displays a lower limit.

The molecular volume V_{mol} was calculated using equation (2).

The temperature dependence of the molecular volume of a PBI with aliphatic substituents in imide position is reported in literature.[126] Calculating the temperature-dependent change in molecular volume of the aliphatic chains it becomes obvious that the change in molecular volume of the aromatic part is rather small. [60,111,124,125] Thus, for the estimation of V_{mol} at elevated temperatures the aromatic volume can be estimated as constant.

The values obtained for the change in molecular volume according to literature procedure are summarized in Table A10.[124-126]

Table A10. Summary of the values corresponding to the temperature-dependent density calculation for **PBI 1T** and **PBI 3T**.

	T (°C)	V_{ar} (Å^3)	V_{aliph} (Å^3)	V_{mol} (Å^3)	ρ (g cm^{-3})
PBI 1T	23	2160	3900	6060	1.03
	230	2160[a]	4770	6930	0.91
PBI 3T	23	2980	3900	6880	1.07
	150	2980[a]	4380	7360	1.00

[a] Assuming a negligible gradient for the expansion of V_{ar} as described above.

The number of molecules Z per columnar stratum was calculated using equation (1)[159]

The volume of the columnar stratum $V_{\mathrm{col-strat}}$ can be calculated according to equation (8) for a Col$_{\mathrm{h}}$ unit cell and according to equation (10) for a columnar oblique (Col$_{\mathrm{obl}}$) unit cell:

$$V_{\mathrm{col-strat,obl}} = a * b * h * \sin(\gamma) \tag{10}$$

Thereby, a and b are the unit cell parameters and h is the height of the columnar stratum, which can be chosen arbitrarily. Since the axial translational subunit is a PBI with the length of 14.3 Å, this has been naturally chosen as stratum height. Using the parameters obtained from X-ray experiments and the density extrapolated to temperatures at which the diffractograms were recorded, the number of molecules per columnar stratum was calculated to be 8.1 ± 0.3 molecules for the Col$_{\mathrm{obl}}$ phase of **PBI 1T** and 7.0 ± 0.4 molecules for the Col$_{\mathrm{h}}$ phase of **PBI 3T** (assuming an error of 0.5 Å for a, b and h and 3° for γ in the determination of the cell parameters). Considering that the experimentally determined density is a lower limit it is reasonable to assume four molecules per columnar stratum for **PBI 1T** as each Col$_{\mathrm{obl}}$ unit cell hosts two columns. This leads to the formation of a quadruple-stranded helix. Therefore, for **PBI 3T** it is reasonable to assume seven molecules per columnar stratum in the hexagonal phase leading to the formation of a septuple-stranded helix.

These values were verified by calculating the correlation length ξ in the LC state according to the Scherrer equation (9).[160]

By this method, we calculated the correlation length for the π-stacked PBIs perpendicular to the columnar direction. $\Delta(2\theta)$ and θ were determined by fitting the signal on the equator belonging to the π–π stacking distance. The number of correlated molecules N was then calculated by dividing the correlation length by the π-distance.

For **PBI 1T** a correlation length of 14.41 Å was determined correlating to 14.41 Å/3.9 Å = 3.7 molecules. For **PBI 3T** a correlation length of 25.48 Å correlating to 25.48 Å/3.9 Å = 6.5 molecules was determined. The obtained values are in good agreement with the above estimated numbers of molecules per columnar stratum.

Integration of the WAXS Patterns Along the Meridian

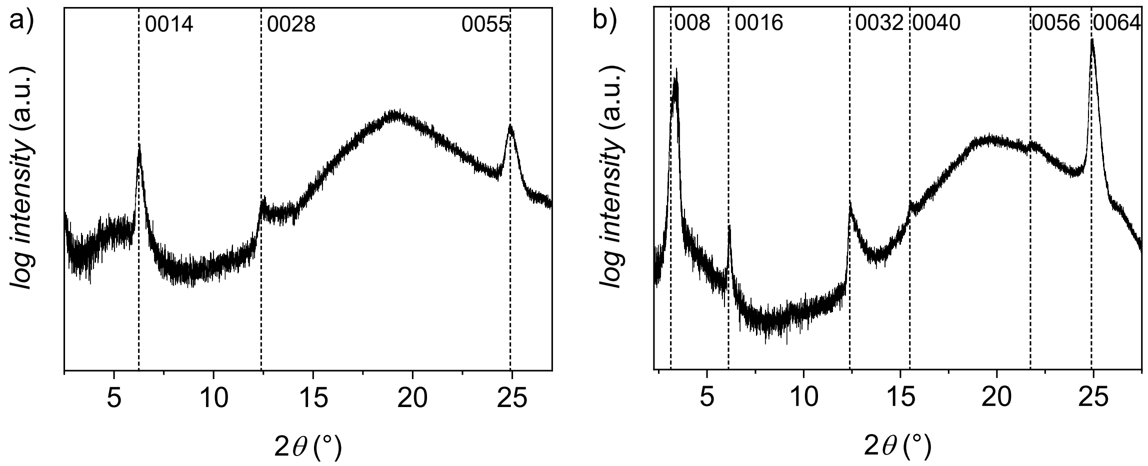

Figure A35. Integrated intensity along the meridian of the WAXS patterns of a) **PBI 1T** at 230 °C and b) **PBI 3T** at 150 °C. Dashed lines indicate the position of the meridional signals on the layerlines.

Molecular Modelling of the Helical Arrangement of PBI 1T

The model of self-assembled **PBI 1T** is based on π-stacked tetramers. These tetrameric units were built by co-facial stacking of the molecules at a π–π distance of 3.9 Å with a longitudinal and rotational displacement of 7.15 Å and 12.85°, respectively (Figure A36a and b). 14 Tetramers were then arranged along the long axis of the PBIs in a distance of 14.3 Å with a rotation of 25.7° per unit to form one helical column (four-stranded 14_1 helix) consisting of 56 molecules (Figure A36c). Two of these assembled structures were placed at ¼, ¼ and ¾, ¾ positions in the *a*,*b*-plane of a P1 unit cell (a = 75.6 Å, b = 51.8 Å, c = 200.2 Å, γ = 86.4°). The helical structure together with the oblique packing in the *a*,*b*-plane renders this to a liquid crystal with 3D positional order, which can be described as a monoclinic centered structure explaining the indexation in Figure 23c. The projection in 2D, however, is a planar oblique unit cell with two columns, thus deviating from the conventional hexagonal or rectangular structures. Therefore, we describe this phase as $\mathrm{Col_{ob}}$ phase. We performed geometry optimization using the forcefield COMPASS II applying the Ewald summation method until the non-bonding energy was strongly negative.

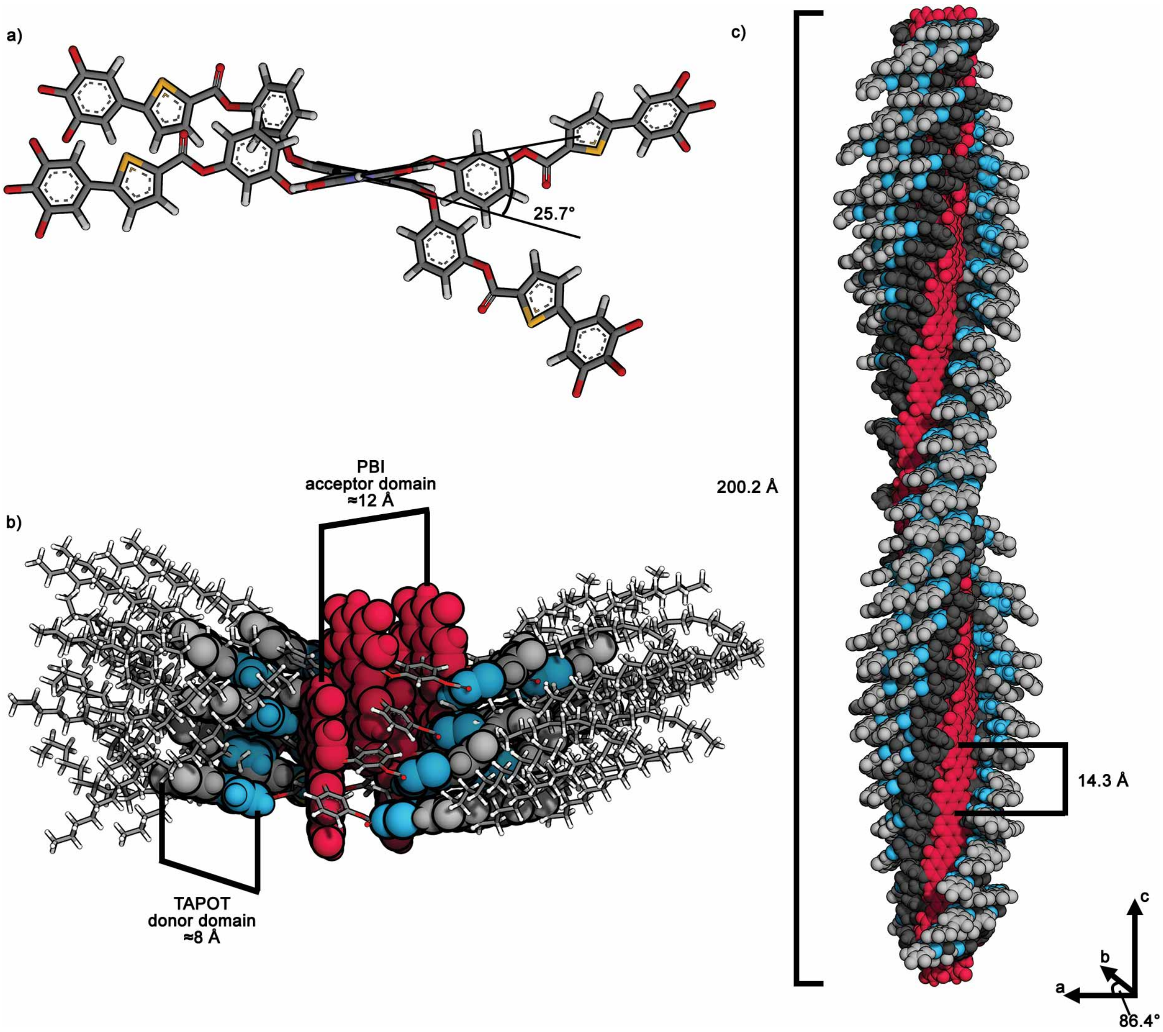

Figure A36. a) Monomeric molecule of **PBI 1T** viewed along the PBI’s *N*,*N*′-axis. The dodecyl chains were omitted for clarity. b) Tetrameric unit in side view with indication of donor and acceptor domain size. c) Side view of the assembled helix. The PBIs are colored in red, phenoxy spacers in dark grey, thiophenes in blue and trialkoxyphenyl units in light grey. The dodecyl chains were omitted for clarity. The helicity in the shown columnar assembly has been chosen to be (*P*) for graphical representation. Please note that **PBI 1T** is racemic and therefore (*P*) and (*M*) helices may coexist in the LC phase.

Molecular Modelling of the Helical Arrangement of PBI 3T

The model of self-assembled **PBI 3T** is based on π-stacked heptamers. These heptameric units were built by co-facial stacking of the molecules in a π–π distance of 3.9 Å with a longitudinal and rotational displacement of 7.15 Å and 11.25 °, respectively (Figure A37a and b). 16 Heptamers were then arranged along the long axis of the PBIs in a distance of 14.3 Å with a rotation of 22.5° per unit to form one helical column (seven-stranded 16_1 helix) consisting of 112 molecules (Figure A37c). This structure was then placed in a P1 unit cell with hexagonal symmetry (a = 64.4 Å, c = 228.8 Å) and geometry optimized using the forcefield COMPASS II applying the Ewald summation method until the non-bonding energy was strongly negative.

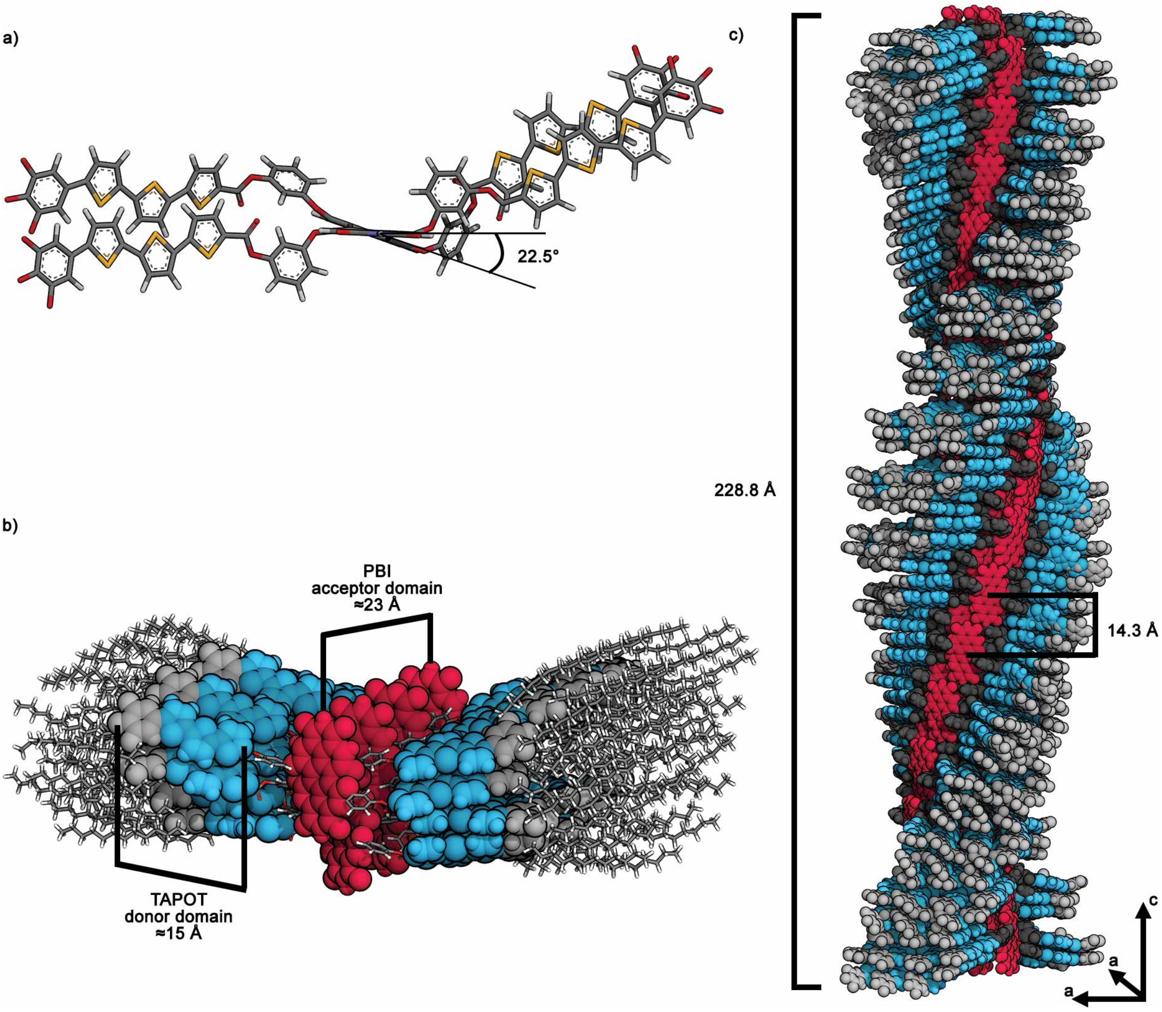

Figure A37. a) Monomeric molecule of **PBI 3T** viewed along the PBI's *N*,*N'*-axis. The dodecyl chains were omitted for clarity. b) Heptameric unit in side view with indication of donor and acceptor domain size. c) Side view of the assembled helix. The PBIs are colored in red, phenoxy spacers in dark grey, terthiophenes in blue and trialkoxyphenyl units in light grey. The dodecyl chains were omitted for clarity. The helicity in the shown columnar assembly has been chosen to be (*P*) for graphical representation. Please note that **PBI 3T** is racemic and therefore (*P*) and (*M*) helices may coexist in the LC phase.

Retrostructural Analysis

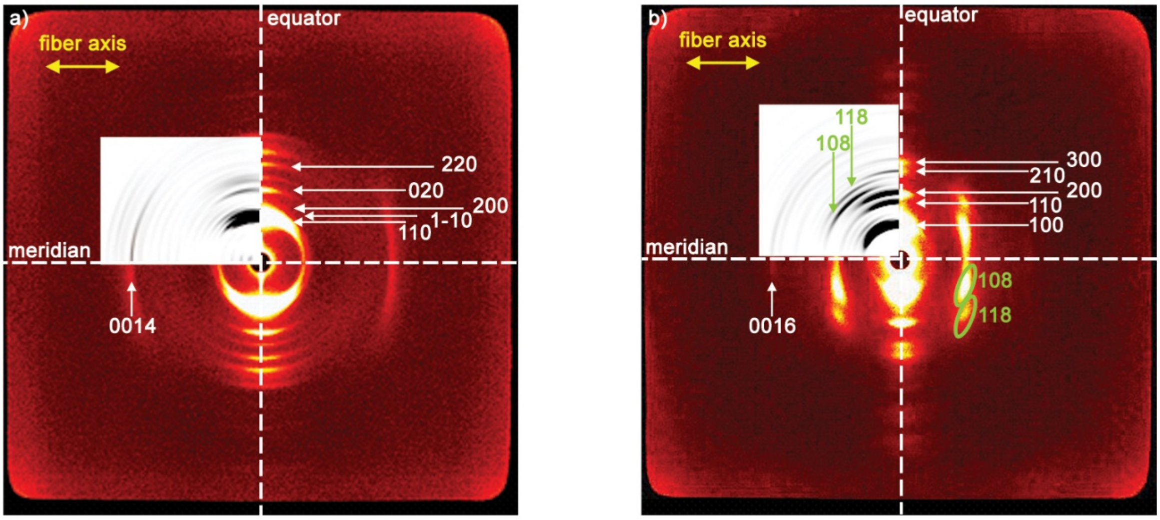

Figure A38. Superposition of the MAXS pattern of a) **PBI 1T** at 230 °C and b) **PBI 3T** at 150 °C and the simulated diffraction patterns calculated using CLEARER and the geometry optimized model generated with Materials Studio. The yellow arrows indicate the orientation of the fiber. The white and green arrows and circles indicate the assignment of the signals according to the respective a) Col$_{obl}$ and b) Col$_h$ phase.

The fiber diffraction patterns were simulated with the program CLEARER[134] using the modelled and geometry optimized structures obtained in Materials Studio.[130] The structures were exported as pdb-file and imported into the fiber diffraction simulation module of CLEARER. The fiber axis was set to (0,0,1). The fiber disorder paramters σ_ϕ and σ_θ were set to infinity and 0.5, respectively. The crystallite size and contrast were adjusted to best fit the experimental patterns. It has to be considered that CLEARER simulates the diffraction pattern based on a perfectly ordered domain. However, a real liquid crystal is not built with identical unit cells. Therefore, the intensity of the simulated signals can vary from the experimentally observed. Nevertheless, it is to note that the position and relative intensity of the signals are in rather good agreement with those observed experimentally.

Polarized Fluorescence Microscopy of Two-Contact Devices

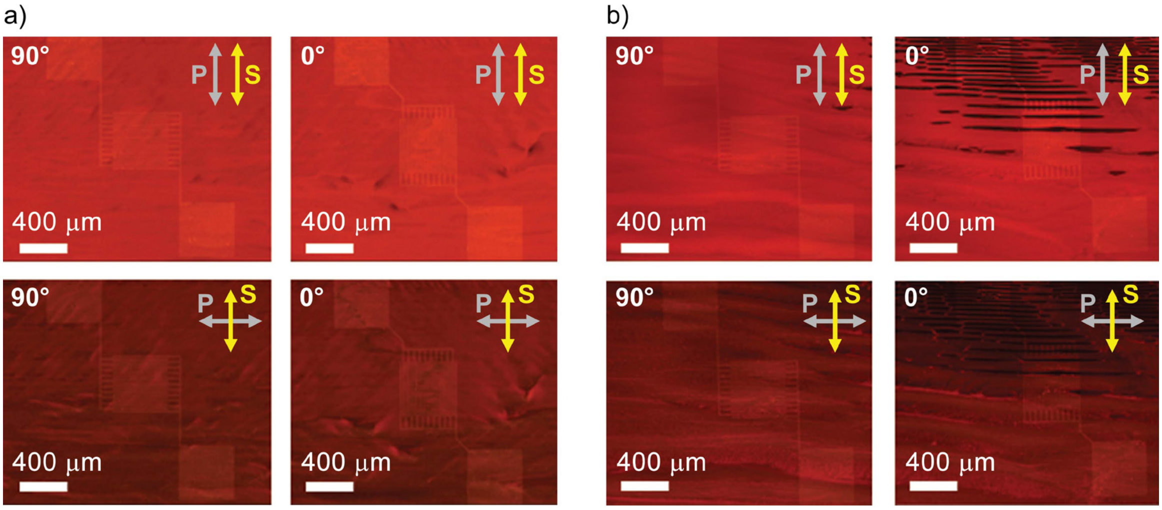

Figure A39. Polarizing fluorescence microscopy images of solution-sheared samples of a) **PBI 1T** and b) **PBI 3T** on bottom-contact substrates (λ_{ex} = 530 – 580 nm). Orientation of the polarized (P) of the excitation light and the shearing direction (S) indicated in grey and yellow arrows, respectively. The orientation of the electrodes is perpendicular (90°) and parallel (0°) to the shearing direction and therefore the columnar long axis.

Lamp Spectrum of White Light Source for Photoconductivity Measurements

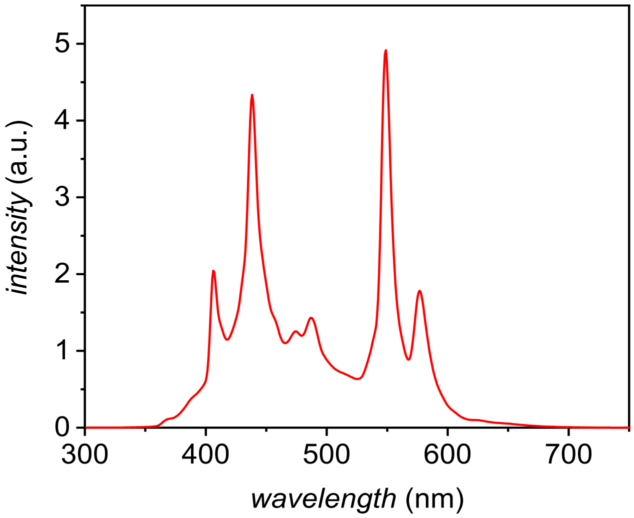

Figure A40. Emission profile of the Hg arc lamp used for photoconductivity measurements.

fsTAS of Liquid-Crystalline Samples

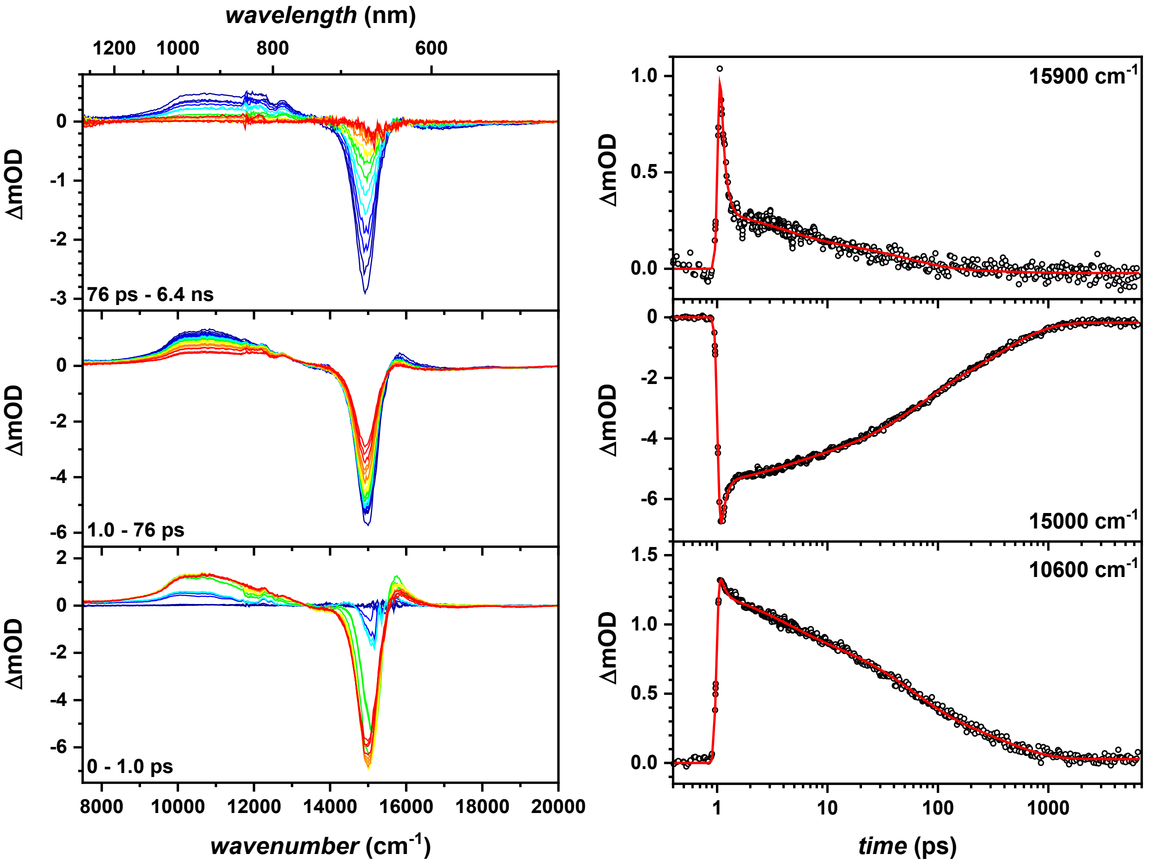

Figure A41. fs-Transient absorption data corrected for chirp and scattered light (excitation at 15400 cm^{-1}) of a **PBI 1T** film (left). Early spectra are in blue, later spectra in red. Time traces at selected wavenumbers for which the zero time delay was set arbitrarily with fit (right).

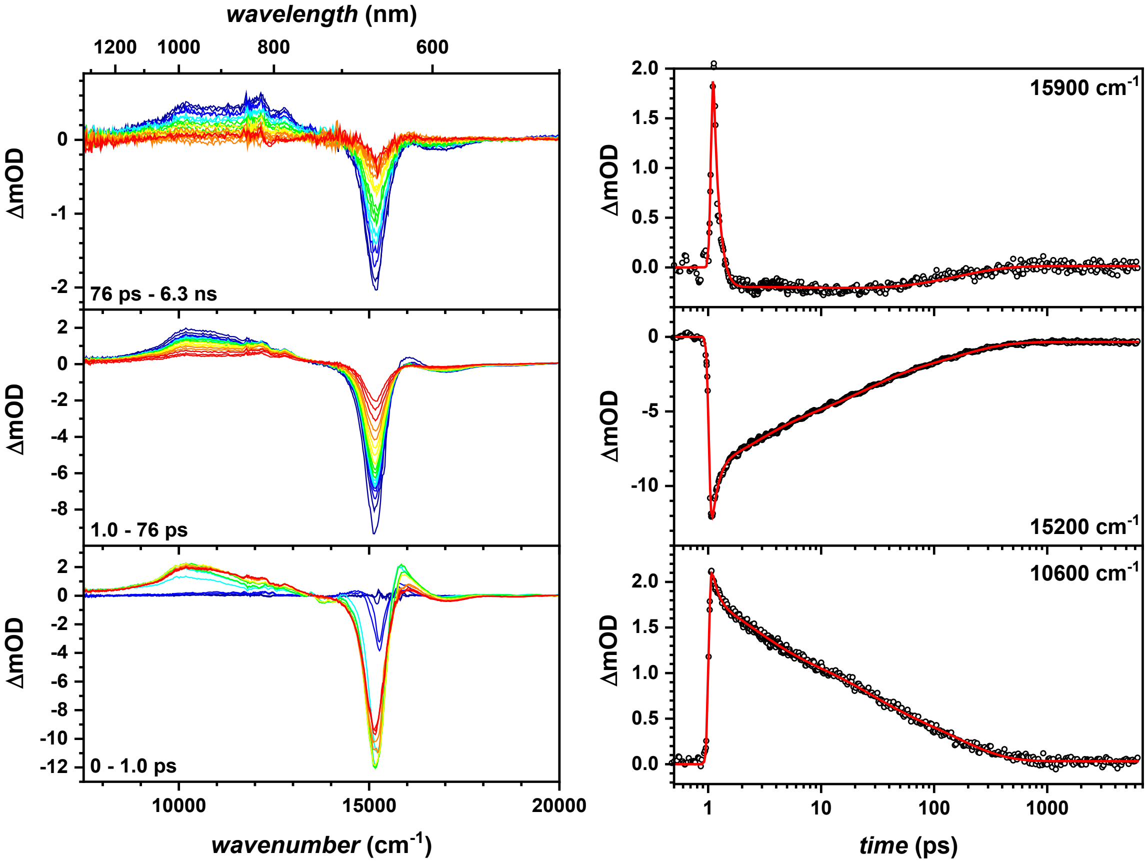

Figure A42. fs-Transient absorption data corrected for chirp and scattered light (excitation at 15400 cm^{-1}) of a **PBI 2T** film (left). Early spectra are in blue, later spectra in red. Time traces at selected wavenumbers for which the zero time delay was set arbitrarily with fit (right).

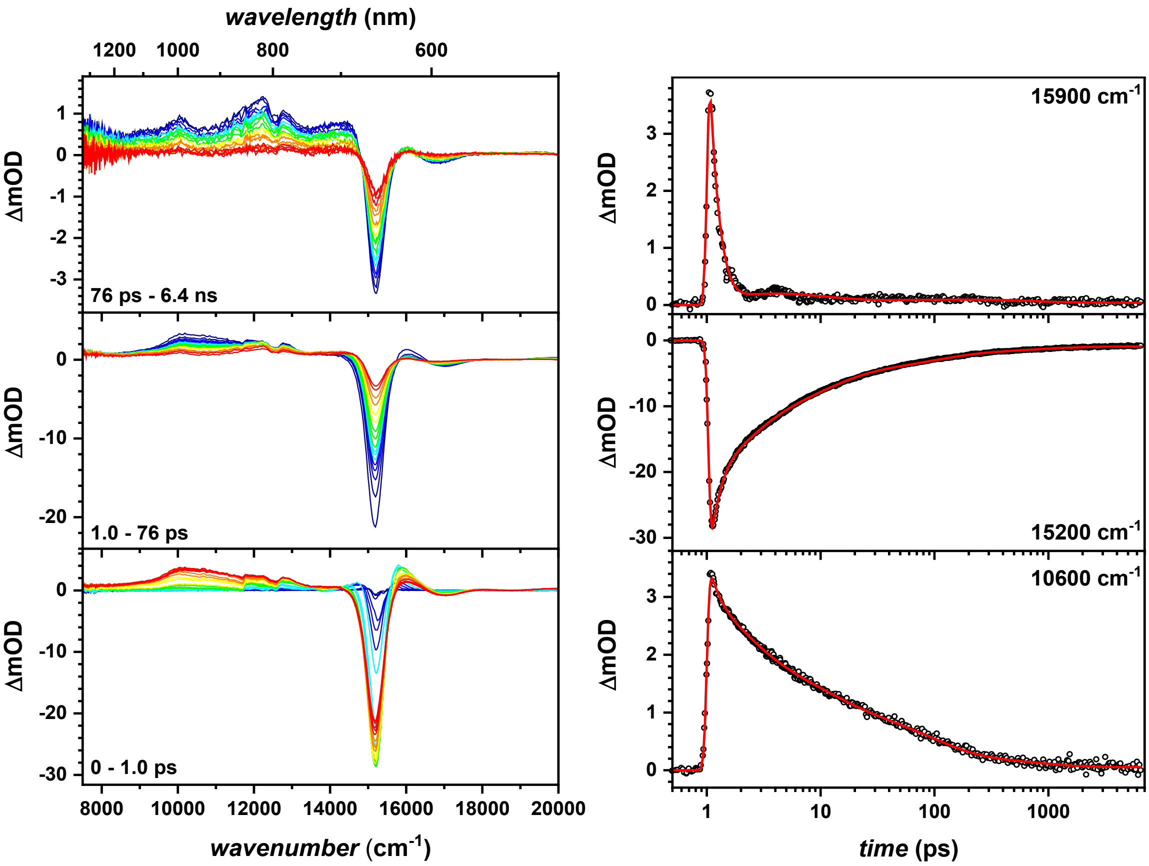

Figure A43. fs-Transient absorption data corrected for chirp and scattered light (excitation at 15400 cm^{-1}) of a **PBI 3T** film (left). Early spectra are in blue, later spectra in red. Time traces at selected wavenumbers for which the zero time delay was set arbitrarily with fit (right).

NMR spectra

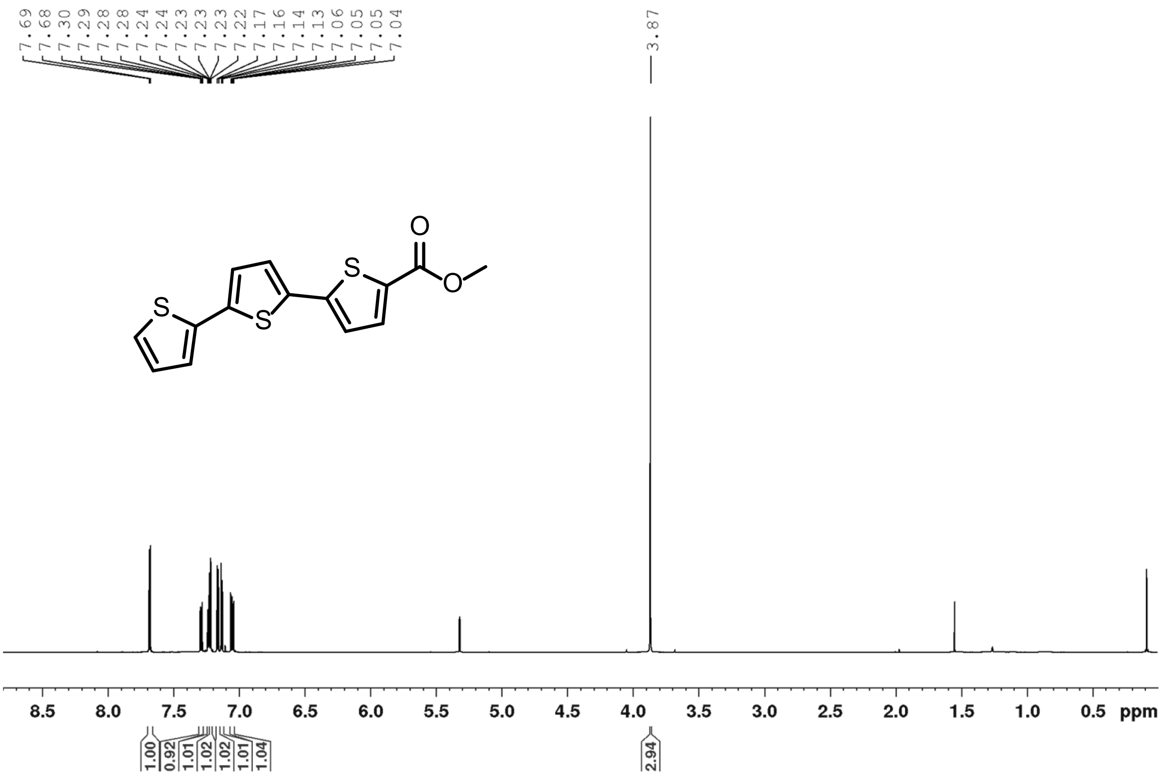

Figure A44. ^{1}H NMR (CD_2Cl_2, 400 MHz, 295 K) of compound **13**.

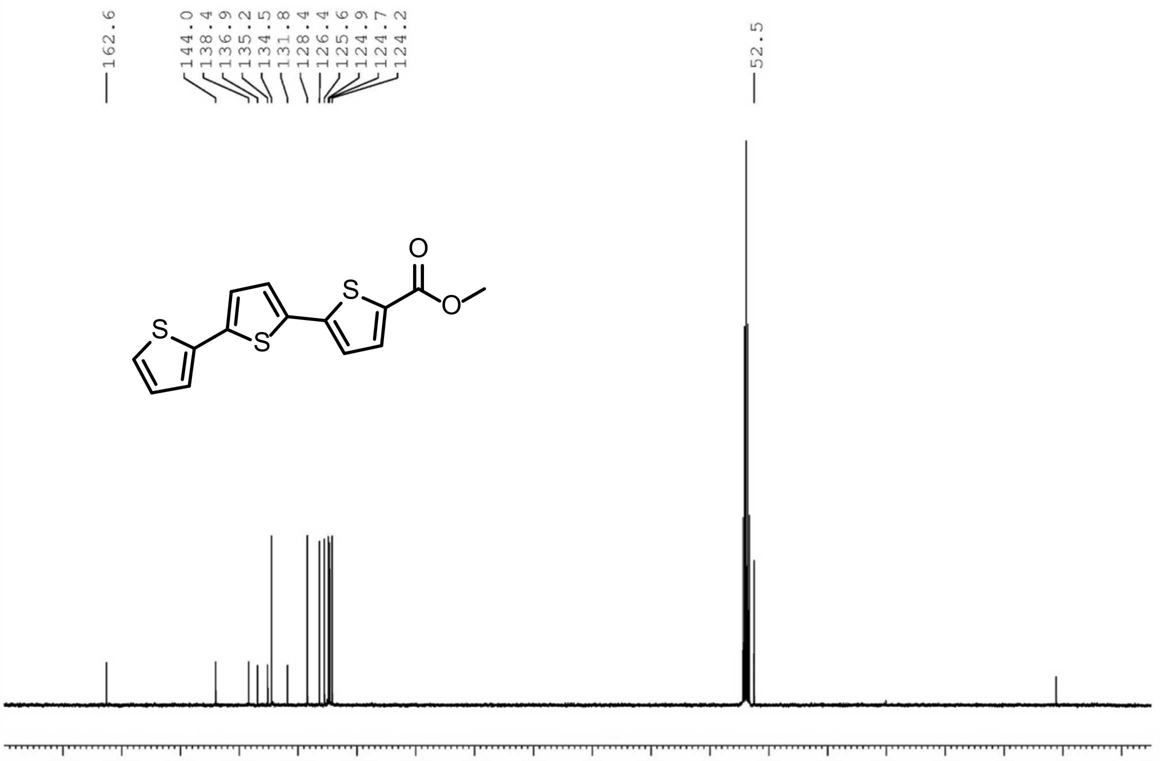

Figure A45. ^{13}C NMR (CD_2Cl_2, 100 MHz, 295 K) of compound **13**.

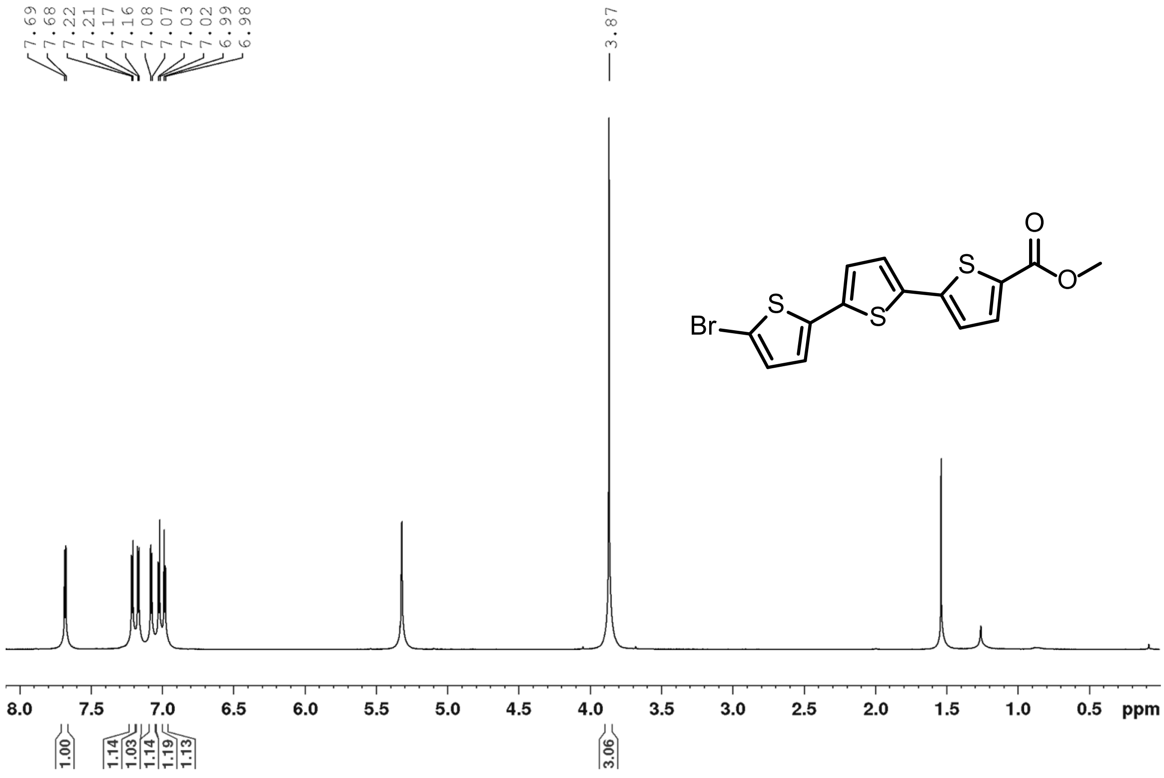

Figure A46. ^{1}H NMR (CD_2Cl_2, 400 MHz, 295 K) of compound **14**.

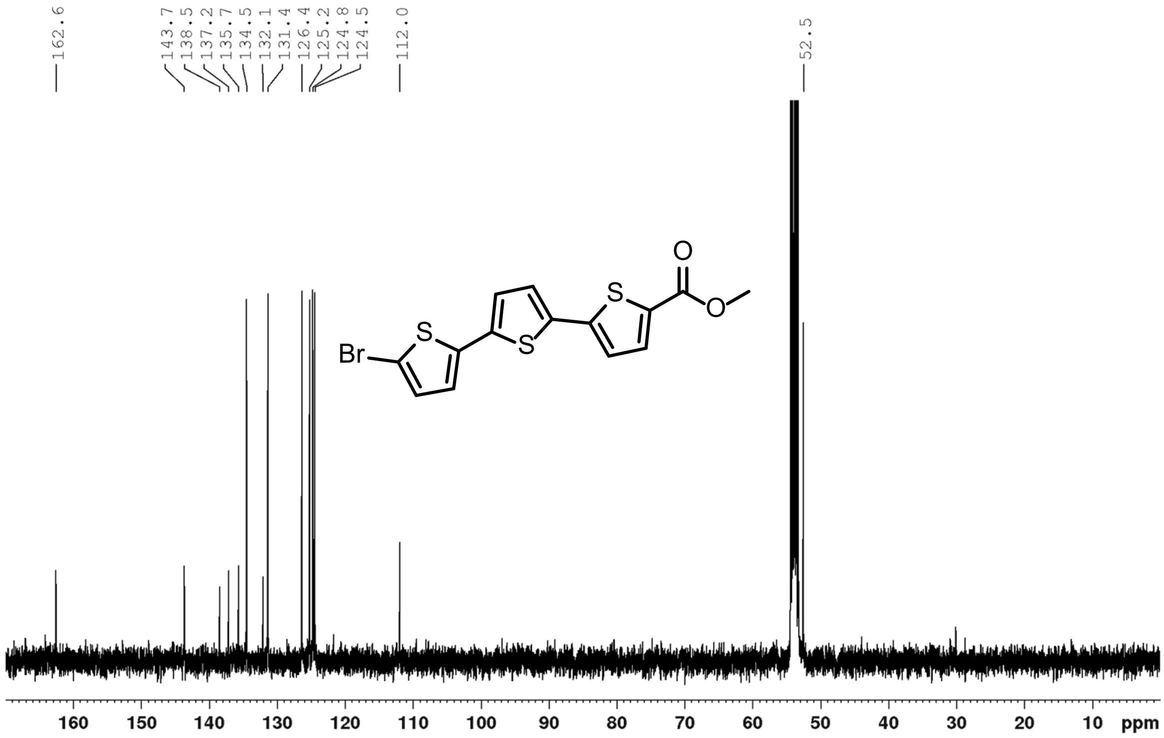

Figure A47. ^{13}C NMR (CD_2Cl_2, 100 MHz, 295 K) of compound **14**.

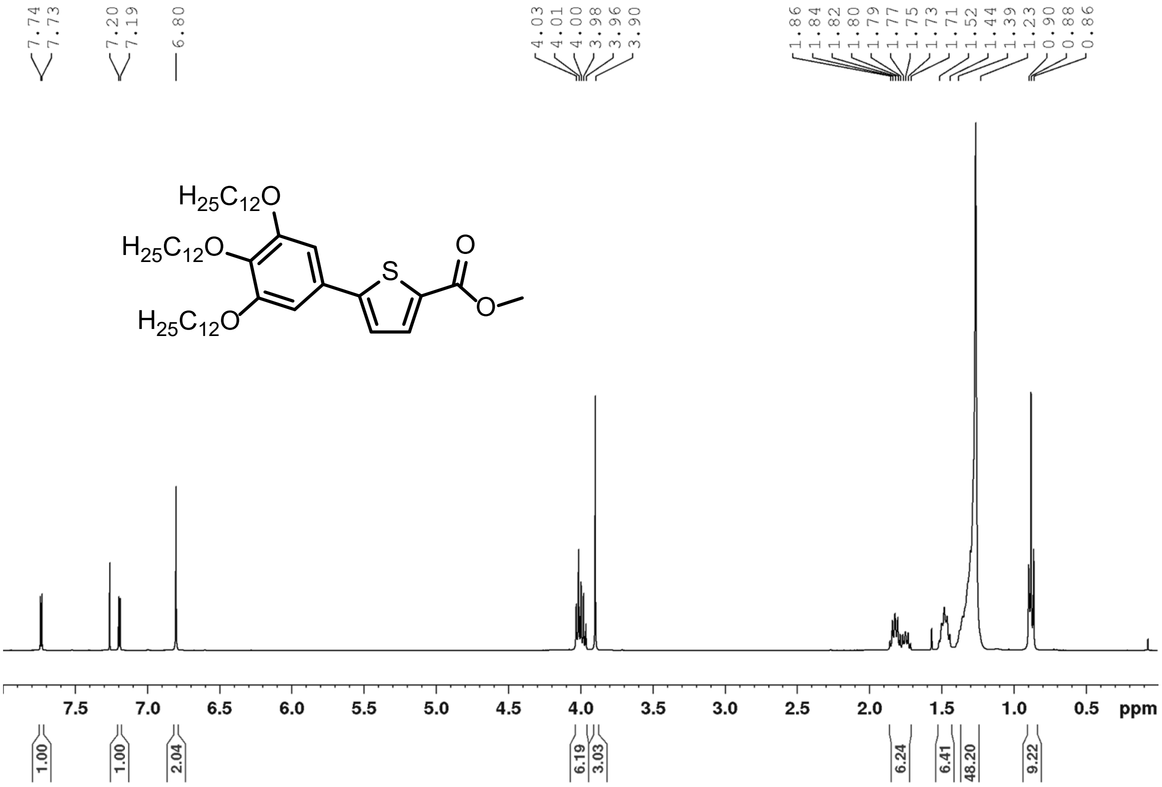

Figure A48. ^{1}H NMR ($CDCl_3$, 400 MHz, 295 K) of **1T**.

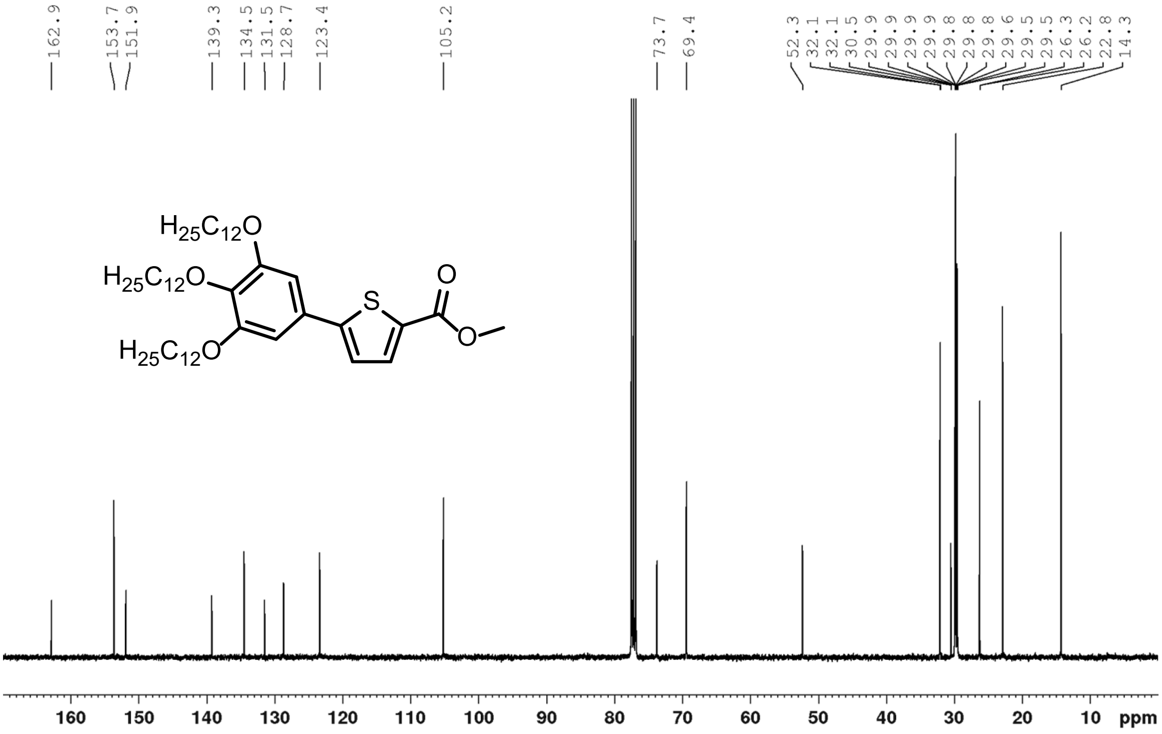

Figure A49. ^{13}C NMR ($CDCl_3$, 100 MHz, 295 K) of **1T**.

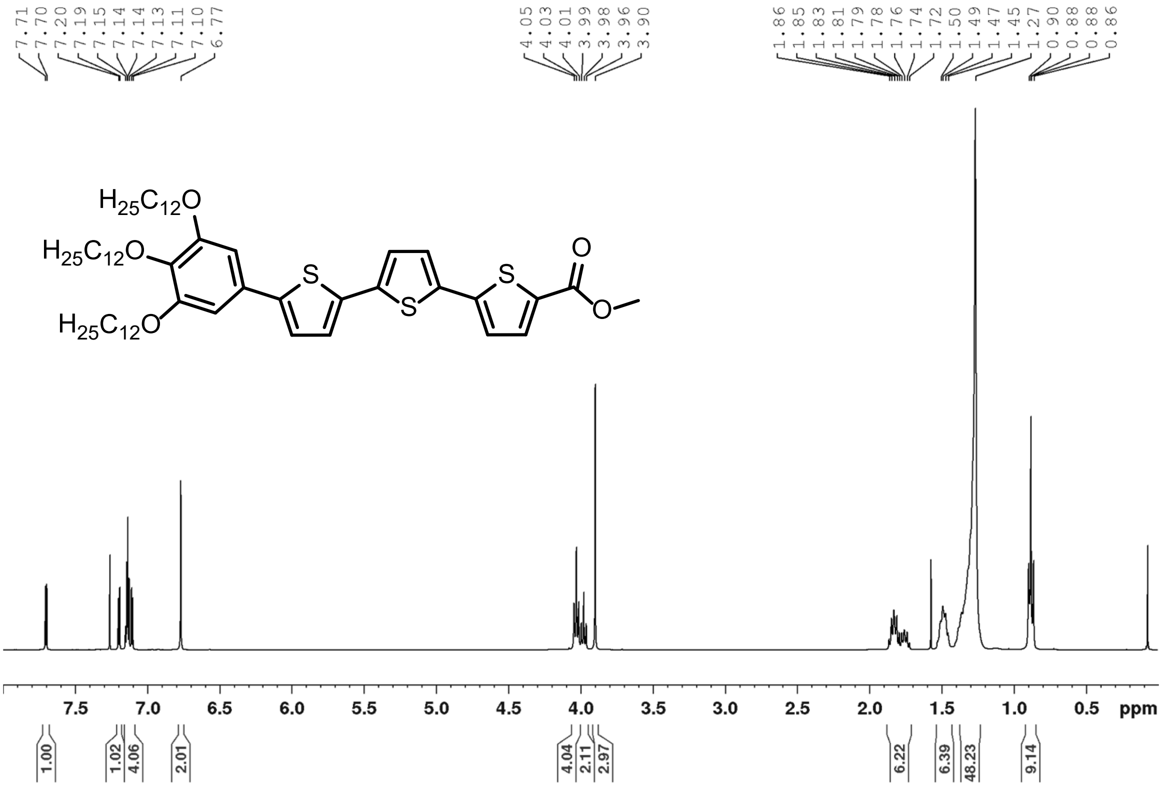

Figure A50. ^{1}H NMR ($CDCl_3$, 400 MHz, 295 K) of **3T**.

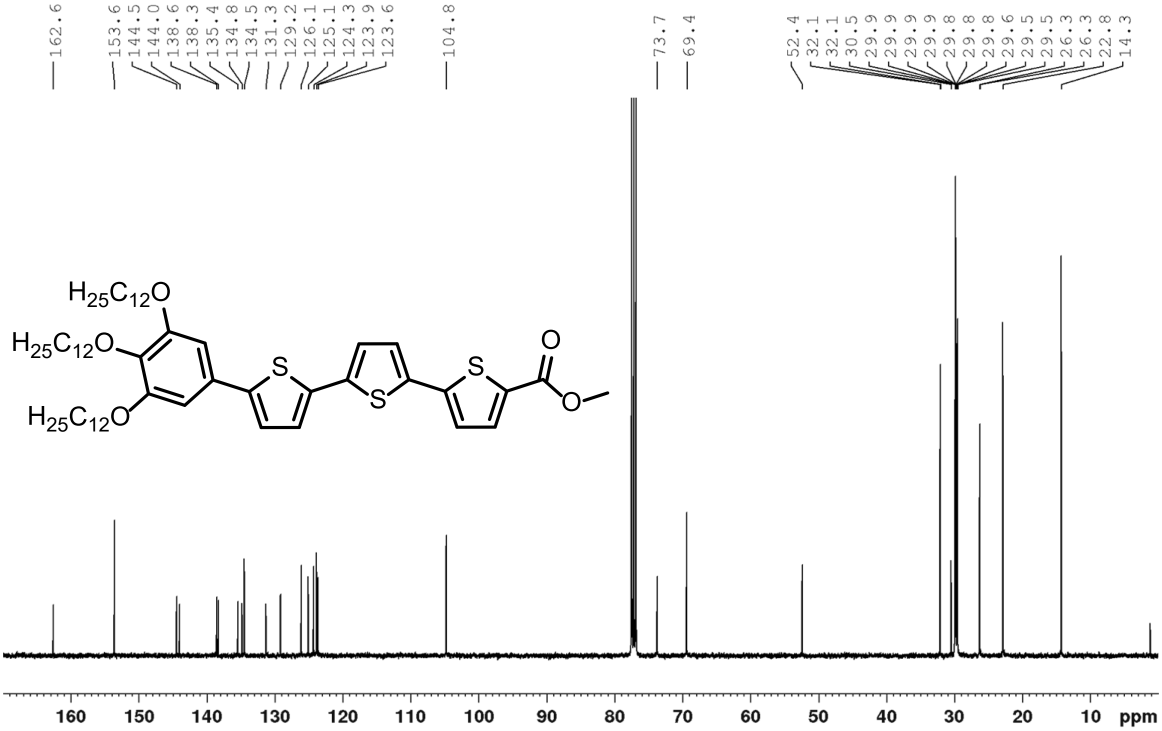

Figure A51. ^{13}C NMR ($CDCl_3$, 100 MHz, 295 K) of **3T**.

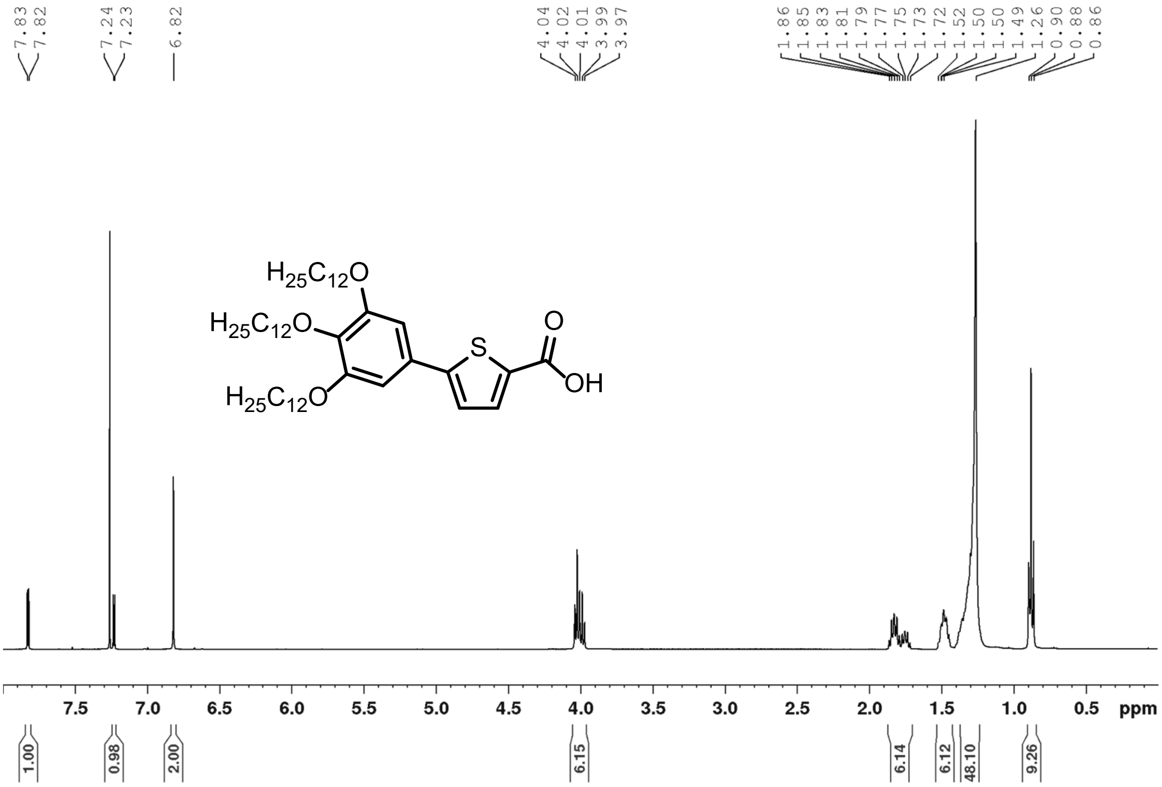

Figure A52. ^{1}H NMR ($CDCl_3$, 400 MHz, 295 K) of **15**.

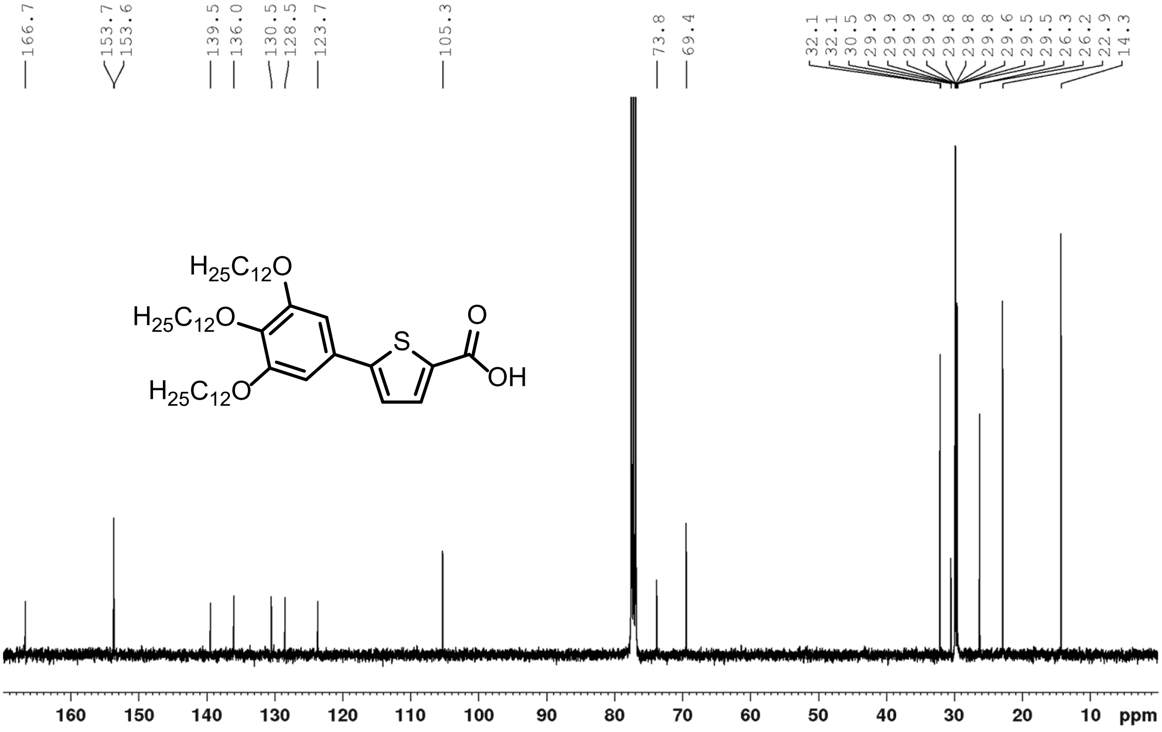

Figure A53. ^{13}C NMR ($CDCl_3$, 100 MHz, 295 K) of **15.**

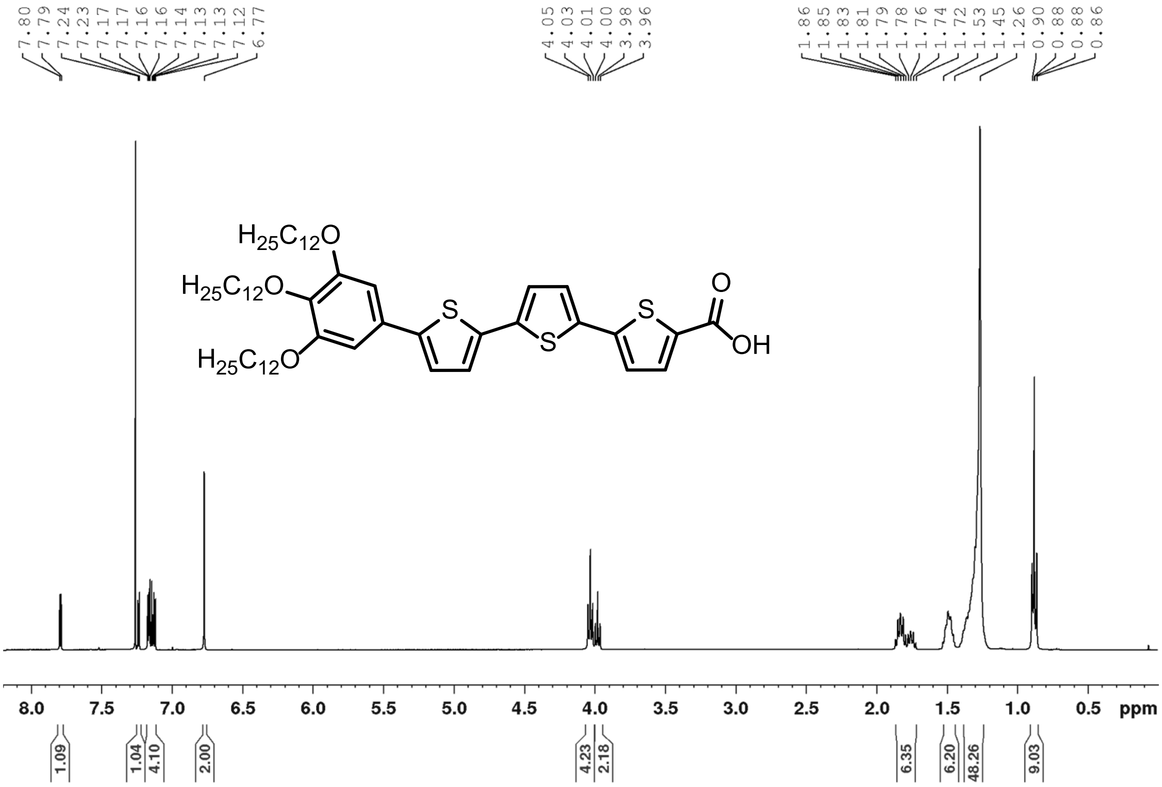

Figure A54. ^1H NMR ($CDCl_3$, 400 MHz, 295 K) of **16**.

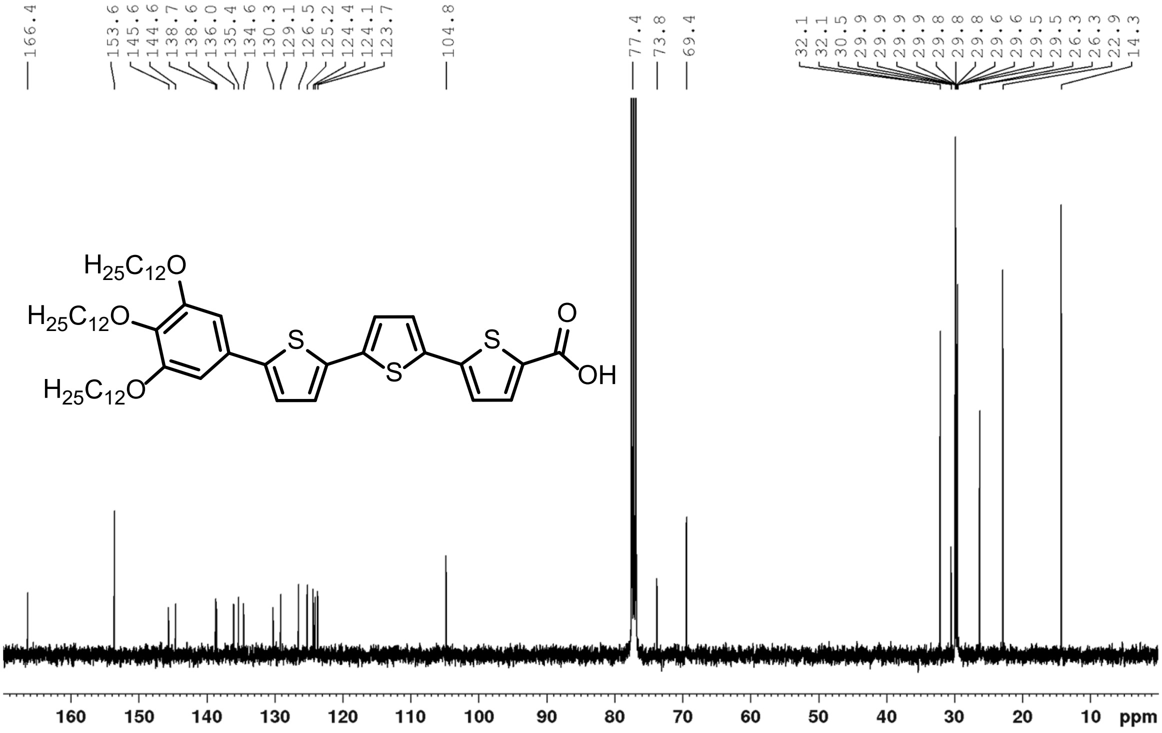

Figure A55. ^{13}C NMR ($CDCl_3$, 100 MHz, 295 K) of **16**.

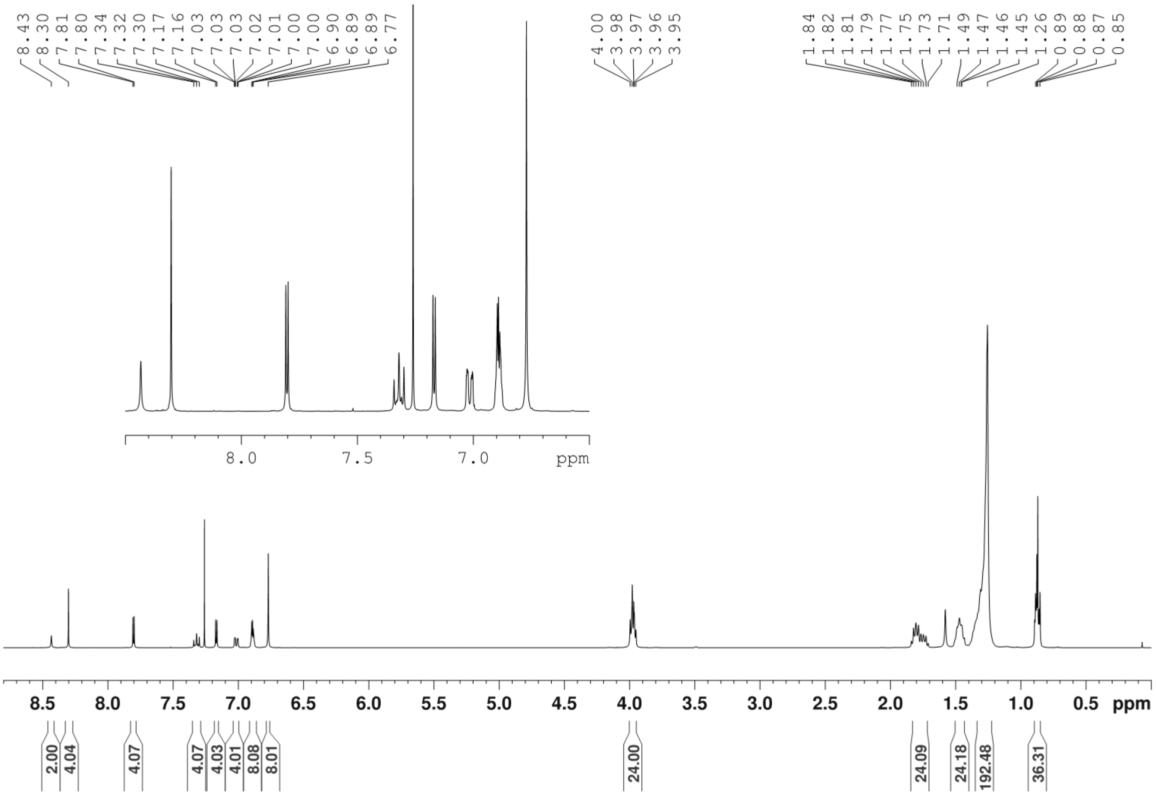

Figure A56. ^{1}H NMR ($CDCl_3$, 400 MHz, 295 K) of **PBI 1T**.

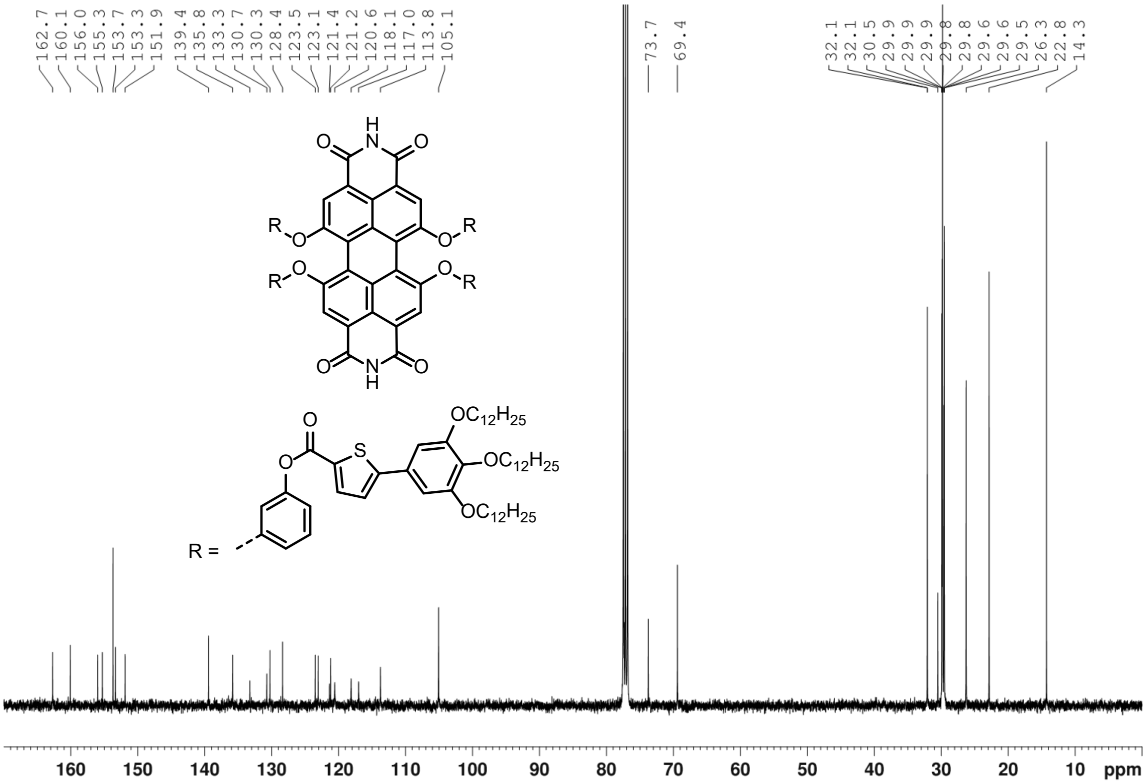

Figure A57. ^{13}C NMR ($CDCl_3$, 100 MHz, 295 K) of **PBI 1T**.

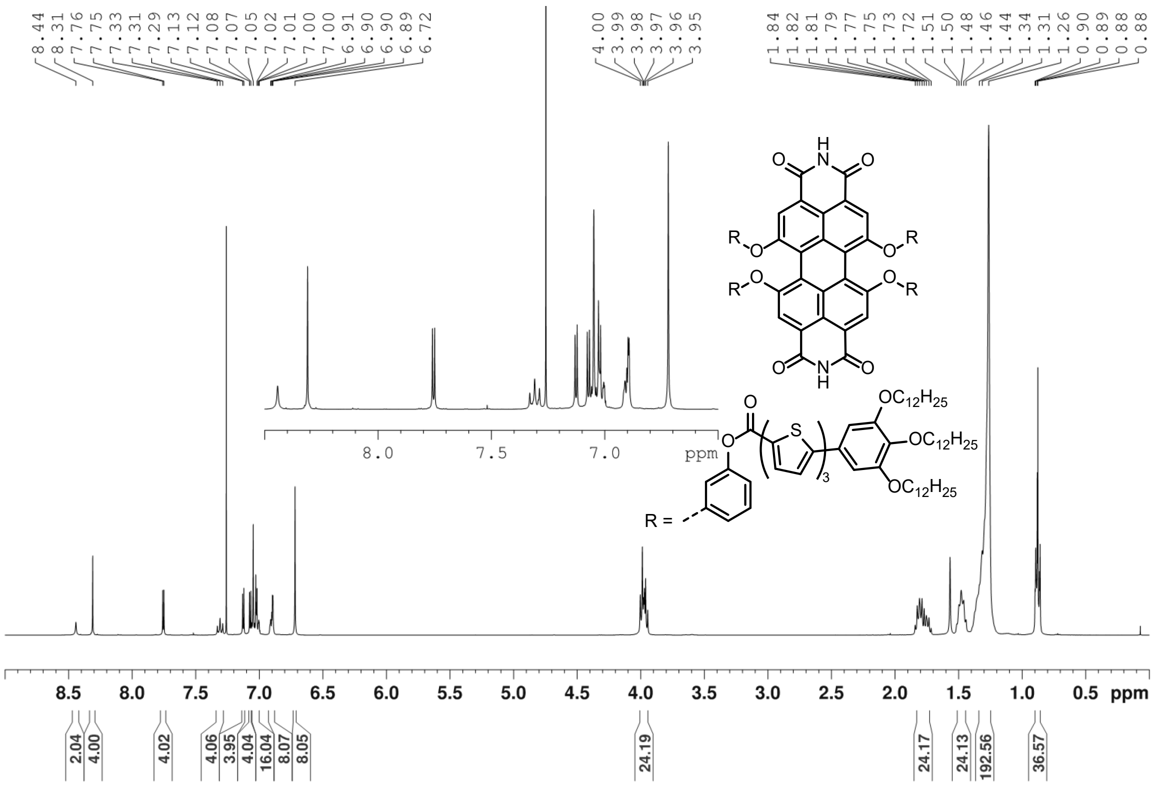

Figure A58. ^{1}H NMR ($CDCl_3$, 400 MHz, 295 K) of **PBI 3T**.

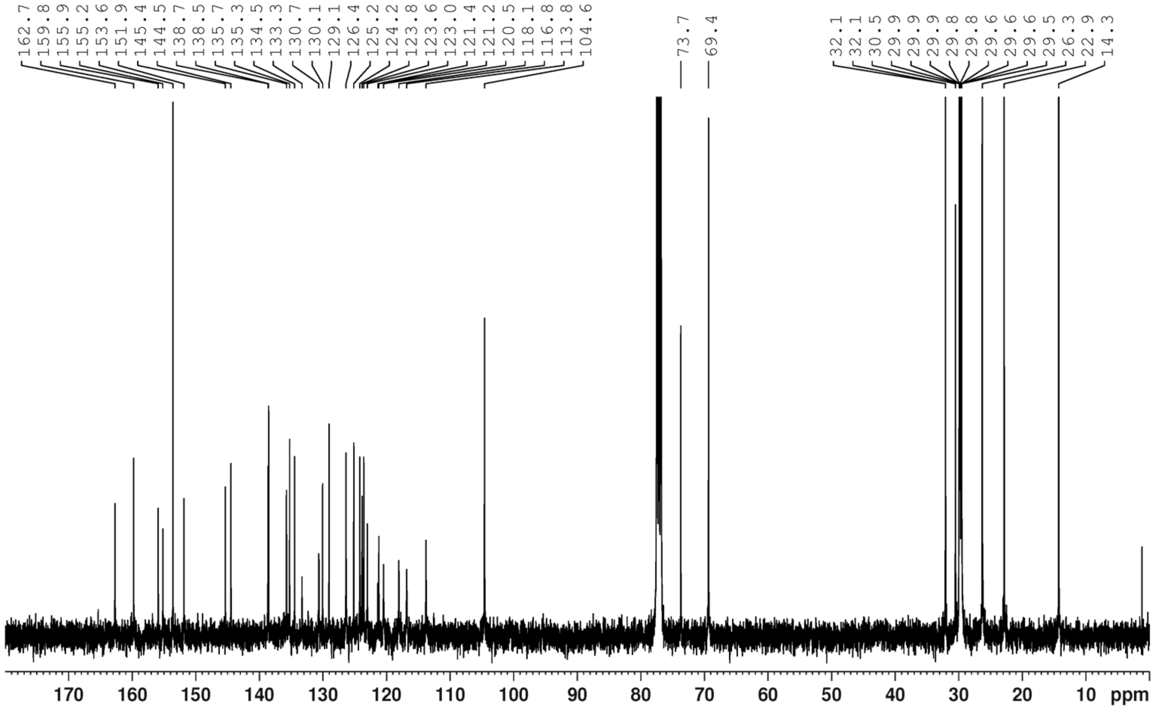

Figure A59. ^{13}C NMR ($CDCl_3$, 100 MHz, 295 K) of **PBI 3T**.

Chapter 5

–

Self-Sorting Supramolecular Polymerization: Helical and Lamellar Aggregates of Tetra-Bay-Acyloxy Perylene Bisimide

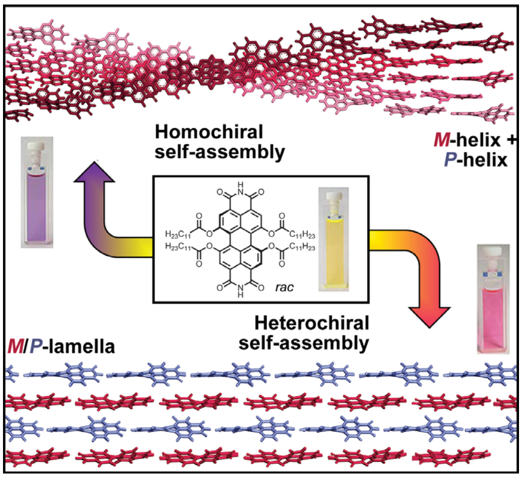

This chapter was published in: M. Hecht, P. Leowanawat, T. Gerlach, V. Stepanenko, M. Stolte, M. Lehmann, F. Würthner, *Angew. Chem. Int. Ed.* **2020**, *59*, 17084–17090.

Abstract: A new PBI, with a fluorescence quantum yield up to unity, self-assembles into two polymorphic supramolecular polymers. This PBI bears four solubilizing acyloxy substituents at bay positions and is unsubstituted at the imide position, thereby allowing H-bond-directed self-assembly in nonpolar solvents. The formation of the polymorphs is controlled by the cooling rate of hot monomer solutions. They show distinctive absorption profiles and morphologies and can be isolated in different polymorphic LC states. The interchromophoric arrangement causing the spectral features was elucidated, revealing the formation of columnar and lamellar phases, which are formed by either homo- or heterochiral self-assembly of the atropoenantiomeric PBIs. Kinetic studies reveal that a narcissistic self-sorting process upon fast cooling, and that the transformation into heterochiral (racemic) sheetlike self-assemblies proceeds by dissociation via the monomeric state.

5.1 Introduction

PBIs are amongst the most studied colorants in supramolecular chemistry due to their unmatched combination of favorable optical and redox properties.[35,43,81,199] Thus, they can afford fluorescence quantum yields close to unity[200] and can be reduced at moderate potentials to give radical anions of high stability.[201] Further, their high tendency to self-assemble via π–π interactions[58,202,203] in solution as well as the solid state allows to construct functional (nano-)materials with tailored properties and has led to the implementation of PBIs in field effect transistors,[9,13,101,204] solar cells[205] and photonic devices.[104,110,116] This is supported by the ease of modification of the monomeric PBI building block allowing the fine-tuning of inter- and intramolecular interactions as well as optical and redox properties.[105] Particularly, substitution in bay position with halogen-,[108,206] cyano-,[207] amino-,[208] methoxy,[65] or phenoxy-substituents[42,187] is widely used to adjust the chromophore's optoelectronic features. However, the substitution in bay positions further causes a distortion of the π-system due to repulsive interactions of substituents in close proximity resulting in a conformational chirality of these dyes.[42] Usually, the interconversion process between the *P*- and *M*-atropoenantiomers in solution is fast and separation of the two is only possible by using sufficiently large, e.g. bromo-substituents,[90] by fixation of the chirality with tethers connecting the 1,7- and / or 6,12-positions,[209,210] or by introduction of 2,2′-biphenol units in 1,12- or 6,7-position.[91] Therefore, in most cases an equilibrium between the two atropoenantiomers exists, which strongly influences the self-assembly pathway by either homo- or heterochiral contacts of the chromophores. [91] Homochiral self-assembly leads to the formation of 1D helical fibers of either *P*- or *M*-chirality. This could be demonstrated for a variety of PBIs which form helices in the self-assembled state in solution[58,59,91] or the columnar LC phase.[60,61,111] In contrast to that, heterochiral self-assembly yields 2D structures of alternating *P*- and *M*-atropoenantiomers as so far, however, only observed in single-crystals of tetra- and octachloro-substituted PBIs.[92,107]

In the current study we introduce **PBI-Ac**, a new well-soluble PBI derivative that exhibits more similar optical properties to the parent core-unsubstituted PBI compared to the widely applied tetraphenoxy-substituted PBIs. **PBI-Ac** is functionalized with four acyloxy groups in bay-position and bears free imides to direct H-bond directed self-assembly into supramolecular polymers (Figure 26a). Most interestingly, **PBI-Ac** is capable of forming both, homochiral 1D fibers and heterochiral 2D sheets, depending on the cooling rate applied to a hot solution of monomers in MCH (Figure 26b) as determined by scanning electron microscopy (SEM) and AFM. The two supramolecular polymorphs,[211,212] **Agg1** and **Agg2**, exhibit distinctive absorption properties originating in the unique interchromophoric arrangement, which they retain in the solid state. POM of the polymorphs revealed their LC behavior which enabled detailed studies of the supramolecular arrangement by a combination of WAXS as well as polarized UV/Vis and FT-IR spectroscopy. The pathway complexity[213-217] of the supramolecular polymerization[36,218,219] that distinguishes between the two polymorphs was investigated by UV/Vis spectroscopy.

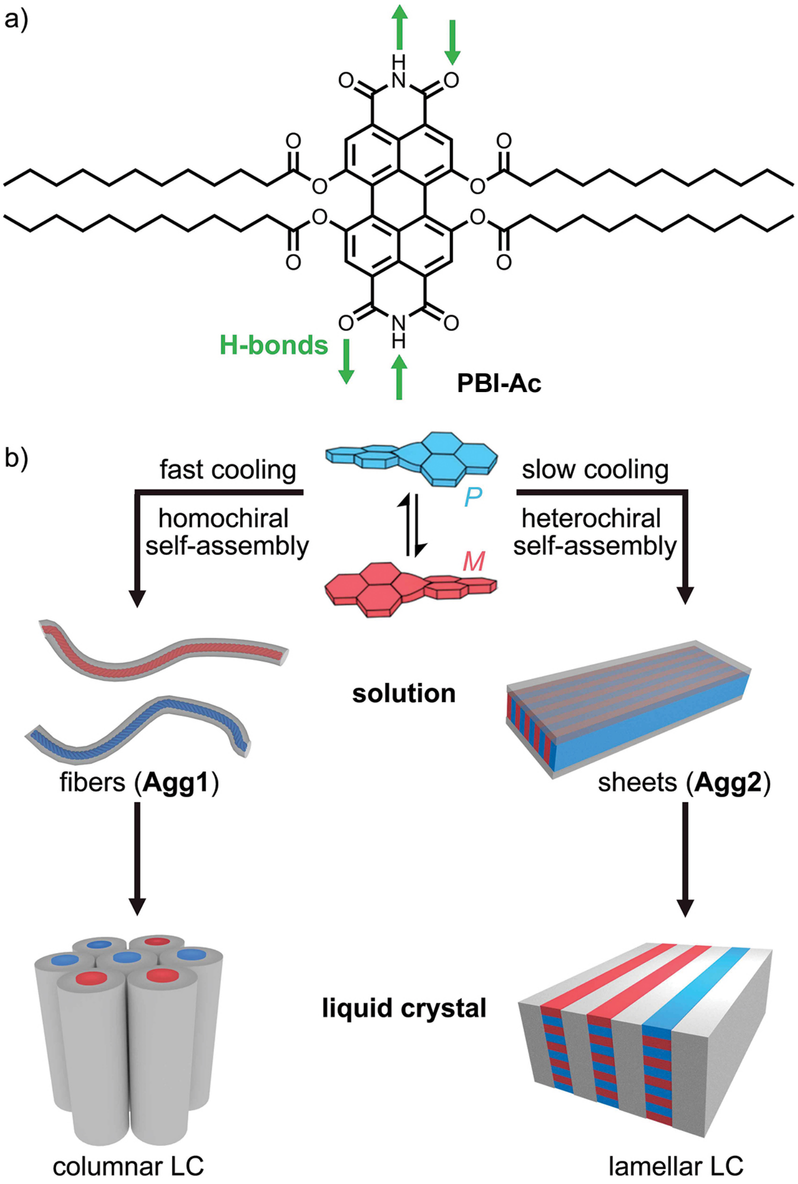

Figure 26. a) Chemical structure of **PBI-Ac**. b) Schematic illustration of the cooling-rate dependent homo- or heterochiral self-assembly into fibers or sheets, respectively, and their subsequent organization into columnar or lamellar liquid crystals.

5.2 Results and Discussion

5.2.1 Synthesis

The new **PBI-Ac** was synthesized in a two-step procedure starting from *N*,*N'*-bis(1-phenylethyl)-1,6,7,12-tetramethoxyperylene-3,4:9,10-tetracarboxylic acid bisimide **18** which was obtained according to a recently reported method towards tetramethoxylated PBIs (Scheme 1).[189] This compound was dealkylated and debenzylated using boronic tribromide in dichloromethane to afford **19**. This is followed by an esterification using dodecanoic acid under peptide coupling conditions using DCC and DPTS in a mixture of CH_2Cl_2 and DMF to obtain **PBI-Ac** in a yield of 38%.

Scheme 1. Synthesis of **PBI-Ac** bearing four acyloxy-functionalities in 1,6,7,12-position.

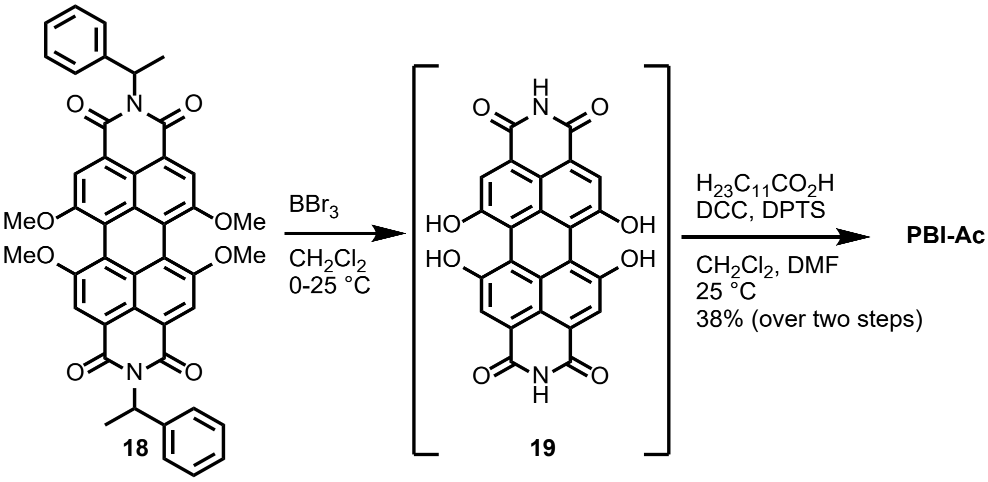

5.2.2 Optical Properties of the Monomeric Dye

The yellow colored solution of monomeric **PBI-Ac** in dichloromethane exhibits its absorption maximum at 512 nm (43000 cm^{-1}M^{-1}), the first vibronic progression at 479 nm (30000 cm^{-1}M^{-1}) and the S_0-S_2 transition at 398 nm (7500 cm^{-1}M^{-1}) (Figure 27a). In comparison to other common PBIs, i.e. PBI **20** (λ_{max} = 527 nm), PBI **17** (λ_{max} = 576 nm) and PBI **21** (λ_{max} = 610 nm) (Figure 27b), **PBI-Ac** absorbs at lower wavelength, i.e. even 15 nm hypsochromically compared to the parent PBI **20**. This blue-shift can be explained by the electron withdrawing effect (–I-effect) and the negligible mesomeric effect (+M-effect) of the acyloxy bay-substituents compared to the +M-effect provided by phenoxy and methoxy in PBI **17** and PBI **21**. Similar to PBI **17** and PBI **21**, **PBI-Ac** shows a broadened lineshape and a less pronounced vibronic fine structure. These features are characteristic for bay-substituted PBIs and are attributed to the core-twist induced by the steric congestion in the PBI bay-area (see Figure A60).[65,220]

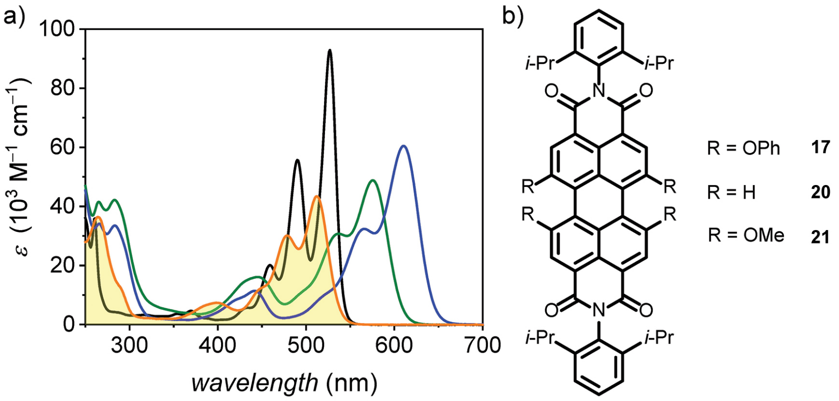

Figure 27. a) UV/Vis absorption spectra of **PBI-Ac** (orange line), **20** (black line), **17** (green line) and **21** (blue line) with $c \approx 10^{-5}$ M in CH_2Cl_2. b) Chemical structures of the reference compounds **17**, **20** and **21**.

The emission properties of **PBI-Ac** were determined in chloroform where the dye exhibits its emission maximum at 544 nm, corresponding to a small Stokes shift of 1100 cm^{-1}. The fluorescence lifetime was determined to 4.8 ns which is in the expected range for monomeric PBIs (see Figure A61).[81] **PBI-Ac** exhibits a fluorescence quantum yield of $\Phi_{\mathrm{Fl}} = 1.0$ similar to PBI **20** and PBI **17**, while substitution by methoxy groups leads to a quenching of the fluorescence to $\Phi_{\mathrm{Fl}} = 0.68$.[189]

5.2.3 Supramolecular Polymorphism

In chlorinated and aromatic solvents like dichloromethane, chloroform, tetrachloromethane or toluene that solubilize **PBI-Ac** well, the dye retains its monomeric state even at higher concentrations (see Figure A62). In contrast, when dissolving **PBI-Ac** in non-polar aliphatic solvents like MCH (c_0 = 40 µM) in which H-bonds and π–π interactions can thrive,[202] the dye self-assembles into two different aggregates (**Agg1** and **Agg2**) depending on the cooling rate applied to a hot solution of monomers (Figure 28c, for FT-IR analyses, see Figure A63). Rapid cooling (10 K/min) leads to the formation of **Agg1**, while slow cooling (0.6 K/min) leads to the formation of **Agg2**. The polymorphs differ distinctively in their absorption profile and accordingly in color. **Agg1** shows a bathochromically shifted absorption maximum at λ_{max} = 600 nm that increases in extinction and exhibits a narrowing of the 0,0 vibronic band with a FWHM of 300 cm^{-1} compared to the monomer with 570 cm^{-1} (Figure 28a). These optical features are characteristic for PBI J-aggregates and have been observed in structurally related tetra-bay-phenoxy substituted PBIs.[58,60,61,72,181] In contrast, **Agg2** exhibits its main transition at 541 nm with a narrowed FWHM of

370 cm^{-1} compared to the monomer, a vibronic progression at 498 nm and a red-shifted weaker band at 588 nm (Figure 28b).

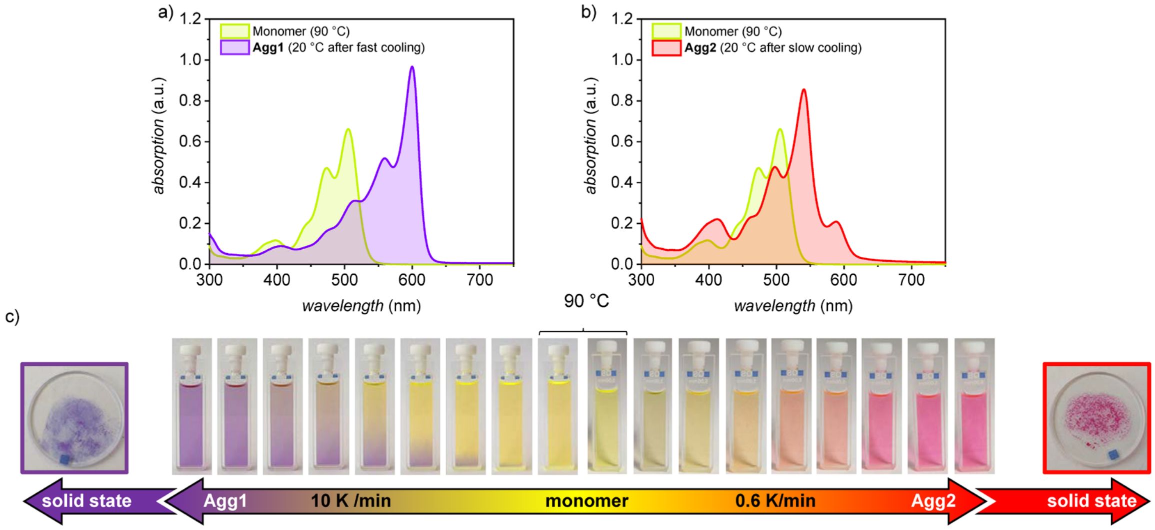

Figure 28. UV/Vis absorption spectra of a solution of monomers of **PBI-Ac** (green line) at 90°C and of the aggregates a) **Agg1** (purple line) and b) **Agg2** (red line) at c_0 = 40 µM in MCH at 20 °C. **Agg1** and **Agg2** self-assemble by cooling a 90 °C hot solution of **PBI-Ac** with c_0 = 40 µM in MCH with 10 K/min and 0.6 K/min, respectively. c) Series of photographs of a solution of **PBI-Ac** with c_0 = 40 µM in MCH applying a cooling rate of 10 K/min to produce **Agg1** (purple) or 0.6 K/min to produce **Agg2** (red) and photographs of the respective polymorphs isolated in the solid state.

At room temperature, **Agg1** transforms into a purple gel-like phase, while **Agg2** forms a red precipitate in MCH (Figure 29). Both polymorphs can be isolated in the solid state and retain their distinctive UV/Vis absorption properties (see Figure A65). The absorption maximum of **Agg1** in the solid state can be observed at 601 nm. The FWHM of the main absorption signal increases only slightly compared to **Agg1** in solution from 300 cm^{-1} to 350 cm^{-1}. The absorption maximum of **Agg2** can be observed at 538 nm and the FWHM also only slightly increases compared to the solution from 370 cm^{-1} to 470 cm^{-1}. This minor increase in FWHM indicates that both polymorphs retain a highly defined intermolecular order in the solid state enabling the elucidation of their structure by means of microscopy and scattering techniques.

5.2.4 Structural Elucidation

We could investigate the morphological properties of both polymorphs by SEM of samples (MCH, c_0 = 40 µM) drop-casted on silicon wafer. **Agg1** shows a network of entangled fibers on the scale of several micrometers. The height of the individual fibers could be determined as 3.1±0.2 nm by AFM (see Figure A66). In contrast, **Agg2** exhibits 2D sheet-like structures with a length of several micrometers and a width of up to 1 micrometer. The height of these sheets was determined as 1.7±0.2 nm by AFM (see Figure A67). These results are in accordance with the observation of a gel-like phase for **Agg1** and the precipitation of **Agg2**.

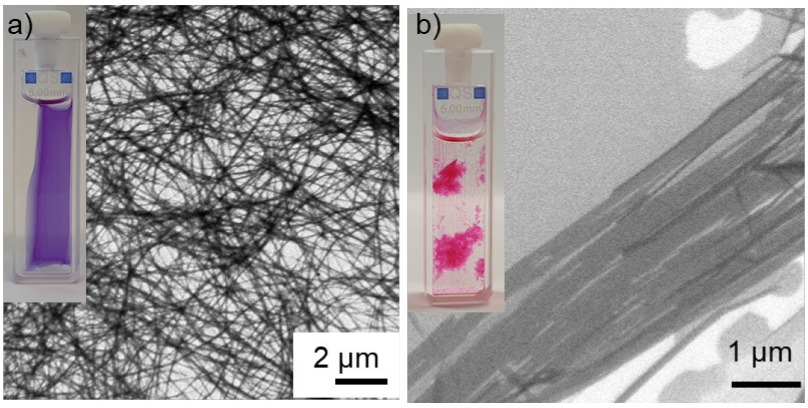

Figure 29. SEM images of samples of a) **Agg1** and b) **Agg2** drop-casted onto silicon wafer (c_0 = 40 µM, MCH). The insets show the corresponding gel-like phase and precipitate, respectively.

Both polymorphs show birefringence when investigated with POM. They can be aligned by mechanical shearing indicating the fluid nature of the material originating in the nanosegregation of the rigid π-core and the flexible alkyl chains (see Figure A68). Accordingly, we were able to investigate the supramolecular assemblies by WAXS experiments of aligned fibers to elucidate the respective intermolecular arrangement. Both polymorphs were prepared on a 10 mg scale applying the required cooling rates to hot solutions of **PBI-Ac** in MCH (c_0 = 40 µM), were isolated by centrifugation and dried under reduced pressure. The resulting LC materials were subsequently aligned by fiber extrusion at ambient temperature from their LC states.

The WAXS pattern of a lying fiber of **Agg1** shows equatorial reflections which can be indexed according to a columnar rhombohedral lattice ($\mathrm{Col_{rhomb}}$) with a = 28.8 Å and γ = 78.8° (Figure 30a). The diffuse halo at 4.4 Å corresponds to the liquid-like alkyl chains. The X-ray diffraction pattern of a standing fiber of **Agg1** shows meridional and off-meridional reflections that indicate a periodic organization of the chromophores along the column (Figure 30b). The first meridional signal corresponds to the length of the axial translation subunit and can be observed at 13.8 Å which is the size of the PBI chromophore along the long axis.[60,61,111] This indicates that the PBIs are oriented parallel to the columnar long axis forming H-bonded strands. This is supported by polarized FT-IR (see Figure A69a) and UV/Vis spectroscopy (see Figure A70a) of shear-aligned thin films, which reveal that NH stretching vibrations in H-bonds and the S_0-S_1 transition of the PBIs are aligned parallel to the shearing and column direction. This is further confirmed by a diffuse signal at 3.6 Å on the equator which is characteristic for such PBI assemblies and originates in the π-π-stacking of the chromophores perpendicular to the columnar long-axis.[60,61,111] The meridional signal at 13.8 Å can be indexed as layer line L=16 of a helical arrangement and consequently all other diffuse meridional and off-meridional signals are positioned at layer lines L=24, 31, 38, 48, 51 and L=62. Accordingly, 16 molecules form the helical repeat of 16×13.8 Å = 220.8 Å. The correlation length of the equatorial signal at 3.6 Å amounts to six molecules (see 5.4 Appendix to *Chapter 5*). This implies that about six strands of H-bonded PBIs form a column and is supported by the reasonable density of 1.05 g cm^{-1} when the columnar stratum is filled by the integer number of six molecules (for details see 5.4 Appendix to *Chapter 5*). Therefore, **Agg1** is composed of a sextuple-stranded 16_1 helix with a 22.5° twist per molecule. Such a helical arrangement can only be formed by homochiral self-assembly leading to the formation of either *P*- or *M*-helices. As **PBI-Ac** is achiral, both *M*- and *P*-helical self-assemblies coexist in the columnar liquid crystal. The individual H-bonded strands are longitudinally displaced by ca. 7 Å, leading to a slip-stacked arrangement causing the absorption spectrum which is typical for PBI J-aggregates.[58,60,61,92]

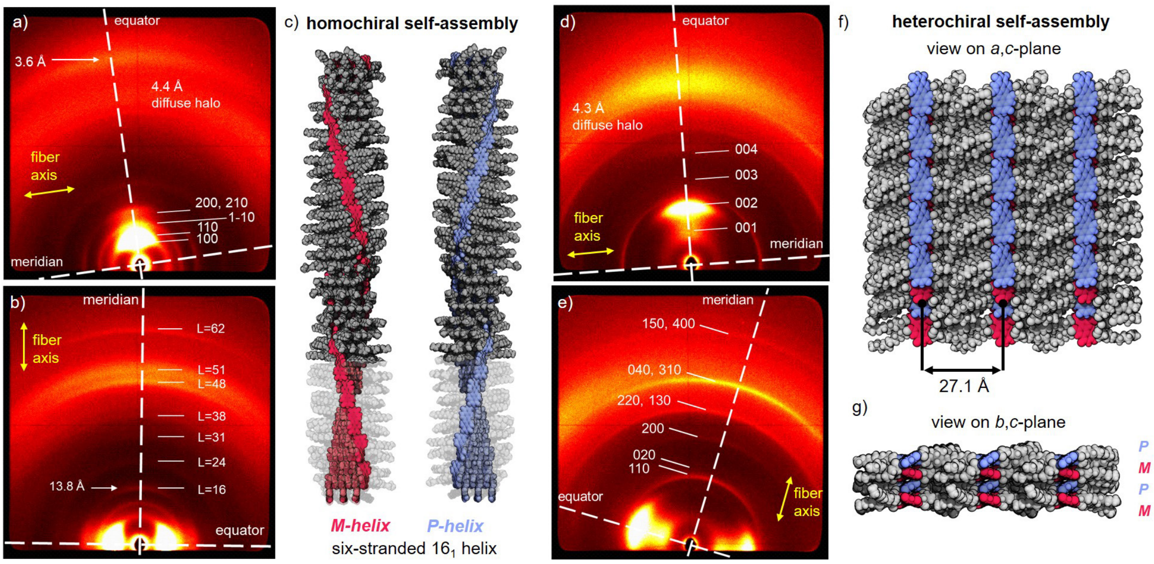

Figure 30. WAXS diffraction patterns of an a,d) lying and b,e) standing fiber of a,b) **Agg1** and d,e) **Agg2** at 25°C. Yellow arrows indicate the relative orientation of the fibers and the meridian and equator are highlighted with white dashed lines. Layerlines in b) are indexed with L. Note: Meridian and equator are defined here with respect to the fiber direction in order to enable a consistent discussion. c) Homochiral self-assembled structure of the six-stranded 16_1-helix of **Agg1** in the respective *M*- (red) or *P*-helix (blue). Parts of the alkyl chains are depicted semitransparent to illustrate the six PBI strands. Heterochiral self-assembled structure of the 2D sheets of **Agg2** which arrange in a lamellar lattice with view on the f) *a*,*c*-plane and g) *b*,*c*-plane. *M*- and *P*-atropoenantiomers of **PBI-Ac** are colored red and blue, respectively.

The self-assembled structure was modelled with the program *Accelrys Materials Studio 2017 R2*. Accordingly, core-twisted PBIs with the same axial chirality were arranged to form H-bonded strands in a slip-stacked in the sextuple-stranded helix (Figure 30c, for details see 5.4 Appendix to *Chapter 5*). The helix was optimized in the rhombohedral unit cell with the force field COMPASS II, applying the Ewald summation method until the nonbonding energy was strongly negative. With the optimized structure, we could simulate the fiber diffraction pattern with the program CLEARER.[134] The simulated pattern is in good agreement with the experiment showing the essential signals corresponding to the $\mathrm{Col_{rhomb}}$ lattice as well as the meridional signal at 13.8 Å (see Figure A72a).

The related analysis of the WAXS pattern of a lying fiber of **Agg2** shows four equidistant reflections that could be indexed as 001, 002, 003 and 004 signals of a lamellar lattice ($c = 27.1$ Å) (Figure 30d). However, these signals are very broad indicating a weak correlation between the lamellae. Accordingly, the correlation length could be calculated to be only two lamellae (for details see 5.4 Appendix to *Chapter 5*). In contrast, the meridional signals related to the intralamellar arrangement of the PBIs are well defined (Figure 30e). They can be apparently indexed according to a rectangular centered lattice ($a = 14.1$ Å, $b = 18.2$ Å). The corresponding unit cell comprises four PBI molecules assuming a reasonable density of 1.11 g $\mathrm{cm^{-3}}$. The PBIs are oriented in parallel with the layer direction, i.e. perpendicular to the *c*-axis as determined with polarized FT-IR (see Figure A69b) and UV/Vis spectroscopy (Figure A70b).

In order to rationalize the absorption spectra of **Agg2** and thus gain further information on the arrangement of the dyes within the unit cell, an interplay between short- and long-range coupling has to be taken into account.[54,55] The latter arises from the interaction of the TDMs as described within the conventional Kasha exciton theory,[52] whereas the short-range coupling is caused by the HOMO-HOMO and LUMO-LUMO overlap of the π–stacked chromophores and is very sensitive to structural arrangements.[55,221] Therefore, small changes of the longitudinal shift of the PBI chromophores can lead to distinctly different absorption spectra enabling to derive information on the chromophore arrangements.[55,222] The absorption spectrum of **Agg2** is in very good agreement with the calculated spectrum for π-stacked perylene dyes exhibiting a longitudinal shift of ~5 Å as reported by Hestand and Spano (see Figure A74).[55] Since the HOMO and LUMO distribution of perylene[52] and PBI[81] chromophores are almost identical, we can use the perylene spectra as reference. Accordingly, the spectral signature of **Agg2** results from the interference of long-range and short-range coupling in the so-called resonant regime (i.e. the Frenkel and charge-transfer state are of similar energy)[54] and shows one intense absorption peak at 539 nm and less intense absorption bands at higher and lower energies (for a detailed discussion see the 5.4 Appendix to *Chapter 5*).

With the help of the exciton-vibrational spectral pattern analysis, the unit cell of LC **Agg2** was generated with PBI chromophores that are longitudinally shifted by 5 Å (see Figure A71). This special in-plane shift, however, breaks the first assigned centered symmetry of the four strands and the planar unit cell must be primitive. Thus the absence of reflection with $h + k = 2n+1$ is accidental, and the cell is apparently only pseudo-centered (see 5.4 Appendix to *Chapter 5*). Figure 30f and g show a supercell of this arrangement that highlights the alternating arrangement of *P*- and *M*-atropoenantiomers. Using the constructed unit cell, the diffraction pattern was simulated using CLEARER, which confirms the absence of the most prominent reflections for the primitive unit cell (see Figure A72b).[134]

5.2.4 Pathway Complexity of the Supramolecular Polymerization

Lastly, we were interested in a more detailed investigation of the supramolecular polymerization and the underlying pathway complexity that leads to the formation of the respective homochiral 1D and heterochiral 2D polymorphs. Temperature-dependent UV/Vis spectroscopy of **PBI-Ac** ($c_0 = 40$ µM, MCH) showed that the self-assembly of both, **Agg1** (cooling rate 10 K/min) and **Agg2** (cooling rate 0.6 K/min), follow a cooperative nucleation-elongation mechanism (see Figure A76). This is reasonable as more than one intermolecular force, namely π-π-interactions and H-bonding, contribute to the formation of the supramolecular polymers. When mixing **Agg1** and **Agg2** in a 1:1 ratio ($c_0 = 40$ µM, MCH), the UV/Vis absorption spectrum shows a superposition of the individual spectra (blue line, Figure 31a). Time-dependent experiments at 35 °C revealed an interconversion of **Agg1** into **Agg2** as indicated by the decreasing absorption at 600 nm and the concomitant shift to 588 nm as well as the increasing absorption at 541 nm (Figure 31a). This suggests that **Agg2** is the thermodynamically favored product, while **Agg1** is formed under kinetic control. The pathway-complexity can be probed by time-dependent UV/Vis experiments at different concentrations.[213,214] Accordingly, the conversion of **Agg1** into **Agg2** was followed at a range of concentrations from $c_0 = 20$ µM to $c_0 = 60$ µM in MCH at 35 °C (see Figure A77). At $c_0 = 60$ µM, no significant spectral change can be observed over a period of 10 mins. However, at lower concentrations the absorption signal at 600 nm corresponding to **Agg1** decreases in intensity whilst the new absorption band at 541 nm corresponding to **Agg2** arises. This change can be followed by the change in absorption at 541 nm over time, thereby demonstrating an increasing rate with decreasing concentration (Figure 31b, see Figure A77).

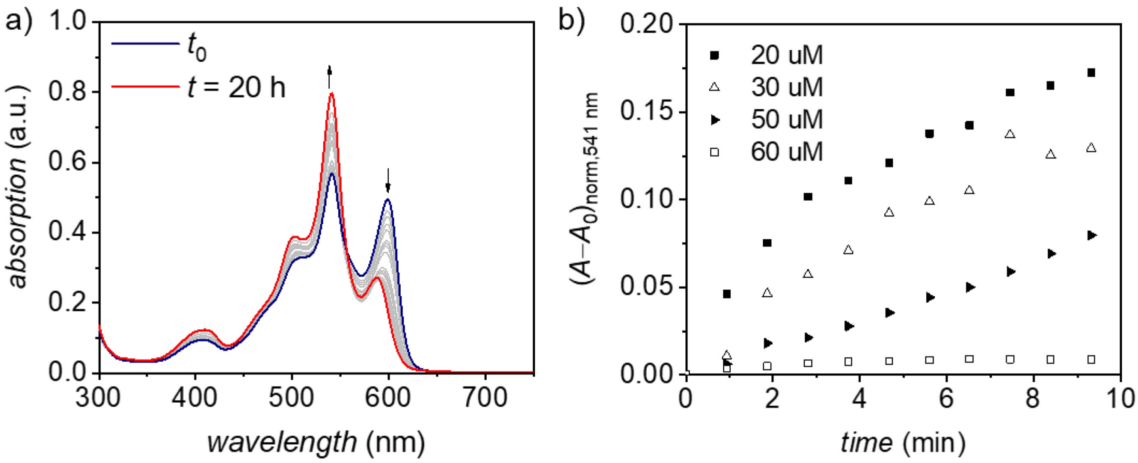

Figure 31. a) Time-dependent UV/Vis absorption spectra of a 1:1 mixture of **Agg1** and **Agg2** (40 µM in MCH) at 35 °C. b) Time course of the transformation from **Agg1** to **Agg2** at 35 °C in dependence of the concentration c_0 of **Agg1** in MCH.

These results indicate that **Agg1** is an off-pathway kinetic product and that the interconversion of **Agg1** into **Agg2** takes place via the fully dissociated monomeric state and is therefore favored at lower concentrations where the concentration of available monomer is higher.[213,214] Putting these results into perspective, it is reasonable to assume that the initial dimer pair formation, i.e. homochiral (*M*/*M* or *P*/*P*) or heterochiral (*P*/*M* or *M*/*P*) determines the outcome of the self-assembly pathway and thereby the final helical fiber or sheet-type morphology. **Agg1** is formed by a homochiral assembly of either only *P*- or only *M*-atropisomers, while the formation of **Agg2** requires an alternating, heterochiral self-assembly. Apparently, once *P*- or *M*-chirality is established within the supramolecular structure of the kinetic product **Agg1**, the fibers cannot come unwound to form the heterochiral, sheet-like structure **Agg2** even though it is the thermodynamically favored product. The pathway via the monomeric state, however, enables the structural transformation due to the fast interconversion between the two atropoenantiomers in solution. It is noteworthy that the herein elucidated narcissistic versus social self-sorting[223] in one- and two-dimensional supramolecular polymerization into **Agg1** and **Agg2** under either kinetic or thermodynamic control directly relates to the formation of conglomerate and racemate crystals in 3D self-assembly. Unfortunately, the conversion of the kinetic polymorph **Agg1** into the thermodynamic polymorph **Agg2** by a seeded[212,224] supramolecular polymerization approach could not be achieved in a satisfactory manner as even at high seed ratios of **Agg2** only a minor transformation into the thermodynamically favored polymorph was observed (see Figure A78).

5.3 Conclusion

In summary, we presented a new **PBI-Ac** dye bearing four acyloxy substituents in bay-position. In this study, we could show that **PBI-Ac** is capable of forming two polymorphs upon cooling a hot solution in MCH depending on the applied cooling rate. The two polymorphs show distinctive absorption profiles in solution and in the LC state which could be related to a difference in the longitudinal shift of the H-bonded strands in the self-assembled structures. The interchromophoric arrangement in the respective one- and two-dimensional polymorph could be elucidated by polarized spectroscopy and XRS revealing the formation of a columnar (**Agg1**) and a lamellar structure (**Agg2**). Based on these results we were able to propose packing models for both polymorphs. While the helical structure of **Agg1** is formed by a homochiral arrangement of the respective *P*- and *M*-atropoenantiomers, the sheets of **Agg2** are formed by an alternating heterochiral arrangement of the two. Accordingly, formation of **Agg1** and **Agg2** are particularly illustrative examples of conglomerate versus racemic self-sorting phenomena. Time-dependent UV/Vis spectroscopy in solution indicated that **Agg2** whose formation is initiated from heterochiral dimer pairs is the thermodynamically favored product while **Agg1** is formed in a kinetic process from homochiral dimer pairs in an off-pathway mechanism. Accordingly, **PBI-Ac** provided unprecedented insights into self-assembly pathways from the monomer via aggregates in solution up to the bulk liquid crystalline state. Due to their interesting (opto)electronic properties, **PBI-Ac** or its derivatives might be also interesting candidates for future applications in photovoltaic and photonic devices.

5.4 Appendix to *Chapter 5*

Materials and Methods

Materials

Reagents were purchased from commercial suppliers and used as received without further purification. DCC was freshly distilled prior to its use. Solvents were distilled and dried by standard procedures. All reactions were carried out under nitrogen atmosphere.

Column Chromatography

Column chromatography was performed with commercial glass columns using silica gel 60M (particle size 0.04-0.063 mm; Macherey-Nagel GmbH & Co. KG, Germany) as stationary phase.

NMR Spectroscopy

^{1}H and ^{13}C nuclear magnetic resonance (NMR) spectra were recorded on a Avance-400 spectrometer (Bruker-Daltonics GmbH, Germany) operating at 400 MHz (^{1}H) or 100 MHz (^{13}C), with the residual protic solvent used as the internal standard. The chemical shifts (δ) are reported in parts per million (ppm). Multiplicities for proton signals are abbreviated as s and m for singlet and multiplet, respectively.

High Resolution Mass Spectrometry

High resolution mass spectra (HRMS) were recorded on an ESI micrOTOF focus spectrometer (Bruker Daltonic GmbH, Germany).

UV/Vis Absorption Spectroscopy in Solution

UV/Vis absorption spectra in solution were recorded using a V-770 spectrophotometer (JASCO Inc., Japan). The spectra were measured in quartz glass cuvettes using spectroscopic grade solvents. Temperature control was accomplished by a PAC-743R Peltier system (JASCO Inc., Japan). Extinction coefficients were calculated from Lambert-Beer's law.

Fluorescence Spectroscopy in Solution

Fluorescence spectroscopy in solution was carried out with an FLS980 spectrometer (Edinburgh Instruments Ltd., UK) by optical dilution method ($OD_{\mathrm{max}} < 0.05$). The fluorescence quantum yield of **PBI-Ac** in chloroform was determined as average value of four different excitation wavelengths (455, 460, 465 and 470 nm) using *N*,*N*'-bis(2,6-diisopropylphenyl)-3,4,9,10-perylenetetracarboxylic diimide as reference.[187] The signals were corrected for the different refractive indices according to common procedure. Time-resolved measurements were performed with a ps laser diode and a TCSPC detection unit.

Cyclic and Square Wave Voltammetry

CV and SWV was carried out in a three electrode single-compartment cell on a standard electrochemical analyser (EC epsilon, BAS Instruments, UK). A glassy carbon disc electrode was used as a working electrode, a platinum wire as a counter electrode and an Ag/AgCl reference electrode using ferrocene/ferrocenium (Fc/Fc^+) as an internal standard for the calibration of the potential. The measurements were carried out under argon atmosphere in dichloromethane and tetrabutylammonium hexafluorophosphate (recrystallized from ethanol/water and dried under vacuum) was added as supporting electrolyte.

Scanning Electron Microscopy

SEM images were recorded using a Zeiss Ultra Plus field emission scanning electron microscope equipped with GEMINI e-Beam column operated at 1.5 kV with an aperture size set to 30 µm to avoid excessive charging and radiation damage of the areas imaged. The sample was prepared by drop-casting of the sample solution in MCH (40 µM) onto silicon wafer.

Atomic Force Mircoscopy

AFM measurements were performed under ambient conditions using a Bruker Multimode 8 SPM system operating in tapping mode in air. Silicon cantilevers (OMCL-AC200TS, Olympus) with a resonance frequency of ~150 kHz and a spring constant of ~10 Nm^{-1} were used.

UV/Vis Absorption Spectroscopy of Thin Films

UV/Vis absorption spectroscopy of thin films was carried out with an Axio Imager 2 (Carl Zeiss AG, Germany) polarizing optical microscope equipped with a cooled CCD spectrometer MCS-CCD PCI (Carl Zeiss AG, Germany).

FT-IR Spectroscopy

FT-IR spectra were recorded with an AIM-8800 infrared microscope connected to a IRAffinity FT-IR spectrometer (Shimadzu Corp., Japan). The sample was prepared as a thin-film on a KBr substrate (thickness 2 mm). Polarization was achieved by using a precision automated polarizer (ZnSe) (PIKE Technologies, USA). This includes the PIKE Technologies Motion Control Unit and AutoPro software.

Polarized Optical Microscopy

The LC materials were examined under an Axio Imager 2 (Carl Zeiss AG, Germany) polarizing optical microscope.

Wide-Angle X-ray Scattering

WAXS measurements were performed on a Bruker Nanostar (Detector Vantec2000, Microfocus copper anode X-ray tube Incoatec). LC samples were prepared by fiber extrusion using a mini-extruder. The measurements were carried out in Mark capillaries (Hilgenberg) positioned perpendicular to the incident X-ray beam. WAXS experiments were performed at a sample-detector distance of 21 cm, with the detector tilted by 14° upwards in order to investigate the angular range of $2\theta = 0.8°\text{-}28°$. This allowed only the investigation of a section of the XRS pattern, therefore samples with lying and standing extruded fibers have been prepared to study the equatorial and the meridional signals in detail. Lying fiber means horizontal oriented fiber with respect to the tilt direction of the detector, while standing fiber means parallel oriented fiber with respect to the tilt direction of the detector. Silver behenate was used as calibration standard for WAXS. All X-ray data were processed and evaluated with the program datasqueeze.

Molecular Modelling

The molecular models were created with Dassault Systèmes BIOVIA, Materials Studio 2017 R2 (San Diego, USA).

Synthesis

Synthesis of 1,6,7,12-tetrahydroxyperylene-3,4:9,10-bis(dicarboximide) (19)

Into a solution of **18** (30.0 mg, 42 µmol) in dry CH_2Cl_2 (5 mL) was added BBr_3 (210 mg, 838 µmol, 20 eq.) in dry CH_2Cl_2 (3 mL) dropwise at 0 °C. The reaction mixture was allowed to stir at 0 °C for 1 h and at 25 °C for 12 h. The solvent was removed by distillation and MeOH:H_2O (1:4) was added slowly to quench the reaction. The solid suspension was sonicated for 30 min followed by filtration and drying in vacuum to give **19** as a dark blue solid which was used for the next step without further purification.

Synthesis of PBI-Ac

DCC (60 mg, 0.29 mmol, 5.3 eq.) in CH_2Cl_2 (0.2 ml) was added to a mixture of **19** (25 mg, 49 µmol), dodecanoic acid (50 mg, 0.25 mmol, 4.5 eq.) and DPTS (30 mg, 0.11 mmol, 2.0 eq.) in DMF:CH_2Cl_2 (2:1, 0.3 ml). The reaction mixture was stirred at room temperature for 48 h. The solution was then concentrated and the solid residue was purified by column chromatography (silica gel, CH_2Cl_2: Et_2O, 100:0 to 98:2), followed by precipitation in cold MeOH to give **PBI-Ac**.

Yield: 22.3 mg (38%) of a purple solid.

^{1}H NMR (400 MHz, $CDCl_3$, ppm): δ = 8.67 (s, 2H), 8.45 (s, 4H), 2.60 (m, 8H), 1.69 (m, 8H), 1.44-1.18 (m, 64H), 0.88 (m, 12H). **^{13}C NMR** (100 MHz, $CDCl_3$, ppm) δ = 171.3, 162.4, 148.5, 131.2, 126.4, 124.1, 123.8, 123.6, 34.4, 32.1, 29.9, 29.8, 29.6, 29.5, 29.4, 29.2, 24.8, 22.8, 14.3. **HRMS** (ESI, acetonitrile/chloroform 1:1, pos. mode): m/z calcd for $C_{72}H_{98}N_2NaO_{12}$: 1205.7012 $[M+Na]^+$, found: 1205.6984. **m.p.** = 230 °C. **UV/Vis** ($CHCl_3$): λ_{max} [nm] (ε [M^{-1} cm^{-1}]) = 513 (40000), 481 (26000). **Φ_{Fl}** ($CHCl_3$)= 1.0. **CV** (CH_2Cl_2, 0.1 M TBAHFP, vs. Fc/Fc^+): E_{red1} = –1.27 V, E_{red2} = –1.53 V.

DFT Calculations

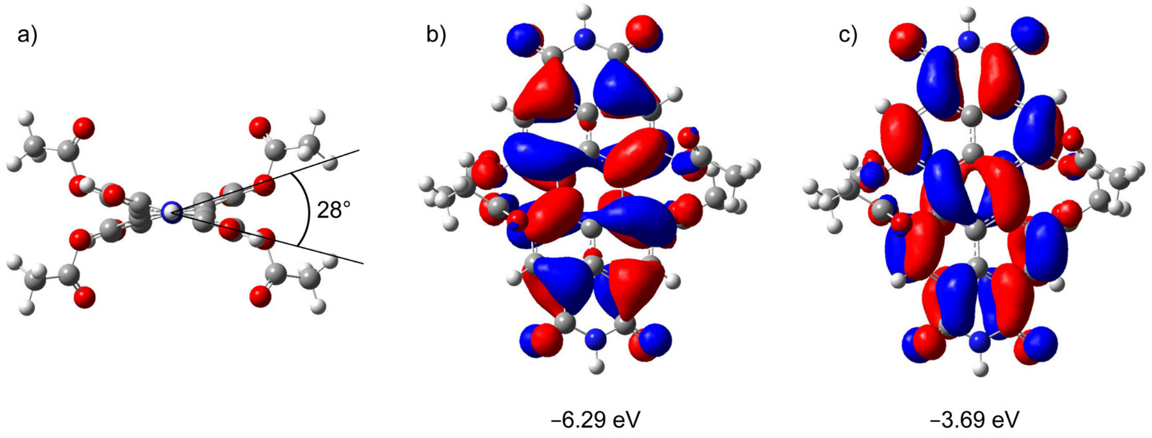

Figure A60. a) Geometry optimized structure of **PBI-Ac** by DFT (RB3LYP/dev2-SVP) in the direction along the long molecular axis to display the torsion between the two naphthalene units of the molecule (the undecyl chains were truncated to methyl groups) and b) HOMO and c) LUMO levels of **PBI-Ac**.

Absorption and Fluorescence Spectroscopy

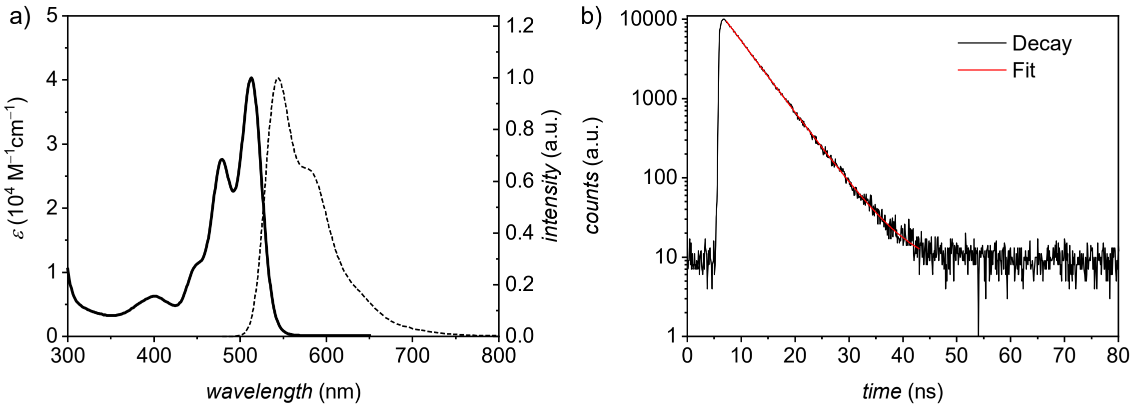

Figure A61. a) UV/Vis absorption (solid line) and normalized fluorescence (dashed line) spectra of **PBI-Ac** in CHCl$_3$ ($c_0 = 9.1 \times 10^{-7}$ M) at 20 °C. b) Fluorescence lifetime measurement of **PBI-Ac** in CHCl$_3$ ($c_0 = 9.1 \times 10^{-7}$ M, $\lambda_{ex} = 485$ nm) at 20 °C as well as the monoexponential fit (red, $\tau = 4.8$ ns) of the decay.

Solvent Dependent UV/Vis Absorption of PBI-Ac

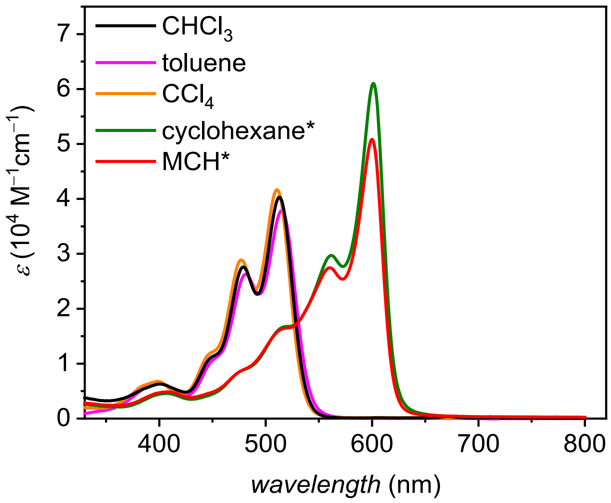

Figure A62. Solvent-dependent absorption spectra of **PBI-Ac** in $CHCl_3$ (black), toluene (pink), CCl_4 (orange), cyclohexane (green) and MCH (red) at $c_0 = 40$ µM and 22 °C. Solutions in cyclohexane and MCH were prepared by heating the solution to dissolve the material and letting it rapidly cool down at ambient conditions. This fast cooling process leads to the formation of the kinetic product **Agg1**. *Please note: in non-polar solvents, the formed aggregate tends to partially separate from the solvent rendering the extinction coefficient error-prone.

FT-IR Spectroscopy in Solution

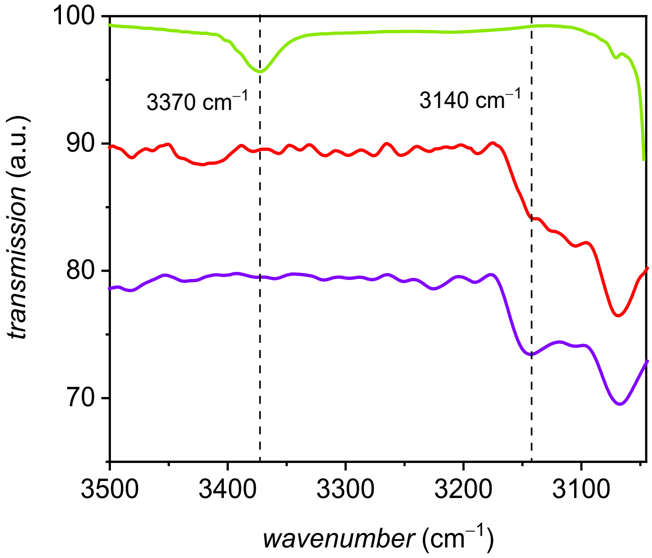

Figure A63. FT-IR spectra of solutions of monomeric **PBI-Ac** in $CHCl_3$ ($c = 200$ µM, green), **Agg1** in MCH ($c = 200$ µM, purple) and **Agg2** in MCH ($c = 200$ µM, red).

The involvement of intermolecular H-bonds in the supramolecular polymerization was investigated with FT-IR spectroscopy. The FT-IR spectra of **Agg1** (purple) and **Agg2** (red) display a N-H stretching signal at 3140 cm^{-1} which is shifted to lower energies compared to the N-H stretching signal of monomeric **PBI-Ac** in chloroform (3370 cm^{-1}), clearly demonstrating the presence of H-bonds in **Agg1** and **Agg2**.

Cyclic and Square Wave Voltammetry

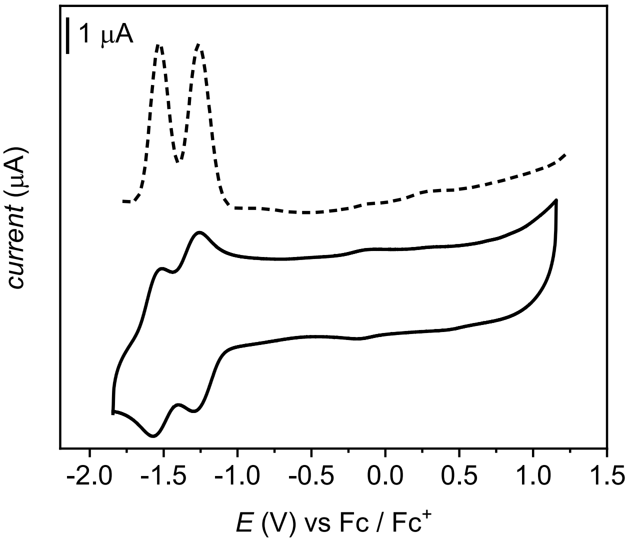

Figure A64. CV (solid line) and SWV traces (dashed line) of **PBI-Ac**. The measurements were performed in dichloromethane ($c_0 \approx 1 \times 10^{-4}$ M) at room temperature with tetrabutylammonium hexafluorophosphate (0.1 M) as electrolyte (scan rate: 100 mV s^{-1}).

The change in electronic properties by the introduction of the four ester functionalities in bay-position was investigated by CV and SWV. These measurements showed two reversible reductions at –1270 mV and –1530 mV *vs*. Fc/Fc+ to the mono- and dianion, respectively (see Figure A64). No oxidation could be observed at potentials up to 1000 mV. Considering the optical bandgap of **PBI-Ac** in dichloromethane, the HOMO and LUMO levels can be estimated as –6.30 eV and –3.88 eV, respectively, with the energy level of Fc/Fc+ set to –5.15 eV *vs*. vacuum.[190] These values are in good agreement with those obtained by DFT calculations (see Figure A60).

UV/Vis Spectroscopy of Thin Films

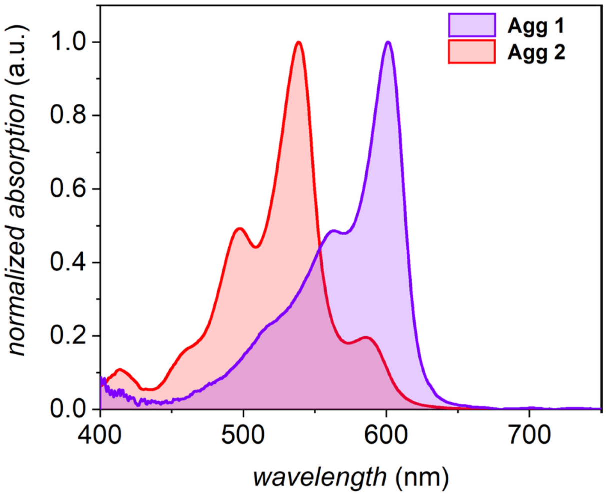

Figure A65. Normalized UV/Vis absorption spectra of drop-casted thin films of **Agg1** (purple) and **Agg2** (red) on quartz at 25 °C.

Atomic Force Microscopy

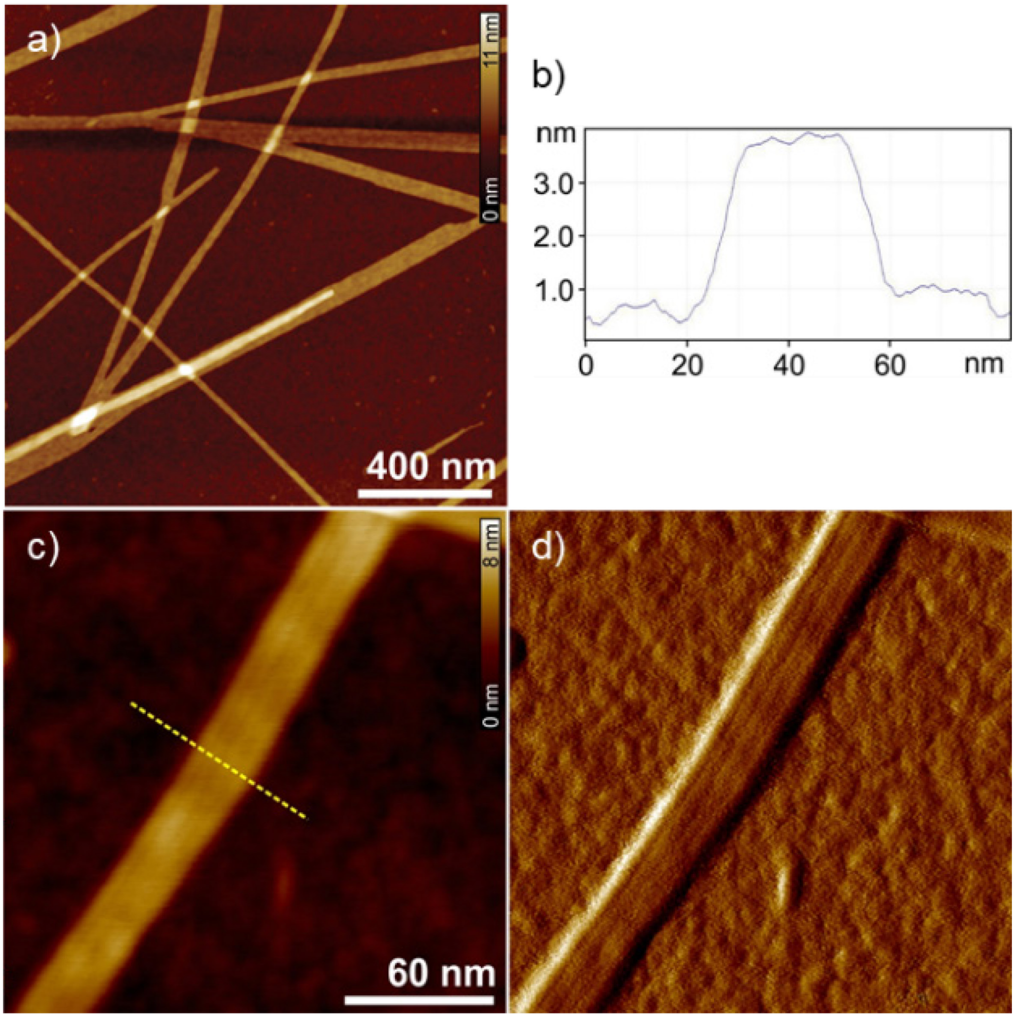

Figure A66. a,c) AFM height images of **Agg1** prepared by spin-coating a solution in MCH (c_0 = 40 µM) onto silicon wafer. b) Cross-section analysis along the yellow dashed line in c). d) Corresponding phase image of c) highlighting the individual fibers within the bundle.

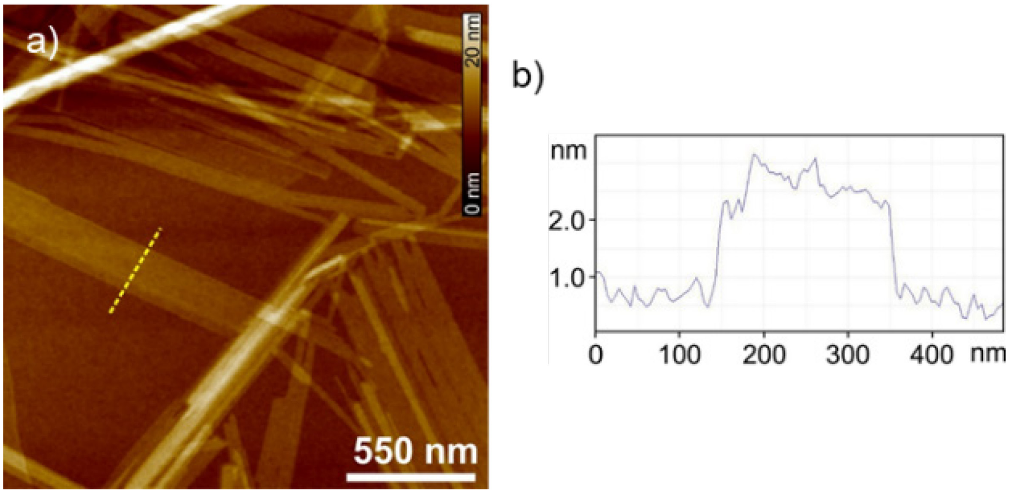

Figure A67. a) AFM height image of **Agg2** prepared by drop-casting a solution in MCH (c_0 = 40 µM) onto silicon wafer. b) Cross-section analysis along the yellow dashed line in a).

Polarized Optical Microscopy

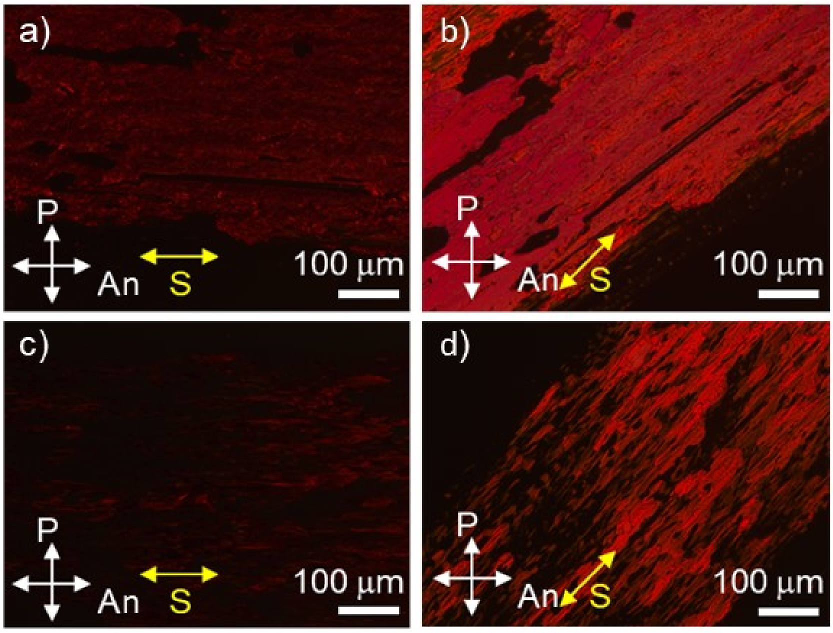

Figure A68. POM images of shear-aligned thin films of a,b) **Agg1** and c,d) **Agg2** with crossed polarizer (P) and analyzer (An) and the shearing direction (S) a,c) parallel or b,d) in a 45°rotational displacement to P and An.

Polarized Spectroscopy of Aligned Thin Films

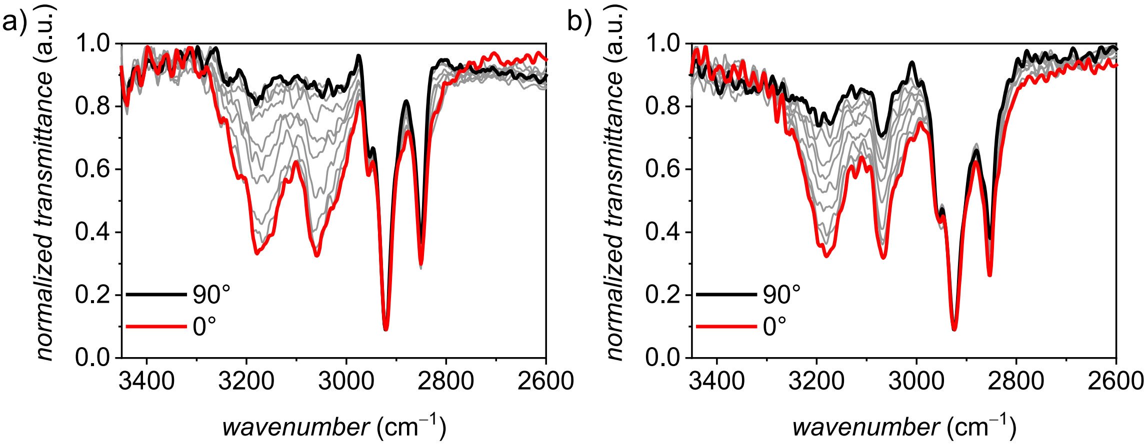

Figure A69. Polarized FT-IR spectra with different polarization angles of an aligned sample of a) **Agg1** and b) **Agg2**. The sample was sheared using an extruded fiber for friction transfer on a KBr substrate. The black and red line show the spectra for the polarizer orientated perpendicular and parallel to the shearing direction, respectively.

The polarized FT-IR measurements show that the NH stretching vibration at 3180 cm^{-1} corresponding to the hydrogen-bonded imide units is maximized when measuring along the shearing direction (red) while it practically disappears when measuring perpendicular to the shearing direction (black). This indicates that the PBIs are oriented with their long axis along the shearing direction and therefore a) along the columnar long axis and b) perpendicular to the lamellar *c*-axis.

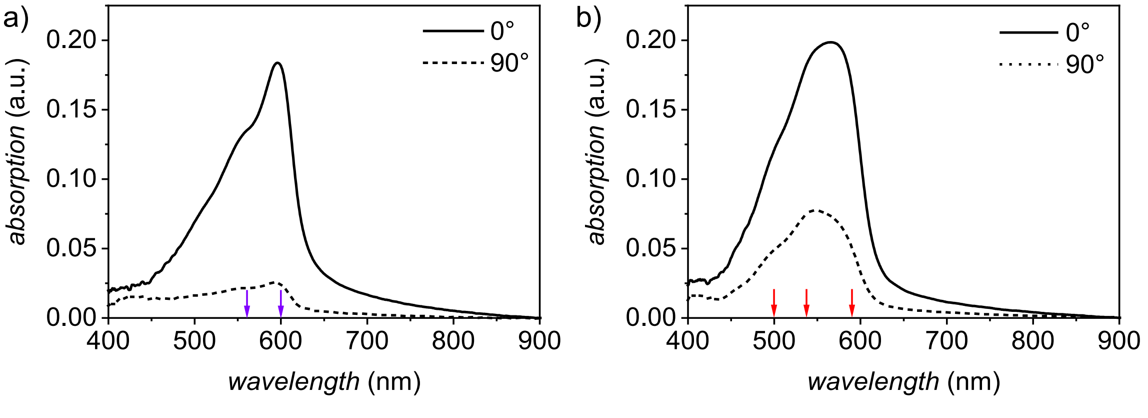

Figure A70. UV/Vis absorption spectra of a shear-aligned thin film of a) **Agg1** and b) **Agg2** on quartz measured with linearly polarized light parallel (solid line) and perpendicular (dashed line) to the shearing direction. Arrows indicate the position of absorption maxima in drop-casted samples (see Figure A65).

The polarized UV/Vis absorption spectra show that the PBI main TDM (S_0-S_1 transition) is oriented parallel to the shearing direction for both, **Agg1** and **Agg2**. Upon shearing, absorption signals get broadened as mechanical shearing partially disrupts the interchromophoric arrangement.

Molecular Modelling

The number of molecules Z in a unit cell can be calculated using equation (1).

In case of **Agg1**, equation (11) can be used to calculate the volume of the unit cell:

$$V_{\text{unit cell}} = V_{\text{col-strat}} = A_{rhombus} * h. \tag{11}$$

Where A_{rhombus} is the area of the rhombus and h the height of the columnar stratum. The height can be in principle chosen arbitrarily, however, since the axial translational subunit is 13.8 Å it has been naturally chosen as stratum height. Accordingly, using equation (1), filling the unit cell with six molecules would require a reasonable density of $\rho = 1.05$ g cm^{-1}.

The model of self-assembled **Agg1** is based on π-stacked hexamers. The hexameric units were built by co-facial packing arrangement of the chromophores in a π-π-stacking distance of 3.6 Å. The PBIs are longitudinally and rotationally displaced by 6.9 Å and 11.5°, respectively. These hexameric units were then translationally positioned at a distance of 13.8 Å rotated by 22.5° to form one helical column consisting of 96 molecules. This six-stranded assembly was placed in a rhombohedral unit cell ($a = 28.8$ Å, $\gamma = 78.8°$) in a P1 cell, i.e. without symmetry restrictions, and geometry optimized with the forcefield COMPASS II applying the Ewald summation method until the non-bonding energy was strongly negative.

In case of **Agg2**, equation (12) can be used to calculate the volume of the unit cell:

$$V_{\text{unit cell}} = a * b * c. \tag{12}$$

Accordingly, four molecules fill the unit cell with a reasonable density of $\rho = 1.11$ g cm^{-1}.

For the structure of **Agg2** the unit cells with plane symmetry have been considered. Owing to the indexation according to a centered rectangular cell with four PBI molecules ($a = 14.1$ Å, $b = 18.2$ Å, $c = 27.1$ Å) we evaluated first the centered unit cells cm and c2mm. The unit cell should consist of two *P*- and *M*-atropoenantiomers, respectively. However, since exciton theory indicates that neighbors are shifted by 5 Å along the *a*-axis (for details see main article and section "Comparison to calculated spectra"), which is less than half of the unit cell, the symmetry breaks and centered plane groups must be excluded.

For symmetry reasons most of the rectangular planar groups can be eliminated. Thus only the monoclinic p1, p2 and the rectangular pg cell remains as possible unit cells. Consequently, the apparent extinction of reflections with h + k = 2n + 1 is accidental and is caused by the specific arrangement of the PBI strands. For steric reasons shifted PBI strands can interact via their π-surfaces only when *M*- and *P*-strands are direct neighbors. Accordingly, a possible unit cell was constructed with the *P*-strands alternatingly shifted by –5 Å and 5 Å with respect to the *M*-strands. The alternating shift is required to prohibit a reduction of the *b*-parameter due to symmetry reasons. This arrangement does not possess symmetry elements and is consequently a p1 unit cell, which however, afforded the best results for the simulated XRS pattern (Figure A72b). Applying geometry optimization at semi-empirical PM7 level of theory,[225] the interchromophoric arrangement (longitudinal shift of 5 Å) between the *P* and *M* chromophores is retained (Figure A71b)

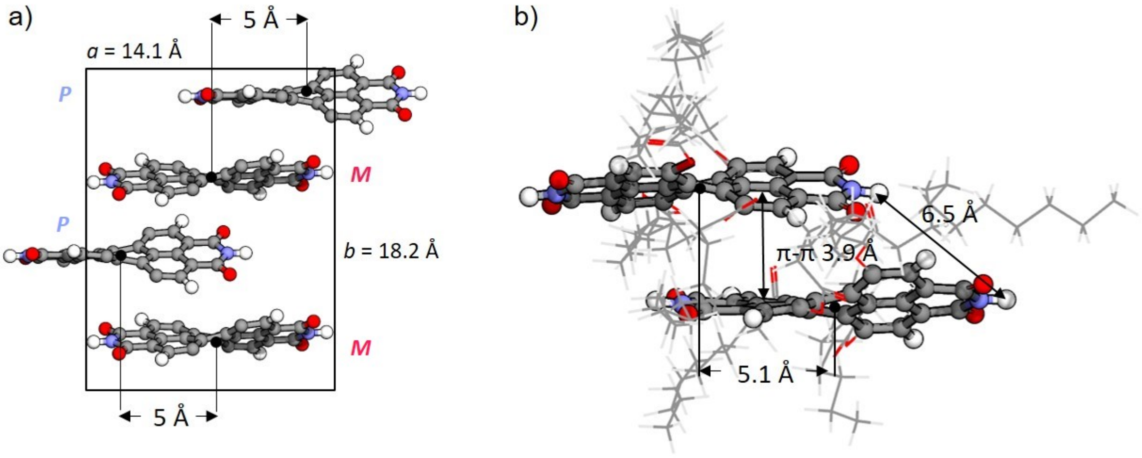

Figure A71. a) View on the *a,b*-plane of the constructed unit cell of **Agg2** containing four PBI molecules. Bay-substituents were omitted for clarity. b) *P*/*M* dimer extracted from geometry optimized unit cell (PM7)[225] with relevant intermolecular distances. Acyloxy-substituents are depicted as lines for clarity. Semi-empirical structure optimization has been performed in MOPAC2016[226] based on the constructed unit cell given in a) using periodic boundary conditions.

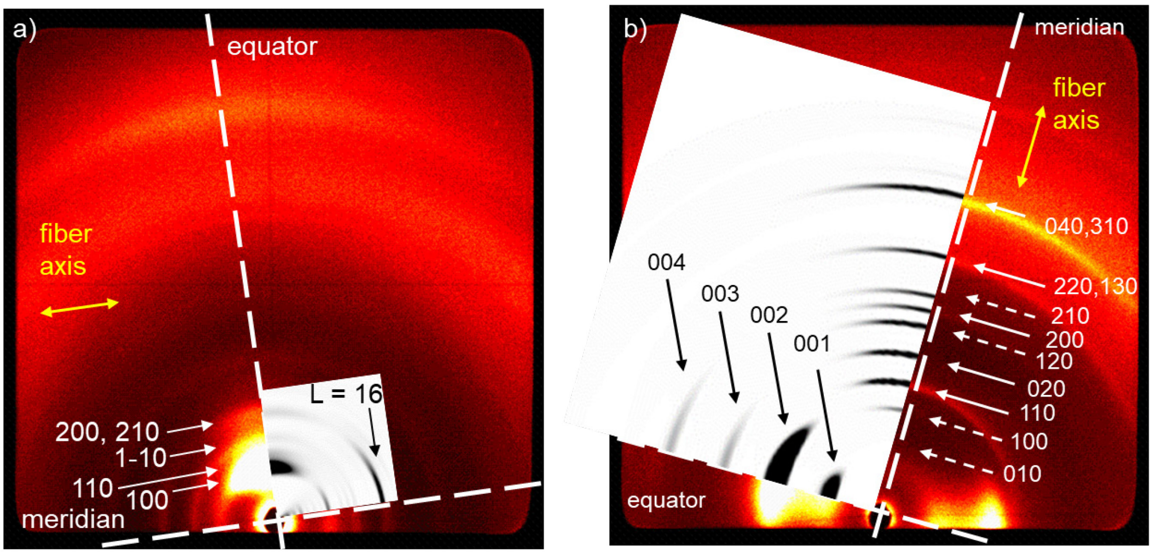

Figure A72. Superposition of the WAXS patterns of a) **Agg1** and b) **Agg2** and the simulated diffraction patterns calculated using CLEARER and the models generated with Materials Studio. The yellow arrows indicate the orientation of the fibers.

The fiber diffraction patterns were simulated with the program CLEARER[134] using the modelled structures obtained in Materials Studio.[130]

For **Agg1**, the structure was exported as pdb-file and imported into the fiber diffraction simulation module of CLEARER. The fiber axis was set to (0,0,1) with a crystallite size of a = 40 nm, b = 40 nm and c = 120 nm. The fiber disorder parameters σ_ϕ and σ_θ were set to infinity and 0.5, respectively.

For **Agg2**, the unit cell was exported- as pdb-file and imported into the fiber diffraction simulation module. The fiber axis was set to (0,0,1) with a crystallite size of a = 120 nm, b = 120 nm and c = 40 nm. The fiber disorder parameters σ_ϕ and σ_θ were set to infinity and 0.5, respectively. The crystallite size and contrast were adjusted to best fit the experimental pattern. Meridional and equatorial signals were simulated separately and superposed for illustration. As the constructed unit cell is not inherently centered due to requirements of the longitudinal shift as determined with exciton-vibrational spectral pattern analysis, signals corresponding to a simple rectangular cell appear (dashed arrows in Figure A72b). However, the most prominent reflections (010, 100) are either absent or very weak. The XRS simulation of a soft phase with conformational disordered mesogens is challenging, and a perfect match is difficult to obtain. The present results, however, support that the given model is a good approximation.

X-Ray Scattering

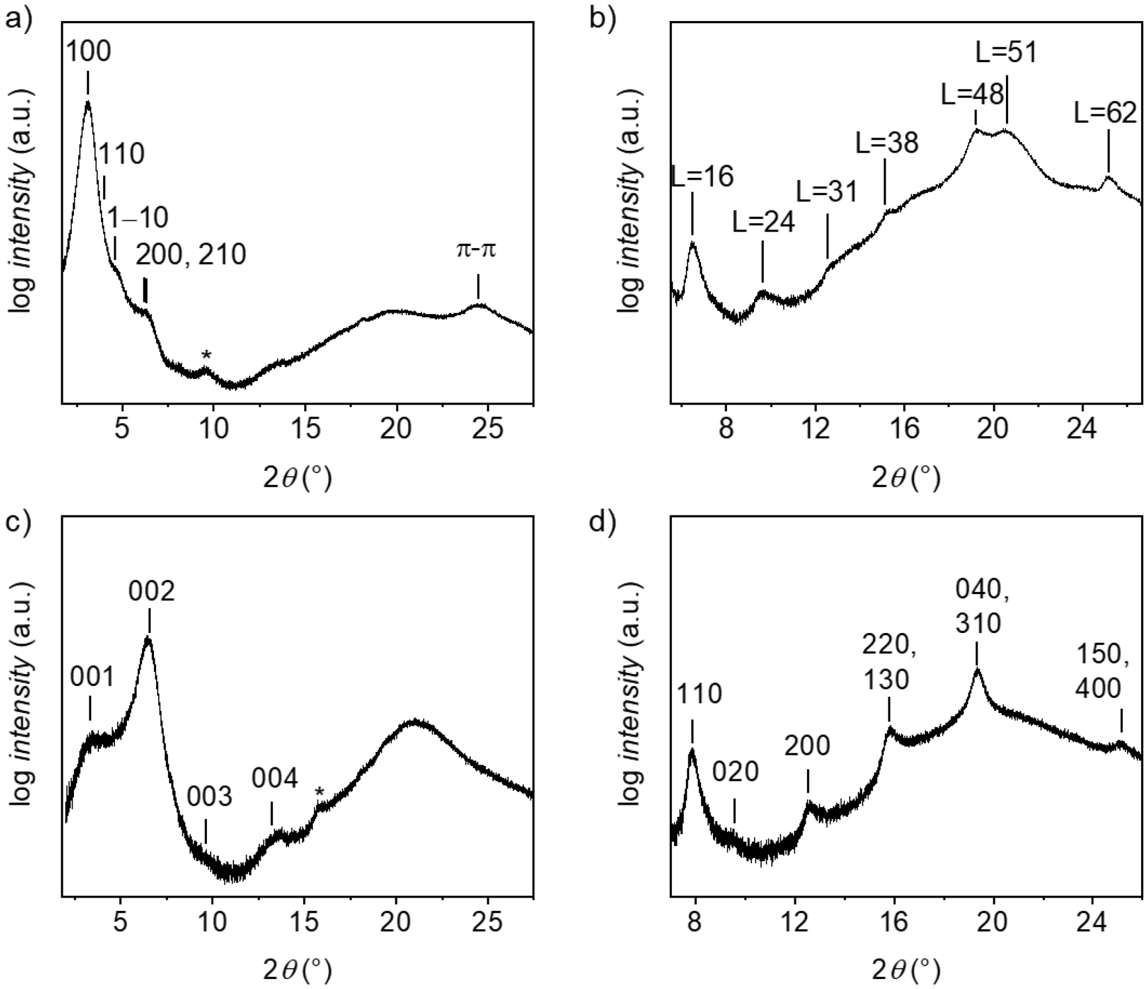

Figure A73. Integrated intensity of the WAXS patterns of **Agg1** (a, b) and **Agg2** (c, d) at 25 °C along the equator (a, c) and along the meridian (b, d). Reflexes indicated with * correspond to residual off-meridional signals.

The correlation length ξ in the LC state can be calculated according to the Scherrer equation (9).[160]

For **Agg1**, we calculated the correlation length for the π-stacked PBIs perpendicular to the columnar direction by this method. $\Delta(2\theta)$ and θ were determined by fitting the signal on the equator belonging to the π–π stacking distance. The number of correlated molecules N was then calculated by dividing the correlation length by the π-distance. Accordingly, a correlation length of 21.5 Å was determined. This correlates to 21.5 Å/3.6 Å = 6.0 molecules and hints towards the formation of a six-stranded arrangement. This is in agreement with the density considerations described above. Furthermore, the number of correlated columns was calculated using the 100 reflection. The correlation length could be determined as 117.0 Å. Accordingly, the number of correlated columns equates to

117.0 Å/28.8 Å = 4.1 columns. This weak correlation causes the broadness of the observed signals.

For **Agg2**, we calculated the correlation length along the *c*-axis. The number of correlated lamellae was then calculated by dividing the correlation length by the *c*-parameter. Accordingly, a correlation length of 49.2 Å could be determined. This correlates to 49.2 Å/27.1 Å = 1.8 lamellae demonstrating the weak correlation along the *c*-axis. As the individual lamellae (2D sheets) grow under thermodynamic conditions from solution and only arrange in the lamellar lattice in the solid state, the weak correlation is expected.

Comparison to Calculated Spectra

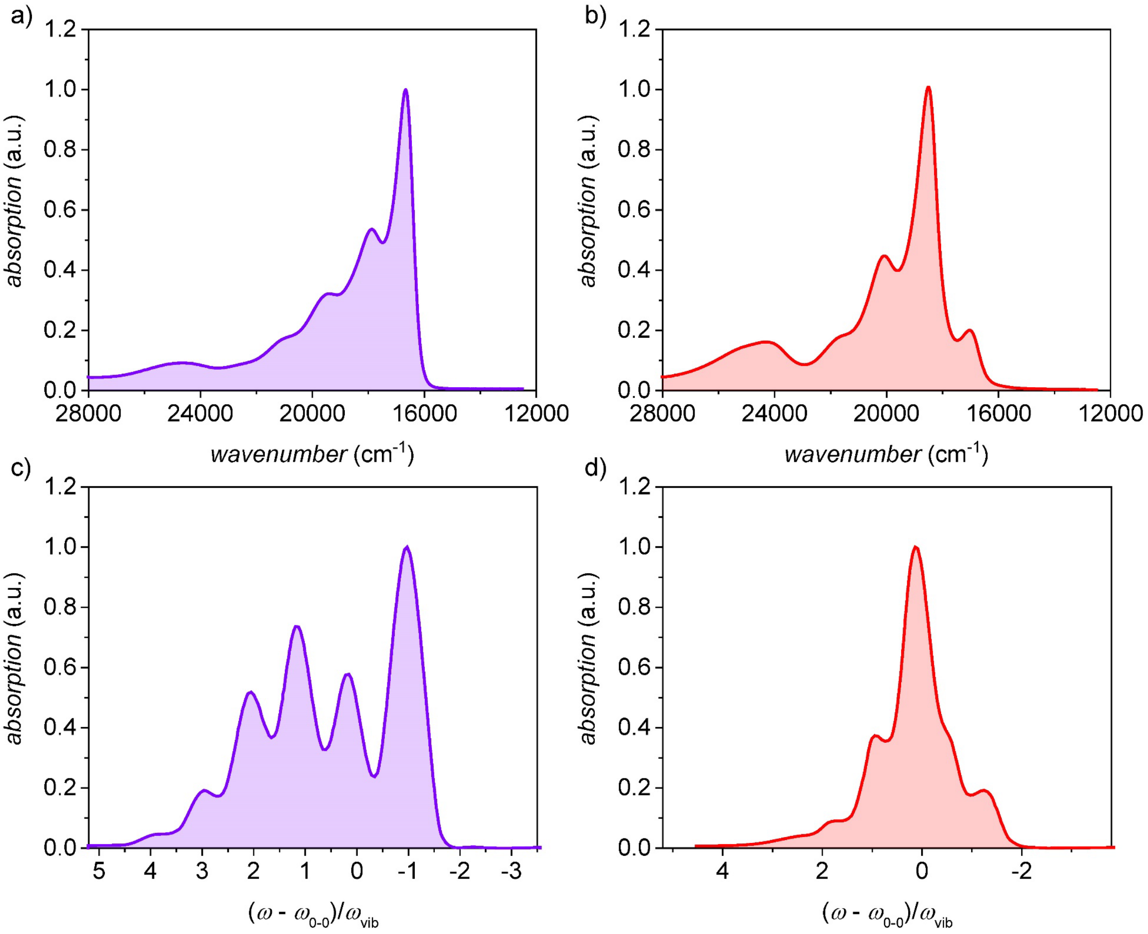

Figure A74. Experimental UV/Vis absorption spectra of a) **Agg1** and b) **Agg2** (c_0 = 40 µM, MCH, 20 °C) and calculated absorption spectra by Hestand and Spano for longitudinal slips of c) 8.0 Å and d) 5.0 Å for a π-stack containing $N = 10$ perylene molecules.[54]

XY data of the calculated spectra was extracted from Reference[54] using WebPlotDigitizer Version 4.2 (San Francisco, USA). In this work, the authors set the diabatic CT energy resonant with the molecular excitation energy E_{CT}–E_{S1} = 0. Please note: Spectra shown in Figure A74 were calculated for perylenes, not PBIs. However, Since the HOMO and LUMO distribution of perylene[55] and PBI[35] chromophores are almost identical, we can use the perylene spectra as reference.[54] The absorption at ca. 400 nm (25000 cm^{-1}) in the experimental spectra is due to the S_0-S_2 transition which is not considered in the calculated spectra.

The spectra were calculated for 1D decamers of perylenes that exhibit short-range coupling only to one perylene on each side of the π-surface.[54] In our case, the PBIs interact with one further chromophore that is longitudinally displaced as the PBIs form H-bonded strands. In case of **Agg1**, this can be neglected as both chromophore on each side of the π-surface are shifted by ca. 7 Å causing the spectral features typical for PBI J-aggregates[35,58-61] in which both, short- and long-range coupling are of J-type.[54] In case of **Agg2**, a longitudinal shift between 3.8 Å and 6.3 Å leads to H-type contributions of both, short-range and long-range coupling, that causes the distinctive absorption spectrum shown in Figure A74d.[54] A longitudinal shift of 5 Å yielded the best result for retrostructural analysis (Figure A72b). Accordingly, a second chromophore on each side of the π-surface is longitudinally displaced by ca. 9 Å (Figure A75). However, as the long-range coupling scales with $\sim r^{-3}$ within the point-dipole approximation, where r is the center-to-center distance between the coupled transition dipoles, and the short-range coupling decreases exponentially with increasing distance,[221] the contribution of the second chromophore on each side that is longitudinally shifted by longer distances can be neglected.

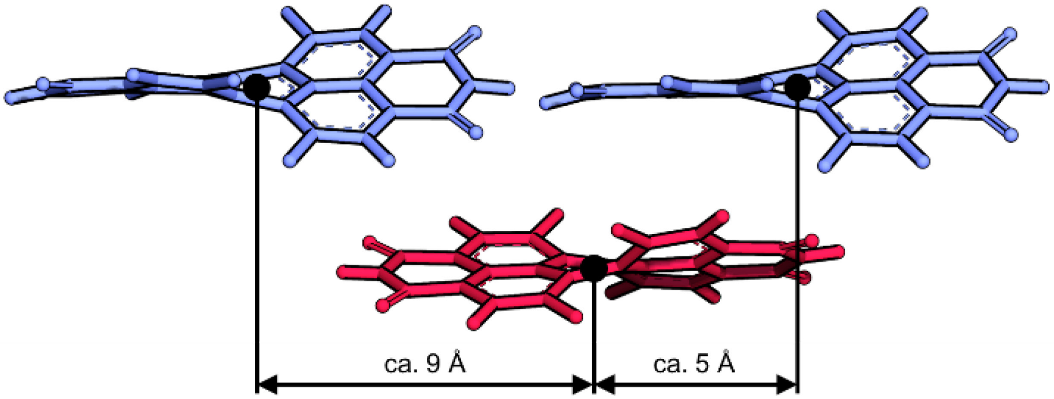

Figure A75. Illustration of the different longitudinal shifts between *M*- (red) and *P*-atropoenantiomers (blue) in **Agg2**.

Temperature-Dependent UV/Vis Absorption Studies

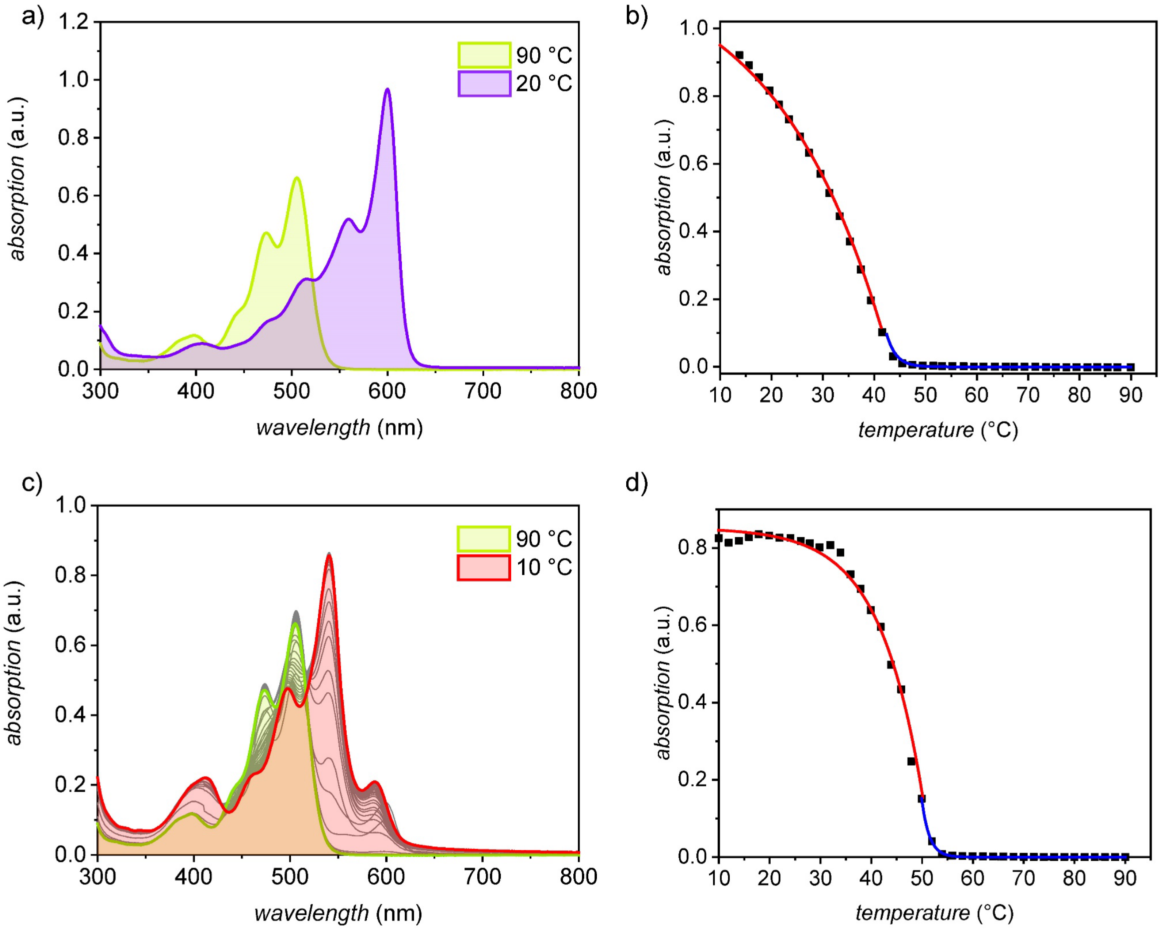

Figure A76. a) Temperature-dependent UV/Vis absorption spectra of **PBI-Ac** with c_0 = 40 µM in MCH starting from a monomer solution (green) and applying a) a cooling rate of 10 K/min to direct self-assembly into **Agg1** (purple) and c) cooling rate of 0.6 K/min to direct self-assembly into **Agg2** (red). Plot of the corresponding absorbance of b) **Agg1** at 600 nm and d) **Agg2** at 541 nm as a function of the temperature and fit according to the cooperative nucleation-elongation model[34,95,158] (elongation in red, nucleation in blue).

The change in absorption upon self-assembly of both, **Agg1** and **Agg2** could be fitted with the cooperative nucleation-elongation model.[34,95,158] For **Agg1** an enthalpy of $\Delta H = -39$ kJ mol^{-1}, an elongation temperature of 44 °C and a value for the dimensionless equilibrium constant of the activation step $K_a = 1.5 \times 10^{-4}$ were obtained (c_0 = 40 µM, MCH). For **Agg2** an enthalpy of $\Delta H = -103$ kJ mol^{-1}, an elongation temperature of 52 °C and $K_a = 1.0 \times 10^{-3}$ were obtained (c_0 = 40 µM, MCH).

Time-Dependent UV/Vis Spectroscopy

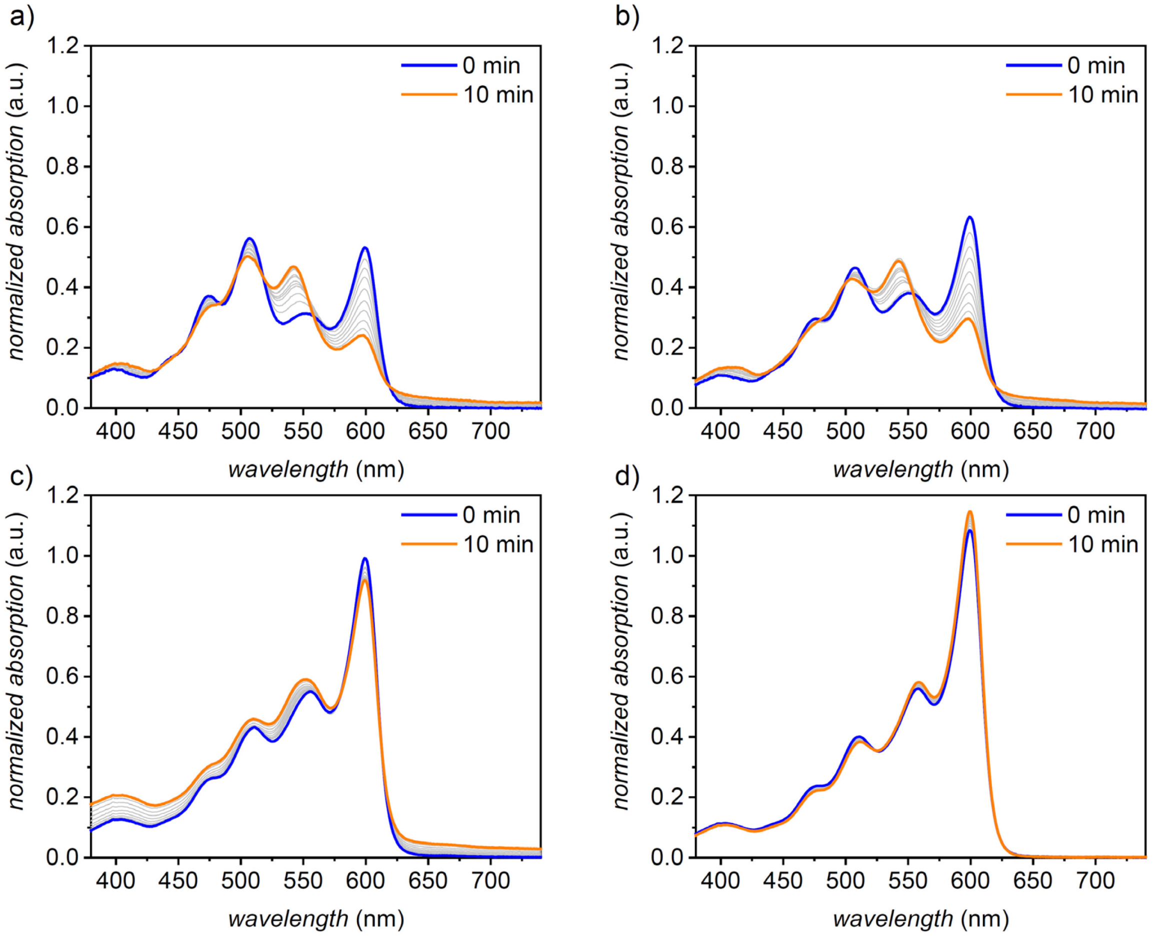

Figure A77. a) Time-dependent UV/Vis absorption spectra of **Agg1** at a) $c_0 = 20$ µM, b) $c_0 = 30$ µM. c) $c_0 = 50$ µM and d) $c_0 = 60$ µM at 35 °C. At lower concentrations **PBI-Ac** is not fully aggregated, as indicated by the absorption signals corresponding to monomeric **PBI-Ac**.

For time-dependent experiments, the sample solutions were heated to 90 °C for 20 mins to ensure a fully monomeric state. After rapidly cooling to 35 °C (15 K/min) to produce **Agg1**, UV/Vis absorption measurements were started immediately and spectra were recorded in one min intervals to monitor the transformation of **Agg1** into **Agg2**.

Seed-induced supramolecular polymerization

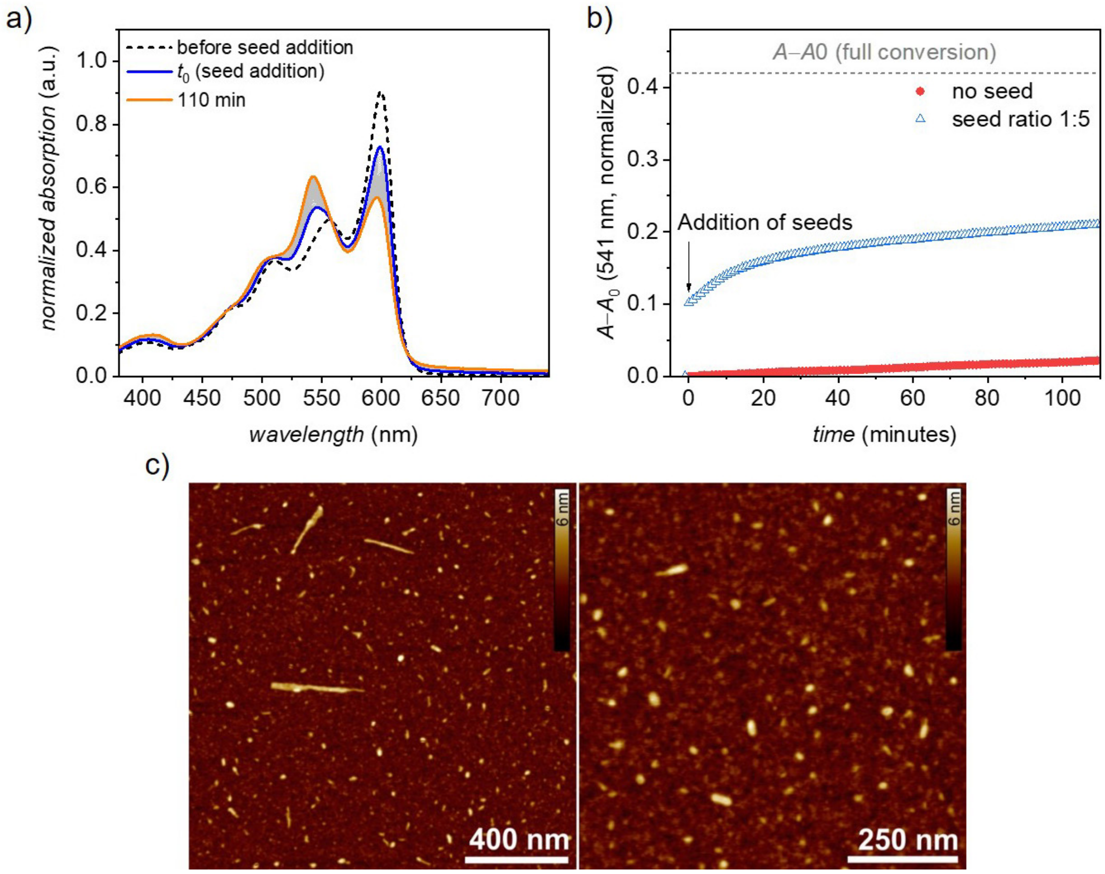

Figure A78. a) Time-dependent UV/Vis absorption spectra for the transformation from **Agg1** into **Agg2** (c_T = 60µM) at 35 °C after addition of seeds of **Agg2** at a **Agg2$_{\text{seed}}$**:**Agg1** ratio of 1:5. b) Time course of the transformation from **Agg1** to **Agg2** at 35 °C after the addition of seeds of **Agg2** at a **Agg2$_{\text{seed}}$**:**Agg1** ratio of 1:5 (blue triangles) and without the addition of seeds (red dots). c) AFM images of seeds of **Agg2** prepared by ultrasonication of **Agg2** in MCH (c = 60µM) for 30 mins and spin-coating the dispersion on silicon wafer (2000 rpm).

Seeds of **Agg2** were prepared by treating a solution of **Agg2** in MCH (c = 60µM) with ultrasound for 30 mins. AFM revealed the high quality of the nanoparticle seeds with sizes between 15-400 nm. Upon the addition of seeds of **Agg2** to a solution of **Agg1** (c = 60µM, MCH, 35 °C, **Agg2$_{\text{seed}}$**:**Agg1** ratio of 1:5), enhanced transformation of **Agg1** into **Agg2** can be observed compared to a solution of **Agg1** without seed. However, despite the high seed quality and a high amount of seed, only a slightly improved conversion of **Agg1** can be detected.

NMR Spectra of PBI-Ac

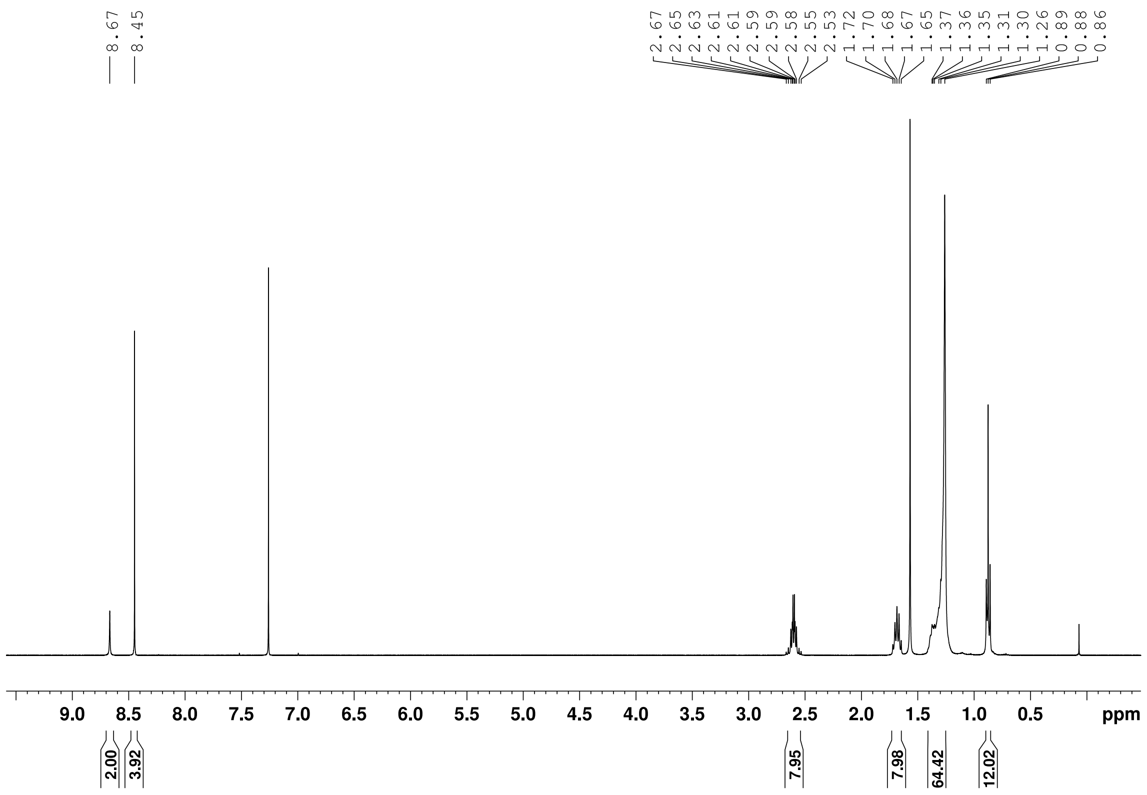

Figure A79. ^{1}H NMR (CDCl$_3$, 400 MHz, 295 K) of **PBI-Ac**.

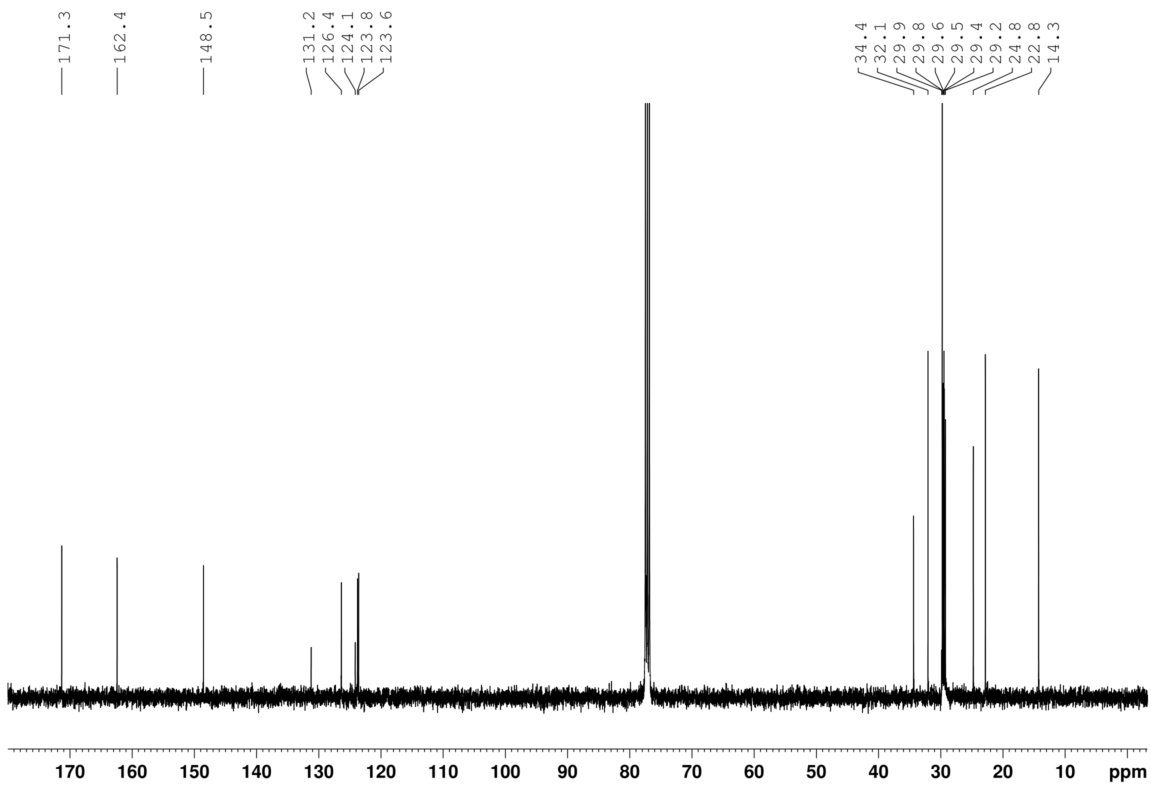

Figure A80. ^{13}C NMR (CDCl$_3$, 100 MHz, 295 K) of **PBI-Ac**.

Chapter 6

–

Anisotropic Microfibers of a Liquid-Crystalline Diketopyrrolopyrrole by Self-Assembly-Assisted Electrospinning

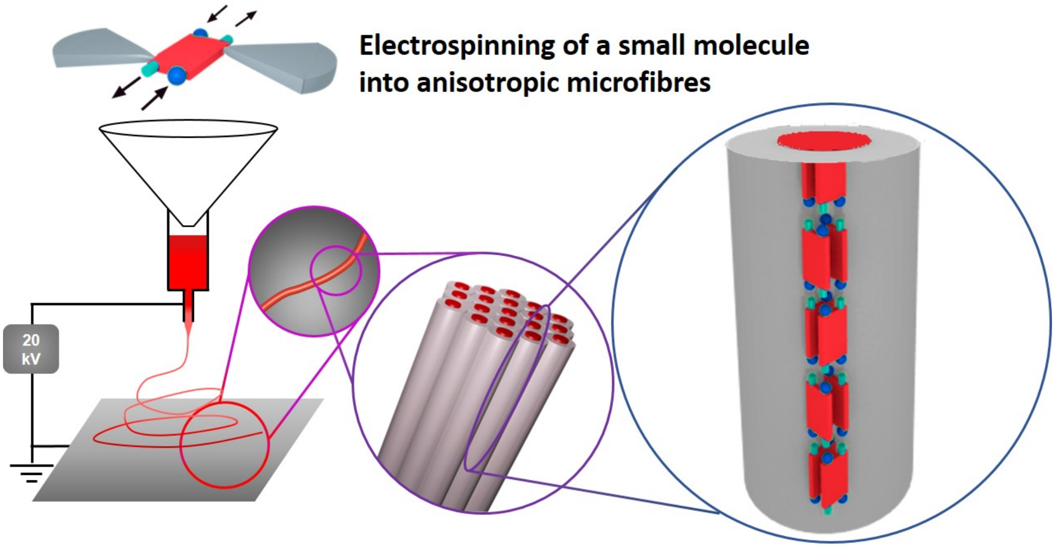

This chapter was published in: M. Hecht, B. Soberats, J. Zhu, V. Stepanenko, S. Agarwal, A. Greiner, F. Würthner, *Nanoscale Horiz.* **2019**, *4*, 169–174.

Abstract: Electrospinning is a well-established technique for the preparation of nanofibers from polymer solution or melt, however rarely applied for small molecules. Here we report a unique example of a LC DPP dye that was successfully used for electrospinning. Micrometric fibers with anisotropic alignment of DPP dye were produced by this process as shown by POM and selected area electron diffraction (SAED). This newly designed DPP dye self-assembles in solution by H-bonding and π–π-interactions and forms columnar LC phases in the bulk. XRS and polarized FT-IR studies in the LC state revealed a hierarchical arrangement of DPP molecules into columnar structures. The successful preparation of anisotropic microfibers by electrospinning is attributed to the H-bond-directed supramolecular polymerization of the new DPP dye in solution and its LC properties.

6.1 Conceptual Insights

DPP dyes are widely applied as red colour pigments (e.g. “Ferrari Red”) and organic electronic materials in devices. Their self-assembly into supramolecular materials with defined arrangement, however, is still challenging and their further hierarchical organization on macroscopic length scales remained so far elusive. Toward this important goal for the implementation of self-assembled supramolecular materials in nanodevices, new processing methods are required to shape and orient the supramolecular materials in a specific direction. In this regard, we envisioned that electrospinning technique might allow the preparation of fibers of small molecules with specific orientation within the fibers. Thus, we have designed a DPP dye that forms LC phases in bulk and self-assembles in solution. This design enables access to the benefits of both the self-assembly of small molecules in solution prior to the electrospinning process and the alignment of liquid crystals under external forces like electric fields. Indeed, electrospinning of the self-assembled DPP dye through H-bonding and π–π-interactions produces anisotropic microfibers. Thus, here we present the first example of a small molecule DPP dye for the preparation of electrospun microfibers.

6.2 Introduction

Self-assembly of organic molecules constitutes a most appealing bottom-up approach for the development of functional nanoscale materials.[16,17,32,35,41] In this context, self-organizing materials based on supramolecular polymers,[34,39,228,229] liquid crystals,[15,22,26,230] and even covalent polymers[231-233] are in the spotlight. Much efforts have been devoted to the elucidation of self-assembly processes with particular attention on the self-assembly mechanisms,[214] structure-functions relationship,[234] and stimuli-responsive properties.[235] These studies revealed the potential of supramolecular polymers, gels and liquid crystals in many applications such as organic electronics,[236,237] photonics,[110,238] or drug delivery.[239,240] However, for the implementation of such molecular materials in devices new processing methods have to be developed. Albeit the advances in this direction are key to satisfy upcoming demands related to the miniaturization of components in modern nanoscale devices, so far comparatively little efforts have been devoted to the development of advanced processing technologies for supramolecular materials.

In the case of LC materials, most approaches are focused on the alignment of the phases along 2D macroscopic arrays. Liquid crystals are usually susceptible to the molecular environment and due to their dynamic and adaptive properties they are easily aligned using chemically modified templating substrates or applying mechanical or electric forces.[22,24,241] In this context, also electrospinning of LC polymers has been applied to prepare anisotropic fibers with well-defined internal structure.[242-244] Electrospinning uses the deformation of droplets in an electric field by induced electrostatic charges leading to jets of material which, if the viscoelasticity is sufficient, form fibers.[245] This technique is widely applied to prepare micro- or nanometric fibers from covalent polymers (solution and/or melts),[246-250] but it has been rarely used for processing of small molecules[251-256] and detailed information about the hierarchy and molecular organization of small molecules in such electrospun fibers is essentially absent. We envisioned that the electrospinning technique might be applicable for the fabrication of micrometric fibers based on hierarchical assemblies of mesogenic low-molecular weight dyes. For this purpose, we considered the use of organic dyes with the ability to self-assemble in solution into supramolecular polymers and to form LC phases in the bulk, i.e. supramolecular liquid crystals. We anticipated that dyes with such properties may be advantageous for this purpose due to: 1) their ability to entangle upon supramolecular polymerization in solution prior to the spinning process and 2) their tendency (as liquid crystals) to align into anisotropic domains under external forces (i.e. electric fields).

Herein, we report on the electrospinning of highly anisotropic microfibers of 1.0 ± 0.5 μm diameter from a DPP dye, namely **DPP 2** (Figure 32a). The anisotropic properties of **DPP 2** microfibers are the result of a cooperative self-assembly through H-bonds and π–π-interactions where the DPPs are oriented parallel to the fiber direction Figure 32b. Studies of the liquid crystallinity and supramolecular polymerization of **DPP 1** and **DPP 2** revealed the key factors for the successful preparation of anisotropic microfibers by electrospinning.

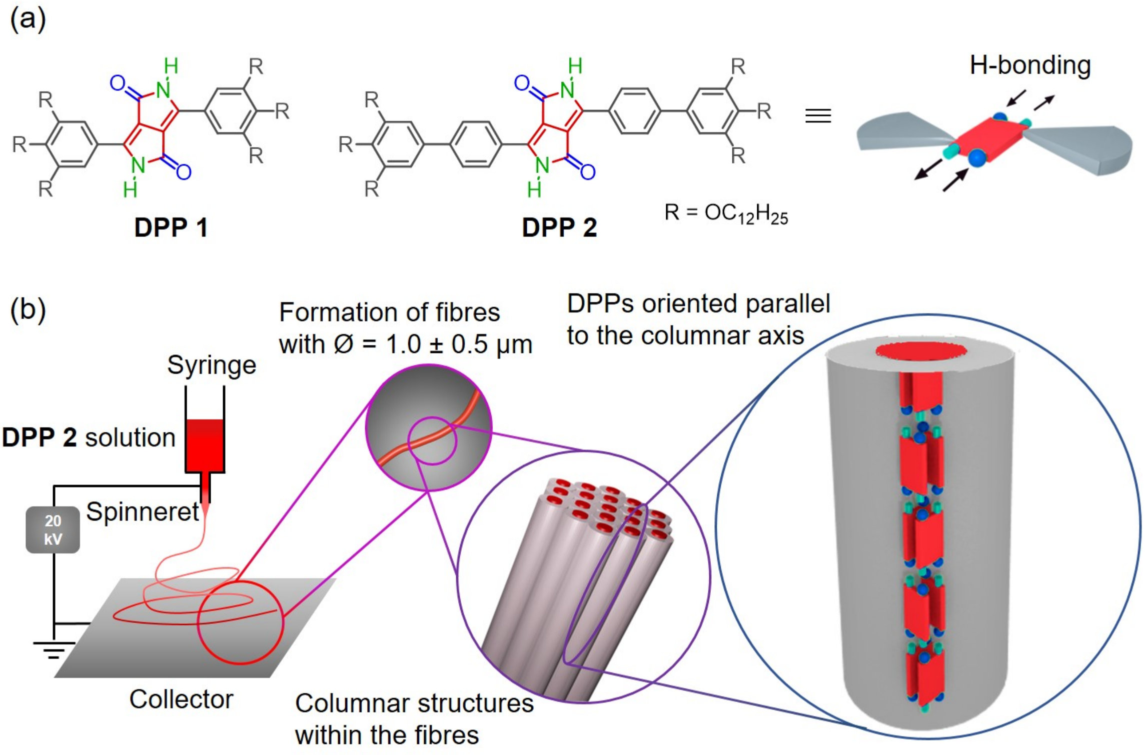

Figure 32. (a) Chemical structures of **DPP 1** and **DPP 2**. (b) Schematic illustration of the electrospinning process (left), the columnar arrangement in the LC phase (middle) and intracolumnar arrangement of the DPP molecules (right).

6.3 Results and Discussion

6.3.1 Material Design and Electrospinning Experiments

The molecular design of **DPP 1** and **DPP 2** consists of a DPP core, which is unsubstituted in lactam positions and functionalized with two 3,4,5-tris(dodecyloxy)phenyl groups in 3,6-positions. In the case of **DPP 1** the wedge-shaped groups are directly connected to the core, while for **DPP 2** a phenyl spacer connects core and dendrons (Figure 32a). This design is expected to promote the H-bond-directed supramolecular polymerization in solution and to induce LC behaviour by nanosegregation in the bulk.[58,60,61] **DPP 1** was prepared as previously described.[257] The new **DPP 2** was synthesized by Suzuki cross-coupling reaction of *tert*-butyloxycarbonyl (BOC)-protected 3,6-bis(4-bromophenyl)-substituted DPP and 3,4,5-tris(dodecyloxy)phenylboronic acid pinacol ester, followed by deprotection of BOC group by heat treatment (for detailed procedure and characterization see 6.5 Appendix to *Chapter 6*).

In a previous work, we have reported the liquid crystallinity of **DPP 1** which assembles *via* a π–stacked dimeric unit by quadruple H-bonds into a 1D supramolecular polymer structure that in turn organizes in a columnar LC phase.[257] Our preliminary experiments confirmed that **DPP 2** also forms LC phases (Figure A81). Furthermore, temperature-dependent UV/Vis experiments in toluene revealed that both DPP dyes self-assemble in solution into supramolecular polymers (Figure A82). Detailed studies of the LC behaviour and supramolecular polymerization are described later in this paper. The high propensity for supramolecular self-assembly makes **DPP 1** and **DPP 2** suitable candidates for electrospinning experiments.

Toluene was chosen as solvent for this process since both **DPP 1** and **DPP 2** self-assemble into aggregates in this solvent (Figure A82 and *vide infra*). For this purpose, 20 mM solutions of both DPPs were prepared. In the case of **DPP 1**, the solution is of purple colour and low viscosity, while **DPP 2** forms a dark red viscous solution that was shown to be a gel in the tube inversion test (Figure A83). These solutions were electrospun on silicon and glass substrates by using a voltage of 20 kV and a flow rate of 0.1 ml/h (for details see 6.5 Appendix to *Chapter 6*). The substrates were then analysed by SEM (Figure 33a-c). While small droplets were obtained for **DPP 1** (Figure 33a), **DPP 2** formed under the same conditions well-defined fibers with a length of several hundred micrometres and uniform thickness of 1 ± 0.5 µm exhibiting a certain rigidity (Figure 33b and c).

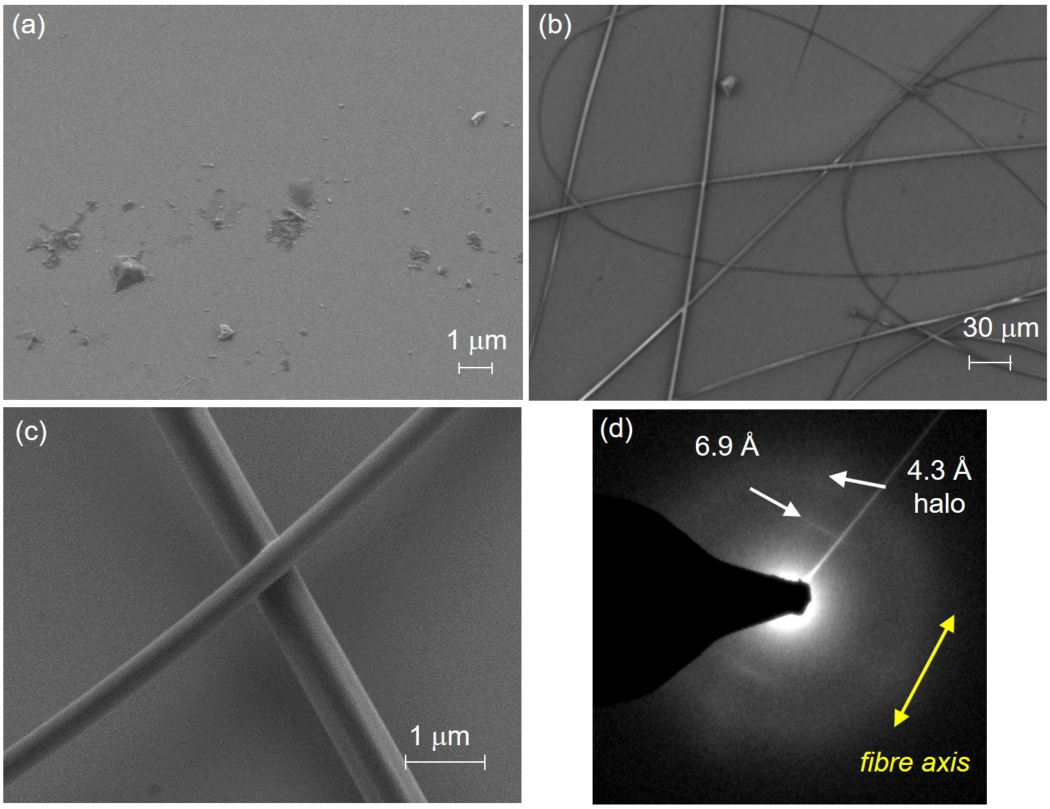

Figure 33. SEM images of electrospun (a) **DPP 1** and (b,c) **DPP 2** on silicon substrates. (d) Electron diffraction pattern of an electrospun fiber of **DPP 2** (diameter ⌀ = 500 nm) as obtained from SAED.

To elucidate the anisotropic properties of the electrospun fibers of **DPP 2**, the material was investigated by POM (Figure A84). The fibers appear dark when they are oriented parallel to the analyzer or polarizer, but become bright (red colour) when the fibers are rotated by 45° to the analyzer due to their birefringence. This indicates that the fibers have a well-defined (macro-)molecular organization and the molecules as well as the supramolecular scaffolds forming the fiber are aligned in a specific direction. To get deeper insight into the exact arrangement of the DPPs, SAED was measured on a spot of an electrospun fiber of **DPP 2**. The electron diffraction pattern showed a broad halo at a distance of 4.3 Å and a sharp signal at 6.9 Å (Figure 33d). The latter appears only perpendicular to the long axis of the fiber which is an indication of the anisotropic nature of the fiber. This signal matches well with the molecular length of a DPP molecule along its long molecular axis bearing two lactam units (6.0 Å) that connect two neighbour molecules by H-bonds (ca. 6.0+0.8 Å) (Figure A85). Accordingly, POM and SAED experiments suggest that the **DPP 2** electrospun fiber is composed of DPP molecules that are hierarchically organized with the long molecular axis of the DPP π-core parallel to the fiber axis. Thus, it is obvious that the electrospinning of **DPP 2** in toluene produces anisotropic fibers with a well-defined packing arrangement of the DPP molecules. Such anisotropic properties have never been achieved by electrospinning of small molecules. In order to figure out their precise organization and the principles that govern the formation of these fibers, the LC properties and aggregation behaviour in solution of **DPP 2** were studied in detail.

6.3.2 Liquid-Crystalline Properties

We have previously reported that **DPP 1** self-assembles into DPP dimers that stack into a columnar structure *via* quadruple H-bonds, where each dimer is rotated by 90° along the columnar axis.[257] These columns further arrange into a columnar rectangular (Col_r) phase between 0 °C and 45 °C and a Col_h phase between 45 °C and 336 °C. In the present work, the LC properties of **DPP 2** have been studied by the same techniques, i.e. POM, DSC, polarized FT-IR and X-ray experiments. DSC and POM experiments revealed that **DPP 2** forms three phases: a soft-crystalline (SC) phase (from 0 °C to 177 °C) and two LC phases, the first one from 177 °C to 225 °C and the second one from 225 °C up to 270 °C, where the material melts (Figure A86). The respective phases of **DPP 2** were identified by MAXS and WAXS studies of aligned fibers prepared with a home-made extruder. Both LC phases show sharp signals in the X-ray pattern, while a broad set of signals was observed for the

SC phase. This latter phase shows a pattern pointing to a columnar phase but, due to the rather broad peaks, this phase could not be elucidated in detail (Figure A87). The MAXS pattern of the first LC phase at 210 °C clearly shows the 200, 110, 310, 220 and 130 reflections along the equator corresponding to a Col$_r$ lattice (a = 65.4 Å, b = 31.5 Å) (Figure 34a). By increasing the temperature to 265 °C, the X-ray pattern becomes simpler showing the 100, 110, 200, 210 and 300 reflections of a Col$_h$ lattice (a = 35.9 Å) on the equator (Figure A88 and Figure A89).

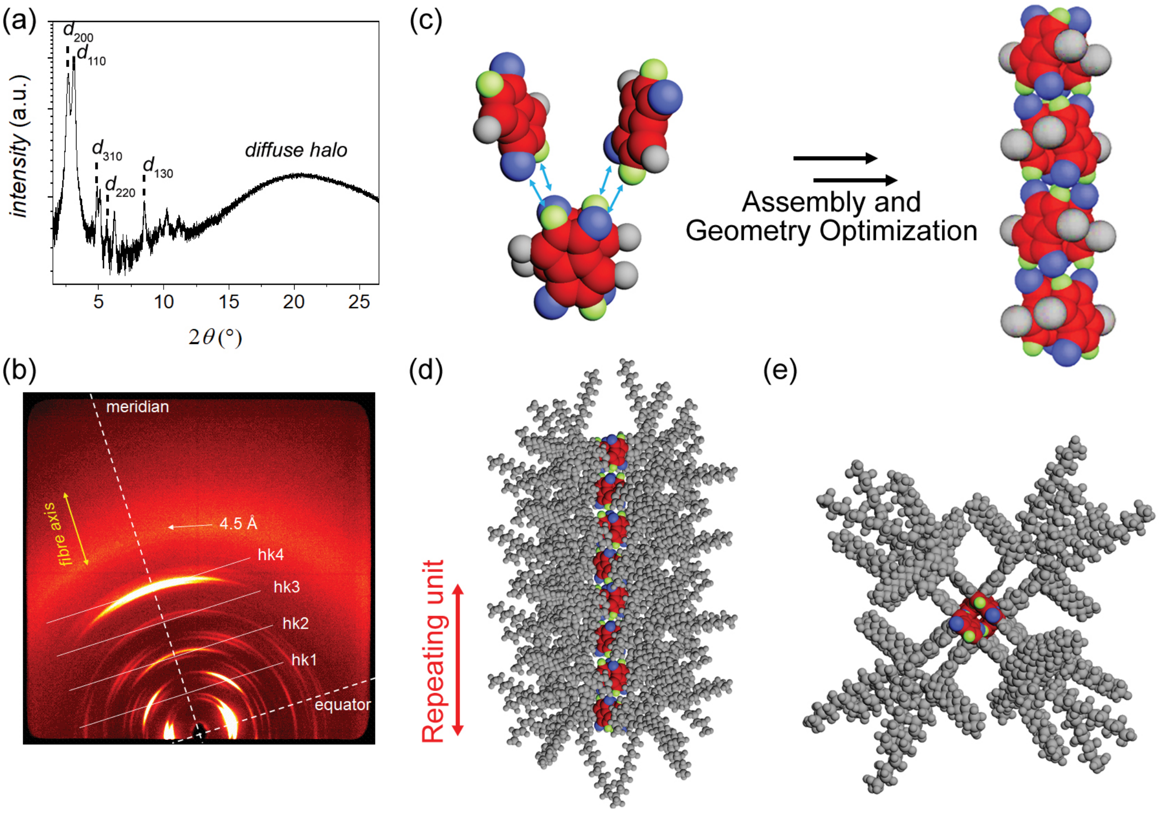

Figure 34. (a) Integrated intensities along the equator of the WAXS pattern of an extruded fiber of **DPP 2** at 210 °C. (b) WAXS pattern of an extruded fiber of **DPP 2** at 210 °C with the fiber axis standing. (c) Assembly of the LC structure by quadruple H-bonds and geometry optimized structure without peripheral substituents for better visualization. (d) Side view and (e) top view of the geometry optimized structure with the attached peripheral substituents.

To gain insight into the molecular arrangement of DPP molecules in the LC phases, polarized FT-IR studies and further analyses of the MAXS and WAXS patterns of aligned **DPP 2** samples were performed. From the polarization of the N-H stretching signals in homogenously aligned (by mechanical shearing) sample of **DPP 2** onto KBr substrates, it was deduced that the lactam units and the H-bonds are oriented parallel to the columnar axis in all the SC and LC phases (Figure A91). This is also supported by the X-ray patterns of both LC phases that exhibit meridional and off-meridional reflections with a representative strong signal on the meridian at 6.8 Å. Taking into account the distance of hydrogen-bonding, this signal matches well with the distance between the two lactam units which is in agreement with the signal observed in the SAED pattern of the electrospun fibers (Figure 33d). These observations support that the DPP cores are oriented with their long molecular axis parallel to the columnar axis in the LC phases. For the $\mathrm{Col_r}$ phase, this signal at 6.8 Å was assigned to layer line *hk4* while the other off-meridional reflections at 27.2 Å, 20.4 Å and 13.6 Å were assigned as *hk1*, *hk2* and *hk3*, respectively (Figure 34b). This implies a correlation between every fifth molecule along the columns with a rotation of 90° with each stratum. The number of molecules per columnar stratum (h = 6.8 Å) was estimated to be two, considering a density of 0.9 g/cm^3 and a reasonable error of 5% of each parameter in the evaluation of the X-ray diffraction data (see 6.5 Appendix).[258] Similar results were obtained from the WAXS and MAXS patterns of the **DPP 2** $\mathrm{Col_h}$ phase (Figure A89).

According to the X-ray data, the packing arrangement in the **DPP 2** $\mathrm{Col_r}$ and $\mathrm{Col_h}$ phases were modelled by using *Materials Studio* software (Figure 34c, d and e, Figure A92). The optimized structure of the $\mathrm{Col_r}$ phase (Figure 34c) supports the formation of dimers that are stacked *via* quadruple H-bonding by rotation of 90° (Figure 34c-e). This columnar arrangement shows a correlation between every fifth molecule, giving a columnar unit cell composed of four dimers. This assembly mode is enabled by the alternate stack of two types of dimers (with mirror image relationship) as reported previously for **DPP 1**.[257] The molecular arrangement in the $\mathrm{Col_h}$ phase of **DPP 1** shows a similar columnar organization, but in this case every third molecule correlates (Figure A90).[257] The modelled molecular structures for all the LC phases were used as input for retrostructural analysis with the program *CLEARER*.[134] The calculated diffraction patterns are in good agreement with the experimental data, supporting the proposed structural models (Figure A88, Figure A89, Figure A93 and Figure A94).

It is noteworthy that both the X-ray patterns of the extruded fibers and the SAED pattern of the electrospun **DPP 2** fibers show a signal at 6.8 Å, which corresponds to the centre-centre distance of hydrogen-bonded DPPs (Figure A85). Since this signal is observed in the SAED pattern in the parallel direction of the electrospun fiber, it can be concluded that the DPP cores are oriented parallel to the fibers (Figure 32b) with a columnar arrangement identical or at least very similar to the one observed in the X-ray experiments of the LC phases.

Despite the relevant findings that unveil the hierarchical anisotropic self-assembly in the electrospun **DPP 2** fibers (Figure 32b), these experiments cannot explain why **DPP 2** is able to form fibers by electrospinning but **DPP 1** not, although respective intracolumnar arrangements are very similar. In order to elucidate the reason for this, we further explored the supramolecular polymerization of both DPPs in solution.

6.3.3 Supramolecular Polymerization in Solution

The supramolecular polymerization studies of **DPP 1** and **DPP 2** in solution were carried out by temperature- and concentration-dependent UV/Vis spectroscopy and AFM experiments. In chloroform ($c = 3 \times 10^{-5}$ M), both materials exhibit the optical features of monomerically dissolved DPPs[45] with a strong absorption band at 519 nm and a vibronic progression at 483 nm and 452 nm for **DPP 1** and at 531 nm with the vibronic progression at 495 nm and 462 nm for **DPP 2**. However, the spectra drastically change in less polar solvents like toluene that are known to reinforce H-bonding,[259] now revealing the characteristics of co-facially aggregated DPPs (Figure A95). Figure 35b and Figure 35d show the concentration-dependent spectra of **DPP 1** and **DPP 2** in toluene. Gradual increase of the concentration leads to a decrease of the absorptions bands corresponding to the monomer, while new bands originate at 510 nm, 540 nm and 590 nm for **DPP 1** and at 478 nm, 508 nm and 542 nm for **DPP 2** due to the formation of aggregated species of the double-stranded supramolecular polymers. The absorption spectrum of an electrospun fiber of **DPP 2** shows similar optical features as the concentrated solution in toluene (Figure A96). In both experiments, the presence of isosbestic points at 423 nm and 530 nm for **DPP 1** and at 426 nm and 548 nm for **DPP 2** indicates the transformation between two distinct species. The calculated degree of aggregation was fitted with the established models showing the best results for the cooperative model of Goldstein and Stryer[94,95,260] for both compounds. From this data analyses, nucleation and elongation constants of $K_{\mathrm{nuc}} = 140$ M^{-1} and $K_{\mathrm{elong}} = 37000$ M^{-1} were obtained for **DPP 1**, pointing at a strongly disfavored dimer nucleus formation (cooperativity factor of $\sigma = 3.7 \times 10^{-3}$) (Figure 35a). Very similar results were obtained for the supramolecular polymerization of **DPP 2** *via* its dimer nucleus with nucleation and elongation constants of $K_{\mathrm{nuc}} < 10$ M^{-1} and $K_{\mathrm{elong}} = 11000$ M^{-1} (cooperativity of $\sigma = 3.9 \times 10^{-4}$). Thus, both dyes show a rather similar self-assembly process in terms of mechanism (strongly cooperative) as well as binding constants. Temperature-dependent UV/Vis absorption studies of both DPPs confirmed the cooperativity of the self-assembly process (Figure A97).

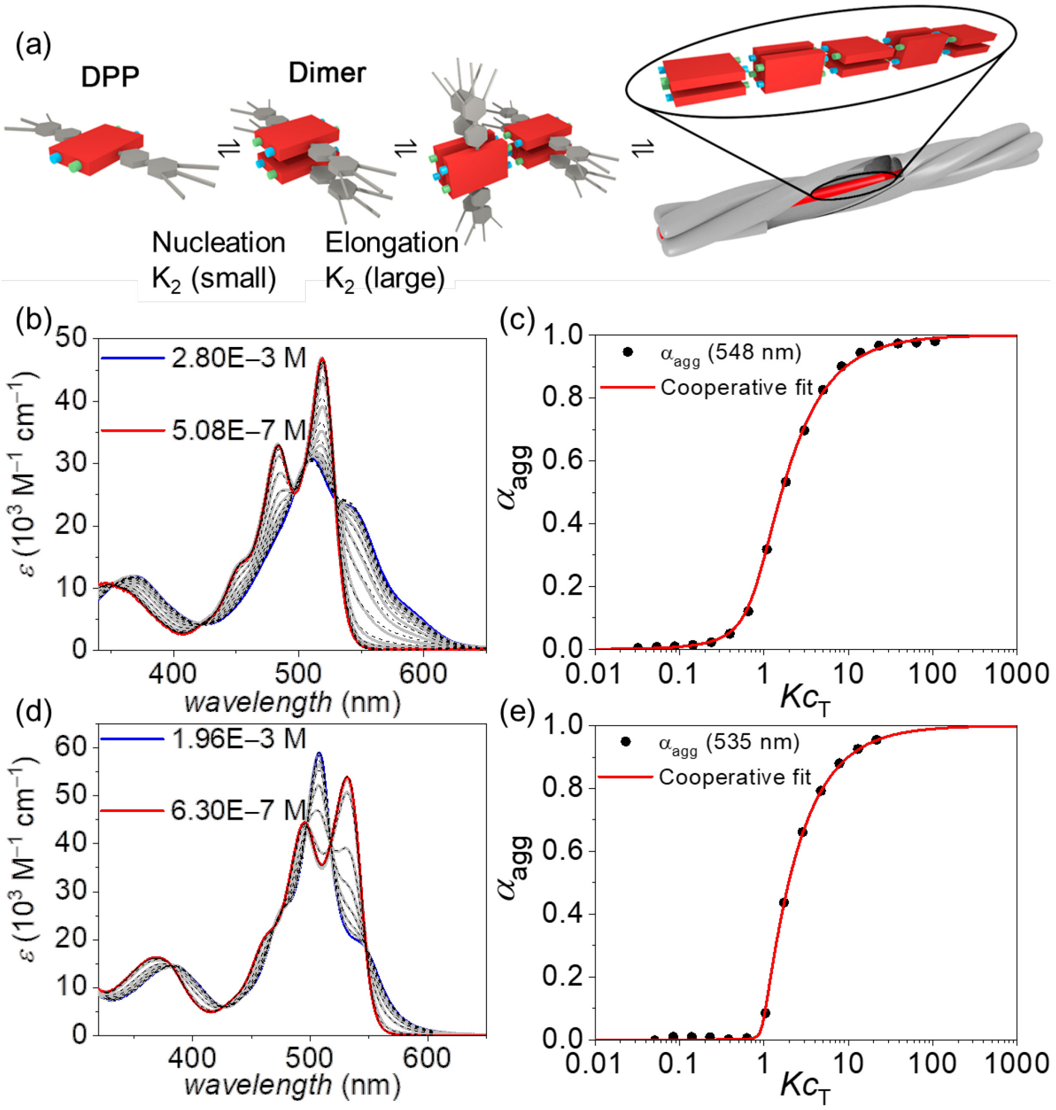

Figure 35. (a) Graphical illustration of the self-assembly process *via* the disfavoured dimeric nucleus. Concentration-dependent UV/Vis absorption spectra (coloured and grey lines) of (b) **DPP 1** between 5.08×10^{-7} M and 2.8×10^{-3} M and (d) **DPP 2** between 6.30×10^{-7} M and 1.96×10^{-3} M in toluene at 295 K and reconstructed spectra from the cooperative nucleation-elongation fit (black dashed lines). Plot of the experimental degree of aggregation α_{agg} over the Kc_T (black dots) for (c) **DPP 1** at 548 nm and (e) **DPP 2** at 535 nm and the corresponding fit according to the cooperative nucleation-elongation model (red).[94]

The visualization of the aggregates in solution of both DPPs was achieved by AFM. For this purpose, solutions of **DPP 1** ($c = 1.0 \times 10^{-4}$ M) and **DPP 2** ($c = 6.5 \times 10^{-4}$ M) in toluene were spin-coated onto highly oriented pyrolytic graphite (HOPG) (Figure 36a and b). These investigations showed that **DPP 1** forms stiff fibers with a thickness of around 1.3 nm and a length of up to 800 nm. The thickness of the fibers is in good agreement with the width of the axis of the molecule along the wedge-shaped residues. This complies with the formation of 1D supramolecular polymers composed of dimeric DPP units as previously observed in the columnar LC phase of **DPP 1**.[257] **DPP 2**, on the other hand, forms more flexible fibers with a thickness of around 2.5 nm and a length of up to 800 nm. The flexibility of these 1D self-assemblies seems to promote the entanglement of the single 1D supramolecular polymers, which is not observed in **DPP 1** assemblies (Figure A83).

The concentration-dependent UV/Vis and AFM studies clearly show that **DPP 1** and **DPP 2** self-assemble into 1D fibers *via* a cooperative mechanism. Based on the AFM profiles, we assume that these structures consist of H-bonded DPP dimers, similar to those which compose a columnar slice in the LC phases (Figure 34c-e). However, significant morphologic differences are found between the **DPP 1** and **DPP 2** fibers in AFM experiments (Figure 36).

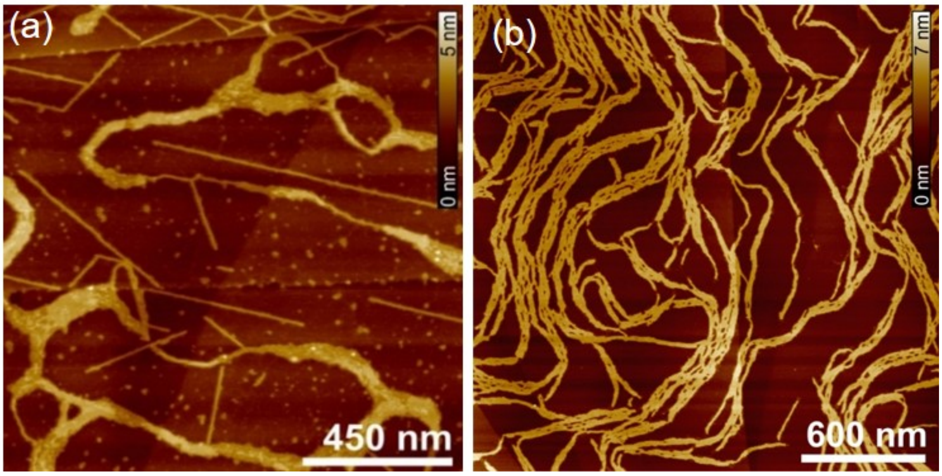

Figure 36. AFM height images of (a) **DPP 1** ($c = 1.0 \times 10^{-4}$ M) and (b) **DPP 2** ($c = 6.5 \times 10^{-4}$ M) spin-coated from solutions in toluene on HOPG.

While **DPP 2** forms flexible fibers which lead to the gelation of toluene solutions at high concentrations, **DPP 1** forms more rigid fibers that do not tend to entangle and hence do not lead to gelation of the solutions. Accordingly, it appears to be that the formation of entangled fibers and gels are a prerequisite for the electrospinning process of such small molecule based supramolecular polymers. As a control experiment, we also attempted to electrospin **DPP 2** in a toluene/DMF mixture where no supramolecular polymers and gels are formed due to the disruption of the H-bonds. This experiment failed to fabricate microfibers (Figure A98), proving the necessity of the formation of supramolecular polymer fibers in solution for the successful electrospinning process.

6.4 Conclusion

In this work, we have achieved the fabrication of anisotropic LC microfibers by electrospinning of hydrogen-bonded supramolecular polymers of **DPP 2** in toluene. The presence of entangled supramolecular polymers in solution appears to be crucial for the success of the electrospinning process of small molecules. Furthermore, we have elucidated the molecular arrangement within the electrospun fiber by POM and SAED investigations showing a homogeneous arrangement of DPP molecules within well-defined LC columnar domains. Accordingly, the electrospinning approach opens a new avenue for the creation of micrometre-sized fibers of organic molecules possessing unique electronic properties with well-ordered LC domains as desired for optoelectronic applications.

6.5 Appendix to *Chapter 6*

Materials and Methods

Materials

Reagents were purchased from commercial suppliers (Sigma-Aldrich, ACROS, Alfa Aesar, Merck) and used as received without further purification. Solvents were distilled and dried by standard procedures. All reactions were carried out under nitrogen atmosphere.

Flash Chromatography

Flash chromatography was carried out with a PuriFlash 450 system from *Interchim* with columns containing silica gel from *Interchim* (PF-30SIHP-F0012, PF-30SIHP-F0025, PF-30SIHP-F0040, PF-25SIHC-F0025 and dry load columns of various sizes that were filled with silica gel 60 M (particle size: 0.040-0.063 mm from *Merck*). Columns were used according to the recommendation from *Interchim*. Used solvents were of HPLC grade purchased from *Fisher scientific*.

Size Exclusion Chromatography

Size exclusion chromatography was performed with commercial glass columns using Bio-Beads® S-X3 from Bio-Rad as stationary phase.

NMR Spectroscopy

^{1}H and ^{13}C NMR spectra were recorded on a Bruker Avance III 400 spectrometer operating at 400 MHz (^{1}H) or 100 MHz (^{13}C), with the residual protonated solvent used as the internal standard. The chemical shifts are reported in parts per million (ppm). Multiplicities for proton signals are abbreviated as s, d, t and m for singlet, duplet, triplet and multiplet, respectively.

Mass Spectrometry

High resolution mass spectra (HRMS) were recorded on an ESI micrOTOF focus spectrometer (Bruker Daltonic GmbH, Germany).

Elemental Analysis

Elemental analyses were performed on a CHN 932 analyzer (Leco Instruments GmbH, Mönchengladbach, Germany).

UV/Vis Spectroscopy

UV/Vis absorption spectra in solution were recorded using a JASCO V-770 spectrophotometer. The spectra were measured in quartz glass cuvettes using spectroscopic grade solvents. Temperature control was accomplished by JASCO PAC-743R Peltier system. Extinction coefficients were calculated according to Lambert-Beer's law. The UV/Vis absorption spectrum of the electrospun fiber was recorded with an Axio Imager 2 (Zeiss, Germany) polarizing optical microscope equipped with a cooled CCD spectrometer MCS-CCD PCI (Zeiss, Germany).

Polarized Optical Microscopy

The LC materials were examined under an Axio Imager 2 (Zeiss, Germany) polarized optical microscope equipped with a LTS420+LNP95 heating stage (Linkam, Great Britain).

Differential Scanning Calorimetry

Thermal analyses by DSC were performed on a TA instrument DSC Q1000 with a DSC refrigerated cooling system.

FT-IR Spectroscopy

Temperature-dependent and polarized FT-IR spectra were recorded with an AIM-8800 infrared microscope connected to a Shimadzu IRAffinity FT-IR spectrometer. Samples were prepared as a thin films on KBr plates (thickness 2 mm), which were placed on a THMS600 heat stage with a Linkam TP94 controller. Polarization dependent FT-IR spectra were measured by using a precision automated polarizer (ZnSe) from PIKE Technologies. This includes the PIKE Technologies Motion Control Unit and AutoPro software.

Wide-Angle and Middle-Angle X-Ray Scattering

Temperature-dependent WAXS and MAXS measurements were performed on a Bruker Nanostar (Detector Vantec2000, Microfocus copper anode X-ray tube Incoatec). LC samples were prepared by fiber extrusion using a mini-extruder. The measurements were carried out in Mark capillaries (Hilgenberg) that were positioned perpendicular to the incident X-ray beam. WAXS experiments were performed at a sample detector distance of 21 cm, with the detector tilted by 14° upwards in order to study the angular range of 2Θ = 0.8° - 28°. Additional MAXS studies were carried out at a distance of 28 cm with a linear assembled detector, covering an angular range of $2\theta = 0.7° - 12°$. The WAXS pattern of

DPP 1 was recorded at a distance of 13 cm. Silver behenate was used as calibration standard for WAXS, MAXS. All X-ray data were processed and evaluated with the program datasqueeze (http://datasqueezesoftware.com/).

Density Measurements

For density measurements, a small mass of sample (~0.4 mg) was placed in a vial, which was filled with ethanol, followed by ultrasonication to remove the air bubbles embedded within the sample. The sample sank to the bottom of the vial due to its high density compared with ethanol. Water was then added at ~0.1 g per aliquot to gradually increase the solution density at an interval of at least 20 min to ensure thermal equilibrium of the solution. When the sample was suspended in the middle of the solution, the density of the sample was identical to that of the solution.

Atomic Force Microscopy

AFM measurements were performed under ambient conditions using a Bruker Multimode 8 SPM system operating in tapping mode in air. Silica cantilevers (OMCL-AC200TS, Olympus) with a resonance frequency of ~150 kHz and a spring constant of ~10 N m^{-1} were used. Samples were prepared by spin-coating of toluene solutions onto HOPG with 7000-10000 rpm.

Selected Area Electron Diffraction

SAED patterns were obtained with the FEI Titan 80-300 transmission electron microscope operated at 300 kV.

Electrospinning

The electrospinning experiments were carried out with a home-made machine basically containing a high voltage source, a collector and the solution container (syringe). The electric field was applied between the needle (0.3 mm diameter) of the syringe and the collector. The distance between the needle and the collector was 20 cm. The applied voltage at the positive electrode and the flow rate were adjusted between 0 kV to 30 Kv and 0.1 ml/h to 2 ml/h for optimized fiber formation. The applied voltage of 20 kV at a flow rate of 0.1 ml/h produced **DPP 2** fibers. The negative electrode used in this experiment was grounded.

Synthetic Procedures

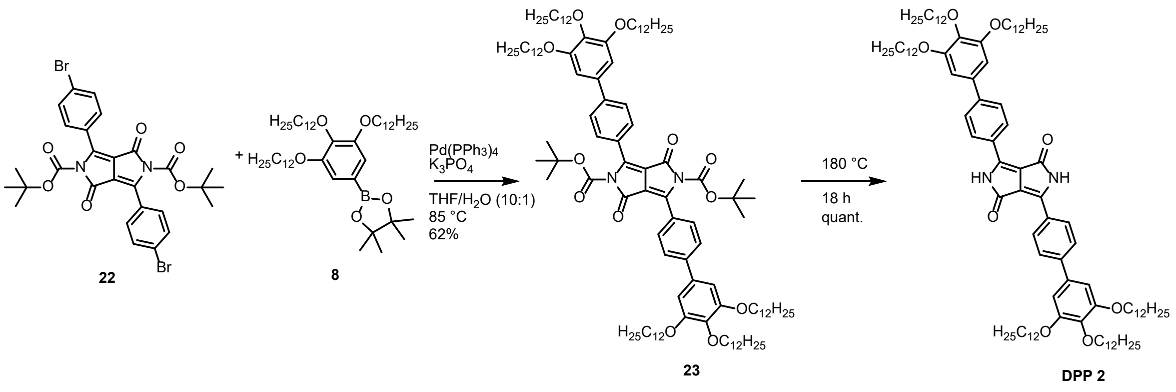

Scheme A4. Synthetic route towards **DPP 2**.

The precursors **22**[261,262] and **8**[263,264] were synthesized according to literature known procedures. The synthesis of **DPP 1** was previously reported by our group.[257]

3,6-Bis(3',4',5'-tris(dodecyloxy)-(1,1'-biphenyl)-4-yl)-2,5-dihydropyrrolo[3,4-*c*]pyrole-1,4-dione dicarboxylic acid di-*tert*-butyl ester (23)

A pressure tube was charged with **22** (211 mg, 0.33 mmol), **8** (586 mg, 0.77 mmol), $Pd(PPh_3)_4$ (52 mg, 45 µmol) and K_3PO_4 (200 mg, 0.94 mmol) under N_2 atmosphere. A mixture of THF and H_2O (10:1) was degassed with N_2 for 1.5 h. The solvent mixture (22 ml) was then added to the pressure tube and the reaction mixture was heated to 85 °C for 5 h. A colour change from bright orange to dark red was observed during the reaction. After being cooled to room temperature, the mixture was diluted with CH_2Cl_2 (150 ml) and water (100 ml). The organic phase was separated and the solvent was removed under reduced pressure. The crude product was purified by flash chromatography (pentane:CH_2Cl_2 1:0 → 7:3) and consecutive size exclusion chromatography (BioBeads SX3, CH_2Cl_2).
Yield: 355 mg (0.20 mmol, 62%) of an orange-red solid.

^{1}H NMR (400 MHz, $CDCl_3$): δ = 7.82 (d, ^3J = 8.6 Hz, 4H, Ar*H*), 7.66 (d, ^3J = 8.6 Hz, 4H, Ar*H*) 6.81 (s, 4H, Ar*H*), 4.03 (m, 12H, OCH_2), 1.81 (m, 12H, $OCH_2C$$H_2$), 1.54-1.44 (m, 12H, $O(CH_2)_2C$$H_2$), 1.49 (s, 18H, boc C$H_3$), 1.40-1.23 (m, 96H, alkyl), 0.87 (m, 18H, CH_3). **^{13}C NMR** (100 MHz, $CDCl_3$): δ = 159.7, 153.6, 148.6, 145.9, 144.7, 138.8, 135.3, 129.1, 126.9, 126.8, 112.4, 106.1, 85.5, 73.7, 69.5, 32.1, 30.5, 29.9, 29.8, 29.6, 29.5, 27.8, 26.3, 22.8, 14.3. **HRMS** (ESI-TOF, positive mode, MeCN/$CHCl_3$ 1:1): *m/z* calculated for $C_{112}H_{180}N_2O_{12}$ $[M+Na]^+$: 1769.3468; found, 1769.3418. **Elemental analysis** calculated (%) for $C_{112}H_{180}N_2O_{12}$ [M = 1746.67 g/mol]: C 77.02 H 10.39 N 1.60; found, C 77.05 H 10.62 N 1.41.

3,6-Bis(3',4',5'-tris(dodecyloxy)-(1,1'-biphenyl)-4-yl)-2,5-dihydropyrrolo[3,4-*c*]pyrrole-1,4-dione (DPP 2)

Precursor **23** (211 mg, 0.14 mmol) was dissolved in CH_2Cl_2 (40 ml). The solvent was removed quickly under reduced pressure to form a thin layer of material in the flask. The flask was then heated to 180 °C for 18 h.
Yield: The product is obtained quantitatively as a dark-red wax-like solid.

^{1}H NMR (400 MHz, $CDCl_3$:DMSO-d_6, 99:1): $\delta = 10.10$ (s, 2H, NH), 8.42 (d, $^3J = 8.5$ Hz, 4H, ArH), 7.68 (d, $^3J = 8.5$ Hz, 4H, ArH), 6.78 (s, 4H, ArH), 3.98 (m, 12H, OCH_2), 1.76 (m, 12H, OCH_2CH_2), 1.44 (m, 12H, $O(CH_2)_2CH_2$), 1.35-1.20 (m, 96H, alkyl), 0.84 (m, 18H, CH_3). **^{13}C NMR** (100 MHz, $CDCl_3$/DMSO-d_6 99:1): $\delta = 163.3$, 153.5, 144.2, 143.9, 138.6, 135.3, 128.5, 127.5, 126.7, 111.4, 105.7, 73.6, 69.3, 32.0, 30.4, 29.8, 29.7, 29.5,29.4, 26.2, 22.7, 14.2. **HRMS** (ESI-TOF, positive mode, $CHCl_3$/MeOH 1:1 + 0.1% CHOOH): *m/z* calculated for $C_{102}H_{164}N_2O_8$ $[M+H]^+$: 1547.2600, found: 1547.2530. **Elemental analysis** calculated (%) for $C_{102}H_{164}N_2O_8$ [M = 1546.44 g/mol]: C 79.22 H 10.69 N 1.81; found, C 79.06 H 10.99 N 1.69. **UV/Vis** ($CHCl_3$, $c = 30$ µM, nm): λ_{max} (ε_{max} M^{-1} cm^{-1}) = 531 (57000). **m.p.** 270 °C.

Polarized Optical Microscopy and Temperature-Dependent UV/Vis Absorption Spectroscopy

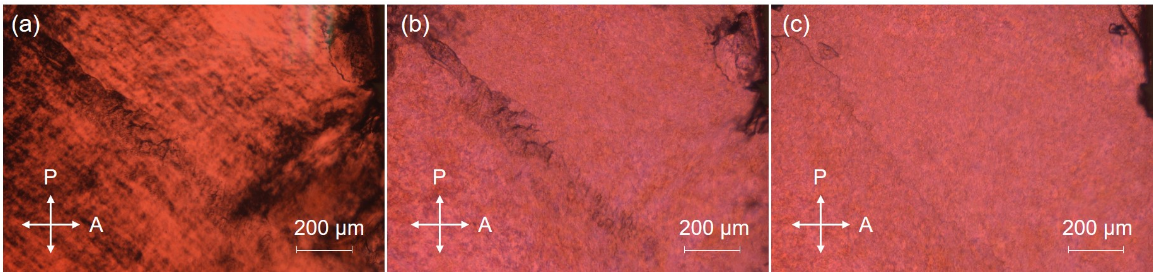

Figure A81. POM images of **DPP 2** at (a) 170 °C, (b) 210 °C and (c) 260 °C.

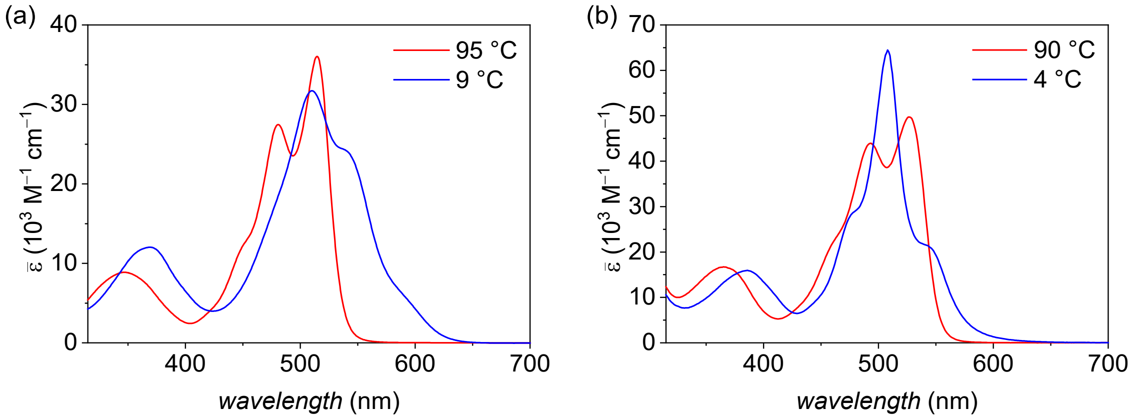

Figure A82. UV/Vis absorption spectra of (a) **DPP 1** in toluene (c = 4.1×10^{-4} M) at 95 °C (red) and 9 °C (blue) and (b) **DPP 2** in toluene (c = 5.0×10^{-4} M) at 90 °C (red) and 4 °C (blue).

Tube Inversion Test for Gelation

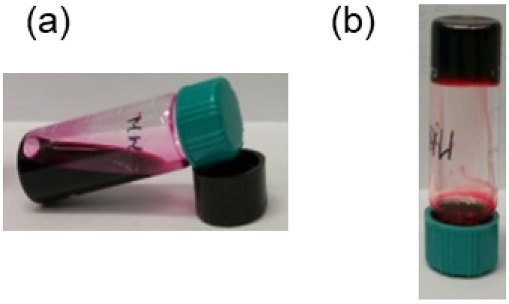

Figure A83. Tube inversion test of (a) **DPP 1** and (b) **DPP 2** at c = 20 mM in toluene.

Polarized Optical Microscopy of Electrospun Fibers of DPP 2

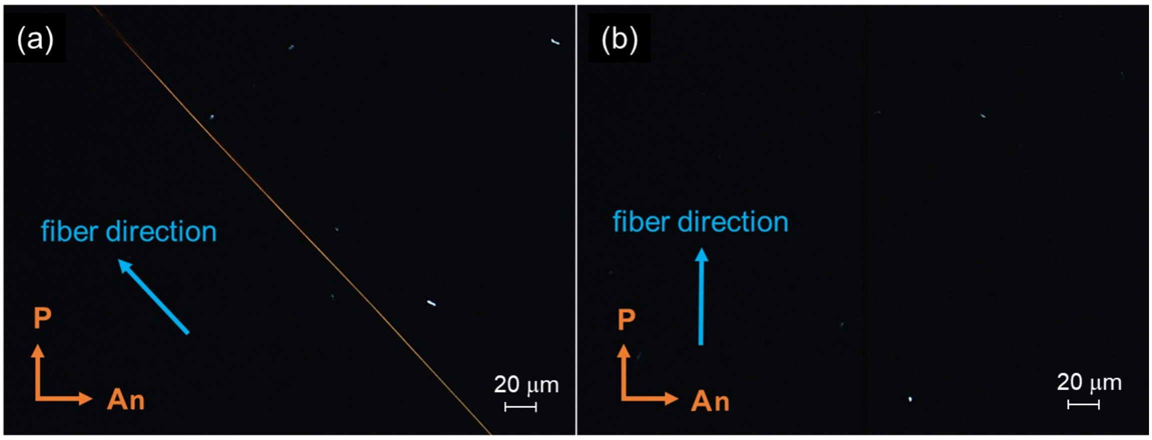

Figure A84. POM images of an electrospun fiber of **DPP 2** on a glass substrate with the fiber rotated (a) 45° and (b) 0°/90° with respect to the polarizer/analyzer.

In order to probe the anisotropic nature of the electrospun fibers, the sample was investigated with a polarized optical microscope. Polarizer and analyzer were perpendicular to each other. The microphotographs were captured with the sample oriented in a 45° displacement (Figure A84a) and along (Figure A84b) the polarizer and analyzer.

Calculated Intra- and Intermolecular Distances

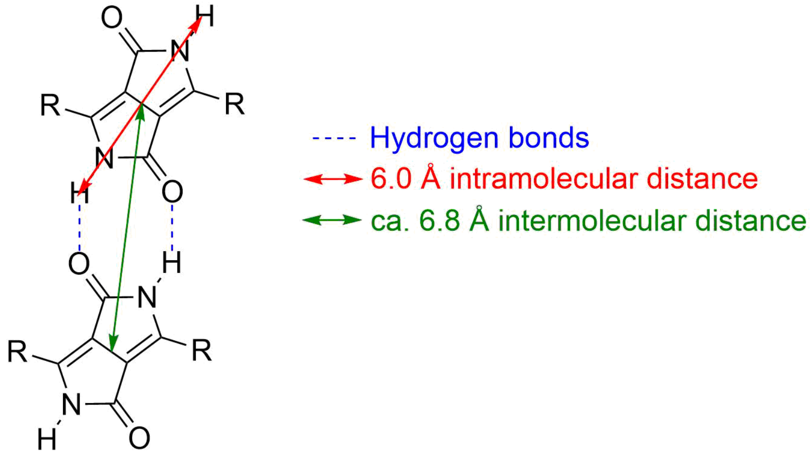

Figure A85. Schematic illustration of the relevant intra- and intermolecular distances. The structure of the molecule was drawn with ChemDraw and imported to Chem3D. After optimizing the structure in a MM2+ forcefield, the intramolecular distance between NH and NH was calculated to be 6.0 Å. The intermolecular distance represents an estimation of the core to core distance considering the H-bonding distance.

Differential Scanning Calorimetry

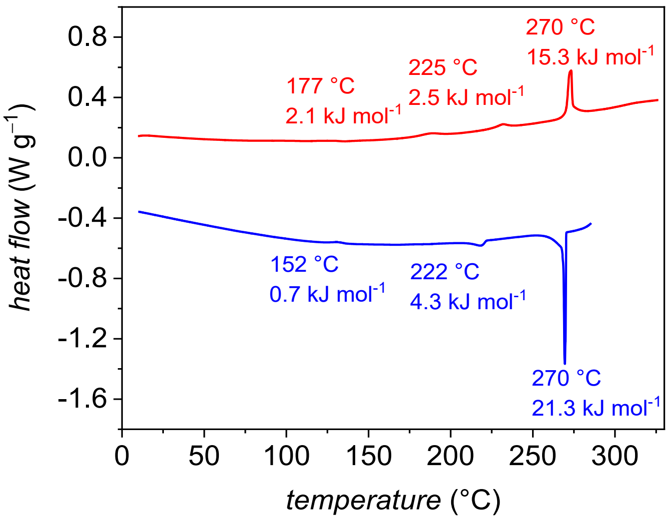

Figure A86. DSC traces of **DPP 2** in the first cooling (blue) and the second heating (red) process. The heating and cooling rates were 5 °C/min.

X-Ray Scattering

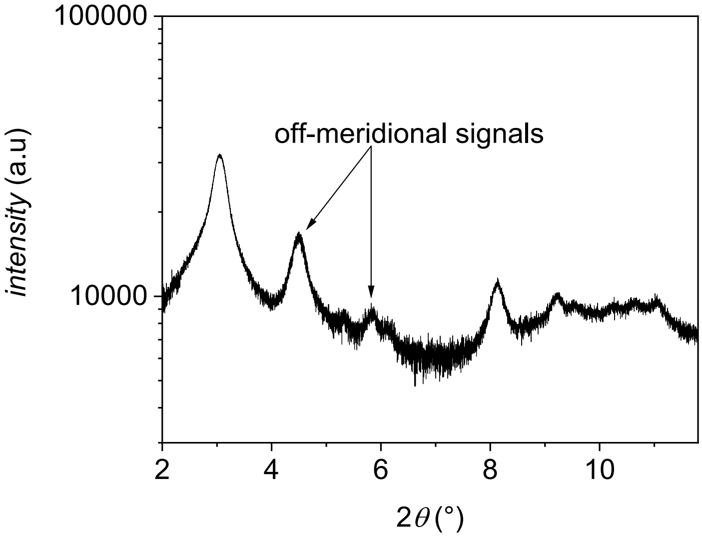

Figure A87. Integrated intensities along the equator of the WAXS pattern of an aligned fiber of **DPP 2** at 150 °C.

The equatorial signals of the SC low temperature phase of **DPP 2** could not be unambiguously identified as a Col$_h$ (a = 33.25 Å) and a columnar centred rectangular (a = 57.85 Å, b = 33.20 Å) unit cell match the experimental signals. Nevertheless, the formation of a columnar unit cell can clearly be seen.

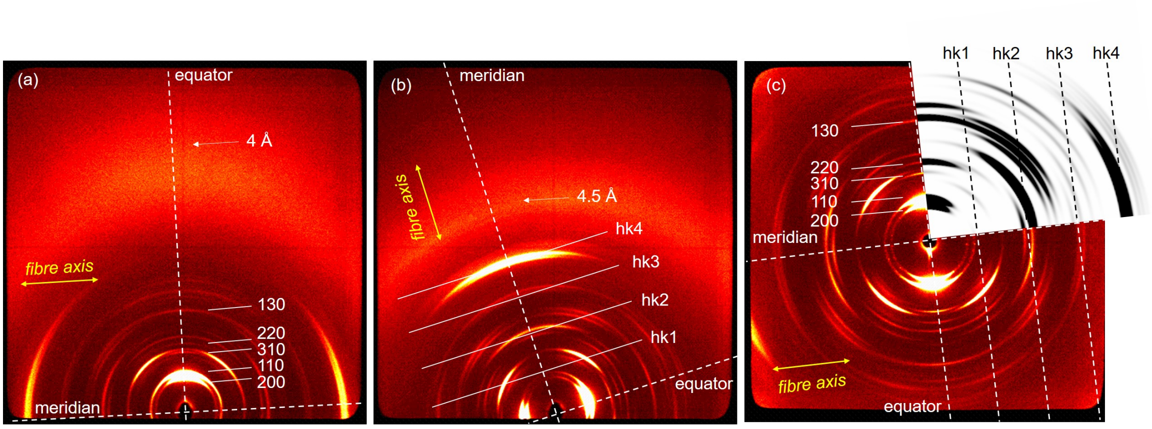

Figure A88. WAXS patterns of an extruded fiber of **DPP 2** at 210 ˚C with the fiber axis (a) lying and (b) standing. (c) Superposition of the simulated diffraction pattern obtained by *CLEARER* and the MAXS pattern of **DPP 2** at 210°C.

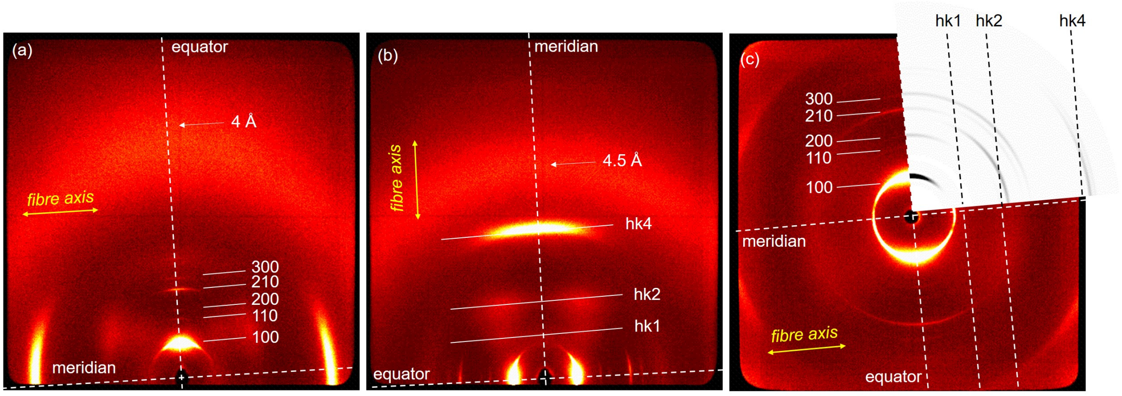

Figure A89. WAXS patterns of an extruded fiber of **DPP 2** at 265 ˚C with the fiber axis (a) lying and (b) standing. (c) Superposition of the simulated diffraction pattern obtained by *CLEARER* and the MAXS pattern of **DPP 2** at 265 °C.

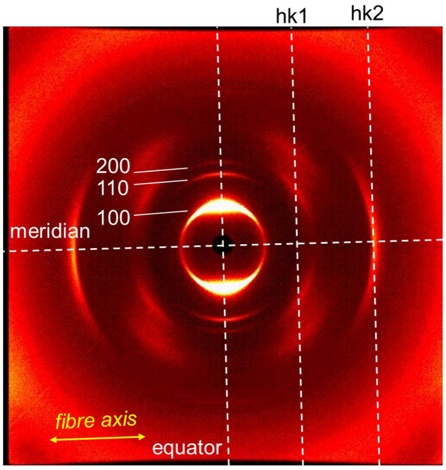

Figure A90. MAXS pattern of an extruded fiber of **DPP 1** at 80 °C.

Polarized FT-IR Spectroscopy

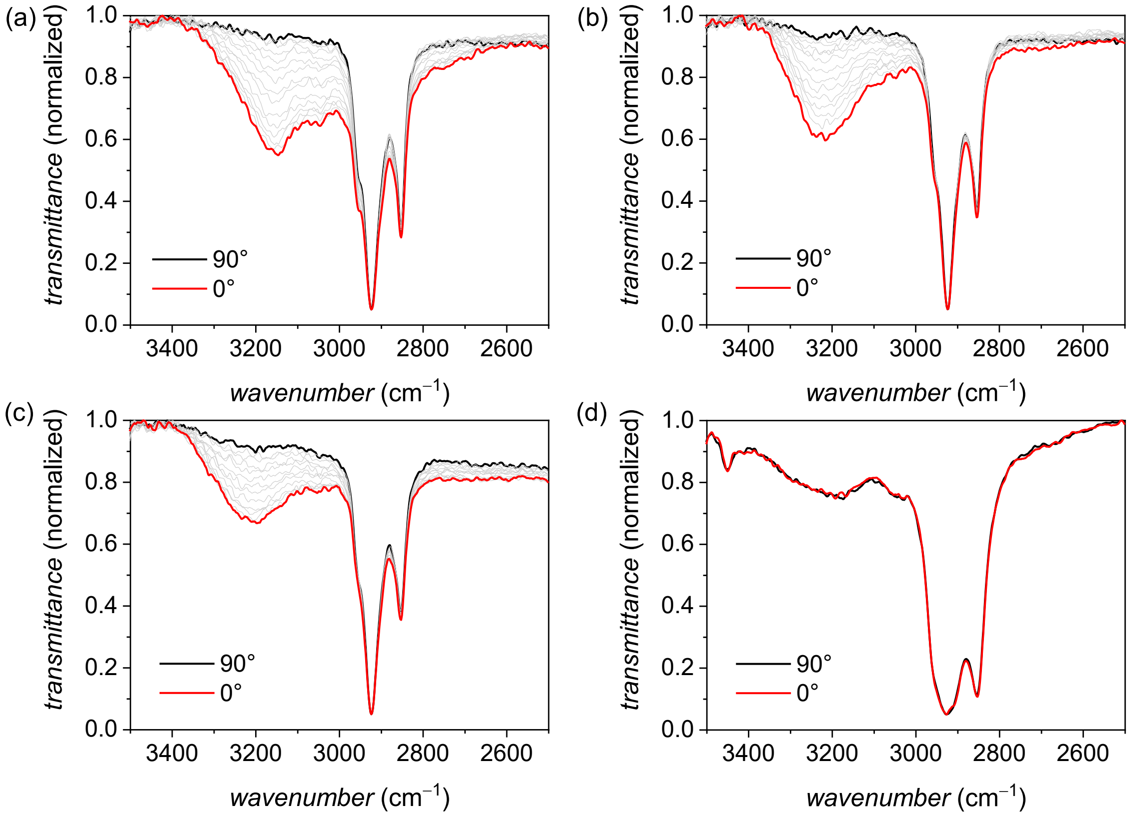

Figure A91. Polarized FT-IR spectra with different polarization angles of an aligned sample of **DPP 2** at (a) 150 °C (SC), (b) 210 °C (Col$_r$), (c) 250 °C (Col$_h$) and (d) 270 °C (melt). The sample was sheared using an extruded fiber for friction transfer on a KBr substrate. The black line shows the FT-IR spectrum when the polarizer is oriented perpendicular to the shearing direction. The red line shows the spectrum when the polarizer is oriented parallel to the shearing direction.

Molecular Modelling

The number of molecules Z per columnar stratum was calculated using equation (1) with δ as the density (assumed to be 0.9 g cm^{-3}, adjusted to high temperatures from experimental value), N_A as Avogadro's constant, M as the molecular mass and $V_{col-strat}$ representing the volume of the columnar stratum which was calculated according to equation (8) for the hexagonal phase and according to

$$V_{col-strat} = a * b * h * 0.5 \tag{13}$$

for the rectangular phase.

Using the parameters obtained from the X-ray diffraction experiments with a reasonable error margin of 5% per parameter, the number of molecules per columnar stratum was calculated to be 2.10 for the Col$_r$ phase and 2.28 for Col$_h$ phase.[258]

The molecular structure of **DPP 2** with the dodecyloxy substituents being shortened to methoxy groups was geometry optimized using the MM2 forcefield with the program Chem3D. The optimized molecular structure was then imported to *Materials Studio* from BIOVIA.[130] Mirror imaged antiparallel dimers were then built with a distance of 4 Å between the π-cores. The two dimers were then alternately stacked by a rotation of 90° with each dimer. To build the unit cell of the $\mathrm{Col_r}$ phase, the structure was placed on the diagonal corners of a rectangular unit cell ($a = 65.4$ Å, $b = 31.5$ Å and $h = 4 \times 6.8$ Å $= 27.2$ Å). The two structures were then moved about *a/4* and *b/4* towards the centre of the unit cell. To build the unit cell of the $\mathrm{Col_h}$ phase, the structure was placed in the centre of a hexagonal unit cell ($a = 35.9$ Å and $h = 4 \times 6.8$ Å $= 27.2$ Å). Both model assemblies were then geometry optimized using the force field COMPASS by Ewald summation method, until the non-bonding energy was strongly negative.

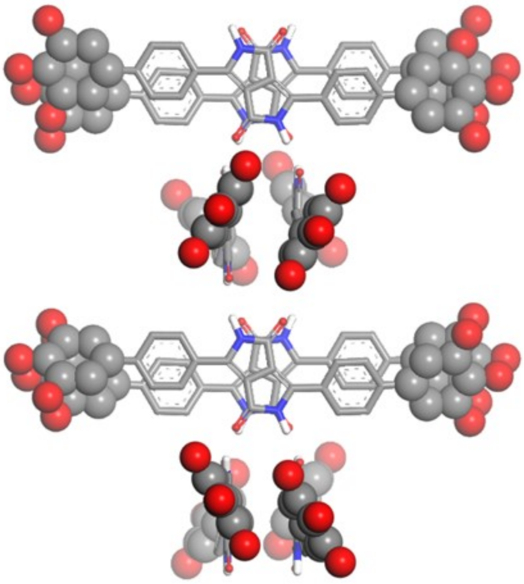

Figure A92. Model of the geometry optimized unit cell of **DPP 2** for the LC phases ($\mathrm{Col_h}$ and $\mathrm{Col_r}$) as obtained with Materials Studio. The alkyl chains were omitted for clarity. The wedge-shaped substituent is highlighted as CPK model to illustrate the correlation between every fifth molecule induced by the rotationally displaced π-cores.

The fiber diffraction patterns of **DPP 2** were simulated with *CLEARER* using the geometry optimized structures obtained from *Materials Studio*. The structure was exported as PDB-file and imported into the Fiber Diffraction Simulation module of *CLEARER*.[134] The fiber axis was set to (0,0,1) with a crystallite size of $a = 100$ nm, $b = 100$ nm and $c = 100$ nm. The fiber disorder parameters σ_Θ and σ_Φ were set to 0.1 radians and infinite, respectively. The sample interval was set to 1 pixel. The contrast was adjusted to best visualize the signals of the pattern.

It needs to be considered that *CLEARER* simulates the diffraction pattern for a perfectly ordered crystalline domain of a given size on the basis of one unit cell where the disorder of orientation is implemented in the unit cell. Therefore, the intensity of the predicted signals can vary from the experimentally observed ones. However, it should be noted that the relative intensity and the position of the predicted signals are in very good agreement with the ones observed in the experiments.

Figure A93. Diffraction pattern as simulated with *CLEARER* for the $\mathrm{Col_r}$ phase of **DPP 2**.

Figure A94. Diffraction pattern as simulated with *CLEARER* for the $\mathrm{Col_h}$ phase of **DPP 2**.

UV/Vis experiments

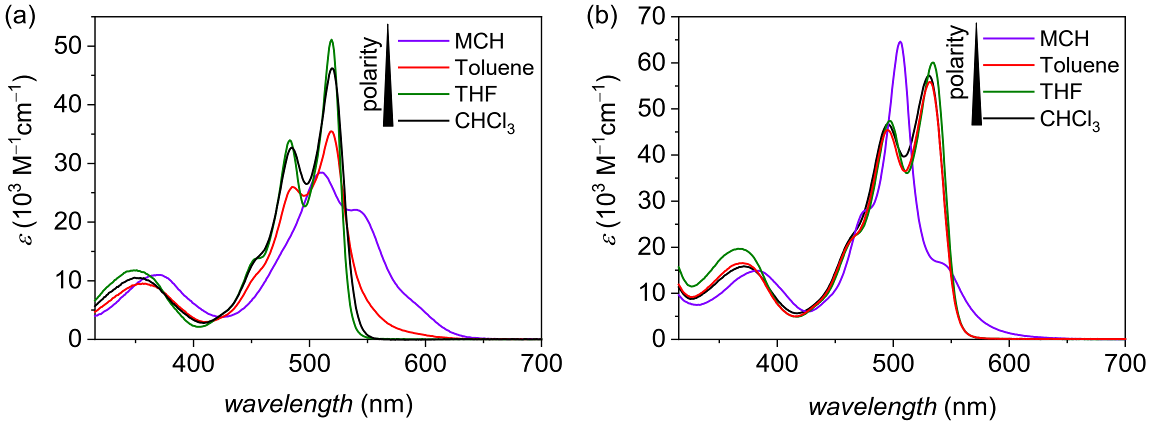

Figure A95. Solvent-dependent UV/Vis absorption studies of (a) **DPP 1** and (b) **DPP 2** in methyl cyclohexane (MCH, purple), toluene (red), THF (green) and chloroform (black) at $c = 3.0 \times 10^{-5}$ M.

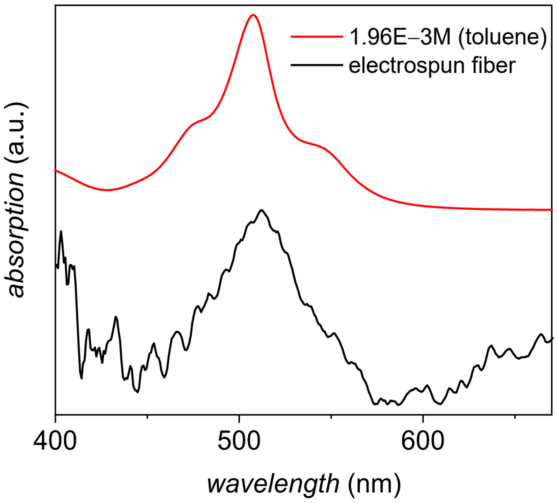

Figure A96. UV/Vis absorption spectra of **DPP 2** in toluene at $c = 1.96 \times 10^{-3}$ M (red) and of an electrospun fiber of **DPP 2** (black).

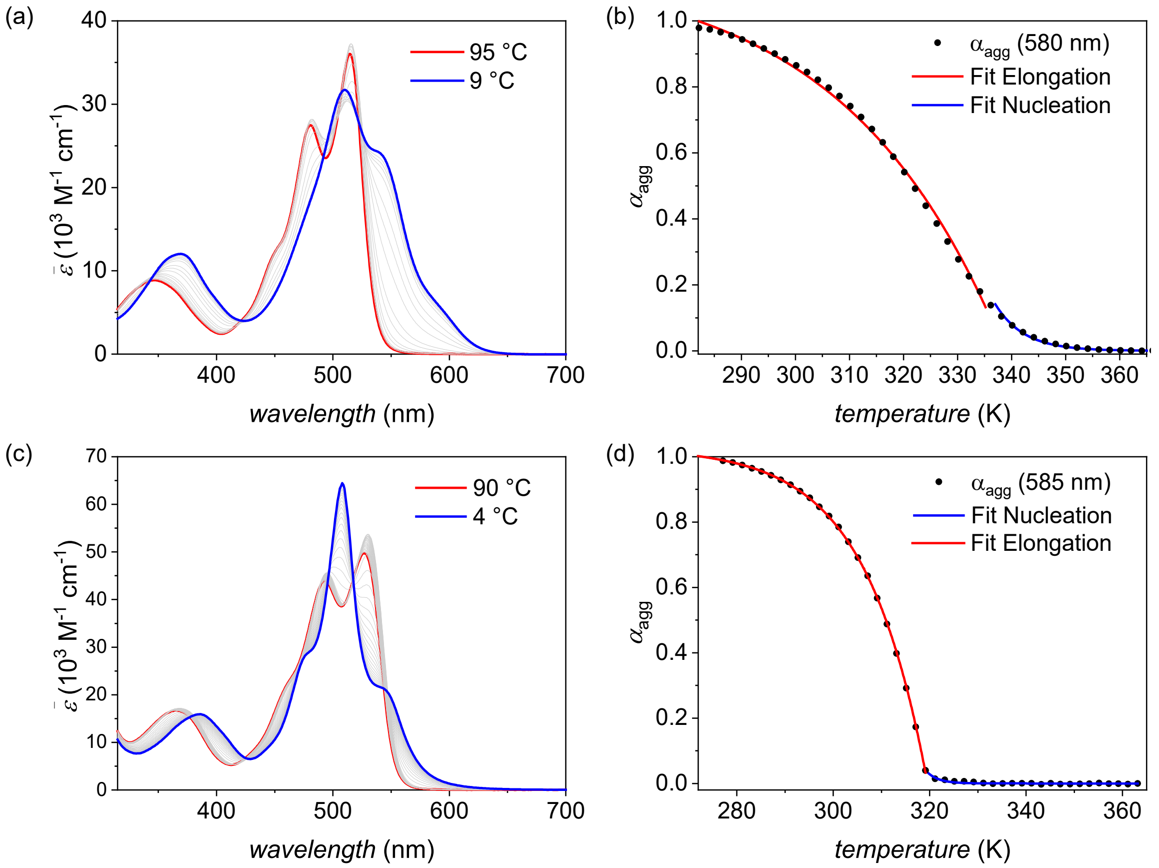

Figure A97. Temperature-dependent UV/Vis absorption studies of (a) **DPP 1** at $c = 4.1 \times 10^{-4}$ M in toluene and (c) **DPP 2** at $c = 5.0 \times 10^{-4}$ M in toluene and fit according to the cooperative nucleation-elongation model for (b) **DPP 1** at 580 nm and (d) **DPP 2** at 585 nm.

The self-assembly of both compounds was studied by temperature-dependent UV/Vis absorption experiments with heating/cooling rates of 1K/min. The calculated degree of aggregation α_{agg} was fitted according to the cooperative nucleation-elongation model.[34,95,158] For **DPP 1**, an enthalpy of $\Delta H = -35$ kJ/mol, an elongation temperature of $T_{\mathrm{elong}} = 339$ K and $K_{\mathrm{a}} = 1 \times 10^{-3}$ were obtained for the self-assembly at $c = 4.1 \times 10^{-4}$ M in toluene. For **DPP 2**, an enthalpy of $\Delta H = -65$ kJ/mol, an elongation temperature of $T_{\mathrm{elong}} = 320$ K and $K_{\mathrm{a}} = 4 \times 10^{-5}$ were obtained for the self-assembly at $c = 5.0 \times 10^{-4}$ M in toluene.

Electrospinning of Monomeric Solutions

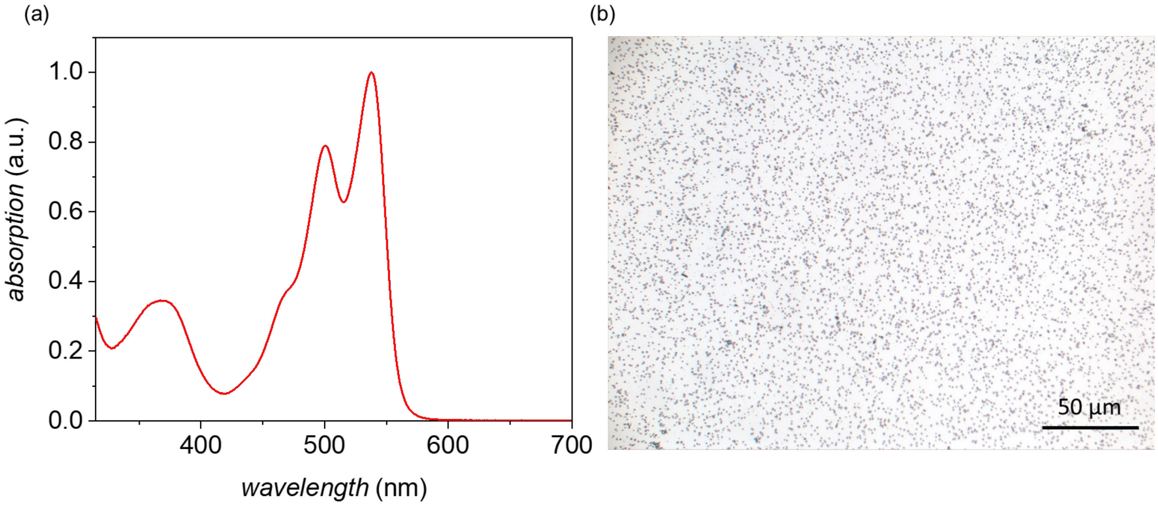

Figure A98. (a) UV/Vis absorption spectrum of a 20 mM solution of **DPP 2** in toluene/DMF (3/1) showing the characteristic features of monomeric DPP. (b) Microscopic image of the droplets collected from the electrospinning trials of a 20 mM solution of **DPP 2** in toluene/DMF (3/1).

NMR Spectra of 23 and DPP 2

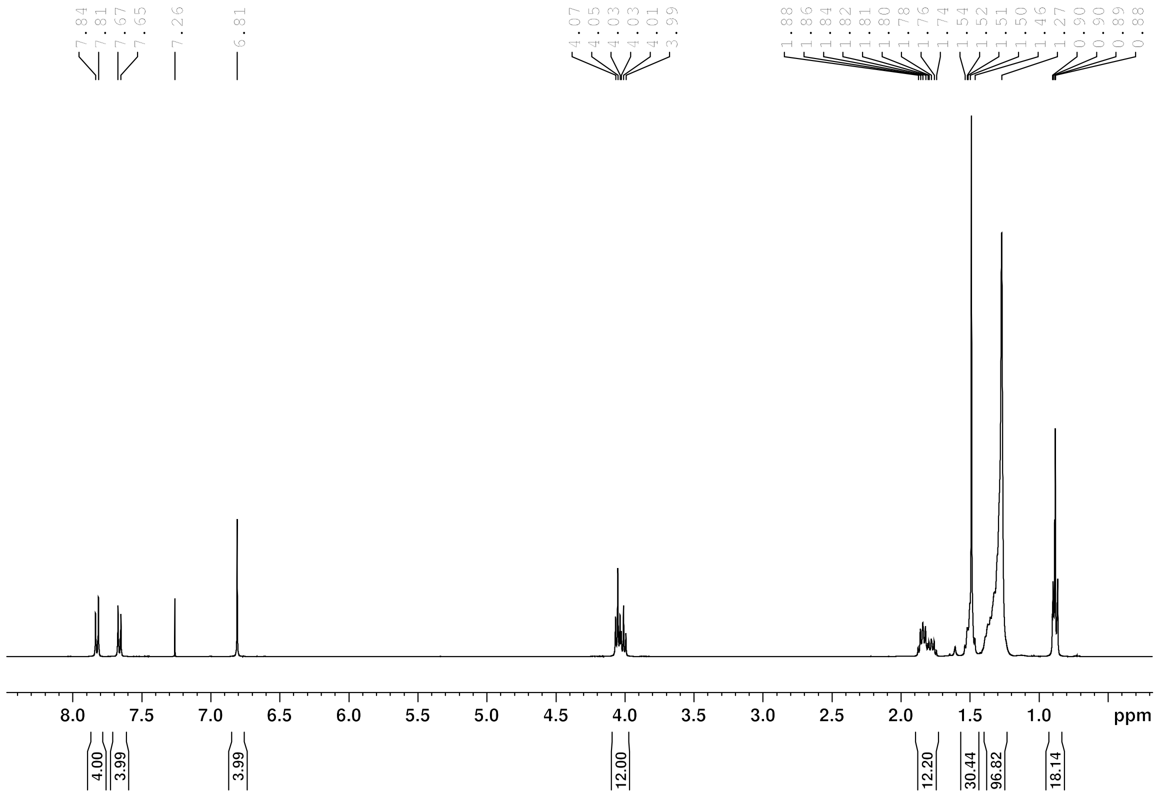

Figure A99. ^{1}H NMR spectrum (400 MHz) of **23** in $CDCl_3$ at 298 K.

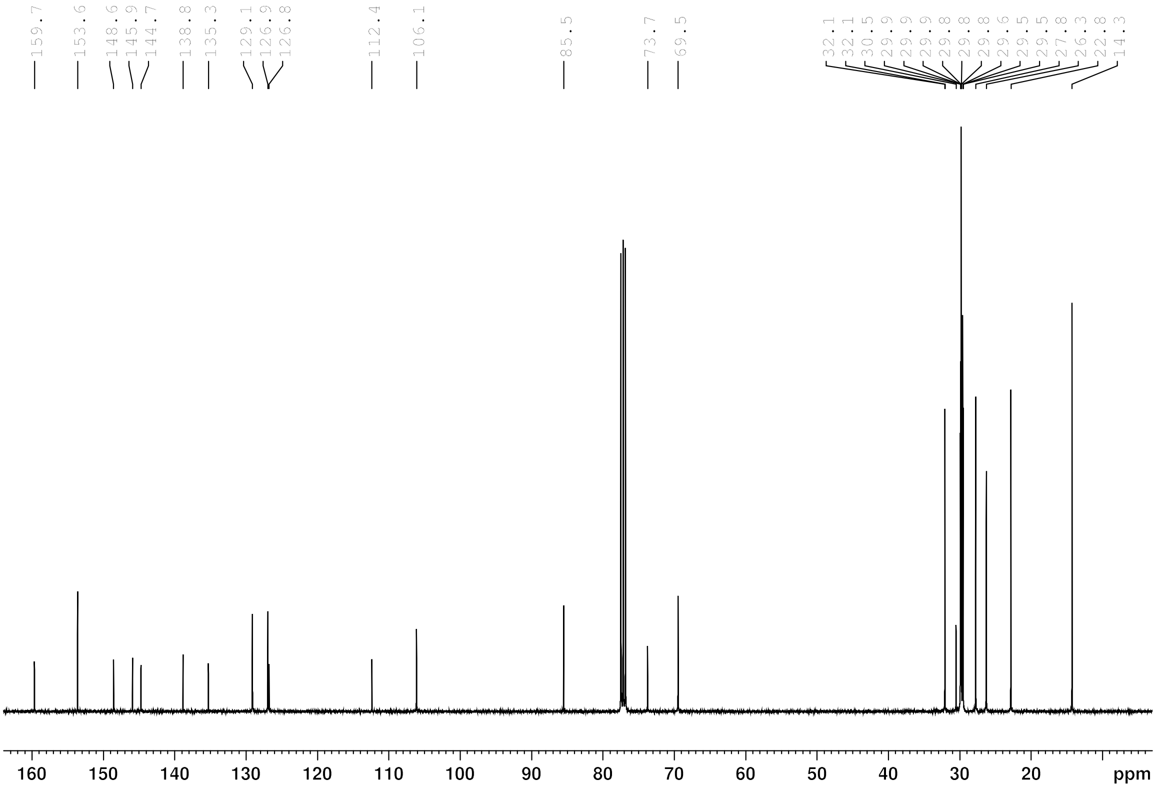

Figure A100. ^{13}C NMR spectrum (100 MHz) of **23** in $CDCl_3$ at 298 K.

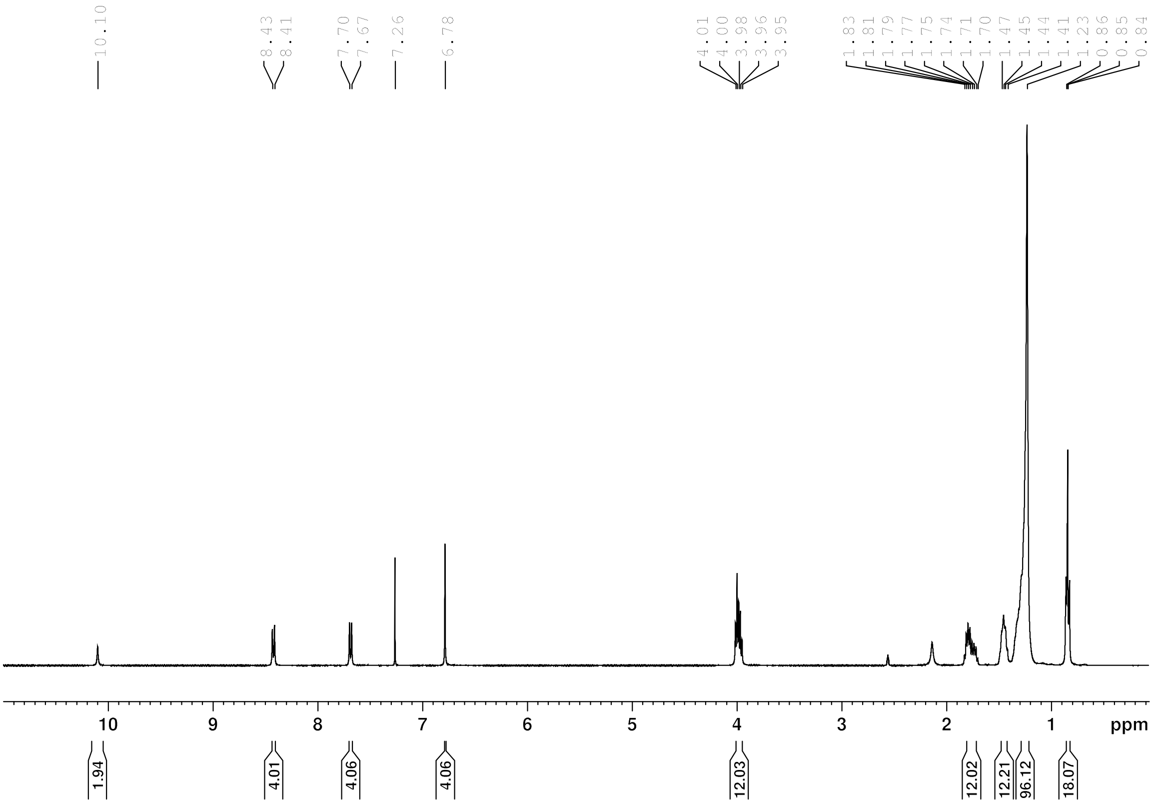

Figure A101. ^{1}H NMR spectrum (400 MHz) of **DPP 2** in $CDCl_3$:DMSO-d_6 (99:1) at 298 K.

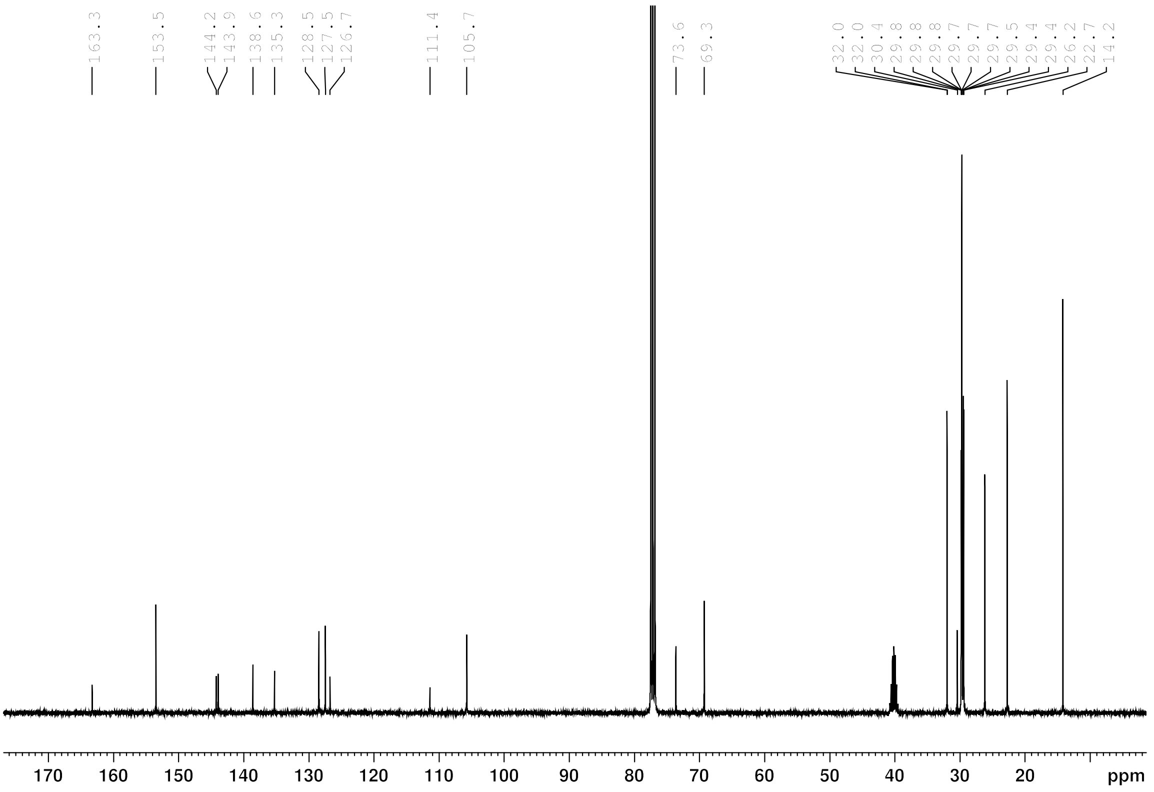

Figure A102. ^{13}C NMR spectrum (100 MHz) of **DPP 2** in $CDCl_3$:DMSO-d_6 (99:1) at 298 K.

Chapter 7

—

Summary and Conclusion

The research presented in this thesis illustrates that self-assembly of organic molecules guided by intermolecular forces is a versatile bottom-up approach towards functional materials. Through the specific design of the monomers, supramolecular architectures with distinct spatial arrangement of the individual building blocks can be realized. Particularly intriguing materials can be achieved when applying the supramolecular approach to molecules forming liquid-crystalline phases as these arrange in ordered, yet mobile structures. Therefore, they exhibit anisotropic properties on a macroscopic level. It is pivotal to precisely control the interchromophoric arrangement as functions originate in the complex structures that are formed upon self-assembly. Consequently, the aim of this thesis was the synthesis and characterization of liquid-crystalline phases with defined supramolecular arrangements as well as the investigation of the structure-property relationship. For this purpose, perylene bisimide and diketopyrrolopyrrole chromophores were used as they constitute ideal building blocks towards functional supramolecular materials due to their thermal stability, lightfastness, as well as excellent optical and electronic features desirable for the application in, e.g., organic electronics.

In *Chapter 3* and *Chapter 4*, donor–acceptor dyads of liquid-crystalline perylene bisimide J-aggregates were discussed. The molecules consist of 1,6,7,12-tetraphenoxy substituted perylene bisimide with trialkoxyphenyl-oligothiophenes appended to the phenoxy units in *meta*-position via an ester functionality (**PBI 1T**, **PBI 2T** and **PBI 3T**, Figure 38a). UV/Vis absorption spectroscopy revealed that no electronic coupling between the individual subunits of the molecules takes place and that these materials self-assemble by an interplay of hydrogen-bonding and π-π-interactions in a cooperative nucleation-elongation mechanism in non-polar solvents. The contorted π-core of the perylene bisimide facilitates the formation of a slip-stacked arrangement of perylene bisimides leading to J-type excitonic coupling of the chromophores causing a significant bathochromic shift of the main absorption band, both, in solution (Figure 37a) and the liquid-crystalline state (Figure 37b, see Appendix 9.1).

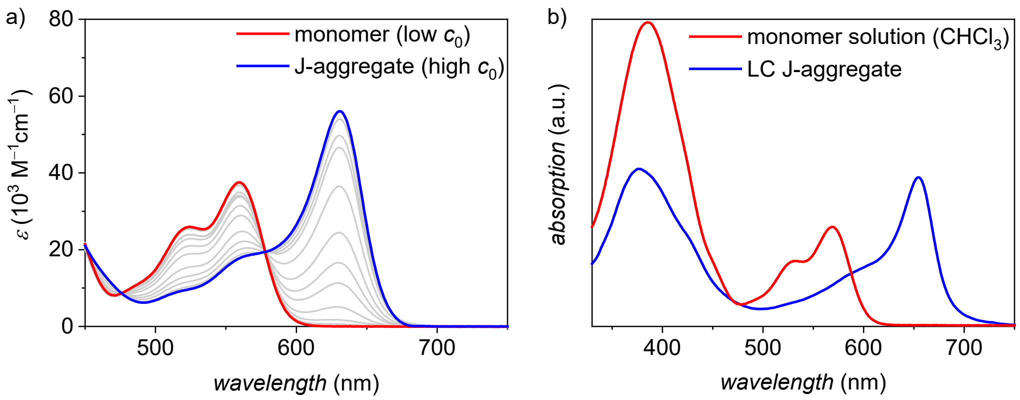

Figure 37. a) Concentration-dependent UV/Vis absorption spectra of **PBI 2T** (c_0 = 3.61 µM – 4.37 mM, toluene) showing monomers (red) at low concentration and PBI J-aggregate (blue) at high concentration. b) UV/Vis absorption spectra of monomeric **PBI 2T** (red, c_0 = 30 µM, chloroform) and **PBI 2T** J-aggregate in the LC thin film (blue).

In the liquid-crystalline state, these supramolecular structures in turn organize in columnar phases as evidenced by X-ray scattering experiments. Polarized UV/Vis and FT-IR spectroscopy of shear-aligned thin films indicated that the S_0-S_1 transition dipole moment of the perylene bisimide chromophore as well as hydrogen bonds are oriented along the columnar long axis. In-depth analysis of the X-ray scattering experiments combined with density measurements of the bulk material showed that the perylene bisimides arrange in multistranded helices, whose number of strands can be adjusted by fine-tuning the steric requirements of the bay substituents (Figure 38b). Accordingly, the formation of four-, six-, and seven-stranded helices was observed for **PBI 1T**, **PBI 2T** and **PBI 3T**, respectively. The influence of the increasing conjugation length of the electron-donating group from **PBI 1T** to **PBI 2T** and **PBI 3T** was investigated with fluorescence spectroscopy and femtosecond transient absorption spectroscopy which revealed an increased tendency for photoinduced electron transfer from **PBI 1T** to **PBI 3T** and the longest lifetime of the photogenerated perylene bisimide radical anion for **PBI 3T**. Moreover, the three materials were used in two-contact photoconductivity devices that were prepared either by spin-coating or solution-shearing to obtain isotropic and anisotropic liquid-crystalline active layers, respectively. Depending on the film-quality, $I_{90°}/I_{0°}$ ratios of up to 90 could be obtained (Figure 38c). Devices prepared with the columnar structures aligned perpendicular to the electrodes showed the highest photoconductivity upon illumination with a white light source. Aligned structures also proved to be superior to devices prepared with isotropic active layers as indicated by a 45-fold increased photoresponse. For reference, the photoconductivity on the supramolecular level was investigated with flash photolysis time resolved microwave conductivity measurements that are not affected by contact resistance and grain boundaries. These studies showed the highest photoconductivity for LC samples of **PBI 3T** compared to the shorter derivatives and, hence, demonstrate that the intrinsic functional properties of liquid crystals can be fine-tuned by tailoring the electronic properties and supramolecular architecture of the nanomaterials.

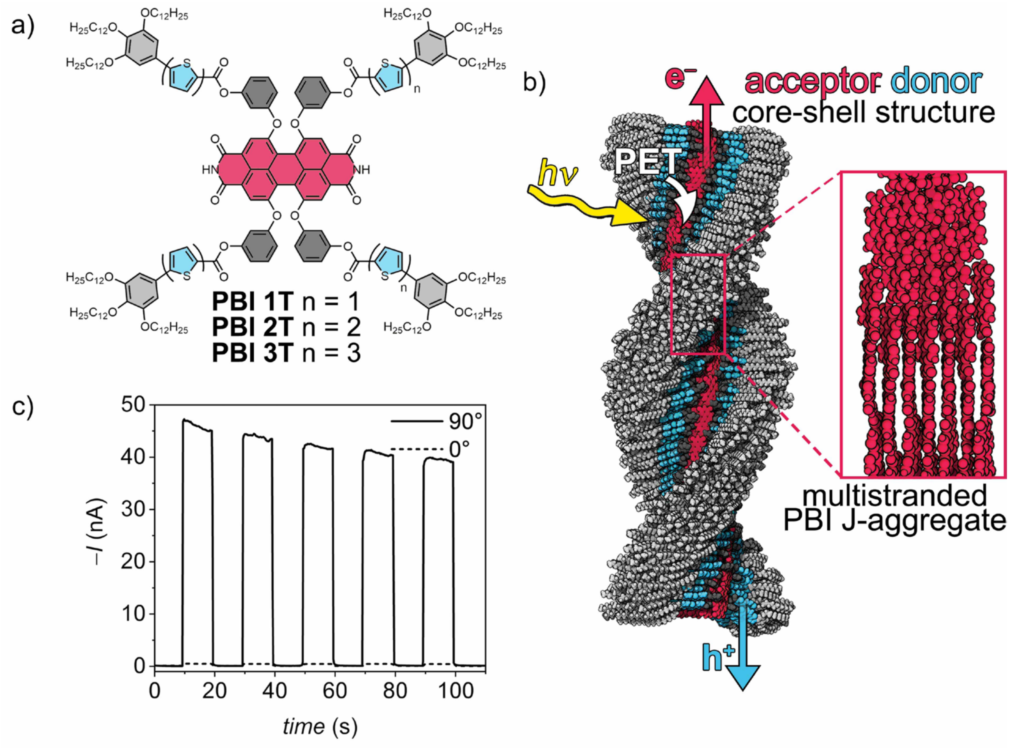

Figure 38. a) Chemical structure of **PBI 1T**, **PBI 2T** and **PBI 3T**. b) Model of the seven-stranded supramolecular acceptor–donor core–shell helix of **PBI 3T** in the columnar LC state. c) Photoresponse of devices of **PBI 2T** with the columnar direction perpendicular (solid lines) or parallel (dashed lines) to the electrodes (V_{DS} = 50 V, ψ = 20 mW cm^{-2}).

In *Chapter 5*, **PBI-Ac** bearing free imides and acyloxy functionalities with linear undecyl chains in bay-positions is presented (Figure 39a). Depending on the cooling rate applied to a hot solution of monomers in methylcyclohexane, the material self-assembles into two supramolecular polymorphs with distinct optical and morphological features, **Agg1** and **Agg2**. The self-assembly process guided by hydrogen-bonding and π-π-interactions was followed by temperature-dependent UV/Vis spectroscopy and FT-IR spectroscopy. Importantly, **Agg1** forms an organogel, while **Agg2** precipitates from solution. This is in accordance with the observation of 1D fibers for **Agg1** and 2D sheets for **Agg2** with atomic force microscopy and scanning electron microscopy (Figure 39c). Both polymorphs form liquid-crystalline phases that were investigated with polarized FT-IR and UV/Vis spectroscopy as well as X-ray scattering experiments. These studies revealed that **Agg1** consists of **PBI-Ac** molecules self-assembled into a six-stranded helical columnar structure of perylene bisimide J-aggregates similar to the supramolecular architectures observed for the tetraphenoxy substituted perylene bisimides in *Chapters 3* and *4*. The fourfold substitution in bay-position leads to a contorted π-core and therefore to the formation of atropoenantiomers of either *P*- or *M*-chirality, which exhibit a low barrier for dynamic interconversion. Accordingly, the helical structure is formed by narcissistic arrangement of homochiral atropoenantiomeric perylene bisimides of either *P*- or *M*-chirality. **Agg2**, on the other hand, forms a lamellar phase that consists of alternating strands of hydrogen-bonded perylene bisimides with either *P*- or *M*-chirality (Figure 39a). This heterochiral self-assembly mode is in contrast to the homochiral arrangement observed in helical columnar phases and displays an illustrative example of racemate vs. conglomerate self-sorting phenomena in (liquid-)crystalline materials. Exciton-vibrational spectral pattern analysis together with in-depth X-ray scattering investigations revealed that the perylene bisimides arrange in a pseudo-rectangular centered unit cell with a longitudinal slip of around 5 Å inducing the distinct absorption profile observed in solution and in the liquid-crystalline state (Figure 39b). Moreover, analysis of the self-assembly process in solution showed that **Agg1** is formed by a kinetically controlled process, while **Agg2** constitutes the thermodynamically favored product. Time-dependent conversion experiments at various concentrations revealed that **Agg1** is an off-pathway aggregate. Approaches towards seed-induced conversion of **Agg1** into the thermodynamically favored **Agg2** led only to a minor transformation even at high seed ratios.

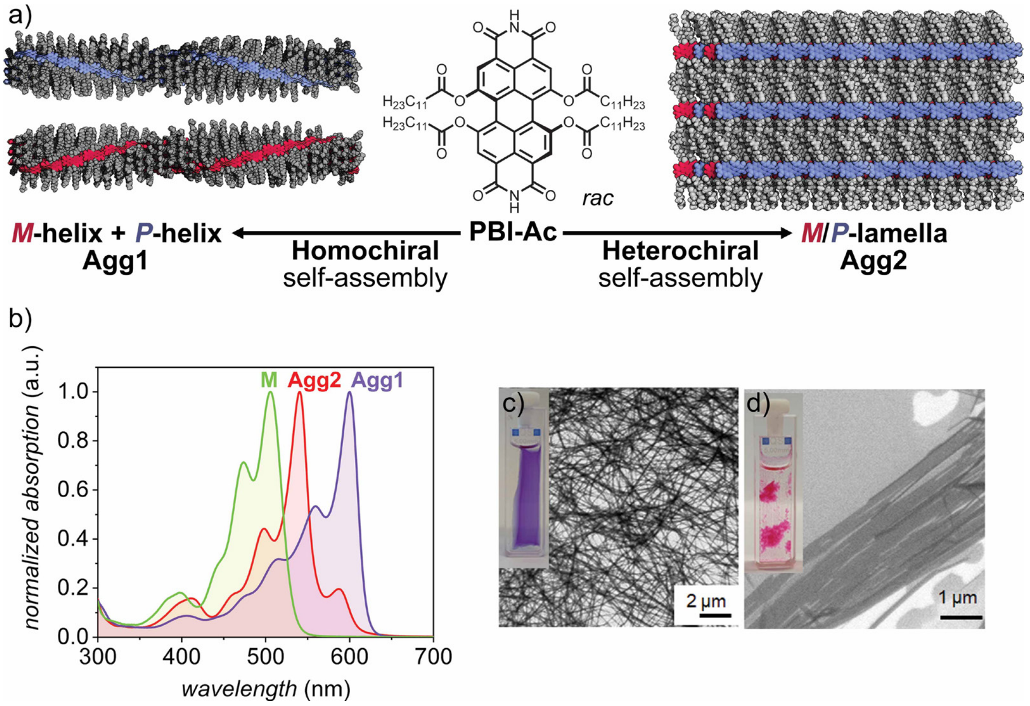

Figure 39. Chemical structure of **PBI-Ac** and homo- vs. heterochiral self-assembly into helical columnar and lamellar liquid-crystalline phases. b) Normalized UV/Vis absorption spectra of 40 µM solutions of monomeric **PBI-Ac** (green, 90 °C), **Agg1** (purple, 20 °C) and **Agg2** (red, 20 °C) in methylcyclohexane. Scanning electron microscopy images of samples of c) **Agg1** and d) **Agg2** drop-casted onto silicon wafer (c_0 = 40 µM, methylcyclohexane). The insets show the corresponding gel-like phase and precipitate.

To put the structural results from *Chapters 3*, *4*, and *5* into perspective and derive a general design rule, they were compared to other liquid-crystalline tetraphenoxy substituted perylene bisimide J-aggregates investigated by Herbst *et al.* (Figure 40, for details see Appendix 9.2).[60,61] Thus, a correlation of the opening angle of the central perylene bisimide and the dendron wedge periphery with the structural features in the liquid-crystalline state could be determined. It appears that large opening angles and a close distance between the central core and the dendron wedges leads to lower strand numbers while the opposite is true for small opening angles and large distances between the core and the dendron wegdes, or the lack thereof. Accordingly, by individually adjusting these parameters, the strand count can be fine-tuned from two to seven strands. For example, substituting the phenoxy groups in bay-positions (PBI **6c**) with methyl groups in *ortho*-position leads to large opening angles beyond the core twist of the central chromophore. Accordingly, and in contrast to PBI **6b**, which differs only in the lack of the *ortho*-methyl grop, **6c** self-assembles into a two-stranded helix, while four strands are incorporated in the columnar structure of PBI **6b**. A similar, yet weaker effect can be achieved by using branched 2-ethylhexyl chains (PBI **6d**) rather than linear dodecyl chains (PBI **6b**). The branching draws the steric constraint closer to the perylene bisimide core and, therefore, leads to larger opening angles. Consequently, and in agreement with the proposed structural model, **6d** incorporates one less strand than **6b** and self-assembles in a three-stranded helix. Towards the preparation of helices with more strands, the distance between the chromophore and the dendron wedges can be extended. This is exemplified by **PBI 2T** and **PBI 3T**, which form six- and seven-stranded helices, respectively. The incremental introduction of thiophene units between the phenoxy substituents and the dendron wedges provides steric conditions that require the incorporation of more strands to achieve optimized space filling.

However, with **PBI-Ac** the limit of the correlation between the strand count, the opening angle of the central chromophore and the dendron wedge periphery is reached. **PBI-Ac** bears single linear undecyl chains connected via an acyloxy unit in bay-positions of the perylene bisimide causing small opening angles. Furthermore, the removal of the entire dendron wedge periphery leads to a situation, where columnar arrangements become disfavored and lamellar phases are formed. **PBI-Ac** is particularly interesting as it can be allocated directly at the intersection of columnar and lamellar LC phases in the proposed qualitative model, since both are formed depending on the processing parameters (Figure 40).

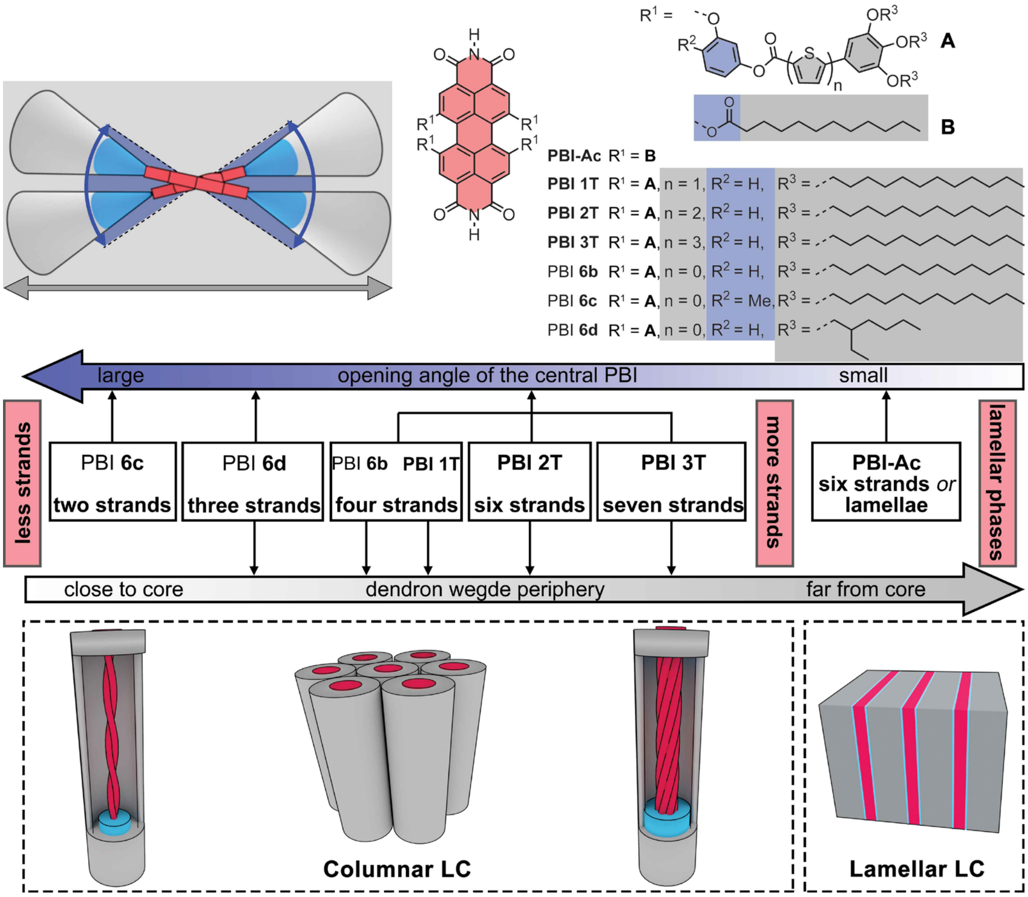

Figure 40. Schematic illustration of the influence of the opening angle of the central PBI and the dendron wedge periphery on the structure in the LC phase. For a detailed discussion of Figure 40 see Appendix 9.2.

In *Chapter 6*, some of the design principles used in *Chapters 3*, *4*, and *5* were translated to diketopyrrolopyrrole dyes. This class of chromophores is widely used as industrial pigment and in organic electronic materials making it an appealing candidate for creating functional materials following supramolecular approach. Thus, **DPP 2** was synthesized with appended trialkoxyphenyl minidendrons attached to the chromophore via a phenyl spacer to increase solubility in organic solvents and enable nanosegregation in the bulk, thereby facilitating the formation of liquid-crystalline phases (Figure 41a). This material differs from **DPP 1** that features the minidendrons directly connected to the π-core. Both dyes bear free lactam units for hydrogen-bond-directed self-assembly and form 1D supramolecular polymers via the cooperative nucleation-elongation mechanism as evidenced by concentration- and temperature-dependent UV/Vis spectroscopy. The aggregates exhibit H-type excitonic coupling due to cofacial arrangement of the chromophores. Furthermore, polarized optical microscopy and differential scanning calorimetry experiments indicated that **DPP 1** and **DPP 2** form liquid-crystalline phases. Polarized UV/Vis and FT-IR spectroscopy together with X-ray fiber diffraction showed that the columnar phases consist of hydrogen-bonded strands of antiparallel π-dimers that translationally stack in a 90° rotational displacement

(Figure 41b). Interestingly, this is only the second class of chromophores to exhibit a liquid-crystalline phase with the dye's π-surface parallel to the columnar long axis besides the perylene bisimides following the design principle employed in this thesis.

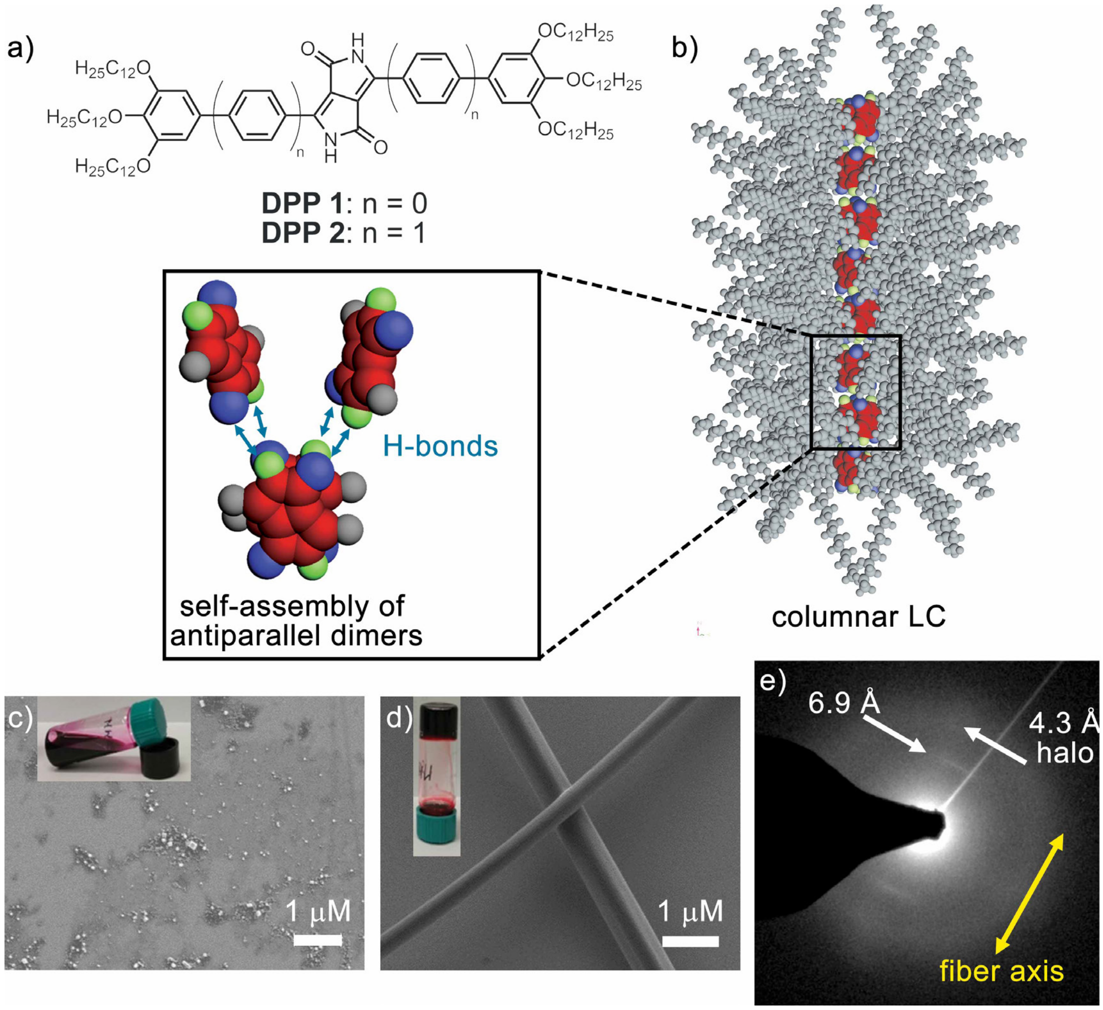

Figure 41. a) Chemical structures of **DPP 1** and **DPP 2**. b) Self-assembled structure of **DPP 2** in the columnar liquid-crystalline phase and illustration of the self-assembly of the antiparallel dimeric units. Scanning electron microscopy images of the electrospun c) **DPP 1** and d) **DPP 2**. The insets show the corresponding solutions in toluene (c_0 = 20 mM). e) Electron diffraction pattern of an electrospun fiber of **DPP 2** as obtained from selected area electron diffraction.

In an attempt towards the preparation of macroscopic functional materials from supramolecular liquid crystals, both dyes were used for electrospinning experiments. This method, commonly applied to polymer melts or solutions, provides access to 1D fibers for applications such as waveguides or membranes and, hence, displays an intriguing method for the advanced processing of supramolecular materials.[247,248,256] At the experimental conditions used for electrospinning (c = 20 mM in toluene) **DPP 2** forms an organogel, while the solution of **DPP 1** retains low viscosity (Figure 41c and d). This is reflected in the outcome of electrospinning experiments, which produced well-defined microscopic fibers of **DPP 2**, while **DPP 1** leads to nanoparticles in an electrospraying process (Figure 41c and d). Accordingly, the higher viscosity is quintessential for the success of electrospinning supramolecular polymers. Hence, preliminary experiments with solutions of PBI **6d**, which showed only a minor increase in solution viscosity, did not yield fibers. The electrospun fibers of **DPP 2** further show a highly defined arrangement of the columnar liquid-crystalline structure parallel to the fiber axis as determined with polarized optical microscopy and selected area electron diffraction experiments (Figure 41e). Thus, a method to process supramolecular polymers into macroscopic 1D objects with defined intermolecular arrangement is provided that shows potential for the implementation in the large-scale production of 1D functional materials.

In conclusion, the synthesis and characterization of functional hydrogen-bonded polymers based on perylene bisimide and diketopyrrolopyrrole dyes and their self-assembly into multistranded helical columnar and lamellar liquid-crystalline phases was investigated. Photoconductivity of the liquid-crystalline perylene bisimides could be achieved by incorporating electron-rich thiophene units into the monomeric structures, facilitating the formation of coaxially separated donor–acceptor domains and thereby providing individual percolation pathways for the transport of charge-carriers along the 1D columnar structures. The library of accessible liquid-crystalline phases of hydrogen-bonded perylene bisimides could be extended from the helical columnar to the lamellar phase applying a fourfold substitution of acyloxy functionalities with linear alkyl chains in bay-position and thereby tuning the steric requirements of the monomeric building block. Accordingly, a rational design approach was established that allows not only to adjust the number of strands within the multistranded columnar liquid-crystalline phases but also to prepare lamellar phases. The design principles that guide the self-assembly into columnar liquid-crystalline phases with the chromophore’s π-core aligned parallel to the columnar long axis could be translated to a set of diketopyrrolopyrrole molecules demonstrating the versatility of this supramolecular approach towards functional materials.

Chapter 8

–

Zusammenfassung und Fazit

Mithilfe von Gestaltungsprinzipien der supramolekularen Chemie können komplexe Strukturen realisiert werden, die mit Ansätzen der kovalenten Chemie nicht erreichbar sind. Ein zentraler Aspekt ist hierbei der systematische Aufbau der Monomereinheiten, welche unter geeigneten Bedingungen über intermolekulare Wechselwirkungen selbstassemblieren und Architekturen mit spezifischer räumlicher Anordnung der einzelnen Bauelemente formen. Flüssigkristalline Materialien zeigen zusätzlich zu positioneller und Orientierungsfernordnung der Moleküle, welche anisotrope Eigenschaften auf makroskopischer Ebene erzeugen, eine gewisse Mobilität. Daher können durch Kombination des supramolekularen Ansatzes mit Flüssigkristallen besonders interessante Materialien erzeugt werden. Da die spezische Anordnung der Moleküle die Funktion des selbstassemblierten Materials stark beeinflusst, ist es von großer Bedeutung, diese exakt kontrollieren zu können. Daher war es Ziel dieser Arbeit, flüssigkristalline Phasen mit einer definierten supramolekularen Struktur zu synthetisieren und zu charakterisieren. Weiterhin war es ein Ziel, diese auf ihre funktionellen Eigenschaften zu untersuchen, die aus der spezifischen Anordnung der Monomereinheiten hervorgehen. Für diesen Zweck wurden Perylenbisimid- und Diketopyrrolopyrrolfarbstoffe als Baueinheiten verwendet, da diese aufgrund ihrer Licht- und Hitzestabilität sowie exzellenten optischen und elektronischen Eigenschaften ideale Materialien für die Anwendung in der organischen Elektronik darstellen.

Die *Kapitel 3* und *4* dieser Arbeit beschäftigen sich mit Perylenbisimid-basierten Donor-Akzeptor Dyaden, welche sowohl in Lösung als auch in der flüssigkristallinen Phase J-Aggregate ausbilden. Die untersuchten Perylenbisimide sind in den 1,6,7,12-Buchtpositinen mit Phenoxyeinheiten substituiert, welche mit Trialkoxyphenyl-Oligothiopheneinheiten in *meta*-Position dekoriert sind (**PBI 1T**, **PBI 2T** und **PBI 3T**, Abbildung 2a). Mithilfe von UV/Vis-Spektroskopie konnte gezeigt werden, dass zwischen den elektronenarmen und -reichen Untereinheiten der Moleküle keine elektronische

Kopplung vorliegt. Weiterhin zeigten konzentrationsabhängige UV/Vis-Studien in unpolaren Lösungsmitteln, dass die Moleküle über den kooperativen Nukleations-Elongationsmechanismus in einem Zusammenspiel aus Wasserstoffbrücken und π-π-Wechselwirkung supramolekulare Polymere formen. Bedingt durch die Verdrillung des π-Kerns, hervorgerufen durch die vierfache Substitution in Buchtposition, führt dies zu einer Anordnung der Perylenbisimidmoleküle die einem versetzten Kartenstapel gleicht, was zu einer J-artigen Exzitonenkopplung führt. Diese J-artige Kopplung führt zu einer ausgeprägten Rotverschiebung der Hauptabsorptionsbande sowohl in Lösung (Abbildung 1a) als auch im flüssigkristallinen Zustand (Abbildung 1b, siehe Appendix 9.1).

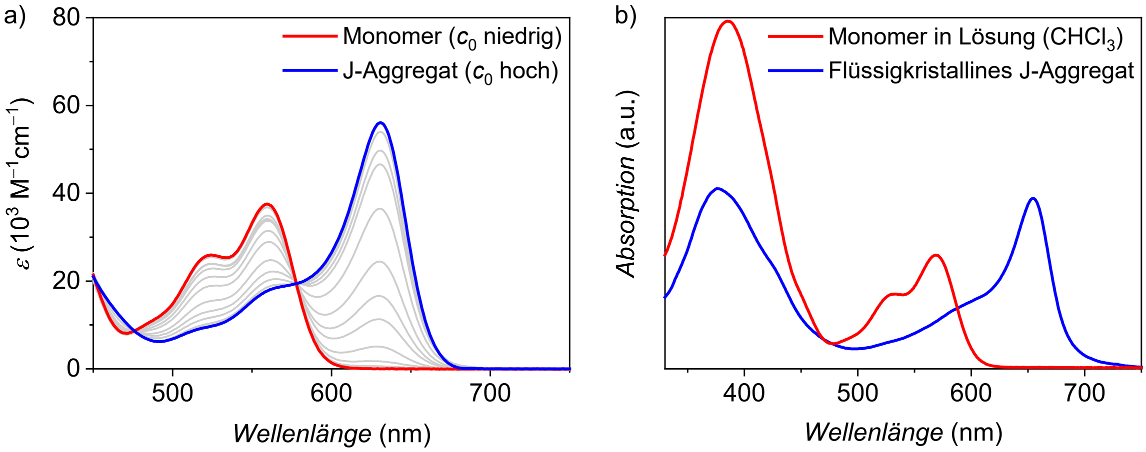

Abbildung 1. a) Konzentrationsabhängige UV/Vis-Absorptionsspektren von **PBI 2T** (c_0 = 3.61 µM – 4.37 mM, Toluol). Während bei niedrigen Konzentrationen Monomere vorliegen (rot), zeigen Spektren bei hohen Konzentrationen die Präsenz von J-aggregaten (blau). b) UV/Vis-Absorptionsspektren von **PBI 2T** Monomeren in Lösung (rot, c_0 = 30 µM, Chloroform) und **PBI 2T** J-Aggregaten im flüssigkristallinen Dünnfilm (blau).

Im flüssigkristallinen Zustand lagern sich diese supramolekularen Strukturen weiter zu kolumnaren Phasen zusammen, was mithilfe von Röntgenstreuungsexperimenten nachgewiesen werden konnte. Polarisierte UV/Vis- und FT-IR-Spektroskopie an gescherten Dünnfilmen zeigte, dass sowohl das S_0-S_1 Übergangsdipolmoment der Farbstoffe als auch die Wasserstoffbrücken entlang der Scherrichtung und damit der kolumnaren Längsachse ausgerichtet sind. Eine tiefergehende Analyse der Röntgenstreuungsdaten kombiniert mit der experimentellen Bestimmung der Materialdichte zeigte, dass die Farbstoffmoleküle mehrsträngige Helices formen. Die exakte Anzahl der Stränge hängt dabei von den sterischen Ansprüchen der Buchtsubstituenten ab. Die Untersuchungen zeigten, dass die Farbstoffe **PBI 1T**, **PBI 2T** und **PBI 3T** vier-, sechs- und siebensträngige Helices in der kolumnar flüssigkristallinen Phase ausbilden. Die Donoreinheiten sind dabei räumlich von den Perylenbisimid-

Akzeptoreinheiten getrennt, welche sich im Inneren der Kolumnen befinden. Dadurch bildet sich eine Art Kern-Schale-Struktur mit narzisstischer Ordnung der elektronischen Antagonisten. Da die Donoreinheiten in **PBI 1T**, **PBI 2T** und **PBI 3T** eine zunehmende Konjugationslänge aufweisen, war es ferner von Interesse, den Einfluss der elektronenreichen Substituenten auf die Eigenschaften der flüssigkristallinen Materialien mithilfe von Fluoreszenz- und Femtosekunden-aufgelöster transienter Absorptionsspektroskopie, zu untersuchen. Dabei hat sich ergeben, dass die Neigung zu photoinduziertem Elektronentransfer in der Reihe von **PBI 1T** zu **PBI 3T** zunimmt und dass die erzeugten Radikalanionen des Perylenbisimids die längsten Lebensdauern aufweisen. Alle drei Verbindungen konnten als aktive Schicht in Zweikontakt-Photoleitfähigkeitsbauteilen angewandt werden. Dabei konnten durch Rotationsbeschichtung isotrope Schichten erzeugt werden, während Lösungsscheren zu ausgerichteten, anisotropen Schichten führte. Bauteile, die mit der Methode des Lösungsscherens hergestellt wurden, zeigten eine Abhängigkeit der Photoleitfähigkeit von der Ausrichtung der kolumnaren Strukturen. Waren die kolumnaren Strukturen senkrecht zu den Elektroden ausgerichtet, konnten die höchsten Photoströme beobachtet werden, während eine Ausrichtung entlang der Eletroden zu niedrigen Photoströmen führte. Abhängig von der Qualität der Ausrichtung der aktiven Schicht konnten so Verhältnisse von $I_{90°}/I_{0°} = 90$ erreicht werden (Abbildung 2c). Weiterhin zeigten die ausgerichteten Strukturen ca. 45-fach höhere Photoströme als Bauteile mit isotropen aktiven Schichten. Da die zuvor genannten Ergebnisse stark von der makroskopischen Beschaffenheit der Filme abhingen, wurden die flüssigkristallinen Materialien zusätzlich mithilfe von zeitaufgelösten Mikrowellenleitfähigkeitsmessungen untersucht. Messwerte die mit dieser Methode erhalten werden, sind nicht von Kontaktwiderständen oder Korngrenzen beeinflusst und geben somit Aufschluss über die intrinsische Ladungsträgermobilität der supramolekularen Strukturen. Die Ladungsträger selbst werden dabei durch Blitzlichtphotolyse erzeugt. Diese Untersuchungen zeigten, dass **PBI 3T** die höchste Photoleitfähigkeit der Molekülserie aufweist. Damit konnte deutlich gemacht werden, dass die intrinsischen funktionellen Eigenschaften supramolekularer Flüssigkristalle durch eine maßgeschneiderte Struktur des Monomers und das dadurch ermöglichte gezielte Modifizieren der zwischenmolekularen Anordnung gesteuert werden können.

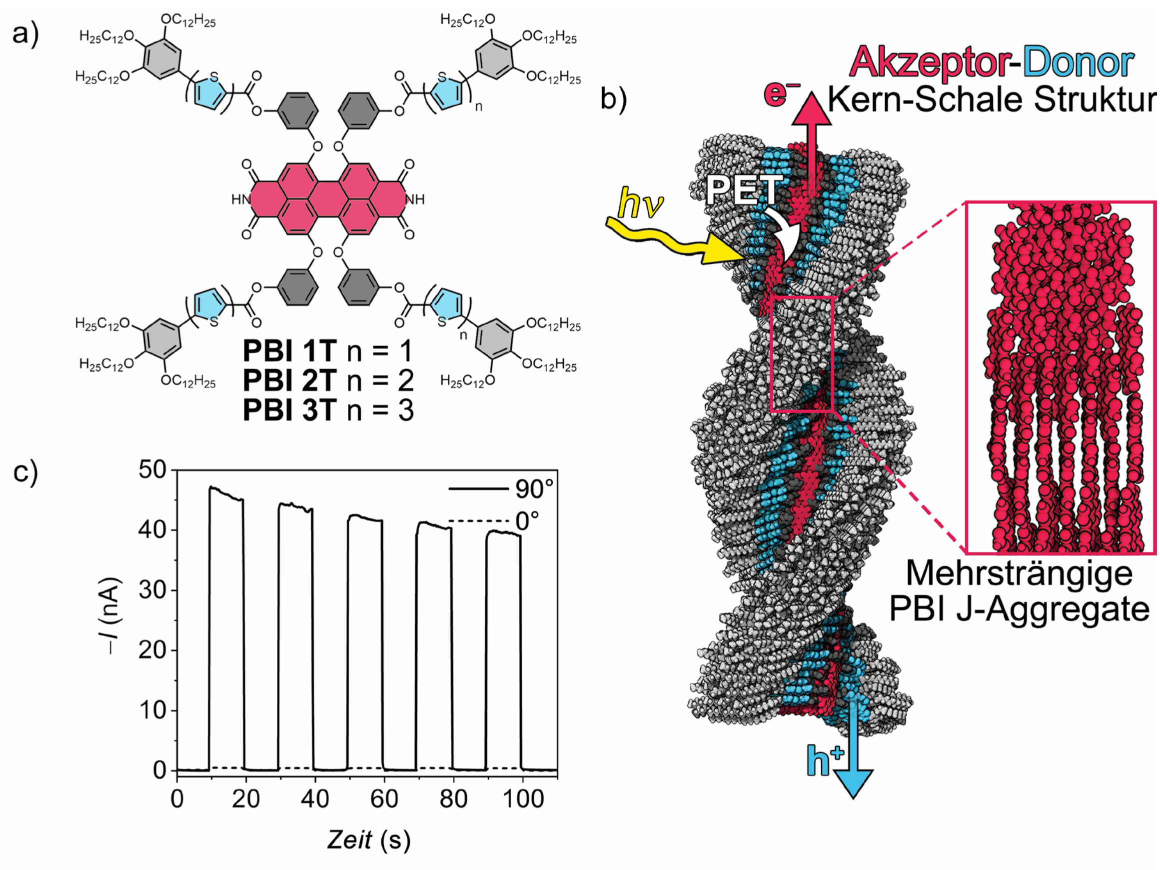

Abbildung 2. Chemische Struktur von **PBI 1T**, **PBI 2T** und **PBI 3T**. b) Modell der siebensträngigen supramolekularen Kern-Schale Akzeptor-Donor Helix von **PBI 3T** in der kolumnar flüssigkristallinen Phase. c) Photoleitfähigkeit eines mit **PBI 2T** präparierten Bauteils mit Ausrichtung der Kolumnen senkrecht (durchgezogene Linie) und parallel (gestrichelte Linie) zu den Elektroden (V_{DS} = 50 V, ψ = 20 mW cm^{-2}).

In *Kapitel 5* geht es um die Selbstassemblierung von **PBI-Ac**, welches unsubstituierte Imidfunktionen und Acyloxysubstituenten mit linearen Undecylketten in Buchtposition trägt (Abbildung 3a). Abhängig von der Kühlrate, die man einer heißen Lösung aus Monomeren in Methylcyclohexan aussetzt, aggregiert **PBI-Ac** zu zwei verschiedenen supramolekularen Polymorphen, **Agg1** und **Agg2**, welche individuelle optische und morphologische Eigenschaften aufweisen. Der durch Wasserstoffbrückenbindungen und π–π-Wechselwirkungen gesteuerte Aggregationsprozess wurde mithilfe von temperaturabhängiger UV/Vis-Spektroskopie und FT-IR-Spektroskopie untersucht. Dabei hat sich gezeigt, dass **Agg1** eine gelartige Phase in Methylcyclohexan bildet, während **Agg2** aus der Lösung präzipitiert. Diese Beobachtung lässt sich mithilfe der in rasterkraft- und rasterelektronenmikroskopischen Untersuchungen nachgewiesenen Morphologien der Polymorphe erklären. Im Detail zeigten die Experimente eindimensionale Fasern für **Agg1**, während zweidimensionale flächige Strukturen für **Agg2** beobachtet werden konnten (Abbildung 3c und d). Da beide Polymorphe im Festkörper eine flüssigkristalline Phase ausbilden, konnte die Struktur auf supramolekularer Ebene mit polarisierter FT-IR- und

UV/Vis-Spektroskopie, sowie Röntgenstreuungsexperimenten untersucht werden. Dadurch konnte nachgewiesen werden, dass **Agg1** aus **PBI-Ac** Molekülen besteht, die eine sechssträngige Helix in der kolumnaren flüssigkristallinen Phase ausbilden. Die optischen sowie strukturellen Eigenschaften von **Agg1** erinnern daher stark an die in *Kapitel 3* und *4* untersuchten Tetraphenoxy-substituierten Perylenbisimide. Solch eine helikale Struktur lässt sich durch die Anordnung homochiraler Atropoenantiomere erklären. Diese Atropoenantiomere entstehen durch die vierfache Substitution des Perylenbisimids in Buchtposition, was zu einer Verdrillung der π-Fläche des Farbstoffs führt. Die Barriere zur Umwandlung der beiden Atropoenantiomere ist jedoch niedrig und abhängig vom Aggregationsprozess können diese entweder homochiral oder heterochiral selbstassemblieren. Im Gegensatz zu **Agg1** formt **Agg2** eine lamellare flüssigkristalline Phase, die sich aus alternierenden Strängen wasserstoffverbrückter Perylenbisimide zusammensetzt, die entweder *P*- oder *M*-Chiralität aufweisen (Abbildung 3a). Somit konnten für **PBI-Ac** kontrastierende Aggregationswege über hetero- oder homochirale Selbstassemblierung nachgewiesen werden, was beispielhaft den Unterschied zwischen Racemat- und Konglomeratbildung in (flüssig)kristallinen Materialen illustriert. Für **Agg2** konnte durch Analyse der Absorptionsspektren unter Berücksichtigung der Exzitonenkopplung gepaart mit eingehender Auswertung der Röntgenstreuungsdaten gezeigt werden, dass die Farbstoffmoleküle mit einem Längsachsenversatz von 5 Å in einer pseudo-rechtwinklig zentrierten Einheitszelle angeordnet sind. Hierdurch lässt sich das Absorptionsprofil erklären, welches deutlich von dem typischer Perylenbisimid J-Aggregate abweicht (Abbildung 3b). Weiterhin konnte mithilfe von UV/Vis Absorptionsspektroskopie gezeigt werden, dass **Agg1** in einem kinetisch kontrollierten Selbstassemblierungsprozess gebildet wird, während **Agg2** das thermodynamisch favorisierte Produkt ist. Zeitabhängige Umwandlungsexperimente bei verschiedenen Konzentrationen gaben Aufschluss über die Details des Aggregationsverlaufs und zeigten, dass **Agg1** ein sogenanntes „off-pathway“ Produkt darstellt. In Versuchen zur saatinduzierten Umwandlung von **Agg1** in **Agg2** konnte selbst bei hohen Saatkonzentrationen nur eine geringfügig erhöhte Umwandlung erreicht werden.

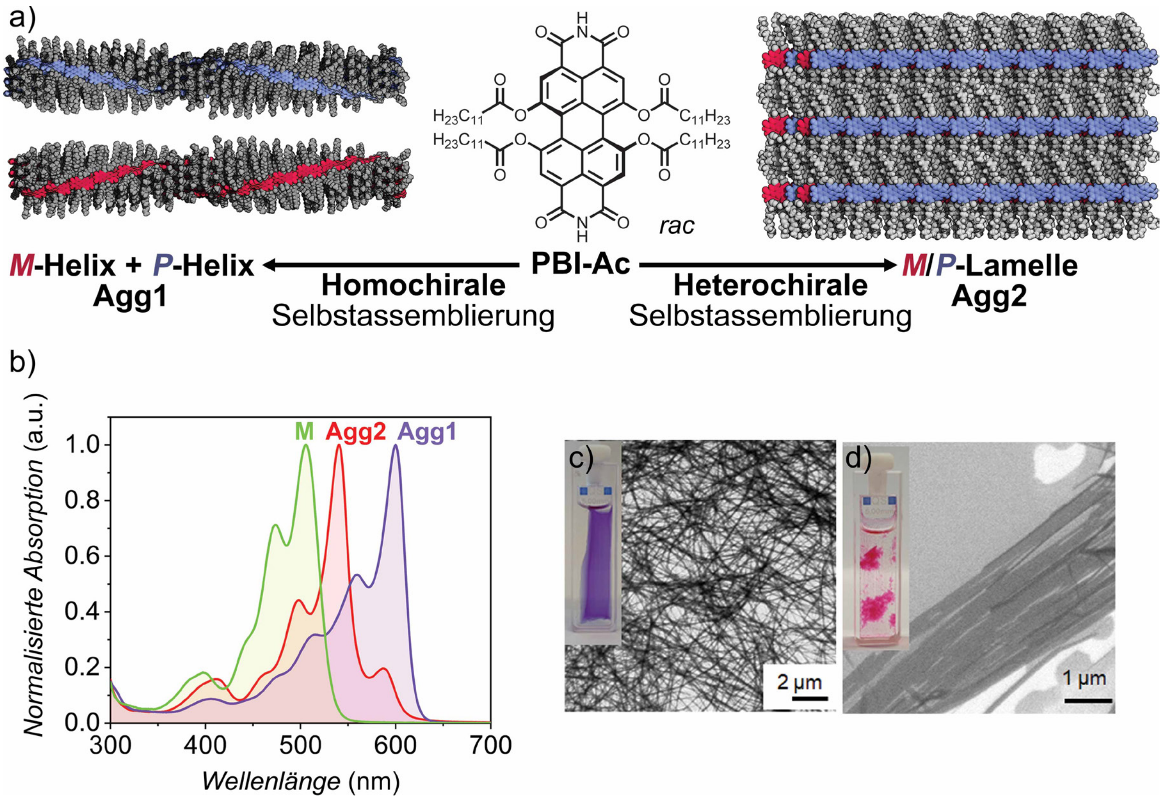

Abbildung 3. Chemische Struktur von **PBI-Ac** und schematische Darstellung der homo- bzw. heterochiralen Selbstassemblierung zu helikalen kolumnaren und lamellaren Flüssigkristallen. b) Normalisierte UV/Vis Absorptionsspektren von **PBI-Ac** Monomeren (grün, 90 °C), **Agg1** (lila, 20 °C) und **Agg2** (rot, 20 °C) mit $c_0 = 40$ µM in Methylcyclohexan. Rasterelektronenmikroskopieaufnahmen von c) **Agg1** und d) **Agg2**, die mittels Tropfbeschichtung auf Siliziumsubstraten präpariert wurden ($c_0 = 40$ µM, Methylcyclohexan). In den Einsätzen sind photographische Aufnahmen der dazugehörigen gelartigen Phase von **Agg1**, sowie des Präzipitats von **Agg2** gezeigt.

Betrachtet man die komplexen Strukturen, die in den *Kapiteln 3*, *4* und *5* beleuchtet wurden, so liegt es nahe, die erhaltenen Einblicke in die strukturellen Eigenschaften mit Ergebnissen für weitere flüssigkristalline Tetraphenoxy-substituierte Perylenbisimid J-Aggregate, welche von Herbst *et al.* untersucht wurden, zu vergleichen.[60,61] Dieser Vergleich ermöglicht es, einen Zusammenhang zwischen der Struktur des Monomers, die sich aus dem Öffnungswinkel des zentralen Perylenbisimidkerns und den periphären Dendroneinheiten zusammensetzt, und der supramolekularen Struktur im flüssigkristallinen Zustand herzustellen (Abbildung 4, siehe Appendix 9.2). Somit lassen sich allgemeine Regeln zur Präparation spezifischer supramolekularer Strukturen ableiten. Demnach führen große Öffnungswinkel des zentralen Farbstoffs und kleine Abstände zwischen dem Perylenbisimid und den Dendroneinheiten zur Ausbildung kolumnar helikaler Strukturen mit niedriger Strangzahl, während das Gegenteil für kleine Öffnungswinkel und große Abstände bzw. den Verzicht auf Dendroneinheiten der Fall ist (Abbildung 4). So führt beispielsweise die Substitution der Phenoxygruppen in Buchtposition mit Methyleinheiten in *ortho*-Position (PBI **6c**) zu großen Öffnungswinkeln die über die Kernverdrillung des zentralen Farbstoffs hinausgehen. Dementsprechend wird für PBI **6c** die Ausbildung einer zweisträngigen Helix beobachtet, während PBI **6b**, welches sich lediglich durch das Fehlen der *ortho*-Methylgruppe von **6c** unterscheidet, eine viersträngige Helix formt. Ein ähnlicher, jedoch schwächerer Effekt kann durch die Substitution der Dendroneinheiten mit verzweigten Ethylhexylketten (PBI **6d**) erreicht werden. Die Verzweigung der Alkylketten führt zu einem erhöhten sterischen Anspruch nahe am Kern und damit zu größeren Öffnungswinkeln des zentralen Chromophors im Vergleich zu einem Perylenbisimid mit linearen Dodecylketten (**6b**). Folglich ist in der dreisträngigen Helix von **6d** ein Strang weniger verbaut als in **6b**. Dieser Zusammenhang ist in guter Übereinstimmung mit dem vorgeschlagenen Strukturmodell (Abbildung 4). Bei gleichbleibendem Öffnungswinkel des zentralen Chromophors wird der Einfluss der peripheren Dendroneinheiten besonders in der Reihe **PBI 1T**, **PBI 2T** und **PBI 3T** deutlich, welche vier-, sechs- und siebensträngige Helices in der flüssigkristallinen Phase bilden. Durch die schrittweise Vergrößerung der Distanz zwischen zentralem Farbstoff und den Dendroneinheiten wird eine zunehmende Anzahl an Strängen benötigt, um den Raum optimal zu füllen.

Die Korrelation aus der Strangzahl, dem Öffnungswinkel des zentralen Perylenbisimids und der peripheren Dendroneinheiten erreicht mit **PBI-Ac** eine Grenze. **PBI-Ac** weist durch sterisch vergleichsweise anspruchslose Acyloxyfunktionalitäten mit linearen Undecylketten geringe Öffnungswinkel auf. Weiterhin führt der Verzicht auf die sterisch anspruchsvollen Dendroneinheiten zu einer Situation, in der nicht kolumnare, sondern lamellare Phasen favorisiert gebildet werden. **PBI-Ac** ist dahingehend besonders interessant, da es, je nach Prozessierungsmethode, eine sechssträngige Helix oder eine lamellare Phase im flüssigkristallinen Zustand bildet. In dem vorgeschlagenen, qualitativen Strukturmodell (Abbildung 4) lässt sich **PBI-Ac** demnach direkt an der Grenze zwischen kolumnaren Phasen mit vielen Strängen und lamellaren Phasen einordnen.

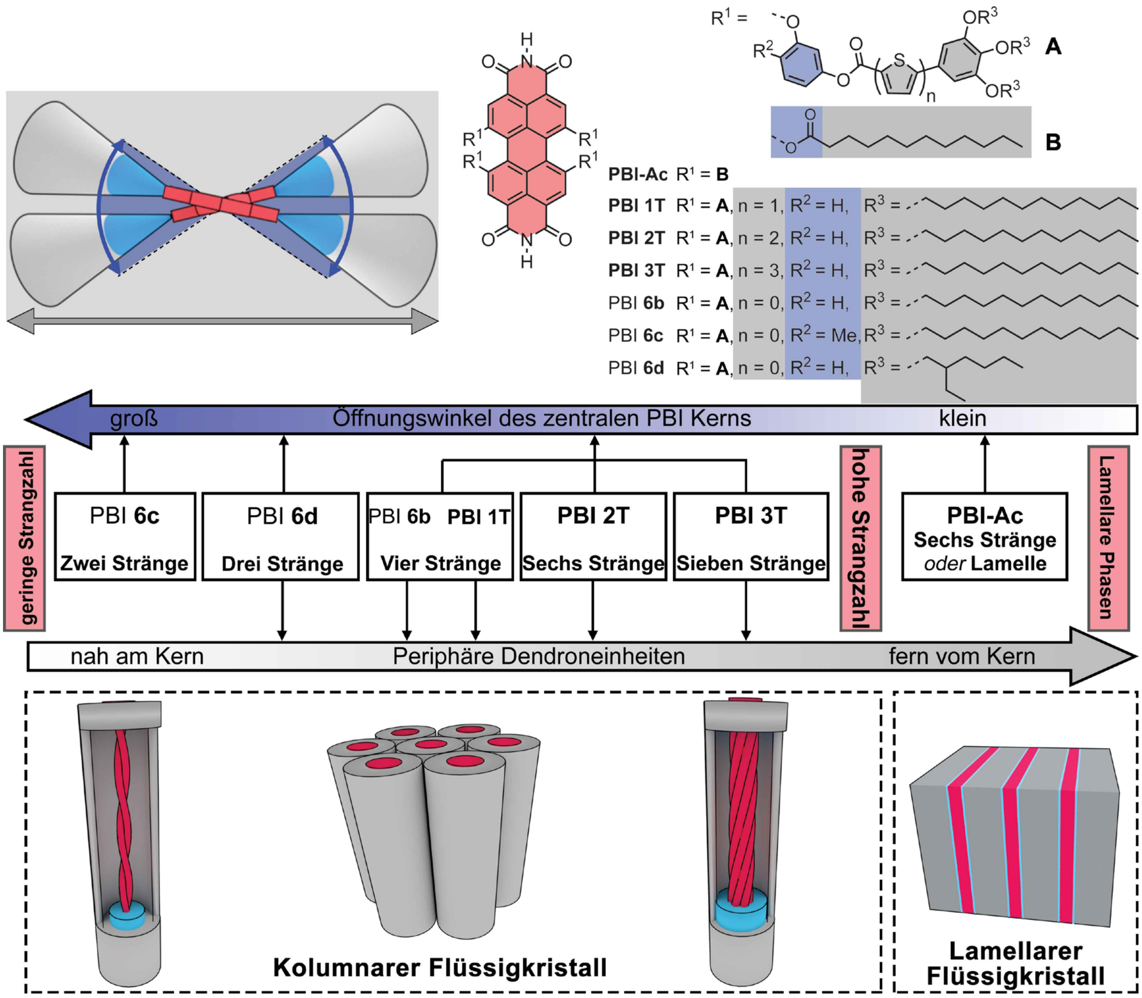

Abbildung 4. Schematische Darstellung des Einflusses des Öffnungswinkels des zentralen PBI-Kerns und der periphären Dendoneinheiten auf die Struktur der flüssigkristallinen Phasen von vierfach buchtsubstituierten PBIs. Siehe Appendix 9.2 für eine detaillierte Diskussion des vorgeschlagenen Strukturmodells.

In *Kapitel 6* konnte gezeigt werden, dass einige Strukturmotive, die in den *Kapiteln 3*, *4* und *5* Verwendung fanden, auch auf die Farbstoffklasse der Diketopyrrolopyrrole angewandt werden können, um kolumnare Mesophasen mit einer analogen Struktur zu erhalten. Diese Farbstoffe werden als Pigmente in industriellen Lacken verwendet und sind aufgrund ihrer elektronischen Eigenschaften beliebt für die Präparation elektronischer Bauelemente. Daher sind Diketopyrrolopyrrole ideale Kandidaten für die Darstellung funktionaler Materialien mittels eines supramolekularen Ansatzes. Aus diesem Grund, wurde **DPP 2** synthetisiert, welches Trialkoxyphenyleinheiten besitzt, die über Phenylgruppen mit dem Farbstoffgrundkörper verbunden sind. **DPP 2** unterscheidet sich dahingehend von **DPP 1**, als dass hierin die Trialkoxyphenyleinheiten direkt mit dem π-Kern verknüpft sind (Abbildung 5a). Die bürstenartigen Substituenten erhöhen einerseits die Löslichkeit des Pigments in organischen Lösungsmitteln und ermöglichen andererseits die Ausbildung flüssigkristalliner Phasen über Nanosegregation. Weiterhin sind beide

Farbstoffe in Lactamposition unsubstituiert, was unter geeigneten Bedingungen zu wasserstoffbrückengesteuerter Selbstassemblierung führt. Sowohl **DPP 1** als auch **DPP 2** aggregieren zu eindimensionalen supramolekularen Polymeren, die in einem kooperativen Nukleations-Elongationsmechanismus gebildet werden, was mithilfe von konzentrations- und temperaturabhängiger UV/Vis Absorptionsspektroskopie nachgewiesen werden konnte. Dabei weisen die Moleküle eine H-artige Exzitonenkopplung auf, die aus der kofazialen Anordnung der Chromophore hervorgeht. Polarisationsmikroskopie sowie Untersuchungen mit dynamischer Differenzkalorimetrie wiesen darauf hin, dass beide Farbstoffe flüssigkristalline Phasen ausbilden. Diese wurden im nächsten Schritt mit polarisierter FT-IR-Spektroskopie und Röntgenstreuungsexperimenten untersucht, welche zeigten, dass **DPP 1** und **DPP 2** kolumnare Phasen ausbilden, die aus wasserstoffverbrückten Molekülen bestehen. Dabei ordnen sich antiparallele π-Dimere translatierend mit einem Rotationsversatz von 90° an, sodass sie komplementäre Wasserstoffbrücken entlang der kolumnaren Längsachse ausbilden (Abbildung 5b). Hierbei ist es erwähnenswert, dass diese Moleküle nach den in Buchtposition vierfach phenoxysubstituierten Perylenbisimiden erst die zweite Farbstoffklasse darstellen, die kolumnare Mesophasen mit Ausrichtung der π-Flächen parallel zur kolumnaren Längsachse formt.

Wie in *Kapitel 6* dargelegt, fehlen dem Gebiet der supramolekularen Chemie Prozessierungsmethoden, die zur Herstellung von Funktionsmaterialien auf makroskopischer Größenskala verwendet werden können. Um hier einen Beitrag leisten zu können, wurden beide Farbstoffe für Versuche zur Präparation makroskopischer Fasern mittels Elektrospinnen herangezogen. Diese Methode ist im Bereich der Polymerchemie weit verbreitet, um Funktionsmaterialien wie Wellenleiter oder Membranen herzustellen.[247,248,256] Die Versuche wurden mit 20 mM Lösungen in Toluol durchgeführt. Unter diesen Bedingungen formte **DPP 2** ein Organogel, während die Lösung von **DPP 1** keine sichtlich erhöhte Viskosität aufwies (Abbildung 5c und d). Die Neigung zur Gelierung hatte einen großen Einfluss auf den Erfolg des Elektrospinnprozess, wie an der erfolgreichen Ausbildung gleichförmiger Fasern von **DPP 2** zu erkennen ist (Abbildung 5c). Im Gegensatz dazu führte der Prozess bei Lösungen von **DPP 1** zu Nanopartikeln (Abbildung 5d). Dieses Ergebnis legt nahe, dass eine hohe Viskosität eine wesentliche Vorraussetzung für den Erfolg des Elektrospinnprozesses supramolekularer Polymere darstellt. Dies spiegelt sich auch in den Ergebnissen für Versuche zum

Elektrospinnen von PBI **6d** wieder, welches vermutlich aufgrund geringer Viskosität der Lösung nicht zu Fasern gesponnen werden konnte. Untersuchungen der elektrogesponnenen **DPP 2** Fasern unter dem Polarisationsmikroskop zeigten eine definierte Anordnung der kolumnaren Längsachse parallel zur Faserachse. Dies konnte in Elektronendiffraktionsexperimenten weiter bestätigt werden (Abbildung 5e), was beweist, dass es möglich ist mithilfe von Elektrospinnen makroskopische Fasern mit definierter Anordnung der Moleküle aus Lösungen supramolekularer Polymere zu präparieren. Dadurch eröffnet sich die Möglichkeit zur Darstellung eindimensionaler supramolekularer Funktionsmaterialien im großen Maßstab.

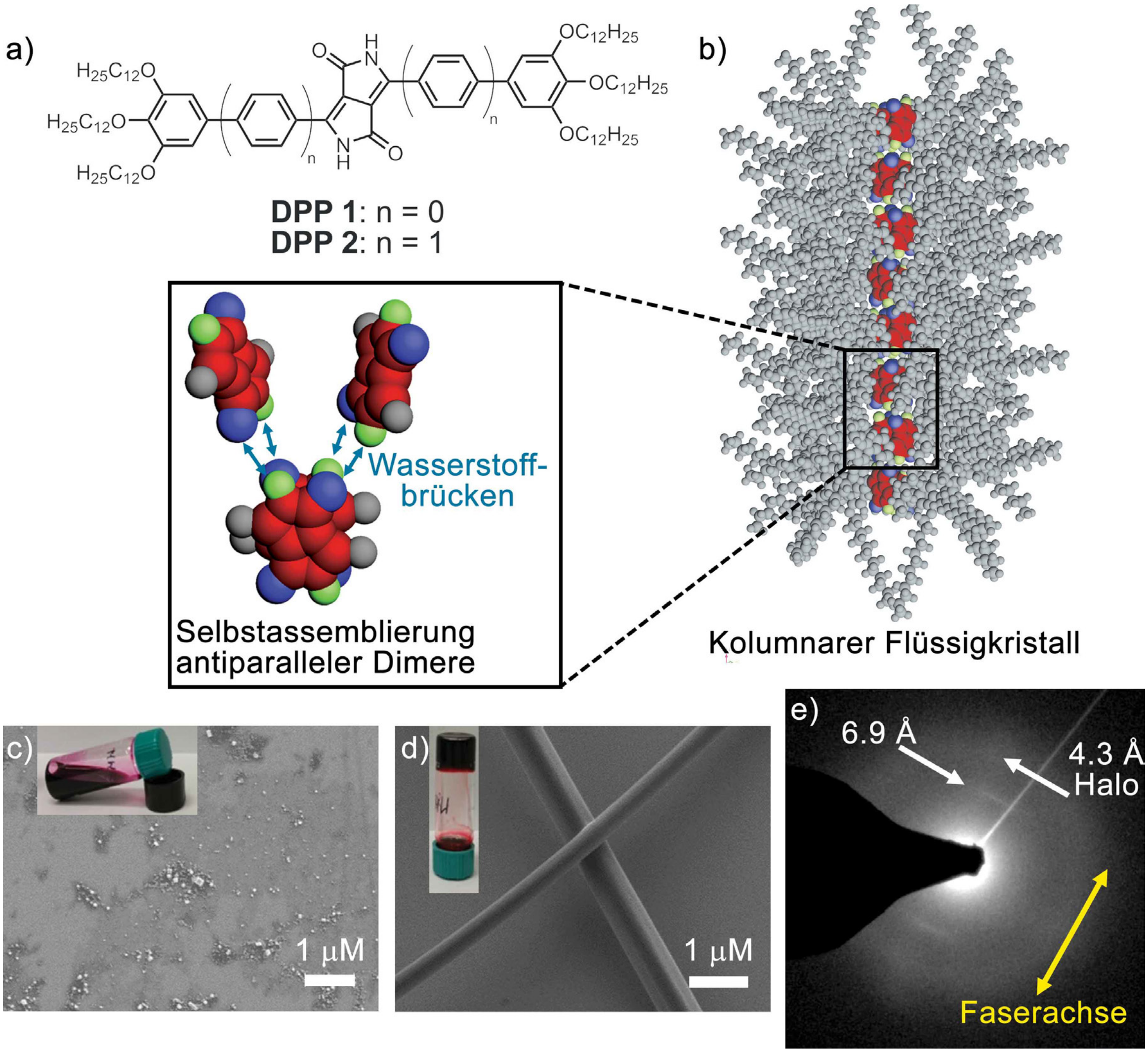

Abbildung 5. a) Chemische Strukturen von **DPP 1** und **DPP 2**. b) Selbstassemblierte Struktur von **DPP 2** in der kolumnaren Flüssigkristallphase, sowie eine Illustration des Assemblierungsprozesses über Wasserstoffbrücken zwischen antiparallelen π-Dimeren. Rasterelektronenmikroskopieaufnahmen der elektrogesponnenen Proben von c) **DPP 1** und d) **DPP 2**. Die Einsätze zeigen die zugehörigen Lösungen in Toluol (c_0 = 20 mM). e) Elektronenbeugungsmuster einer **DPP 2** Faser, die mittels Elektrospinnen präpariert wurde.

Abschließend lässt sich zusammenfassen, dass in dieser Arbeit die Synthese und Charakterisierung funktionaler supramolekularer Polymere basierend auf Perylenbisimid-und Diketopyrrolopyrrolfarbstoffen, sowie deren Selbstassemblierung zu mehrsträngigen helikal kolumnaren und lamellaren flüssigkristallinen Phasen untersucht wurden. Dabei konnte durch den Einbau elektronenreicher Thiopheneinheiten in die Monomerstruktur der flüssigkristallinen Perylenbisimide die Ausbildung koaxial separierter Donor- und Akzeptordomänen realisiert werden. Dadurch entstanden Ladungstransportkanäle entlang der eindimensionalen kolumnaren Strukturen welche eine makroskopische Photoleitfähigkeit der Materialien ermöglichten. Gleichzeitig konnten die experimentell zugänglichen flüssigkristallinen Phasen vierfach buchtsubstituierter Perylenbisimide von kolumnaren zu lamellaren Phasen erweitert werden. Durch einen Vergleich der in dieser Arbeit erhaltenen Ergebnisse mit früheren Erkenntnissen konnte ein rationaler Ansatz zur Feineinstellung der Strangzahl in der helikalen kolumnaren Phase bis hin zur durchgehenden Lamelle etabliert werden. Die für Perylenbisimide verwendeten Strukturmotive konnten weiterhin auf die Farbstoffklasse der Diketopyrrolopyrrole angewandt werden, um so die Ausbildung kolumnarer Flüssigkristalle mit paralleler Ausrichtung der Chromophor π-Flächen zu forcieren.

Chapter 9

–

Appendix

9.1 Longitudinal Shifts in PBI J-Aggregates

In *Chapter 2.1*, the structural features necessary to encode J-type excitonic coupling in aggregates of PBI molecules were discussed in detail. It was shown that longitudinal displacements larger than ≈6.5 Å are required to ensure J-type contributions of, both, long-range Coulomb as well as short-range CT coupling. The longitudinal shifts present in the PBI J-aggregates discussed in *Chapters 2–5* are summarized in Table A11. These values demonstrate that all discussed PBI dyes fulfill this essential criterion. Additionally, the particular excitonic coupling is sensitive to lateral displacement of the chromophores. Spano and co-workers could show for perylenes[54,55] and PBIs[265] that lateral displacements in the range of 1 Å can already lead to a change of sign for the short-range CT coupling. For LC PBI J-aggregates, the precise lateral displacement cannot be determined from XRS experiments and the helical nature of the assemblies renders shifts extracted from the modelled structures unreliable. However, as already a small lateral displacement should cause significant changes in the optical signature, no pronounced displacement is expected based on the available UV/Vis absorption spectra.

Table A11. Longitudinal shifts observed in (liquid-)crystalline PBI J-aggregates.

	Crystalline[a]		**Liquid-crystalline**[c]						
PBI	**1**[92]	**2**[b][93]	**PBI 1T**[161]	**PBI 2T**[111]	**PBI 3T**[161]	**PBI-Ac (Agg 1)**[191]	**6b**[60]	**6c**[60]	**6d**[61]
Longitudinal shift [Å]	7.24	7.00, 7.40	7.15	7.15	7.15	6.90	6.90	7.10	7.05

[a] Longitudinal shifts were derived from single crystal structures. The longitudinal shift was determined as the distance between two centroids in the central ring of the PBI cores projected on the plane of one PBI scaffold.
[b] In the crystal structure of PBI **2**, an asymmetrical displacement of two H-bonded PBI strands was observed. Consequently, two slightly different longitudinal shifts are present in the structure.
[c] Due to the fluid nature of LC materials, the longitudinal shift cannot be precisely determined from XRS data. However, the shift can be estimated as half of the axial translational subunit, which is defined by the first meridional reflection in fiber X-ray diffraction experiments. It has to be noted that that a reasonable error of ±0.5 Å is assumed for lattice distances obtained by XRS experiments of soft matter.

9.2 Supporting Information to the Structural Model

The precise packing arrangement in solids is determined by the optimization of intermolecular interactions and the maximization of the density, which strongly depends on the steric requirements of the individual building block. Accordingly, a wide range of parameters play a crucial role for the self-assembly mode of the dyes. In order to provide a simple, yet comprehensive graphic explanation for the different strand counts in the individual columnar LC phases presented in this thesis[111,161,191] and previous ones by Herbst *et al.*,[60,61] two parameters, namely the opening angle of the central PBI, and the connectivity and the sterics of the dendron wegde, have been chosen to establish a qualitative correlation of structural parameters with the supramolecular architecture in the LC state (Figure 40 in *Chapter 7*, Abbildung 4 in *Chapter 8*). In this qualitative model, large opening angles and a close distance between the central core and the dendron wedges leads to lower strand numbers in the helical columnar phase. In contrast, small opening angles and large distances between the core and the dendron wedge, or the lack of such sterically demanding groups, support the formation of helical structures with more strands and, eventually, lamellar phases. In the following, three individual sets of molecules have been chosen to illustrate the dominant structural parameter, that can help to explain the particular supramolecular arrangement.

PBIs **6c** and **6b** are both tetraphenoxy bay-substituted PBIs that bear 3,4,5-tris(dodecyloxy)phenyl minidendrons at the *meta*-position of the phenoxy group attached via an ester functionality. The phenoxy groups in PBI **6c** are additionally decorated with methyl substituents in *ortho*-position, which increases the steric demand close to the PBI π-core and enlarges the opening angle beyond the core twist. In contrast, PBI **6b**, which lacks the *ortho*-methyl group, exhibits a smaller opening angle of the central PBI. This is in good agreement with structures observed in single crystal X-ray structures and geometry optimized structures by DFT calculations. Figure A103b shows a single molecule of the crystal structure of PBI **2** (Chart 2 in *Chapter 2.1*), which employs *ortho*-methyl groups at the phenoxy bay-substituents.[93] The repulsive interactions of the substituents in close proximity to the PBI induce an opening angle beyond the core-twist between the two naphthalene units of the PBI (Figure A103b and d). This effect is less pronounced for PBI **6c**, which lacks the *ortho*-methyl group and can be illustrated by a geometry optimized structure (DFT, ωB97/def2-SVP), which shows a better overlap between the phenoxy substituents and therefore a smaller opening angle of the central core (red and blue parts in the schematic illustrations, Figure A103c and e). This is in good agreement with crystal structures observed for tetraphenoxy substituted PBIs that also show overlapping rings, particularly in one bay area.[209] Consequently, and in agreement with the proposed correlation, PBI **6c** forms a two-stranded helix (⌀$_{\text{column}}$ ≈ 54 Å) in the columnar LC structure, while PBI **6b** is able to incorporate four strands (⌀$_{\text{column}}$ ≈ 62 Å, Table A12).

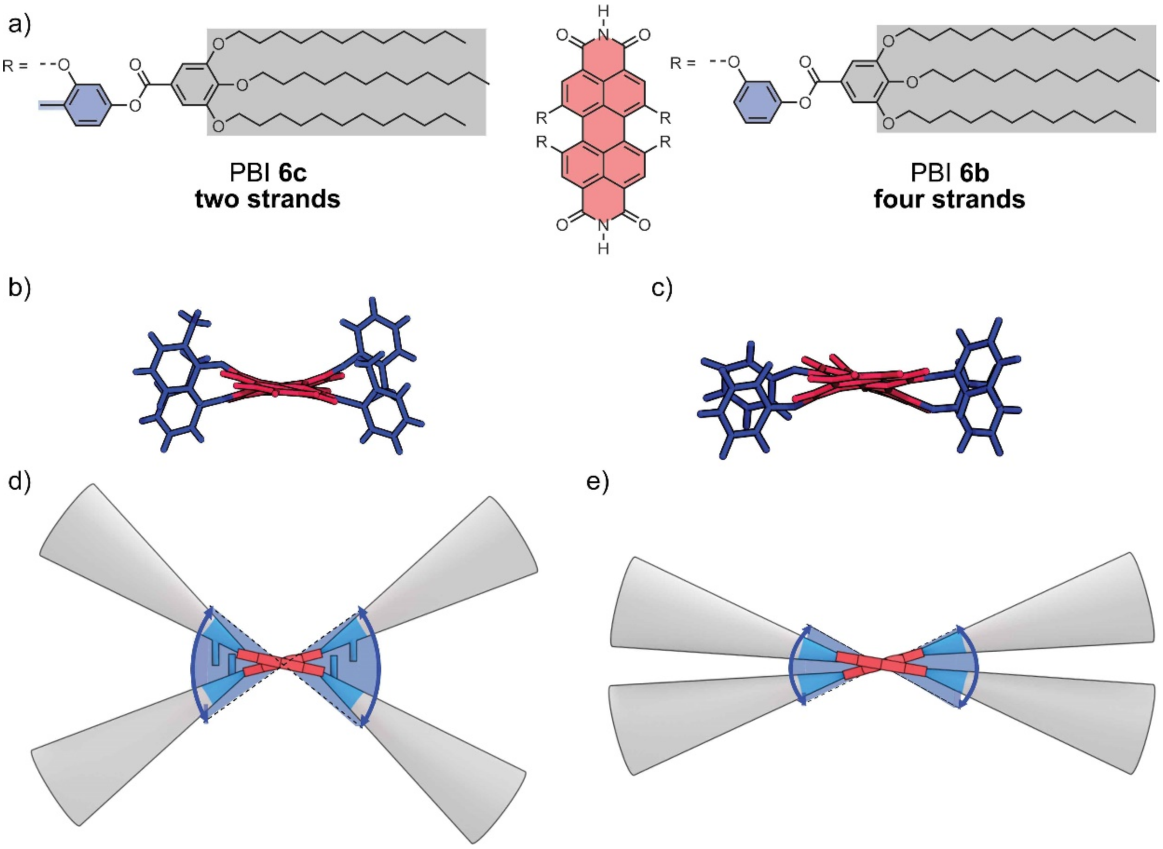

Figure A103. a) Chemical structures and color code of PBIs **6c** and **6b**. View along the *N*,*N'*-axis of a tetraphenoxy bay-substituted PBI b) with and c) without *o*-methyl groups at the phenoxy substituents. The structure depicted in b) is extracted from the single-crystal structure of PBI **2**[93] (Chart 2 in *Chapter 2.1*) and the structure depicted in c) is a geometry optimized structure of a tetraphenoxy bay-substituted PBI by DFT (ωB97/def2-SVP). Schematic illustration of the steric requirements in PBIs d) **6c** and e) **6b** that lead to the formation of two- and four-stranded helices, respectively.

However, steric constraint implemented further in the periphery also influences the precise supramolecular structure. This is demonstrated by PBIs **6d** and **6b**. The two molecules differ only in the alkyl chains that are appended to the dendron wedges (Figure A104). While PBI **6d** bears branched ethylhexyl chains, PBI **6b** is decorated with linear dodecyl chains. The branching increases the steric demand close to the core compared to linear alkyl chains. This effect, however, is not as pronounced as in **6c** due to the larger distance of the steric constraint to the central core and, therefore, leads to the formation of a three-stranded helix in the columnar LC state. Moving the steric constraint closer to the core by applying shorter, branched alkyl chains results in a pronounced difference of the columnar diameter of 39 Å (**6d**) and 62 Å (**6b**, Table A12). Consequently, in this case, both parameters, the opening angle of the central PBI and the dendron-wedge periphery play a role to establish the particular supramolecular architecture.

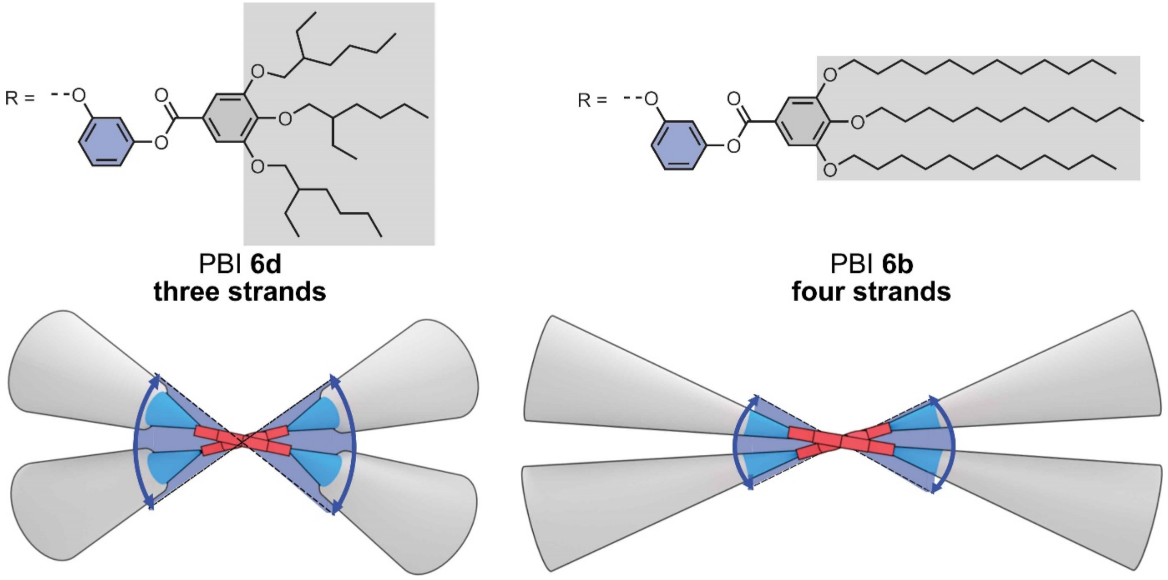

Figure A104. Molecular structure with color code and schematic illustration of the steric requirements in PBI **6d** and PBI **6b** that lead to the formation of three- and four-stranded helices, respectively.

In order to explain the structural properties of **PBI 1T**, **PBI 2T** and **PBI 3T**, which exhibit four-, six- and seven-stranded helices in the columnar LC phase, it is helpful to discuss the influence of the dendron wedge periphery. The molecular structure close to the PBI core is identical in all three compounds. Accordingly, no significant deviation regarding the opening angle of the central PBI core is expected. However, with the incremental increase of the number of thiophene units incorporated in the side arms, the distance between the central core and the dendron wedges increases from 10.2 Å (**PBI 1T**) to 15.3 Å (**PBI 2T**) and 17.2 Å (**PBI 3T**). Consequently, with the location of the sterically demanding wedges further in the periphery, more strands are required to optimize the close packing in the columnar LC structure. This also manifests in the increasing columnar diameter of ca. 65 Å (**PBI 1T**), 86 Å (**PBI 2T**) and 90 Å (**PBI 3T,** Table A12).

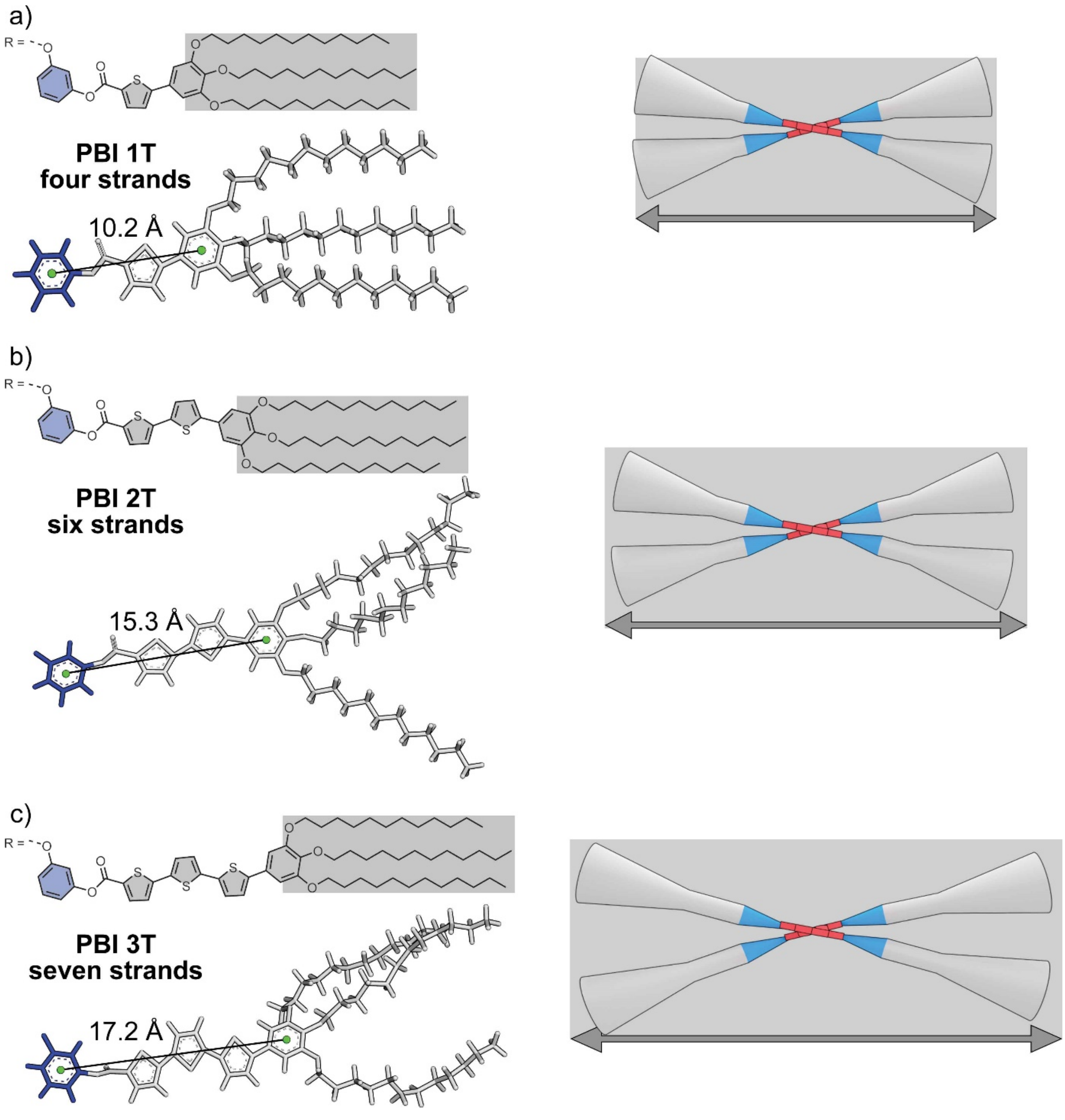

Figure A105. Molecular structure with color code and schematic illustration of the steric requirements in a) **PBI 1T**, b) **PBI 2T** and c) **PBI 3T** that lead to the formation of four-, six- and, seven-stranded helices, respectively. Molecular models of the side arms were extracted from the geometry optimized helices. The distances between the centroids of the phenoxy group in bay-positions and the centroid of the phenyl ring of the dendron wedge are shown.

Interestingly, comparing PBI **6b** (Figure A104) to **PBI 1T** (Figure A105), which differ in the dendron wegde periphery by the extension with a thiophene unit in **PBI 1T** reveals that this structural change is not sufficient to cause the incorporation of a different number of strands in the columnar LC phase. This is also reflected in the similar unit cell sizes of **PBI 1T** (Col$_{ob}$, a = 75.6 Å, b = 51.8 Å, γ = 86.4°) and **6b** (Col$_r$, a= 69.7 Å, b=47.8 Å) and columnar diameters of 65 Å (**PBI 1T**) and 62 Å (**6b**, Table A12).

Table A12. Number of strands and columnar diameters of helical LC PBI J-aggregates.

PBI	**6c**[60]	**6d**[61]	**6b**[60]	**PBI 1T**[161]	**PBI 2T**[111]	**PBI 3T**[161]	**PBI-Ac** (**Agg 1**)[191]
Number of strands	2	3	4	4	6	7	6
$\varnothing_{\mathbf{column}}$[a] [Å]	54	39	62	65	86	90	42

[a] Columnar diameters were determined determined as the largest distance between two atoms of a single geometry optimized helix (Materials Studio,[130] COMPASS II) in the *ab*-plane of the unit cells.

In the case of **PBI-Ac**, which forms a six-stranded helical columnar structure or a lamellar phase depending on the processing method, both proposed parameters have to be discussed. **PBI-Ac** bears single linear undecyl chains connected via an acyloxy unit in bay-positions of the PBI. These substituents exhibit comparatively little steric demand leading to small opening angles of the central PBI. Additionally, no peripheral dendron wedges are incorporated in the molecular structure. Therefore, **PBI-Ac** can be allocated on the far right of the qualitative model displayed in Figure 40 (Abbildung 4), supporting the proposed correlation between the opening angle of the central core and the dendron wedge periphery with the supramolecular arrangement.

To conclude, the qualitative model presented in Figure 40 provides a graphical visualization of the relationship between the steric requirements of the monomeric dyes and the supramolecular architecture established in the self-assembled LC state. While causality is difficult to prove, the good correlation of the proposed parameters with the supramolecular architecture supports the structural model.

Bibliography

[1] H. Ling, S. Liu, Z. Zheng, F. Yan, *Small Methods* **2018**, *2*, 1800070.

[2] J. Lewis, *Mater. Today* **2006**, *9*, 38–45.

[3] A. N. Sokolov, B. C. K. Tee, C. J. Bettinger, J. B. H. Tok, Z. Bao, *Acc. Chem. Res.* **2012**, *45*, 361–371.

[4] M. Irimia-Vladu, P. A. Troshin, M. Reisinger, L. Shmygleva, Y. Kanbur, G. Schwabegger, M. Bodea, R. Schwödiauer, A. Mumyatov, J. W. Fergus, V. F. Razumov, H. Sitter, N. S. Sariciftci, S. Bauer, *Adv. Funct. Mater.* **2010**, *20*, 4069–4076.

[5] C. Sekine, Y. Tsubata, T. Yamada, M. Kitano, S. Doi, *Sci. Technol. Adv. Mat.* **2014**, *15*, 034203.

[6] S. R. Forrest, *Nature* **2004**, *428*, 911–918.

[7] J. A. Rogers, T. Someya, Y. Huang, *Science* **2010**, *327*, 1603–1607.

[8] B. Walker, A. B. Tamayo, X.-D. Dang, P. Zalar, J. H. Seo, A. Garcia, M. Tantiwiwat, T.-Q. Nguyen, *Adv. Funct. Mater.* **2009**, *19*, 3063–3069.

[9] A. Nowak-Król, K. Shoyama, M. Stolte, F. Würthner, *Chem. Commun.* **2018**, *54*, 13763–13772.

[10] Y. Li, *Acc. Chem. Res.* **2012**, *45*, 723–733.

[11] A. Facchetti, *Chem. Mater.* **2011**, *23*, 733–758.

[12] C. J. Brabec, S. Gowrisanker, J. J. M. Halls, D. Laird, S. Jia, S. P. Williams, *Adv. Mater.* **2010**, *22*, 3839–3856.

[13] X. Zhan, A. Facchetti, S. Barlow, T. J. Marks, M. A. Ratner, M. R. Wasielewski, S. R. Marder, *Adv. Mater.* **2011**, *23*, 268–284.

[14] R. K. Gupta, A. A. Sudhakar, *Langmuir* **2019**, *35*, 2455–2479.

[15] T. Kato, J. Uchida, T. Ichikawa, T. Sakamoto, *Angew. Chem. Int. Ed.* **2018**, *57*, 4355–4371.

[16] T. Kato, M. Yoshio, T. Ichikawa, B. Soberats, H. Ohno, M. Funahashi, *Nat. Rev. Mater.* **2017**, *2*, 17001.

[17] S. S. Babu, V. K. Praveen, A. Ajayaghosh, *Chem. Rev.* **2014**, *114*, 1973–2129.

[18] M. Funahashi, *J. Mater. Chem. C* **2014**, *2*, 7451–7459.

[19] C. Tschierske, *Angew. Chem. Int. Ed.* **2013**, *52*, 8828–8878.

[20] J. Uchida, M. Yoshio, S. Sato, H. Yokoyama, M. Fujita, T. Kato, *Angew. Chem. Int. Ed.* **2017**, *56*, 14085–14089.

[21] B. Ni, H.-L. Xie, J. Tang, H.-L. Zhang, E.-Q. Chen, *Chem. Commun.* **2016**, *52*, 10257–10260.

[22] J. W. Goodby, C. Tschierske, P. Raynes, H. Gleeson, T. Kato, P. J. Collings, *Handbook of Liquid Crystals*, 2nd ed., Wiley-VCH Verlag GmbH & Co. KGaA, **2014**.

[23] W. Helfrich, *Mol. Cryst. Liq. Cryst.* **1973**, *21*, 187–209.

[24] B. Soberats, E. Uchida, M. Yoshio, J. Kagimoto, H. Ohno, T. Kato, *J. Am. Chem. Soc.* **2014**, *136*, 9552–9555.

[25] H. Kawamoto, *Proc. IEEE* **2002**, *90*, 460–500.

[26] T. Wöhrle, I. Wurzbach, J. Kirres, A. Kostidou, N. Kapernaum, J. Litterscheidt, J. C. Haenle, P. Staffeld, A. Baro, F. Giesselmann, S. Laschat, *Chem. Rev.* **2016**, *116*, 1139–1241.

[27] J. Eccher, W. Zajaczkowski, G. C. Faria, H. Bock, H. von Seggern, W. Pisula, I. H. Bechtold, *ACS Appl. Mater. Interfaces* **2015**, *7*, 16374–16381.

[28] X. Guo, S. Xiao, M. Myers, Q. Miao, M. L. Steigerwald, C. Nuckolls, *Proc. Natl. Acad. Sci. U.S.A.* **2009**, *106*, 691–696.

[29] V. Percec, M. Glodde, T. K. Bera, Y. Miura, I. Shiyanovskaya, K. D. Singer, V. S. K. Balagurusamy, P. A. Heiney, I. Schnell, A. Rapp, H. W. Spiess, S. D. Hudson, H. Duan, *Nature* **2002**, *419*, 384–387.

[30] S. Sergeyev, W. Pisula, Y. H. Geerts, *Chem. Soc. Rev.* **2007**, *36*, 1902–1929.

[31] P. M. Beaujuge, J. M. J. Fréchet, *J. Am. Chem. Soc.* **2011**, *133*, 20009–20029.

[32] T. Aida, E. W. Meijer, S. I. Stupp, *Science* **2012**, *335*, 813–817.

[33] F. Würthner, T. E. Kaiser, C. R. Saha-Möller, *Angew. Chem. Int. Ed.* **2011**, *50*, 3376–3410.

[34] T. F. A. De Greef, M. M. J. Smulders, M. Wolffs, A. P. H. J. Schenning, R. P. Sijbesma, E. W. Meijer, *Chem. Rev.* **2009**, *109*, 5687–5754.

[35] F. Würthner, C. R. Saha-Möller, B. Fimmel, S. Ogi, P. Leowanawat, D. Schmidt, *Chem. Rev.* **2016**, *116*, 962–1052.

[36] M. Wehner, F. Würthner, *Nat. Rev. Chem.* **2020**, *4*, 38–53.

[37] L. Brunsveld, B. J. B. Folmer, E. W. Meijer, R. P. Sijbesma, *Chem. Rev.* **2001**, *101*, 4071–4098.

[38] R. P. Sijbesma, F. H. Beijer, L. Brunsveld, B. J. B. Folmer, J. H. K. K. Hirschberg, R. F. M. Lange, J. K. L. Lowe, E. W. Meijer, *Science* **1997**, *278*, 1601–1604.

[39] L. Yang, X. Tan, Z. Wang, X. Zhang, *Chem. Rev.* **2015**, *115*, 7196–7239.

[40] E. Krieg, M. M. C. Bastings, P. Besenius, B. Rybtchinski, *Chem. Rev.* **2016**, *116*, 2414–2477.

[41] B. M. Rosen, C. J. Wilson, D. A. Wilson, M. Peterca, M. R. Imam, V. Percec, *Chem. Rev.* **2009**, *109*, 6275–6540.

[42] F. Würthner, *Pure Appl. Chem.* **2006**, *78*, 2341–2349.

[43] T. Seki, X. Lin, S. Yagai, *Asian J. Org. Chem.* **2013**, *2*, 708–724.

[44] D. Görl, X. Zhang, F. Würthner, *Angew. Chem. Int. Ed.* **2012**, *51*, 6328–6348.

[45] M. Grzybowski, D. T. Gryko, *Adv. Opt. Mater.* **2015**, *3*, 280–320.

[46] Y. Li, P. Sonar, L. Murphy, W. Hong, *Energy Environ. Sci.* **2013**, *6*, 1684–1710.

[47] S. Qu, H. Tian, *Chem. Commun.* **2012**, *48*, 3039–3051.

[48] C. B. Nielsen, M. Turbiez, I. McCulloch, *Adv. Mater.* **2013**, *25*, 1859–1880.

[49] M. Kaur, D. H. Choi, *Chem. Soc. Rev.* **2015**, *44*, 58–77.

[50] A. S. Davydov, *Sov. Phys. Usp.* **1964**, *7*, 145–178.

[51] M. Kasha, *Radiat. Res.* **1963**, *20*, 55–70.

[52] M. Kasha, H. R. Rawls, M. Ashraf El-Bayoumi, *Pure Appl. Chem.* **1965**, *11*, 371–392.

[53] F. C. Spano, *Acc. Chem. Res.* **2010**, *43*, 429–439.

[54] N. J. Hestand, F. C. Spano, *J. Chem. Phys.* **2015**, *143*, 244707.

[55] N. J. Hestand, F. C. Spano, *Acc. Chem. Res.* **2017**, *50*, 341–350.

[56] N. J. Hestand, F. C. Spano, *Chem. Rev.* **2018**, *118*, 7069–7163.

[57] T. Kobayashi, *J-Aggregates (volume 2)*, World Scientific: Signapore **2012**.

[58] T. E. Kaiser, H. Wang, V. Stepanenko, F. Würthner, *Angew. Chem. Int. Ed.* **2007**, *46*, 5541–5544.

[59] T. E. Kaiser, V. Stepanenko, F. Würthner, *J. Am. Chem. Soc.* **2009**, *131*, 6719–6732.

[60] S. Herbst, B. Soberats, P. Leowanawat, M. Stolte, M. Lehmann, F. Würthner, *Nat. Commun.* **2018**, *9*, 2646.

[61] S. Herbst, B. Soberats, P. Leowanawat, M. Lehmann, F. Würthner, *Angew. Chem. Int. Ed.* **2017**, *56*, 2162–2165.

[62] R. F. Fink, J. Seibt, V. Engel, M. Renz, M. Kaupp, S. Lochbrunner, H.-M. Zhao, J. Pfister, F. Würthner, B. Engels, *J. Am. Chem. Soc.* **2008**, *130*, 12858–12859.

[63] F. Würthner, C. Thalacker, S. Diele, C. Tschierske, *Chem. Eur. J.* **2001**, *7*, 2245–2253.

[64] H. Marciniak, X.-Q. Li, F. Würthner, S. Lochbrunner, *J. Phys. Chem. A* **2011**, *115*, 648–654.

[65] A. Nowak-Król, M. I. S. Röhr, D. Schmidt, F. Würthner, *Angew. Chem. Int. Ed.* **2017**, *56*, 11774–11778.

[66] W. Wagner, M. Wehner, V. Stepanenko, F. Würthner, *CCS Chemistry* **2019**, *1*, 598–613.

[67] W. Wagner, M. Wehner, V. Stepanenko, S. Ogi, F. Würthner, *Angew. Chem. Int. Ed.* **2017**, *56*, 16008–16012.

[68] V. Grande, B. Soberats, S. Herbst, V. Stepanenko, F. Würthner, *Chem. Sci.* **2018**, *9*, 6904–6911.

[69] C. Rehhagen, M. Stolte, S. Herbst, M. Hecht, S. Lochbrunner, F. Würthner, F. Fennel, *J. Phys. Chem. Lett.* **2020**, *11*, 6612-6617.

[70] J. Dostál, F. Fennel, F. Koch, S. Herbst, F. Würthner, T. Brixner, *Nat. Commun.* **2018**, *9*, 2466.

[71] T. E. Kaiser, I. G. Scheblykin, D. Thomsson, F. Würthner, *J. Phys. Chem. B* **2009**, *113*, 15836–15842.

[72] H. Lin, R. Camacho, Y. Tian, T. E. Kaiser, F. Würthner, I. G. Scheblykin, *Nano Lett.* **2010**, *10*, 620–626.

[73] A. Merdasa, A. Jiménez, R. Camacho, M. Meyer, F. Würthner, I. G. Scheblykin, *Nano Lett.* **2014**, *14*, 6774–6781.

[74] Y. Tian, V. Stepanenko, T. E. Kaiser, F. Würthner, I. G. Scheblykin, *Nanoscale* **2012**, *4*, 218–223.

[75] G. Scheibe, *Angew. Chem.* **1937**, *50*, 212–219.

[76] G. Scheibe, L. Kandler, H. Ecker, *Naturwissenschaften* **1937**, *25*, 75–75.

[77] E. E. Jelley, *Nature* **1936**, *138*, 1009–1010.

[78] E. E. Jelley, *Nature* **1937**, *139*, 631–632.

[79] J. C. Chang, *J. Chem. Phys.* **1977**, *67*, 3901–3909.

[80] X.-Y. Li, X.-S. Tang, F.-C. He, *Chem. Phys.* **1999**, *248*, 137–146.

[81] F. Würthner, *Chem. Commun.* **2004**, 1564–1579.

[82] G. Klebe, F. Graser, E. Hädicke, J. Berndt, *Acta Cryst. B* **1989**, *45*, 69–77.

[83] D. M. Eisele, D. H. Arias, X. Fu, E. A. Bloemsma, C. P. Steiner, R. A. Jensen, P. Rebentrost, H. Eisele, A. Tokmakoff, S. Lloyd, K. A. Nelson, D. Nicastro, J. Knoester, M. G. Bawendi, *Proc. Natl. Acad. Sci. U.S.A.* **2014**, *111*, E3367–3375.

[84] J. M. Chan, J. R. Tischler, S. E. Kooi, V. Bulovic, T. M. Swager, *J. Am. Chem. Soc.* **2009**, *131*, 5659–5666.

[85] K. Cai, J. Xie, D. Zhang, W. Shi, Q. Yan, D. Zhao, *J. Am. Chem. Soc.* **2018**, *140*, 5764–5773.

[86] K. Cai, J. Xie, D. Zhao, *J. Am. Chem. Soc.* **2014**, *136*, 28–31.

[87] Z. Chen, Y. Liu, W. Wagner, V. Stepanenko, X. Ren, S. Ogi, F. Würthner, *Angew. Chem. Int. Ed.* **2017**, *56*, 5729–5733.

[88] H. Tamiaki, *Photochem. Photobiol. Sci* **2005**, *4*, 675–680.

[89] S. Sengupta, F. Würthner, *Acc. Chem. Res.* **2013**, *46*, 2498–2512.

[90] P. Osswald, F. Würthner, *J. Am. Chem. Soc.* **2007**, *129*, 14319–14326.

[91] Z. Xie, V. Stepanenko, K. Radacki, F. Würthner, *Chem. Eur. J.* **2012**, *18*, 7060–7070.

[92] M. Gsänger, J. H. Oh, M. Könemann, H. W. Höffken, A.-M. Krause, Z. Bao, F. Würthner, *Angew. Chem. Int. Ed.* **2010**, *49*, 740–743.

[93] M. Stolte, R. Hecht, Z. Xie, L. Liu, C. Kaufmann, A. Kudzus, D. Schmidt, F. Würthner, *Adv. Opt. Mater.* **2020**, DOI: 10.1002/adom.202000926.

[94] R. F. Goldstein, L. Stryer, *Biophys. J.* **1986**, *50*, 583–599.

[95] M. M. Smulders, M. M. Nieuwenhuizen, T. F. de Greef, P. van der Schoot, A. P. Schenning, E. W. Meijer, *Chem. Eur. J.* **2010**, *16*, 362–367.

[96] T. Pullerits, V. Sundström, *Acc. Chem. Res.* **1996**, *29*, 381–389.

[97] J. M. Giaimo, A. V. Gusev, M. R. Wasielewski, *J. Am. Chem. Soc.* **2002**, *124*, 8530–8531.

[98] H. Wang, T. E. Kaiser, S. Uemura, F. Würthner, *Chem. Commun.* **2008**, 1181–1183.

[99] Z. Xie, V. Stepanenko, B. Fimmel, F. Würthner, *Mater. Horiz.* **2014**, *1*, 355–359.

[100] F. Würthner, M. Stolte, *Chem. Commun.* **2011**, *47*, 5109–5115.

[101] R. Schmidt, J. H. Oh, Y.-S. Sun, M. Deppisch, A.-M. Krause, K. Radacki, H. Braunschweig, M. Könemann, P. Erk, Z. Bao, F. Würthner, *J. Am. Chem. Soc.* **2009**, *131*, 6215–6228.

[102] B. A. Jones, M. J. Ahrens, M.-H. Yoon, A. Facchetti, T. J. Marks, M. R. Wasielewski, *Angew. Chem. Int. Ed.* **2004**, *43*, 6363–6366.

[103] C. Yan, S. Barlow, Z. Wang, H. Yan, A. K. Y. Jen, S. R. Marder, X. Zhan, *Nat. Rev. Mater.* **2018**, *3*, 18003.

[104] M. Signoretto, N. Zink-Lorre, I. Suárez, E. Font-Sanchis, Á. Sastre-Santos, V. S. Chirvony, F. Fernández-Lázaro, J. P. Martínez-Pastor, *ACS Photonics* **2017**, *4*, 114–120.

[105] A. Nowak-Król, F. Würthner, *Org. Chem. Front.* **2019**, *6*, 1272–1318.

[106] Z. Xie, B. Xiao, Z. He, W. Zhang, X. Wu, H. Wu, F. Würthner, C. Wang, F. Xie, L. Liu, Y. Ma, W.-Y. Wong, Y. Cao, *Mater. Horiz.* **2015**, *2*, 514–518.

[107] H. Liu, X. Cao, Y. Wu, Q. Liao, Á. J. Jiménez, F. Würthner, H. Fu, *Chem. Commun.* **2014**, *50*, 4620–4623.

[108] Z. Chen, M. G. Debije, T. Debaerdemaeker, P. Osswald, F. Würthner, *Chemphyschem* **2004**, *5*, 137–140.

[109] X. Cao, S. Bai, Y. Wu, Q. Liao, Q. Shi, H. Fu, J. Yao, *Chem. Commun.* **2012**, *48*, 6402–6404.

[110] P. Lova, V. Grande, G. Manfredi, M. Patrini, S. Herbst, F. Würthner, D. Comoretto, *Adv. Opt. Mater.* **2017**, *5*, 1700523.

[111] M. Hecht, T. Schlossarek, M. Stolte, M. Lehmann, F. Würthner, *Angew. Chem. Int. Ed.* **2019**, *58*, 12979–12983.

[112] D. G. Lidzey, D. D. C. Bradley, M. S. Skolnick, T. Virgili, S. Walker, D. M. Whittaker, *Nature* **1998**, *395*, 53–55.

[113] L. Tropf, C. P. Dietrich, S. Herbst, A. L. Kanibolotsky, P. J. Skabara, F. Würthner, S. D. W. Ifor, M. C. Gather, S. Höfling, *Appl. Phys. Lett.* **2017**, *110*, 153302.

[114] C. P. Dietrich, S. Höfling, M. C. Gather, *Appl. Phys. Lett.* **2014**, *105*, 233702.

[115] M. Dusel, S. Betzold, S. Brodbeck, S. Herbst, F. Würthner, D. Friedrich, B. Hecht, S. Höfling, C. P. Dietrich, *Appl. Phys. Lett.* **2017**, *110*, 201113.

[116] S. Betzold, S. Herbst, A. A. P. Trichet, J. M. Smith, F. Würthner, S. Höfling, C. P. Dietrich, *ACS Photonics* **2018**, *5*, 90–94.

[117] H. W. Schmidt, F. Würthner, *Angew. Chem. Int. Ed.* **2020**, *59*, 8766–8775.

[118] M. Pfletscher, S. Hölscher, C. Wölper, M. Mezger, M. Giese, *Chem. Mater.* **2017**, *29*, 8462–8471.

[119] T. Kato, N. Mizoshita, K. Kishimoto, *Angew. Chem. Int. Ed.* **2006**, *45*, 38–68.

[120] I. Dierking, *Textures of liquid crystals*, Wiley-VCH, Weinheim, **2003**.

[121] G. A. Andreev, M. Hartmanoá, *Phys. Status Solidi A* **1989**, *116*, 457–468.

[122] S. Mao, Z. Duan, *J. Chem. Thermodyn.* **2008**, *40*, 1046–1063.

[123] M. Lehmann, M. Jahr, B. Donnio, R. Graf, S. Gemming, I. Popov, *Chem. Eur. J.* **2008**, *14*, 3562–3576.

[124] B. Donnio, B. Heinrich, H. Allouchi, J. Kain, S. Diele, D. Guillon, D. W. Bruce, *J. Am. Chem. Soc.* **2004**, *126*, 15258–15268.

[125] D. Uhríková, P. Rybár, T. Hianik, P. Balgavý, *Chem. Phys. Lipids* **2007**, *145*, 97–105.

[126] Y. Xiao, X. Su, L. Sosa-Vargas, E. Lacaze, B. Heinrich, B. Donnio, D. Kreher, F. Mathevet, A.-J. Attias, *CrystEngComm* **2016**, *18*, 4787–4798.

[127] W. H. de Jeu, *Basix X-Ray Scattering for Soft Matter*, Oxford University Press, Oxford (UK), **2016**.

[128] T. C. Huang, H. Toraya, T. N. Blanton, Y. Wu, *J. Appl. Crystallogr.* **1993**, *26*, 180–184.

[129] P. A. Heiney, Datasqueeze, Version 3.0.7, Pennsylvania, **2018**.

[130] BIOVIA, Materials Studio 2017, Release 17.1.0.48, San Diego, **2017**.

[131] H. Sun, *J. Phys. Chem. B* **1998**, *102*, 7338–7364.

[132] H. Sun, Z. Jin, C. Yang, R. L. C. Akkermans, S. H. Robertson, N. A. Spenley, S. Miller, S. M. Todd, *J. Mol. Model.* **2016**, *22*, 47.

[133] P. P. Ewald, *Ann. Phys.* **1921**, *369*, 253–287.

[134] O. S. Makin, P. Sikorski, L. C. Serpell, *J. Appl. Crystallogr.* **2007**, *40*, 966–972.

[135] S. Yagai, *Bull. Chem. Soc. Jpn.* **2015**, *88*, 28–58.

[136] A. Kaeser, A. P. H. J. Schenning, *Adv. Mater.* **2010**, *22*, 2985–2997.

[137] S. S. Babu, S. Prasanthkumar, A. Ajayaghosh, *Angew. Chem. Int. Ed.* **2012**, *51*, 1766–1776.

[138] Y. Hirai, S. S. Babu, V. K. Praveen, T. Yasuda, A. Ajayaghosh, T. Kato, *Adv. Mater.* **2009**, *21*, 4029–4033.

[139] K. Sakakibara, P. Chithra, B. Das, T. Mori, M. Akada, J. Labuta, T. Tsuruoka, S. Maji, S. Furumi, L. K. Shrestha, J. P. Hill, S. Acharya, K. Ariga, A. Ajayaghosh, *J. Am. Chem. Soc.* **2014**, *136*, 8548–8551.

[140] A. C. Grimsdale, K. Müllen, *Angew. Chem. Int. Ed.* **2005**, *44*, 5592–5629.

[141] J. A. A. W. Elemans, R. Van Hameren, R. J. M. Nolte, A. E. Rowan, *Adv. Mater.* **2006**, *18*, 1251–1266.

[142] A. Wicklein, A. Lang, M. Muth, M. Thelakkat, *J. Am. Chem. Soc.* **2009**, *131*, 14442–14453.

[143] V. Percec, M. Peterca, T. Tadjiev, X. Zeng, G. Ungar, P. Leowanawat, E. Aqad, M. R. Imam, B. M. Rosen, U. Akbey, R. Graf, S. Sekharan, D. Sebastiani, H. W. Spiess, P. A. Heiney, S. D. Hudson, *J. Am. Chem. Soc.* **2011**, *133*, 12197–12219.

[144] A. Nowak-Król, B. Fimmel, M. Son, D. Kim, F. Würthner, *Faraday Discuss.* **2015**, *185*, 507–527.

[145] Y. Yamamoto, T. Fukushima, Y. Suna, N. Ishii, A. Saeki, S. Seki, S. Tagawa, M. Taniguchi, T. Kawai, T. Aida, *Science* **2006**, *314*, 1761–1764.

[146] S. Prasanthkumar, S. Ghosh, V. C. Nair, A. Saeki, S. Seki, A. Ajayaghosh, *Angew. Chem. Int. Ed.* **2015**, *54*, 946–950.

[147] A. T. Haedler, K. Kreger, A. Issac, B. Wittmann, M. Kivala, N. Hammer, J. Köhler, H.-W. Schmidt, R. Hildner, *Nature* **2015**, *523*, 196.

[148] W. Pisula, M. Kastler, D. Wasserfallen, J. W. F. Robertson, F. Nolde, C. Kohl, K. Müllen, *Angew. Chem. Int. Ed.* **2006**, *45*, 819–823.

[149] G. Fernández, E. M. Pérez, L. Sánchez, N. Martín, *Angew. Chem. Int. Ed.* **2008**, *47*, 1094–1097.

[150] L. F. Dössel, V. Kamm, I. A. Howard, F. Laquai, W. Pisula, X. Feng, C. Li, M. Takase, T. Kudernac, S. De Feyter, K. Müllen, *J. Am. Chem. Soc.* **2012**, *134*, 5876–5886.

[151] W.-S. Li, A. Saeki, Y. Yamamoto, T. Fukushima, S. Seki, N. Ishii, K. Kato, M. Takata, T. Aida, *Chem. Asian J.* **2010**, *5*, 1566–1572.

[152] P. Leclère, M. Surin, P. Viville, R. Lazzaroni, A. F. M. Kilbinger, O. Henze, W. J. Feast, M. Cavallini, F. Biscarini, A. P. H. J. Schenning, E. W. Meijer, *Chem. Mater.* **2004**, *16*, 4452–4466.

[153] G. Seybold, G. Wagenblast, *Dyes Pigm.* **1989**, *11*, 303–317.

[154] R. Sens, K. H. Drexhage, *J. Lumin.* **1981**, *24-25*, 709–712.

[155] C. Würth, M. Grabolle, J. Pauli, M. Spieles, U. Resch-Genger, *Nat. Protoc.* **2013**, *8*, 1535–1550.

[156] T. Klingstedt, H. Shirani, J. Mahler , B. M. Wegenast-Braun , S. Nyström, M. Goedert, M. Jucker , K. P. R. Nilsson, *Chem. Eur. J.* **2015**, *21*, 9072–9082.

[157] H. Maeda, K. Chigusa, T. Sakurai, K. Ohta, S. Uemura, S. Seki, *Chem. Eur. J.* **2013**, *19*, 9224–9233.

[158] M. M. Smulders, A. P. Schenning, E. W. Meijer, *J. Am. Chem. Soc.* **2008**, *130*, 606–611.

[159] M.-A. Muth, G. Gupta, A. Wicklein, M. Carrasco-Orozco, T. Thurn-Albrecht, M. Thelakkat, *J. Phys. Chem. C* **2014**, *118*, 92–102.

[160] P. Scherrer, *Nachr. Ges. Wiss. Göttingen, Math.-Phys. Kl.* **1918**, *2*, 98–100.

[161] M. Hecht, T. Schlossarek, Y. Tsutsui, A. Schmiedel, M. Holzapfel, M. Stolte, C. Lambert, S. Seki, M. Lehmann, F. Würthner, *ACS Appl. Nano Mater.* **2020**, DOI: 10.1021/acsanm.1020c02189.

[162] F. Ishiwari, Y. Shoji, T. Fukushima, *Chem. Sci.* **2018**, *9*, 2028–2041.

[163] D. González-Rodríguez, A. P. H. J. Schenning, *Chem. Mater.* **2011**, *23*, 310–325.

[164] S. I. Stupp, L. C. Palmer, *Chem. Mater.* **2014**, *26*, 507–518.

[165] V. K. Praveen, B. Vedhanarayanan, A. Mal, R. K. Mishra, A. Ajayaghosh, *Acc. Chem. Res.* **2020**, *53*, 496–507.

[166] J. López-Andarias, M. J. Rodriguez, C. Atienza, J. L. López, T. Mikie, S. Casado, S. Seki, J. L. Carrascosa, N. Martín, *J. Am. Chem. Soc.* **2015**, *137*, 893–897.

[167] R. Charvet, Y. Yamamoto, T. Sasaki, J. Kim, K. Kato, M. Takata, A. Saeki, S. Seki, T. Aida, *J. Am. Chem. Soc.* **2012**, *134*, 2524–2527.

[168] A. M. van de Craats, J. M. Warman, K. Müllen, Y. Geerts, J. D. Brand, *Adv. Mater.* **1998**, *10*, 36–38.

[169] Z. Chen, V. Stepanenko, V. Dehm, P. Prins, L. D. A. Siebbeles, J. Seibt, P. Marquetand, V. Engel, F. Würthner, *Chem. Eur. J.* **2007**, *13*, 436–449.

[170] A. Das, S. Ghosh, *Angew. Chem. Int. Ed.* **2014**, *53*, 2038–2054.

[171] F. Würthner, Z. Chen, F. J. M. Hoeben, P. Osswald, C.-C. You, P. Jonkheijm, J. v. Herrikhuyzen, A. P. H. J. Schenning, P. P. A. M. van der Schoot, E. W. Meijer, E. H. A. Beckers, S. C. J. Meskers, R. A. J. Janssen, *J. Am. Chem. Soc.* **2004**, *126*, 10611–10618.

[172] P. Jonkheijm, N. Stutzmann, Z. Chen, D. M. de Leeuw, E. W. Meijer, A. P. H. J. Schenning, F. Würthner, *J. Am. Chem. Soc.* **2006**, *128*, 9535–9540.

[173] M. Lehmann, M. Dechant, M. Holzapfel, A. Schmiedel, C. Lambert, *Angew. Chem. Int. Ed.* **2019**, *58*, 3610–3615.

[174] Á. J. Jiménez, R. M. K. Calderón, M. S. Rodríguez-Morgade, D. M. Guldi, T. Torres, *Chem. Sci.* **2013**, *4*, 1064–1074.

[175] P. E. Hartnett, S. M. Dyar, E. A. Margulies, L. E. Shoer, A. W. Cook, S. W. Eaton, T. J. Marks, M. R. Wasielewski, *Chem. Sci.* **2015**, *6*, 402–411.

[176] T. Yasuda, T. Shimizu, F. Liu, G. Ungar, T. Kato, *J. Am. Chem. Soc.* **2011**, *133*, 13437–13444.

[177] A. R. Mallia, P. S. Salini, M. Hariharan, *J. Am. Chem. Soc.* **2015**, *137*, 15604–15607.

[178] S. Lucas, T. Leydecker, P. Samorì, E. Mena-Osteritz, P. Bäuerle, *Chem. Commun.* **2019**, *55*, 14202–14205.

[179] C. Röger, Y. Miloslavina, D. Brunner, A. R. Holzwarth, F. Würthner, *J. Am. Chem. Soc.* **2008**, *130*, 5929–5939.

[180] Y. Yamamoto, T. Fukushima, A. Saeki, S. Seki, S. Tagawa, N. Ishii, T. Aida, *J. Am. Chem. Soc.* **2007**, *129*, 9276–9277.

[181] T. Brixner, R. Hildner, J. Köhler, C. Lambert, F. Würthner, *Adv. Energy Mater.* **2017**, *7*, 1700236.

[182] H. A. Becerril, M. E. Roberts, Z. Liu, J. Locklin, Z. Bao, *Adv. Mater.* **2008**, *20*, 2588–2594.

[183] M. Gsänger, E. Kirchner, M. Stolte, C. Burschka, V. Stepanenko, J. Pflaum, F. Würthner, *J. Am. Chem. Soc.* **2014**, *136*, 2351–2362.

[184] M. Stolte, M. Gsänger, R. Hofmockel, S.-L. Suraru, F. Würthner, *Phys. Chem. Chem. Phys.* **2012**, *14*, 14181–14185.

[185] Z. Lu, C. Wang, W. Deng, M. T. Achille, J. Jie, X. Zhang, *J. Mater. Chem. C* **2020**.

[186] R. S. Becker, J. Seixas de Melo, A. L. Maçanita, F. Elisei, *J. Phys. Chem.* **1996**, *100*, 18683–18695.

[187] G. Seybold, *Dyes Pigm.* **1989**, *11*, 303–317.

[188] E. Lang, F. Würthner, J. Köhler, *Chemphyschem* **2005**, *6*, 935–941.

[189] P. Leowanawat, A. Nowak-Król, F. Würthner, *Org. Chem. Front.* **2016**, *3*, 537–544.

[190] C. M. Cardona, W. Li, A. E. Kaifer, D. Stockdale, G. C. Bazan, *Adv. Mater.* **2011**, *23*, 2367–2371.

[191] M. Hecht, P. Leowanawat, T. Gerlach, V. Stepanenko, M. Stolte, M. Lehmann, F. Würthner, *Angew. Chem. Int. Ed.* **2020**, *59*, 17084–17090.

[192] S. Seki, A. Saeki, T. Sakurai, D. Sakamaki, *Phys. Chem. Chem. Phys.* **2014**, *16*, 11093–11113.

[193] S. Wolter, K. Magnus Westphal, M. Hempel, F. Würthner, O. Kühn, S. Lochbrunner, *J. Phys. B* **2017**, *50*, 184005.

[194] F. Würthner, A. Sautter, *Chem. Commun.* **2000**, 445–446.

[195] I. H. M. van Stokkum, D. S. Larsen, R. van Grondelle, *Biochim. Biophys. Acta* **2004**, *1657*, 82–104.

[196] J. J. Snellenburg, S. P. Laptenok, R. Seger, K. M. Mullen, I. H. M. van Stokkum, *J. Stat. Softw.* **2012**, *49*, 1–22.

[197] S. Lightowler, M. Hird, *Chem. Mater.* **2005**, *17*, 5538–5549.

[198] G. M. Fischer, E. Daltrozzo, A. Zumbusch, *Angew. Chem. Int. Ed.* **2011**, *50*, 1406–1409.

[199] N. R. Ávila-Rovelo, A. Ruiz-Carretero, *Org. Mater.* **2020**, *02*, 047–063.

[200] L. B. Å. Johansson, H. Langhals, *Spectrochim. Acta A* **1991**, *47*, 857–861.

[201] J. Salbeck, H. Kunkely, H. Langhals, R. W. Saalfrank, J. Daub, *Chimia* **1989**, *43*, 6–9.

[202] F. Würthner, C. Thalacker, A. Sautter, W. Schärtl, W. Ibach, O. Hollricher, *Chem. Eur. J.* **2000**, *6*, 3871–3886.

[203] S. Yagai, M. Usui, T. Seki, H. Murayama, Y. Kikkawa, S. Uemura, T. Karatsu, A. Kitamura, A. Asano, S. Seki, *J. Am. Chem. Soc.* **2012**, *134*, 7983–7994.

[204] B. A. Jones, A. Facchetti, T. J. Marks, M. R. Wasielewski, *Chem. Mater.* **2007**, *19*, 2703–2705.

[205] R. Shivanna, S. Shoaee, S. Dimitrov, S. K. Kandappa, S. Rajaram, J. R. Durrant, K. S. Narayan, *Energy Environ. Sci.* **2014**, *7*, 435–441.

[206] B. E. Partridge, P. Leowanawat, E. Aqad, M. R. Imam, H.-J. Sun, M. Peterca, P. A. Heiney, R. Graf, H. W. Spiess, X. Zeng, G. Ungar, V. Percec, *J. Am. Chem. Soc.* **2015**, *137*, 5210–5224.

[207] M. J. Ahrens, M. J. Fuller, M. R. Wasielewski, *Chem. Mater.* **2003**, *15*, 2684–2686.

[208] A. S. Lukas, Y. Zhao, S. E. Miller, M. R. Wasielewski, *J. Phys. Chem. B* **2002**, *106*, 1299–1306.

[209] P. Osswald, D. Leusser, D. Stalke, F. Würthner, *Angew. Chem. Int. Ed.* **2005**, *44*, 250–253.

[210] M. M. Safont-Sempere, V. Stepanenko, M. Lehmann, F. Würthner, *J. Mater. Chem.* **2011**, *21*, 7201–7209.

[211] M. Wehner, M. I. S. Röhr, M. Bühler, V. Stepanenko, W. Wagner, F. Würthner, *J. Am. Chem. Soc.* **2019**, *141*, 6092–6107.

[212] T. Fukui, S. Kawai, S. Fujinuma, Y. Matsushita, T. Yasuda, T. Sakurai, S. Seki, M. Takeuchi, K. Sugiyasu, *Nat. Chem.* **2017**, *9*, 493–499.

[213] P. A. Korevaar, S. J. George, A. J. Markvoort, M. M. J. Smulders, P. A. J. Hilbers, A. P. H. J. Schenning, T. F. A. De Greef, E. W. Meijer, *Nature* **2012**, *481*, 492–496.

[214] D. van der Zwaag, P. A. Pieters, P. A. Korevaar, A. J. Markvoort, A. J. H. Spiering, T. F. A. de Greef, E. W. Meijer, *J. Am. Chem. Soc.* **2015**, *137*, 12677–12688.

[215] F. Fennel, S. Wolter, Z. Xie, P.-A. Plötz, O. Kühn, F. Würthner, S. Lochbrunner, *J. Am. Chem. Soc.* **2013**, *135*, 18722–18725.

[216] H. Wang, Y. Zhang, Y. Chen, H. Pan, X. Ren, Z. Chen, *Angew. Chem. Int. Ed.* **2020**, *59*, 5185–5192.

[217] E. E. Greciano, B. Matarranz, L. Sánchez, *Angew. Chem. Int. Ed.* **2018**, *57*, 4697–4701.

[218] T. Aida, E. W. Meijer, *Isr. J. Chem.* **2020**, *60*, 33–47.

[219] J. Matern, Y. Dorca, L. Sánchez, G. Fernández, *Angew. Chem. Int. Ed.* **2019**, *58*, 16730–16740.

[220] Á. J. Jiménez, M.-J. Lin, C. Burschka, J. Becker, V. Settels, B. Engels, F. Würthner, *Chem. Sci.* **2014**, *5*, 608–619.

[221] G. D. Scholes, K. P. Ghiggino, *J. Phys. Chem.* **1994**, *98*, 4580–4590.

[222] C. Kaufmann, D. Bialas, M. Stolte, F. Würthner, *J. Am. Chem. Soc.* **2018**, *140*, 9986–9995.

[223] M. M. Safont-Sempere, G. Fernández, F. Würthner, *Chem. Rev.* **2011**, *111*, 5784–5814.

[224] S. Ogi, K. Sugiyasu, S. Manna, S. Samitsu, M. Takeuchi, *Nat. Chem.* **2014**, *6*, 188–195.

[225] J. J. P. Stewart, *J. Mol. Model.* **2013**, *19*, 1–32.

[226] J. J. P. Stewart, MOPAC2016, Stewart Computational Chemistry, Colorado Springs, CO, USA, **2016**.

[227] M. Hecht, B. Soberats, J. Zhu, V. Stepanenko, S. Agarwal, A. Greiner, F. Würthner, *Nanoscale Horiz.* **2019**, *4*, 169–174.

[228] C. Rest, R. Kandanelli, G. Fernández, *Chem. Soc. Rev.* **2015**, *44*, 2543–2572.

[229] H. Kar, D. W. Gehrig, N. K. Allampally, G. Fernández, F. Laquai, S. Ghosh, *Chem. Sci.* **2016**, *7*, 1115–1120.

[230] D. J. Broer, C. M. W. Bastiaansen, M. G. Debije, A. P. H. J. Schenning, *Angew. Chem. Int. Ed.* **2012**, *51*, 7102–7109.

[231] C. J. Mueller, C. R. Singh, M. Fried, S. Huettner, M. Thelakkat, *Adv. Funct. Mater.* **2015**, *25*, 2725–2736.

[232] F. Wieberger, C. Neuber, C. K. Ober, H. W. Schmidt, *Adv. Mater.* **2012**, *24*, 5939–5944.

[233] G. R. Whittell, M. D. Hager, U. S. Schubert, I. Manners, *Nat Mater* **2011**, *10*, 176.

[234] Z. Chen, A. Lohr, C. R. Saha-Möller, F. Würthner, *Chem. Soc. Rev.* **2009**, *38*, 564–584.

[235] M. Wei, Y. Gao, X. Li, M. J. Serpe, *Polym. Chem.* **2017**, *8*, 127–143.

[236] B. R. Kaafarani, *Chem. Mater.* **2011**, *23*, 378–396.

[237] A. P. Schenning, E. W. Meijer, *Chem. Commun.* **2005**, 3245–3258.

[238] H. Coles, S. Morris, *Nat. Photonics* **2010**, *4*, 676–685.

[239] A. Rösler, G. W. M. Vandermeulen, H.-A. Klok, *Adv. Drug Deliv. Rev.* **2001**, *53*, 95–108.

[240] C. Guo, J. Wang, F. Cao, R. J. Lee, G. Zhai, *Drug Discov. Today* **2010**, *15*, 1032–1040.

[241] M. Yoshio, T. Mukai, H. Ohno, T. Kato, *J. Am. Chem. Soc.* **2004**, *126*, 994–995.

[242] K. Nakashima, K. Tsuboi, H. Matsumoto, R. Ishige, M. Tokita, J. Watanabe, A. Tanioka, *Macromol. Rapid Commun.* **2010**, *31*, 1641–1645.

[243] D. K. Kim, M. Hwang, J. P. F. Lagerwall, *J. Polym. Sci. Pol. Phys.* **2013**, *51*, 855–867.

[244] Y. Wu, Q. An, J. Yin, T. Hua, H. Xie, G. Li, H. Tang, *Colloid. Polym. Sci.* **2008**, *286*, 897–905.

[245] D. H. Reneker, A. L. Yarin, H. Fong, S. Koombhongse, *J. Appl. Phys.* **2000**, *87*, 4531–4547.

[246] S. Jiang, S. Agarwal, A. Greiner, *Angew. Chem. Int. Ed.* **2017**, *56*, 15520–15538.

[247] T. D. Brown, P. D. Dalton, D. W. Hutmacher, *Prog. Polym. Sci.* **2016**, *56*, 116–166.

[248] S. Agarwal, A. Greiner, J. H. Wendorff, *Prog. Polym. Sci.* **2013**, *38*, 963–991.

[249] X. Shi, W. Zhou, D. Ma, Q. Ma, D. Bridges, Y. Ma, A. Hu, *J. Nanomater.* **2015**, *2015*, 20.

[250] J. D. Schiffman, C. L. Schauer, *Polym. Rev.* **2008**, *48*, 317–352.

[251] A. Celebioglu, T. Uyar, *Chem. Commun.* **2010**, *46*, 6903–6905.

[252] X. Yan, M. Zhou, J. Chen, X. Chi, S. Dong, M. Zhang, X. Ding, Y. Yu, S. Shao, F. Huang, *Chem. Commun.* **2011**, *47*, 7086–7088.

[253] D. Kluge, J. C. Singer, B. R. Neugirg, J. W. Neubauer, H.-W. Schmidt, A. Fery, *Polymer* **2012**, *53*, 5754–5759.

[254] K. Wang, C.-Y. Wang, Y. Wang, H. Li, C.-Y. Bao, J.-Y. Liu, S. X.-A. Zhang, Y.-W. Yang, *Chem. Commun.* **2013**, *49*, 10528–10530.

[255] J. C. Singer, A. Ringk, R. Giesa, H.-W. Schmidt, *Macromol. Mater. Eng.* **2015**, *300*, 259–276.

[256] X. Wang, Y. Han, Y. Liu, G. Zou, Z. Gao, F. Wang, *Angew. Chem. Int. Ed.* **2017**, *56*, 12466–12470.

[257] B. Soberats, M. Hecht, F. Würthner, *Angew. Chem. Int. Ed.* **2017**, *56*, 10771–10774.

[258] D. Sahoo, M. Peterca, E. Aqad, B. E. Partridge, P. A. Heiney, R. Graf, H. W. Spiess, X. Zeng, V. Percec, *J. Am. Chem. Soc.* **2016**, *138*, 14798–14807.

[259] S. Ogi, V. Stepanenko, J. Thein, F. Würthner, *J. Am. Chem. Soc.* **2016**, *138*, 670–678.

[260] G. Fernández, M. Stolte, V. Stepanenko, F. Würthner, *Chem. Eur. J.* **2013**, *19*, 206–217.

[261] Y.-H. Jeong, C.-H. Lee, W.-D. Jang, *Chem. Asian J.* **2012**, *7*, 1562–1566.

[262] M. Fukuda, K. Kodama, H. Yamamoto, K. Mito, *Dyes Pigm.* **2004**, *63*, 115–125.

[263] W.-S. Li, Y. Yamamoto, T. Fukushima, A. Saeki, S. Seki, S. Tagawa, H. Masunaga, S. Sasaki, M. Takata, T. Aida, *J. Am. Chem. Soc.* **2008**, *130*, 8886–8887.

[264] H. Maeda, K. Chigusa, R. Yamakado, T. Sakurai, S. Seki, *Chem. Eur. J.* **2015**, *21*, 9520–9527.

[265] A. Oleson, T. Zhu, I. S. Dunn, D. Bialas, Y. Bai, W. Zhang, M. Dai, D. R. Reichman, R. Tempelaar, L. Huang, F. C. Spano, *J. Phys. Chem. C* **2019**, *123*, 20567–20578.

Individual Contributions

The coauthors of the publications presented in this cumulative thesis are informed and agree with the reprint as well as with the individual contributions stated below.

Photoconductive Core–Shell Liquid-Crystal of a Perylene Bisimide J-Aggregate Donor-Acceptor Dyad

M. Hecht, T. Schlossarek, M. Stolte, M. Lehmann, F. Würthner, *Angew. Chem. Int. Ed.* **2019**, *58*, 12979–12983.

Author	**M.H.**	**T.S.**	**M.S.**	**M.L.**	**F.W.**
Design of research	35%	-	10%	15%	40%
Synthesis and characterization	100%	-	-	-	-
UV/Vis spectroscopy	100%	-	-	-	-
Molecular modelling	70%	10%	-	20%	-
FT-IR spectroscopy	100%	-	-	-	-
X-ray scattering	70%	10%	-	20%	-
Fluorescence spectroscopy	100%	-	-	-	-
Cyclic voltammetry	100%	-	-	-	-
Differential scanning calorimetry	100%	-	-	-	-
Investigation of photoconductivity	70%	-	30%	-	-
Polarized optical microscopy	100%	-	-	-	-
Publication writing	70%	-	10%	10%	10%
Publication correction	-	-	10%	30%	60%
Publication coordination	30%	-	30%	-	40%

Nanoscale Columnar Bundles Based on Multistranded Core-Shell Liquid Crystals of Perylene Bisimide J-Aggregate Donor-Acceptor Dyads for Photoconductivity Devices with Enhanced Performance Through Macroscopic Alignment

M. Hecht, T. Schlossarek, Y. Tsutsui, A. Schmiedel, M. Holzapfel, M. Stolte, C. Lambert, S. Seki, M. Lehmann, F. Würthner, *ACS Appl. Nano Mater.* **2020**, DOI: 10.1021/acsanm.1020c02189.

Author	**M.He.**	**T.S.**	**S.G.**	**Y.T.**	**A.S.**	**M.Ho.**	**M.S.**	**C.L.**	**S.S.**	**M.L.**	**F.W.**
Design of research	35%	-	-	-	-	-	10%	-	-	15%	40%
Synthesis and characterization	20%	80%	-	-	-	-	-	-	-	-	-
UV/Vis spectroscopy	80%	20%	-	-	-	-	-	-	-	-	-
Fluorescence spectroscopy	60%	40%	-	-	-	-	-	-	-	-	-
Optical spectroscopy in the solid state (FT-IR, UV/Vis)	50%	50%	-	-	-	-	-	-	-	-	-
Molecular modelling	60%	20%	-	-	-	-	-	-	-	20%	-
X-ray scattering	60%	20%	-	-	-	-	-	-	-	20%	-
Cyclic voltammetry	100%	-	-	-	-	-	-	-	-	-	-
Preparation of two-contact devices	90%	-	-	-	-	-	10%	-	-	-	-
Electrical characterization	90%	-	-	-	-	-	10%	-	-	-	-
Transient absorption spectroscopy	10%	-	-	-	30%	30%	-	30%	-	-	-
Flash photolysis time-resolved microwave conductivity	10%	-	30%	30%	-	-	-	-	30%	-	-
Publication writing	65%	-	5%	-	-	5%	-	5%	5%	5%	10%
Publication correction	-	-	-	-	-	-	-	-	-	20%	80%
Publication coordination	50%	-	-	-	-	-	-	-	-	-	50%

Self-Sorting Supramolecular Polymerization into Helical or Lamellar Aggregates of Tetra-Bay-Acyloxy Perylene Bisimide

M. Hecht, P. Leowanawat, T. Gerlach, V. Stepanenko, M. Stolte, M. Lehmann, F. Würthner, *Angew. Chem. Int. Ed.* **2020**, *59*, 17084–17090.

Author	**M.H.**	**P.L.**	**T.G.**	**V.S.**	**M.S.**	**M.L.**	**F.W.**
Design of research	30%	-	-	-	10%	-	60%
Synthesis and characterization	10%	70%	20%	-	-	-	-
UV/Vis spectroscopy	90%	10%	-	-	-	-	-
Fluorescence spectroscopy	90%	10%	-	-	-	-	-
Atomic force microscopy	10%	-	-	90%	-	-	-
Scanning electron microscopy	10%	-	-	90%	-	-	-
Optical spectroscopy in the solid state (FT-IR, UV/Vis)	100%	-	-	-	-	-	-
Molecular modelling	70%	-	-	-	-	30%	-
X-ray scattering	90%	-	-	-	-	10%	-
Cyclic voltammetry	100%	-	-	-	-	-	-
Polarized optical microscopy	100%	-	-	-	-	-	-
Publication writing	70%	-	-	-	10%	10%	10%
Publication correction	-	-	-	-	20%	20%	60%
Publication coordination	30%	-	-	-	20%	-	50%

Anisotropic Microfibers of a Liquid-Crystalline Diketopyrrolopyrrole by Self-Assembly-Assisted Electrospinning

M. Hecht, B. Soberats, J. Zhu, V. Stepanenko, S. Agarwal, A. Greiner, F. Würthner, *Nanoscale Horiz.* **2019**, *4*, 169–174.

Author	**M.H.**	**B.S.**	**J.Z.**	**V.S.**	**S.A.**	**A.G.**	**F.W.**
Design of research	30%	10%	-	-	10%	10%	40%
Synthesis and characterization	100%	-	-	-	-	-	-
X-ray scattering	70%	30%	-	-	-	-	-
Molecular modelling	50%	50%	-	-	-	-	-
FT-IR spectroscopy	100%	-	-	-	-	-	-
Atomic force microscopy & scanning electron microscopy	10%	-	-	90%	-	-	-
Selected area electron diffraction	-	-	-	100%	-	-	-
UV/Vis spectroscopy	100%	-	-	-	-	-	-
Electrospinning	30%	-	50%	-	10%	10%	-
Polarized optical microscopy	80%	20%	-	-	-	-	-
Publication writing	60%	10%	-	-	5%	5%	20%
Publication correction	-	40%	-	-	-	-	60%
Publication coordination	20%	20%	-	-	-	-	60%

Danksagung

Mein besonderer Dank gilt Prof. Dr. Frank Würthner für die Vergabe des interessanten Forschungsthemas und die Freiheiten zur Entwicklung der Projekte. Weiterhin danke ich Ihm für seine stete Unterstützung und die hervorragenden Arbeitsbedingungen am Institut für Organische Chemie und am Center for Nanosystems Chemistry.

Mein weiterer Dank gilt Prof. Dr. Matthias Lehmann für die fachliche Unterstützung im Gebiet der Flüssigkristalle und die konstruktiven Diskussionen.

Weiterhin bedanke ich mich bei Dr. Matthias Stolte für ein stets offenes Ohr, die zahlreichen fachlichen Diskussionen über Spektroskopie und organische Elektronik, sowie die exzellente Zusammenarbeit beim Erstellen von Manuskripten.

Dr. Bartolome Soberats danke ich für die Einführung in das Fachgebiet der Flüssigkristalle während meiner Masterarbeit, welche den Grundstein für meine weiteren Arbeiten gelegt hat.

Bei Dr. Vladimir Stepanenko bedanke ich mich für AFM-, SEM- und SAED-Untersuchungen.

Dr. David Bialas danke ich für zahlreiche Diskussionen zur Exzitonenkopplung und Hilfe bei theoretischen Rechnungen.

Dr. Chantu Saha-Möller danke ich für das sorgfältige Korrekturlesen einiger Manuskripte.

Mein weiterer Dank gilt den Mitarbeitern der Abteilungen für NMR Spektroskopie, Massenspektrometrie und Elementaranalyse für die Durchführung von Experimenten sowie die Hilfe bei deren Auswertung.

Tim Schlossarek und Tabea Gerlach danke ich für die ausgezeichnete Zusammenarbeit im Rahmen ihrer Masterarbeiten.

Moritz Dechant und Martin Lambov danke ich für die Unterstützung bei technischen Fragen zum Röntgengerät.

Julius Albert, Olga Anhat, Joachim Bialas, Ann-Kathrin Lenz, Ana-Maria Krause und Astrid Kudzus danke ich für das freundliche Arbeitsklima und die Hilfsbereitschaft im

Laboralltag. Christiana Toussaint, Eleonore Klaus, Jennifer Begall, Sarah Bullnheimer und Lisa Weidner danke ich für die Hilfe bei allen bürokratischen Angelegenheiten.

Bei Prof. Dr. Seema Agarwal, Prof. Dr. Andreas Greiner und Dr. Jian Zhu bedanke ich mich für die nette Zeit in Bayreuth und die erfolgreiche Kollaboration. Bei Prof. Dr. Shu Seki, Dr. Samrat Ghosh, Dr. Yusuke Tsutsui, Prof. Dr. Lambert, Dr. Marco Holzapfel und Alexander Schmiedel bedanke ich mich für die Zusammenarbeit im Bereich der Mikrowellenleitfähigkeit und Ultrakurzzeitspektroskopie.

Bei allen aktuellen und ehemaligen Mitgliedern des AK Würthner, AK Beuerle, AK Nowak-Król und AK Lehmann möchte ich mich herzlich für die angenehme Arbeitsatmosphäre und die schöne gemeinsame Zeit bedanken.

Zuletzt möchte ich mich bei meiner Familie, meinen Freunden und Christina für ihre fortwährende Unterstützung bedanken.

List of Publications

6 M. Hecht, T. Schlossarek, Y. Tsutsui, A. Schmiedel, M. Holzapfel, M. Stolte, C. Lambert, S. Seki, M. Lehmann, F. Würthner, *ACS Appl. Nano Mater.* **2020**, DOI: 10.1021/acsanm.1020c02189.

5 C. Rehhagen, M. Stolte, S. Herbst, M. Hecht, S. Lochbrunner, F. Würthner, F. Fennel, *J. Phys. Chem. Lett.* **2020**, *11*, 6612-6617.

4 M. Hecht, P. Leowanawat, T. Gerlach, V. Stepanenko, M. Stolte, M. Lehmann, F. Würthner, *Angew. Chem. Int. Ed.* **2020**, *59*, 17084–17090.

3 M. Hecht, T. Schlossarek, M. Stolte, M. Lehmann, F. Würthner, *Angew. Chem. Int. Ed.* **2019**, *58*, 12979–12983.

2 M. Hecht, B. Soberats, J. Zhu, V. Stepanenko, S. Agarwal, A. Greiner, F. Würthner, *Nanoscale Horiz.* **2019**, *4*, 169–174.

1 B. Soberats, M. Hecht, F. Würthner, *Angew. Chem. Int. Ed.* **2017**, *56*, 10771-10774.